Imperial College London

One-pot extraction and purification of vanadium from industrial by-products using ionic liquids followed by simultaneous in-situ vanadium and solvent recovery

Amir Hossein Mohammad Dezashibi

Thesis submitted as partial fulfilment of the requirements for the degree of Doctoral of Philosophy

Department of Chemical Engineering, Imperial College London, London SW7 2AZ, 2018-2022

DECLARATION OF ORIGINALITY AND COPYRIGHT

The work detailed in this thesis was performed at Imperial College London from October 2018 to September 2022. Unless otherwise stated the work is my own and has not been previously submitted for a degree at Imperial College London or any other university.

The copyright of this thesis rests with the author. Unless otherwise indicated, its contents are licensed under a Creative Commons Attribution-Non-commercial 4.0 International Licence (CC BY-NC). Under this licence, you may copy and redistribute the material in any medium or format. You may also create and distribute modified versions of the work. This is on the condition that: you credit the author and do not use it, or any derivative works, for a commercial purpose. When reusing or sharing this work, ensure you make the licence terms clear to others by naming the licence and linking to the licence text. Where a work has been adapted, you should indicate that the work has been changed and describe those changes. Please seek permission from the copyright holder for uses of this work that are not included in this licence or permitted under UK Copyright Law.

Abstract

The recovery of ultra-pure vanadium(V) from gasifier ash produced by a gasification unit has been investigated by a purely hydrometallurgical technique which uses a task-specific ionic liquid, tetramethylammonium hydroxide (TMA^+OH^-), for the selective extraction of vanadium(V) from the ash matrix containing 24 elements.

The leaching kinetics behaviour of vanadium(V) was investigated from the gasifier at high pH and the effects of the following conditions were investigated: temperature, ionic liquid concentration, liquid-to-solid ratio, and oxidant concentration. An oxidant was used because vanadium was only partially oxidised under the reductive environment of the gasification units. The extraction of silicon and aluminium compounds was almost negligible due to the unfavourable chemical interaction with the ionic liquid, solving one of the biggest challenges in the hydrometallurgical extraction of vanadium(V). Recoverable and unrecoverable vanadium phases were identified and characterised in the gasifier ash which accurately explained and predicted the leaching efficiency. The results may be used to predict the equilibrium vanadium(V) extraction yield of samples from other sources. Control experiments were also conducted to mimic the extraction behaviour of vanadium(V) from phases consisting of M-V-O with M being an alkali or a transition metal.

Highly concentrated and pure vanadium(V) solutions were obtained that encouraged the development of a technique for the recovery of both the leached vanadium(V) and the ionic liquid. Membrane electrolysis technology was utilised to separate the ionic liquid cations from the leach liquor and to regenerate it in the cathode chamber of the electrochemical reactor. In the anode chamber, vanadium(V) was deposited as a novel vanadium compound onto the surface of the anode which was later recovered in a ternary mixture and purified as V_2O_5 for the final product.

In order to keep the process sustainable i.e., eliminate the use of oxidant, a method was developed by which partially oxidised vanadium was electrochemically oxidised through a heterogenous reaction mechanism. The electrochemically oxidised ash was then used as a feedstock to leach vanadium(V). This third step is optional and can be integrated into the leaching and recovery steps.

The process which is called the ionoLeach process was developed as a green and selective method for the extraction and purification of vanadium(V) from wastes/by-

products using ionic liquids as solvents with no ongoing chemical use. The process uses heat, electricity, water and vanadium-bearing waste and produces hydrogen gas, oxygen gas and ultra-pure V_2O_5.

A techno-economic assessment was performed based on the parameters that were calculated in this research. Three scenarios were considered to find the best possible path in terms of IRR, NPV and capital investment for the recovery of the vanadium(V).

Keywords:

- Vanadium Extraction
- Kinetics Analysis
- Oxidative Leaching
- Activation energy
- Task Specific Ionic Liquids
- Circular economy

Acknowledgement

Firstly, I am very proud to be a member of the Hallett group and have enjoyed taking part in this exciting journey which is about to come to an end. It all started from an inside feeling that I knew I could accomplish and contribute significantly to the field of science rather than working in an office.

I would like to thank my parents who constantly provided support all the way through this journey. You provided help in lots of different shapes and forms and in countless numbers of ways.

I would like to thank my academic supervisors:

- Professor Jason Hallett: Not only did he give me this great opportunity, but he also put me on the right path to fulfil this research work. It always fascinates me how a single person can completely change one's life and so, I cannot thank him enough for his inspiration.
- Professor Geoff Kelsall: For all of the effort he put into this project. He was very patient with me when giving support, advice, and supervision. He is one of those people whose kindness I will remember forever.
- Professor Paul Fennell: For directing me to the right path. He inspired me to choose the most sustainable approach in my research work.

I would like to thank my industrial supervisors, Dr Peter Klusener and Dr Paul Corbett for supporting this research work. It was such a great experience working with you.

Special thanks must be given to Patricia Carry in the analytical suite who provided help and advice while running what must have been over a thousand of ICP-MS samples. To Gwilherm Kerherve for spending the time explaining the XPS technique. And finally, to all the postdocs who helped mastering the required analytical techniques to fulfil this research work. Last but not least, I would like to thank Amir (the other Amir) for giving life and career advice as well as for saving me in an evening when no-one was in the college, James for letting me use your Spotify premium account in the lab, Raul for being there whenever I needed your help with the instruments, Yiyan and Coby for the valuable chemistry knowledge you provided, Liem for inspiring me to stay fit and healthy, Aida for being such an inspiring person, Pedro (V) for being the best safety officer in the world, Pedro (N) for being such an inspiring lab manager and all the friends who shared nice moments together.

Okay, well, sometimes science is more art than science, Morty.

— Rick, Rick and Morty, “Rick Potion #9”

Contents

1. Introduction....25
1.1 Why Vanadium? Why Now?....26
1.1.1 The Importance of vanadium: Supply chain aspects....26
1.1.2 The importance of vanadium: circular sustainable economy aspects ..27
2. Literature Review....30
2.1 Vanadium refining challenges....31
2.2 Ionic liquids in metal extraction....32
2.2.1 Phosphonium based ionic liquids for metal extraction....32
2.2.2 Group 5 and 6 metals of the periodic table of elements....34
2.2.3 Imidazolium based ionic liquids for metal extraction....35
2.3 Vanadium Refining Vanadium Refining....36
2.3.1 Slags – Vanadium refining....36
2.3.2 Petroleum ash – Vanadium refining....37
2.4 Chemical Composition of vanadium-bearing materials....38
2.4.1 Vanadium-bearing slag – Chemical composition....38
2.4.1 Petroleum ash – Chemical composition....40
2.1 Mineralogical characterisation of vanadium-bearing materials....40
2.1.1 Vanadium-bearing slag – Mineralogical characterisation....40
2.1.2 Petroleum ash – Mineralogical characterisation....41
2.2 Roasting....41
2.2.1 Sodium roasting technology....42
2.2.2 Calcium roasting technology....43
2.2.3 Non-salt roasting....45
2.3 Leaching....45
2.3.1 Water leaching....45
2.3.2 Acid leaching – Oxidative and non-oxidative....46

2.3.3 Alkaline leaching – Oxidative and non-oxidative 47
2.4 Vanadium separation and purification techniques 48
2.4.1 Desilication 49
2.4.2 Dephosphorisation 49
2.4.3 Precipitation by hydrolysis 50
2.4.4 Ammonium salt precipitation 50
2.4.5 Adsorption 51
2.4.6 Solvent extraction 52
2.4.7 Ion exchange 53
2.4.8 Adsorption using ionic liquids 54
2.4.9 Membrane electrolysis 55
2.5 Vanadium recovery from petroleum ash 56
2.5.1 The SOTEX process 56
2.6 Comparison of different extraction methods of vanadium and discussion ...59
3. Gasifier ash characterisation, vanadium(V) extraction kinetics and reaction mechanism 63
3.1 Introduction 64
3.1.1 Tetramethylammonium hydroxide as the leaching and the extractant agent 64
3.1.2 Chapter objective 65
3.2 Methodology 66
3.2.1 Leaching experiments 66
3.2.2 Inductively coupled plasma mass spectrometry 67
3.2.3 Microwave digestion 68
3.2.4 Thermogravimetric analysis 69
3.2.5 Density measurements 69
3.2.6 X-ray diffraction 70

3.2.7 X-ray photoelectron spectroscopy 70
3.2.8 XRF 71
3.3 Results and Discussion 72
3.3.1 Gasifier ash characterization 72
3.3.1.1 Elemental analysis of the gasifier ash 72
3.3.1.2 TGA analysis 75
3.3.1.3 Physical properties of the gasifier ash 75
3.3.1.4 XRD analysis of the as-received gasifier ash sample 82
3.3.1.5 Distribution of the mixed vanadium oxides 82
3.3.1 Concomitant cations effect vs. pH– Control experiments 84
3.3.2 Preliminarily leaching experiments 128
3.3.2.1 Effect of temperature – Preliminary experiments 128
3.3.2.2 Effect of TMA^+OH^- concentration – Preliminary experiments 128
3.3.2.3 Effect of liquid-to-solid ratio – Preliminary experiments 129
3.3.2.4 Effect of reaction time – Preliminary experiments 131
3.3.2.5 Effect of oxidising agent - Preliminary experiments 132
3.3.2.6 Vanadium(V) dissolution reaction - with oxidant 135
3.3.2.7 Vanadium(V) dissolution reaction - without oxidant 135
3.3.3 Vanadium oxide phase determination in the residue 136
3.3.4 Extractable and non-extractable vanadium oxide fraction 137
3.3.5 Fudge factor calibration line 139
3.3.6 Kinetics study 142
3.3.6.1 Kinetic models 142
3.3.6.2 Effect of temperature 145
3.3.6.3 Oxidative dissolution mechanism 150
3.3.6.4 Effect of TMA^+OH^- concentration 157
3.3.6.5 Effect of oxidant ($NaClO_2$) concentration 158

3.3.6.6 Effect of liquid-to-solid ratio 160
3.3.6.7 Complete model 161
3.4 Conclusions 162
4. Electrochemical recovery of vanadium(V) and the ionic liquid from the leach liquor 164
4.1 Introduction 165
4.2 Methodology 167
4.2.1 Membrane choice and preparation 167
4.2.2 Electrochemical reactor equipment 167
4.2.2.1 Three-electrode electrochemical cell 169
4.2.3 Membrane-electrolysis and data analysis procedure 170
4.2.4 UV-Vis calibration curve 171
4.2.4.1 TMA^+ concentration measurement 171
4.2.5 Charge yield (membrane transference coefficient) 172
4.2.6 TMA^+ recovery over time 173
4.2.7 Specific electrical energy consumption 173
4.2.8 Deposition rate of vanadium(V) oxide aggregates 174
4.2.9 LC-MS for trace TMA^+OH^- analysis 174
4.2.10 TMA Vanadate Recovery from Residue 175
4.3 Results and discussion 176
4.3.1 Membrane electrolysis mechanism 176
4.3.2 UV-Vis Calibration Curve for TMA^+ 182
4.3.2.1 Effect of current density on vanadium(V) recovery by electrolysis .183
4.3.2.2 Effect of initial vanadium(V) concentration on recovery by electrolysis 187
4.3.2.3 Effect of Initial TMA^+ Concentration in the Anolyte on Vanadium(V) Recovery by Electrolysis 189
4.3.3 Specific Electrical Energy Consumption 190

4.3.3.1 Effect of Current Density 191
4.3.3.2 Effect of Initial Vanadium(V) Concentration 192
4.3.3.3 Effect of initial TMA^+ Concentration in Anolyte 193
4.3.3.4 Specific Electrical Energy Consumption Summary 194
4.3.4 Deposition rate of vanadium(V) phases 195
4.3.5 TMA^+ Recovery from Residue 196
4.3.6 Vanadium(V) Processing routes 197
4.3.6.1 Vanadium Processing route 1 199
4.3.6.2 Vanadium(V) Processing route 2 203
4.3.7 Characterisation of the vanadium(V) aggregates 205
4.3.7.1 Core Structure Determination 205
4.3.7.2 Stoichiometric Determination of Hydrates 208
4.4 Conclusions 209
5. Indirect electrochemical oxidation of the gasifier ash: Practical procedure to maximise the extraction of vanadium from the gasifier ash 211
5.1 Introduction 212
5.2 Methodology 213
5.2.1 Electrooxidation experimental setup 213
5.2.2 Electrooxidation procedure 215
5.2.3 Cyclic Voltammetry of TMA^+ containing vanadium(IV) sulfate 216
5.2.4 V^V purity in the calcined solids 217
5.2.5 Specific Electrical Energy Consumption 217
5.3 Results and discussion 218
5.3.1 Reaction Mechanism 218
5.3.2 Effect of Current Density and Temperature in Electrooxidation on V^V Extraction Yield 224
5.3.3 Electrode Polarisation 226

5.3.4 Specific Electrical Energy Consumption 228
5.3.5 Product characteristics and purity 229
5.3.6 Cyclic Voltammetry 235
5.4 Conclusions 237
6. Techno-economic assessment of the ionoLeach chemical plant 239
6.1 Introduction 240
6.2 The studied pathways and the scenarios 242
6.3 Estimation of Fixed Capital Investment 245
6.3.1 Introduction 245
6.3.2 Purchased equipment cost 245
6.3.2.1 Electrodes costs - Membrane electrolysis 245
6.3.2.2 Electrode costs - Oxidative chemical reactor 246
6.3.3 Total cost of the divided reactor 246
6.3.4 Distillation Column investment cost via ASPEN® 247
6.3.5 Total Fixed Capital costs 248
6.4 Estimation of Fixed Operating Costs 248
6.4.1 Cost of manufacturing 249
6.5 The minimum break-even price differential for V_2O_5 250
6.6 Plant Characteristics 251
6.6.1 General Parameters 251
6.6.2 Process inputs 252
6.6.3 Process Outputs 252
6.6.4 Financial Parameters and Indices 253
6.7 Results and Discussion 256
6.7.1 Operating costs 256
6.7.2 Total Investment Cost 258
6.7.3 Economic Performance of an ionoLeach Commercial Plant 259

6.1 Not-too-conservative ionoLeach techno-economics: Pathway 2 266
7. Conclusions, Further work, and recommendations 268
7.1 Conclusions 269
7.2 Further work and recommendations 273
8. References 276
9. Appendix A 284

List of figures

Figure 1-1. (a) left, Vanadium consumption breakdown by applications in 2021 and (b) right, vanadium production by region.[1] 26
Figure 2-1. Vanadium processing paths from different raw materials.[45] 38
Figure 2-2. Flowsheet of vanadium recovery from a vanadium source to vanadium pentoxide.[16] 43
Figure 2-3. V^{V} activity-pH diagram for species in equilibrium with $V_2O_5.H_2O$ at 298 K, 0.1 MPa. 46
Figure 2-4. Process flow diagram of the SOTEX process for the extraction of vanadium and nickel from soot and flue ash. 57
Figure 2-5. Oil fly ash treatment using different techniques.[129] 58
Figure 3-1. Typical ICP-MS calibration line for vanadium. 74
Figure 3-2. TGA data for the as-received SARU sample. 74
Figure 3-3. Particle size distribution for the as-received gasifier ash. 76
Figure 3-4. X-ray diffraction pattern for the as-received gasifier ash and the identified phases. 78
Figure 3-5. X-ray diffraction pattern for the calcined gasifier ash at 350 °C 79
Figure 3-6. X-ray diffraction pattern for the calcined gasifier ash at 550 °C 79
Figure 3-7. X-ray diffraction pattern for the calcined gasifier ash at 700 °C 80
Figure 3-8. X-ray diffraction pattern for the calcined gasifier ash at 900 °C 81
Figure 3-9. XP spectra for $V2P_{3/2}$ region. The peak positions extracted from the fitted scan suggest the presence of V^{V} and V^{IV} in the as-received SARU. 83
Figure 3-10. (a), top, (reprinted Figure 2-3) V^{V} activity-pH diagram for species in equilibrium with V_2O_5 (b),bottom, V^{IV} activity-pH diagram for species in equilibrium with V_2O_4 ; at 298 K, 0.1 MPa. These calculations omitted consideration of the presence of TMA^{+} ions. 86
Figure 3-11. XRD diagram of the precipitate in the presence of TMA^{+} cations vs. the shown pH and the concomitant cation. 88
Figure 3-12. XRD diagram of the precipitate in the presence of TMA^{+} cations vs. the shown pH and the concomitant cation. 89
Figure 3-13. XRD diagram of the precipitate in the presence of TMA^{+} cations vs. the shown pH and the concomitant cation. 90

Figure 3-14. XRD diagram of the precipitate in the presence of TMA^+ cations vs. the shown pH and the concomitant cation. 91
Figure 3-15. XRD diagram of the precipitate in the presence of TMA^+ cations vs. the shown pH and the concomitant cation. 92
Figure 3-16. XRD diagram of the precipitate in the presence of TMA^+ cations vs. the shown pH and the concomitant cation. 93
Figure 3-17. XRD diagram of the precipitate in the presence of TMA^+ cations vs. the shown pH and the concomitant cation. 94
Figure 3-18. XRD diagram of the precipitate in the presence of TMA^+ cations vs. the shown pH and the concomitant cation. 95
Figure 3-19. XRD diagram of the precipitate in the presence of TMA^+ cations vs. the shown pH and the concomitant cation. 96
Figure 3-20. XRD diagram of the precipitate in the presence of TMA^+ cations vs. the shown pH and the concomitant cation. 97
Figure 3-21. XRD diagram of the precipitate in the presence of TMA^+ cations vs. the shown pH and the concomitant cation. 98
Figure 3-22. XRD diagram of the precipitate in the presence of TMA^+ cations vs. the shown pH and the concomitant cation. 99
Figure 3-23. XRD diagram of the precipitate in the presence of TMA^+ cations vs. the shown pH and the concomitant cation. 100
Figure 3-24. XRD diagram of the precipitate in the presence of TMA^+ cations vs. the shown pH and the concomitant cation. 101
Figure 3-25. XRD diagram of the precipitate in the presence of TMA^+ cations vs. the shown pH and the concomitant cation. 102
Figure 3-26. XRD diagram of the precipitate in the presence of TMA^+ cations vs. the shown pH and the concomitant cation. 103
Figure 3-27. XRD diagram of the precipitate in the presence of TMA^+ cations vs. the shown pH and the concomitant cation. 104
Figure 3-28. XRD diagram of the precipitate in the presence of TMA^+ cations vs. the shown pH and the concomitant cation. 105
Figure 3-29. XRD diagram of the precipitate in the presence of TMA^+ cations vs. the shown pH and the concomitant cation. 106

Figure 3-30. XRD diagram of the precipitate in the presence of TMA^+ cations vs. the shown pH and the concomitant cation. 107
Figure 3-31. XRD diagram of the precipitate in the presence of TMA^+ cations vs. the shown pH and the concomitant cation. 108
Figure 3-32. XRD diagram of the precipitate in the presence of TMA^+ cations vs. the shown pH and the concomitant cation. 109
Figure 3-33. XRD diagram of the precipitate in the presence of TMA^+ cations vs. the shown pH and the concomitant cation. 110
Figure 3-34. XRD diagram of the precipitate in the presence of TMA^+ cations vs. the shown pH and the concomitant cation. 111
Figure 3-35. XRD diagram of the precipitate in the presence of TMA^+ cations vs. the shown pH and the concomitant cation. 112
Figure 3-36. XRD diagram of the precipitate in the presence of TMA^+ cations vs. the shown pH and the concomitant cation. 113
Figure 3-37. XRD diagram of the precipitate in the presence of TMA^+ cations vs. the shown pH and the concomitant cation. 114
Figure 3-38. XRD diagram of the precipitate in the presence of TMA^+ cations vs. the shown pH and the concomitant cation. 115
Figure 3-39. XRD diagram of the precipitate in the presence of TMA^+ cations vs. the shown pH and the concomitant cation. 116
Figure 3-40. XRD diagram of the precipitate in the presence of TMA^+ cations vs. the shown pH and the concomitant cation. 117
Figure 3-41. XRD diagram of the precipitate in the presence of TMA^+ cations vs. the shown pH and the concomitant cation. 118
Figure 3-42. XRD diagram of the precipitate in the presence of TMA^+ cations vs. the shown pH and the concomitant cation. 119
Figure 3-43. XRD diagram of the precipitate in the presence of TMA^+ cations vs. the shown pH and the concomitant cation. 120
Figure 3-44. XRD diagram of the precipitate in the presence of TMA^+ cations vs. the shown pH and the concomitant cation. 121
Figure 3-45. XRD diagram of the precipitate in the presence of TMA^+ cations vs. the shown pH and the concomitant cation. 122

Figure 3-46. XRD diagram of the precipitate in the presence of TMA^+ cations vs. the shown pH and the concomitant cation. 123
Figure 3-47. XRD diagram of the precipitate in the presence of TMA^+ cations vs. the shown pH and the concomitant cation. 124
Figure 3-48. XRD diagram of the precipitate in the presence of TMA^+ cations vs. the shown pH and the concomitant cation. 125
Figure 3-49. XRD diagram of the precipitate in the presence of TMA^+ cations vs. the shown pH and the concomitant cation. 126
Figure 3-50. XRD diagram of the precipitate in the presence of TMA^+ cations vs. the shown pH and the concomitant cation. 127
Figure 3-51. Preliminarily data for the time dependence of vanadium(V) extraction from the gasifier ash: Effect of reaction temperature. 550 rpm, 5 $cm^3\ g^{-1}$ and 2.78 mol dm^{-3} TMA^+OH^- concentration. 130
Figure 3-52. Effect of TMA^+OH^- concentration on vanadium(V) extraction yield and purities. 550 rpm, 5 $cm^3\ g^{-1}$, 180 min reaction time, 50 °C reaction temperature and 2.78 mol dm^{-3} TMA^+OH^- concentration.....130
Figure 3-53. Effects of TMA^+OH^- concentration and liquid-to-solid ratio on vanadium(V) extraction yield. 550 rpm, 90 °C reaction temperature, 960 min reaction time and zero mol dm^{-3} $NaClO_2$. 131
Figure 3-54. Effect of leaching time on the vanadium(V) extraction yield. 550 rpm, 10 $cm^3\ g^{-1}$, 90 °C reaction temperature and 2.78 mol dm^{-3} TMA^+OH^- concentration. ...131
Figure 3-55. Effect of TMA^+OH^- concentration and the liquid-to-solid ratio on the vanadium(V) extraction yield. 550 rpm, 90 °C reaction temperature, 300 min reaction time, and 0.221 mol dm^{-3} $NaClO_2$. 133
Figure 3-56. Effect of oxidising agent and time on the vanadium(V) extraction yield. 0.221 mol dm^{-3} for both $NaClO_2$ and $NaClO_3$ concentrations, and 1:5 v/v 30% H_2O_2 in the solution; 550 rpm, 90 °C reaction temperature, 2.78 mol dm^{-3} TMA^+OH^- concentration.....134
Figure 3-57. X-ray diffraction pattern for the post-extraction solids (a), left, with no additives and 7 days leaching time, and (b),right with 0.221 mol dm^{-3} $NaClO_2$ and 300 min leaching time. Both experiments were conducted under the following conditions: 550 rpm, 10 $cm^3\ g^{-1}$, 90 °C reaction temperature and 2.78 mol dm^{-3} TMA^+OH^- concentration.....137

Figure 3-58. Vanadium oxidations states breakdown in extractable and unextractable phases. 139
Figure 3-59. (a), left, Effects of V^{V} concentration on A: Density of $TMA^{+}OH^{-}$ + V^{V} mixture, and (b), right, correction factor calibration line for $TMA^{+}OH^{-}$ + V^{V} mixtures. 142
Figure 3-60. Effect of leaching temperature on time dependences of vanadium(V) extraction yields (a), left, as-received. (b), right in 0.221 mol dm^{-3} $NaClO_2$; 550 rpm, 10 cm^3 g^{-1}, 90 °C reaction temperature and 2.78 mol dm^{-3} $TMA^{+}OH^{-}$ concentration. 146
Figure 3-61. Time dependences of vanadium extraction yields fitted by the four kinetics equations in Model (A) to (D) for (a), left, as-received and (b), right, oxidatively, in 0.221 mol dm^{-3} $NaOCl_2$; 550 rpm, 10 cm^3 g^{-1}, 90 °C reaction temperature and 2.78 mol dm^{-3} $TMA^{+}OH^{-}$ concentration. 147
Figure 3-62. (a), left, Time dependences of vanadium(V) extraction yields fitted by Model (D), and (b), right Arrhenius plot for activation energy determination. 147
Figure 3-63. SEM images of the residue at the following reaction condition: in 0.221 mol dm^{-3} $NaOCl_2$; 550 rpm, 10 cm^3 g^{-1}, 90 °C reaction temperature and 2.78 mol dm^{-3} $TMA^{+}OH^{-}$ concentration and 300 min reaction time. (a)1800x (b) 2500 x, (c)5000 and (d) 8000x magnifications. 151
Figure 3-64. Schematic diagram of Model (D). The reaction is affected by both interface transfer and diffusion across product layer. 152
Figure 3-65. (a) SEM image of the pristine ash (b) vanadium distribution (c) Iron distribution (d) Nickel distribution and (e) the EDS spectra of CPS. 153
Figure 3-66. (a) SEM image of the gasifier ash after 15 min oxidative leaching (b) vanadium distribution (c) Iron distribution (d) Nickel distribution and (e) the EDS spectra of CPS. 154
Figure 3-67. (a) SEM image of the gasifier ash after 30 min oxidative leaching (b) vanadium distribution (c) Iron distribution (d) Nickel distribution and (e) the EDS spectra of CPS. 155
Figure 3-68. (a) SEM image of the gasifier ash after 300 min oxidative leaching (b) vanadium distribution (c) Iron distribution (d) Nickel distribution and (e) the EDS spectra of CPS. 156

Figure 3-69. (a) top, Time dependence of vanadium(V) extraction yield for four different TMA^+OH^- concentrations. (b) bottom left, Data fitted for Model (D). (c) bottom right, Plot of KC versus TMA^+OH^- concentration; 550 rpm, 10 $cm^3 g^{-1}$, 0.221 mol dm^{-3} $NaClO_2$ and 90 °C reaction temperature. 158
Figure 3-70 A: Time dependence of vanadium(V) extraction yield for four different $NaClO_2$ concentrations; B: Data fitted by Model (D.); C: log plot of effect of oxidant concentration on rate coefficient ; 550 rpm, 10 cm^3 g^{-1}, and 2.78 mol dm^{-3} TMA^+OH^- concentration. 159
Figure 3-71. (a) top, Time dependences of vanadium(V) extraction yields for three different liquid-to-solid ratios. (b), bottom left, Kinetic data fitted to Model (D), and (c) bottom right, log plot of the rate coefficient and the liquid-to-solid ratio; 550 rpm, 0.221 mol dm^{-3} $NaClO_2$ and 2.78 mol dm^{-3} TMA^+OH^- concentration. 161
Figure 4-1. (a) Real pictures and (b) schematic of electrolyser. The anode compartment contained an agitator with a speed controller, an IrO2 coated titanium electrode connecd to the S+WE connectors and a reference electrode (RE). The counter electrode (CE) (cathode) was stainless steel 316. 168
Figure 4-2. Control compound - (a), left, Dried anode deposits (b), right, X-ray diffraction pattern of the electrode deposits 176
Figure 4-3. Control compound - (a), left, Dried precipitates of the anolyte pH < 3, Soxhlet treated and dried. (b), right, X-ray diffraction pattern of the precipitates. 177
Figure 4-4. Control compound - (a) Control compound - Dried precipitates from prolonged membrane electrolysis of anolyte, pH = 2 (b) X-ray diffraction pattern the dried precipitates. 178
Figure 4-5. Typical electrolysis equipment. The anolyte pH < 3 caused rapid formation of hydrated $H_3TMA_3V_{10}O_{28}$ in the form of a yellow dispersion. 178
Figure 4-6. Potential-pH diagram for vanadium-H_2O system at 298 K, 0.1 MPa and activity of dissolved vanadium species = 10^{-1} 179
Figure 4-7. (reprinted Figure 2-3) V^V activity-pH diagram for species in equilibrium with $V_2O_5.H_2O$ at 298 K, 0.1 MPa. These calculations omitted consideration of the presence of TMA^+ ions, which, as reported below, were found to lead to formation of solid phases in addition to $V_2O_5.H_2O$. 179

Figure 4-8 (a, left, Absorption spectra of TMA+OH- solutions of different concentrations in water (b), right, Effect of TMA+OH- concentration on peak absorbances of TMA+OH- solutions at λmax = 208 nm. Path length =10 mm 182
Figure 4-9. Time dependences of: (a), left, fractional TMA^+ recovery to catholyte, and (b), right, of anolyte pH; both for current densities of 700, 1 000 and 1 300 A m^{-2}. Initial TMA^+ concentration in anolyte = 2.78 mol dm^{-3}; initial vanadium(V) concentration in anolyte = 0.589 mol dm^{-3}.....186
Figure 4-10. TMA^+ cations flux under zero electric fields. 187
Figure 4-11. Time dependences of: (a), left, fractional recovery to the catholyte of TMA^+ ions, and (b), right, anolyte pH; both for 3 initial vanadium(V) concentrations. Initial TMA^+ concentration in anolyte = 2.78 mol dm^{-3}; current density = 1 000 A m^{-2} 188
Figure 4-12. Time dependences of: (a), left, fractional TMA^+ recovery to the catholyte, and (b), right, anolyte pH; both for 3 initial TMA^+ concentrations. Initial vanadium(V) concentration in anolyte = 0.589 mol dm^{-3}; current density = 1 000 A m^{-2} 189
Figure 4-13. Effect of current density on both charge yield and specific electrical energy consumption. Initial TMA^+ concentration in anolyte = 2.78 mol dm^{-3}, initial vanadium(V) concentration in anolyte = 0.589 mol dm^{-3} 192
Figure 4-14. Effect of initial vanadium(V) concentration on charge yields and specific electrical energy consumptions. Initial TMA^+ concentration in anolyte = 2.78 mol dm^{-3}; current density = 1 000 A m^{-2} 193
Figure 4-15. Effect of initial TMA^+ concentration on charge yield and specific electrical energy consumption. Initial vanadium(V) concentration in anolyte = 0.589 mol dm^{-3} , Current density = 1000 A m^{-2} 194
Figure 4-16. (a), left, Time dependence of measured weight of deposits per unit area of anode. (b), right, Effect of vanadium(V) concentration on deposition rate of deposits per unit area. 195
Figure 4-17 (a), left, Mass spectrum of TMA^+ and (b), right, Retention time of TMA^+ At 74 m/z. 196
Figure 4-18 (a) Calibration curve for TMA+ concentration from LC-MS using 6 different reference solutions of TMA+OH-. (b) TMA+OH- equivalent loss per initial unit mass of ash for different number of washing steps. 197

Figure 4-19 Simplified process flow diagram of the ionoLeach process to produce pure V_2O_5 by membrane electrolysis, depicted for the two vanadium processing routes. 198
Figure 4-20 Control compound – (a) left, Post-reaction suspension and dried solids of the AMV reaction and (b), right, X-ray diffraction pattern of the white solids recovered from the precipitates from the ammonia exchange process (Reaction 4-8).....200
Figure 4-21. (a), Control compound - left, Lumps of V2O5 collected after calcination of NH_4VO_3 and (b), right, X-ray diffraction pattern of the calcination product which was identical to the V_2O_5 reference patterns. 204
Figure 4-22. Data from X-ray photoelectron spectroscopy (XPS) of vanadium(V) aggregates and precipitates: atomic percent of V^{IV} and V^{V} in the $V2P_{3/2}$ environment as a function of iteration number. Each iteration is 3 scans for 0.15 s each at a power of 80 W on an area of 400 μm^2 (a), left, for the deposited vanadium aggregates onto the surface of the electrode for a solution pH of 3 < pH <6 and (b), right, for compounds precipitated from anolyte at pH < 3. 205
Figure 4-23. Thermogravimetric analysis (TAG) data for formation of V_2O_5 by decomposition of (a), left, $H_4TMA_2V_{10}O_{28}.5H_2O$, MW = 1199.75 g mol^{-1} and (b), right, $H_3TMA_3V_{10}O_{28}.6H_2O$, MW = 1290.89 g mol^{-1}.....208
Figure 5-1. (a) Real picture and (b) schematic of undivided electrochemical reactor. The anode was a dimesonally stable RuO_2 coated titanium electrode (DSA-Ti/RuO_2) connected to the S+WE connectors, the counter electrode (CE) (cathode) was stainless steel 316 and the Ag/AgCl reference electrode. Solution was agitated using a magnetic stirrer bar. 214
Figure 5-2. Activity-pH diagram for chlorine-water system at 298 K. Initial chloride activity = 0.5 mol dm^{-3}, conversion = 0.1 and $P(Cl_2)$ = 101.325 kPa. 220
Figure 5-3. Physical appearance of the electrooxidised ash. Yellow particles appeared after the electrooxidation step. 222
Figure 5-4. (a), left, Effect of current density on the final vanadium(V) extraction yield at 90 °C; (b), right, effect of temperature on the final vanadium(V) extraction yield at 500 A m^{-2}.....225
Figure 5-5(a), left, Polarization curve of electrode in 0.5 mol dm^{-3} TMA^+Cl^- solution, pH ca. 8 and 90 °C (b), right, Breakdown of cell potential difference for the production of hypochlorite in a 0.5 mol dm^{-3} NaCl at near-neutral pH. 227

Figure 5-6. Effect of current density on specific energy required for the electrooxidation process to produce 1 tonne of V_2O_5. Experimental conditions: 0.5 mol dm^{-3} TMA^+Cl^- solution, pH ca. 8, 90 °C for time = equilibrium extraction yield time. 229
Figure 5-7. SEM image of oxidised V^{IV} to V^V flakes after some electrooxidation period in 0.5 mol dm^{-3} TMA^+Cl^- solution. 230
Figure 5-8. Chemical composition of leach liquor obtained from electrooxidised gasifier ash. 231
Figure 5-9. Real sample - XRD diagram of the yellow precipitates obtained from the electrolysis of the leach liquor. 231
Figure 5-10. $H_4TMA_2V_{10}O_{28}$ morphology and composition: (a) top SEM image and (b), bottom, energy dispersive X-ray spectroscopy elemental data from the crystal structures. 232
Figure 5-11. Real sample - XRD diagram of the calcined yellow precipitates. 233
Figure 5-12. Needle-like V_2O_5 crystal morphology: (a), left, SEM image and (b), right, Energy dispersive X-ray spectroscopy elemental data from the crystal structures..234
Figure 5-13. Cyclic voltammograms of the electrolyte with different additive amounts of $TMA^+HSO_4^-$ at room temperature at a scan rate of 20 mV s^{-1} on graphite felt electrode. Each curve had a different TMA^+ : V^{IV} ratio and the reference contained 1.6 mol dm^{-3} V^{IV} / 3M free H_2SO_4 with no TMA^+ cations. 236
Figure 6-1. Schematic of the techno-economic assessment study for the ionoLeach process.....240
Figure 6-2. Process flow diagram for pathway 1 – base case pathway. 241
Figure 6-3. Schematic of the proposed electrochemical reactor whereby vanadium(V) aggregates can be continuously removed. 242
Figure 6-4. ASPEN® plus process scheme of the distillation columns for the ammonia and methanol recover in ionoLeach process. 247
Figure 6-5. Comparison of the net levelised operating cost for the three pathways per ton of produced V_2O_5 (or equivalent). 256
Figure 6-6. Major factors impacting the project's NPV_{20} for (a) top left, Pathway 1; (b) top right, Pathway 2 and (c) bottom, Pathway 3. Note that the multiplier points of 0.5 and the 1.5 for Discount rate correspond to 9 % and 12 %; and for cost-to-capacity scale factor to 0.5 and 0.7, respectively. 261

Figure 6-7. Impact of TMA^+OH^- price and V_2O_5 selling price on the (a), top left, NPV; (b) top right, (IRR) and (c) bottom, (ROI) of the ionoLeach plant for pathway 2. Base price for vanadium pentoxide = \$23 142 ton^{-1}. 263
Figure 6-8. NPV sensitivity to TMA^+OH^- price for different V_2O_5 selling price. $\$V_{2}O_{5,base}$ = \$23 142 t^{-1} 264

List of tables

Table 2-1. Chemical composition of vanadium-bearing slags from different iron and steel-making plants. 39
Table 2-2. Chemical composition of different ashed petroleum fractions.[14] 40
Table 2-3. A comparison of different metallurgical methods for extracting vanadium from vanadium-bearing slag.[130] 62
Table 3-1. Composition of the gasifier ash measured by ICP-MS 73
Table 3-2. Composition of the volatile contents of the gasifier ash measured by XRF 73
Table 3-3 physiochemical characterisation of the as-received gasifier ash. 76
Table 3-4 Summary of the XPS reference data for vanadium with various oxidation states 85
Table 3-5. Crystal structure of the phases identified in the precipitates vs. pH 2, 6 and 13 with a combination of vanadate ions and various concomitant cations after calcination in the muffle oven. 87
Table 3-6. Square of correlation coefficients of four kinetic models at four leaching temperatures in 0.221 mol dm^{-3} $NaOCl_2$; 550 rpm, 10 cm^3 g^{-1}, and 2.78 mol dm^{-3} TMA^+OH^- concentration. 148
Table 4-1. Kinetics study of Reaction 4-8 with three variables: temperature, NH_4OH concentration, and $H_4TMA_2V_{10}O_{28}$ loading. 201
Table 6-1. The selected pathway and their corresponding products 244
Table 6-2. Key inputs for the analysis of cost of manufacturing. 250
Table 6-3. Summary of general plant parameters 252
Table 6-4. Summary of process inputs for a commercial ionoLeach plant 253

Table 6-5. Summary of process outputs for the base-case 253
Table 6-6 Summary of the financial parameters for the base-case 255
Table 6-7 Indices used in modelling.....255
Table 6-8. The total operating cost of each pathway for ionoLeach V_2O_5.....257
Table 6-9. Total investment costs and the contributing elements. 258
Table 6-10. Summary of the key economic parameters 259
Table 6-11. Less conservative input parameters 265
Table 6-12 More realistic economic performance of Pathway 2 265

1. Introduction

1.1 Why Vanadium? Why Now?

Vanadium is mostly utilised in the steel industry to make metal alloys for rebar and structural steel, as well as in aircraft. Vanadium can lighten steel by up to 30 % and boost its strength by up to 100 % when it is added in modest amounts.[1] Today, the steel and titanium industries consume more than 90 % of the vanadium produced worldwide as a high-strength alloy as shown in Figure 1-1(a). The emerging energy storage market is forecasted to be the next large market for vanadium. According to a study by Bloomberg, the global energy storage market will double six times to a total of 305 gigawatt-hours in 2030.[2] Thus, the production of minerals such as graphite, lithium, and cobalt could increase by nearly 500 % in order to meet the ever-increasing demand for clean energy technologies, as suggested by a recent World Bank report titled Minerals for Climate Action: The Mineral Intensity of the Clean Energy Transition.[3] It was forecasted that 3 billion tonnes of minerals and metals will be required to install the wind, solar, and geothermal power systems, as well as the energy storage systems, needed to satisfy the 2015 Paris Agreement's carbon reduction targets.

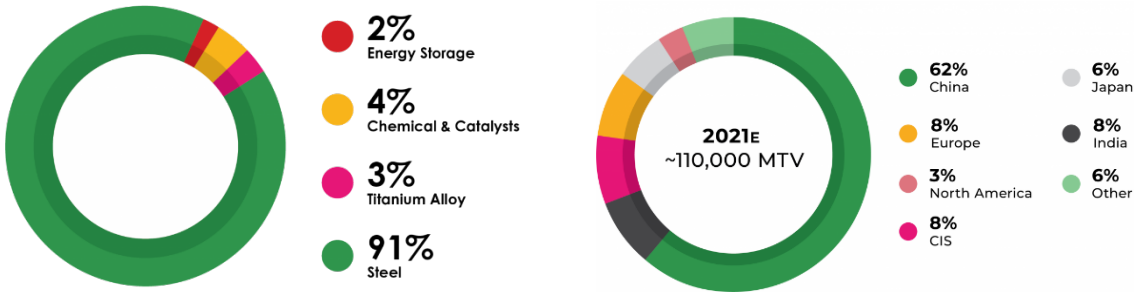


Figure 1-1. (a) left, Vanadium consumption breakdown by applications in 2021 and (b) right, vanadium production by region.[1]

1.1.1 The Importance of vanadium: Supply chain aspects

Although there are different types of energy storage, vanadium redox flow batteries (VRFB) have gained significant attention from both academic and industrial researchers due to their long cycle life, full discharge ability, low running cost, fast response, environmental credentials, and non-flammability. Moreover, at the end of the life of a VRFB system, up to 97 % of the vanadium in the electrolyte can be recycled as suggested by a report from INVINITY Energy Systems.[4] While the vanadium market

is dominated by the steel industry, the global effort towards clean energy technology and the requirement for the grid (utility) scale energy storage system is anticipated to push demand for vanadium in the very near future.

The United Kingdom government conducted a crucial analysis of the relative importance of sourcing and reliance of the country on critically important minerals. Department of Business, Energy and Industrial Strategy (BEIS) published a report[5] recently in which vanadium, among some other minerals, was recognised to have high criticality for the UK. The British Geological Survey (BGS) carried out its first assessment on the criticality of a range of minerals in order to support the launch of the UK strategy which is to secure the supply chains by boosting domestic capability in a way that generates new jobs and wealth as well as bringing investment. The BGS report[6] set out only one critical application for vanadium for the UK policy objectives which was for VRFB with the following description: 'Vanadium redox flow batteries may become increasingly important for stationary energy storage'. Vanadium was allocated the highest UK economic vulnerability score in two key areas (i) Price Volatility and (ii) Substitutability. The overall UK economic vulnerability for vanadium was 10 and lithium was 13 while the lowest and the highest scores were 4 for silicon and 15 for nickel, respectively. Moreover, the global supply risk of vanadium was recognised to be the second highest among other commodities due to being predominantly produced as a by-product of titaniferous magnetite processing as well as having a low recycling rate. To put this in perspective, titaniferous magnetite ore, which is the primary source of vanadium production, is geographically concentrated in a small number of countries. As can be seen from Figure 1-1(b), China has been the biggest producer of vanadium supplying 61 % of the global demand in 2021 followed by Russia (17 %) and South Africa (7 %). Considering most of the vanadium deposits are located in China and if an earthquake strikes, vanadium mines are forced to shut, causing a significant increase in the vanadium price.[7]

1.1.2 The importance of vanadium: circular sustainable economy aspects

The global vanadium supply by the primary source is dominated by the direct and indirect (from slag) production from titaniferous magnetite ores, each contributing about 17 % and 73 %, respectively.[8] Titaniferous magnetite ores are largely located in China, Russia, Australia and South Africa. Some other countries such as Brazil, Canada, North America, Finland and Madagascar have much smaller deposits of

vanadium.[9] There was a large spread for the vanadium content of the primary source in the literature but none was exceeding 4.9 wt % and the average was 1.5 wt % V_2O_5 equivalent.[10] Vanadium refining from the primary source conventionally starts with roasting the feedstock with sodium salts such as sodium carbonate and sodium chloride at high temperatures to produce water-soluble vanadium species, followed by the ammonium polyvanadate precipitation process to separate solid vanadium species from the aqueous phase. This seemingly simple vanadium processing method comes at the cost of emitting hazardous gases into the atmosphere in addition to the production of hazardous tailings which is inherent to the salt-roasting water-leaching processing method and the release of vanadium(V) to the environment can potentially be hazardous. Unfortunately, limited attention has been given to vanadium(V) toxicity and there are limited studies on vanadium geochemistry relative to similar trace metals despite being classified as a potentially toxic metal. The most recent research on vanadium pollution and health risks in marine ecosystems revealed that children are at the highest health risk.[11]

The crucial role of vanadium in the steel industry and the rapid growth in the deployment of vanadium redox flow batteries have led to an ever-increasing demand for vanadium. The primary production of vanadium has severe environmental impacts while being highly susceptible to political and geopolitical decisions. Consequently, it is of great importance to identify a more elegant approach to produce vanadium from more available sources such as the secondary source gasifier ash to secure circular economy implementation as well as to expand the supply chain network. The secondary source is found in lesser quantities but with the advantage of not being geographically concentrated. Some examples of secondary vanadium are bottom/fly ash, petroleum boiler ash, gasifier ash, alumina slag, and spent catalysts from sulfuric acid production units. The reason for petroleum ash being an attractive source of vanadium is that crude oils contain organo-vanadium compounds as well as some other transition metals such as nickel. The vanadium content of crude oils greatly varies according to their origin and nature. For example, Venezuelan crude oils may contain up to 1204 ± 87 ppm elemental V, some may contain less than 20 ppm, but the majority contain around 200 ppm.[12] Egyptian crude oils may contain 15 to 184 ppm elemental V.[13] During the crude oil refining process, the heavy metals are concentrated in the heavier fraction of distillation columns such as the bitumen fraction which either

is used as a binder in different applications such as road construction or further processed to petroleum ash and lighter hydrocarbons. Fuel oil or heavy fuel oil combustion in power plants also leaves behind high vanadium content fly ash. The vanadium content of petroleum or fly ash is considerably higher than the primary source, ranging from 8 to 40 wt % elemental vanadium.[14]

"If we were to recover all the vanadium in crude oil, it would have been 3x today's global vanadium consumption"[15,*]

The objectives of the project were to:

- Demonstrate the use of a task-specific ionic liquid to selectively leach vanadium(V) from a secondary source of vanadium
- Establish a recovery method for both the solvent and the vanadium
- Characterise the vanadium phases with the aim of extractability of vanadium(V) ions from such phases to expand the application to other feedstocks
- Find a sustainable approach to maximise the recovery of vanadium(V)
- Design a vanadium(V) recovery process with the aim of a circular sustainable economy
- Assess whether sustainable purification of vanadium(V) is economically viable

[*]Based on the annual 4.2 billion tons production of crude oil and 80 ppm V on average.

2. Literature Review

2.1 Vanadium refining challenges

Vanadium extraction faces several unique challenges compared to other metals such as nickel, cobalt, iron, and chromium. Firstly, vanadium is typically found in low concentrations in ores, which makes it challenging to extract it economically. In contrast, other metals like nickel and cobalt are often found in higher concentrations in ores, making them more cost-effective to extract. Secondly, the extraction process of vanadium is complex and involves multiple steps, including salt roasting, leaching, precipitation, and solvent extraction.[16] This can be more challenging than the extraction of other metals, which may require fewer steps or simpler processes i.e. leaching and electrowinning. Thirdly, vanadium extraction can produce waste materials that pose environmental concerns. For example, the salt roasting process releases sulfur dioxide and other pollutants into the air, while the leaching process generates acidic wastewater. Hence, the management of these environmental concerns is crucial to ensure the sustainability of vanadium extraction whereas the salt roasting step is not a requirement for the extraction of iron or nickel. Lastly, vanadium is often recovered as a by-product of the steel industry and has low recycle rate.[7] Hence, the production is vastly dependant on the steel industry market.

Nickel refining starts with the mining of nickel ore from underground or open-pit mines, followed by a number of processing stages to extract and purify the nickel. The process includes crushing and grinding the ore, froth floatation to separate the nickel concentrate, smelting to produce nickel matte, converting to separate copper and iron from nickel, and refining through electrolysis to obtain pure nickel. Copper is similarly refined by electrowinning. Vanadium however cannot be recovered via the electrowinning process using aqueous systems, as it has an oxidation potential of approximately -1.2V. Vanadium(V) purification process uses an ammonium salt as the precursor to precipitate ammonium polyvanadate, followed by the calcination of the solids to produce V_2O_5.[17]

Relatively speaking, vanadium extraction is more challenging as the leaching step requires salt roasting of titanomagnetite ore which has a low vanadium concentration. The purification/precipitation step must be done via the use of chemicals such as ammonium salts whereas for copper and nickel refining, electrowinning is the primary step.

2.2 Ionic liquids in metal extraction

Despite their high cost, ILs are increasingly being considered as potential extractants for metals in hydrometallurgical processes, as they offer better characteristics such as high distribution ratios, selectivity, reusability, and stability compared to existing large-tonnage industrial extractants.[18,19] However, the high viscosity of ILs is a challenge, which is why they are dissolved in molecular solvents to produce highly efficient extraction systems. This approach has been successful in the recovery of indium(III) and gold(III) from electronic waste and in extracting Mo(VI) in high yields. While undiluted ILs have also been used as extractants in some studies, they tend to become saturated with water during extraction, which significantly reduces their viscosity.[20,21] For instance, tantalum(V) and Pd(II) have been extracted with high efficiency using this approach.[22]

2.2.1 Phosphonium based ionic liquids for metal extraction

Ionic liquids containing phosphonium cations have been identified as promising extractants for noble metals, rare earth elements, transition metals, and radionuclides. These ILs can also be used to separate transition and rare earth metals. Among them, Cyphos 104 and Cyphos 101 have emerged as the most popular and promising. Cyphos 104, in particular, has been found to be an efficient extractant for gallium(III), indium(III), zinc(II), and tin(II) recovery from electronic waste, which is crucial for both environmental and economic aspects. The extraction efficiency of gallium from 3 mol dm^{-3} HCl can reach 99.8%,[23] while indium(III), zinc(II), and tin(II) can be recovered from LCD screen leach liquor with purities of 100 %, 98.9 %, and 100 %, respectively. The mechanism of indium extraction from chloride medium is described by the following equation[24]:

$$In^{3+}_{aq} + 3Cl^{-}_{aq} + 2[R_3P'P^+A^-]_{org} \leftrightarrow [InCl_3.2R_3P'P^+A^-]_{org} \quad \text{(Reaction 2-1)}$$

Where $R_3R'P^+$ is trihexyl(tetradecyl)phosphonium, and A is bis(2,4,4-trimethylpentyl) phosphinate.

When comparing the extraction of europium(III) from a chloride medium using the organophosphorus D2EHPA extractant, the Cyphos 104 ionic liquid, and a combination of the two, researchers found that a quantitative europium recovery could be achieved using only a mixture of 0.05 mol dm^{-3} D2EHPA and 0.02 mol dm^{-3} Cyphos 104. The authors also observed that Cyphos 104 has a higher loading

capacity than D2EHPA. However, for the separation of yttrium(III) and europium(III), D2EHPA is a more suitable extractant. Extraction with D2EHPA resulted in the highest separation factors β (Y(III)/Eu(III)) of 10 546, while Cyphos 104 yielded a separation factor of 629.7.[25]

ILs such as Cyphos 101 and its analogs have demonstrated the capability to separate rare earth metals from transition metals, including iron(III), cobalt(II), copper(II), manganese(II), and zinc(II). This liquid can be used undiluted and serves as both the organic phase and the extractant.

An example of the application of $[P_{66614}][NO_3]$, an analogue of Cyphos 101 with a nitrate anion, includes its use for the highly efficient separation of samarium(III) and lanthanum(III) rare earth elements from cobalt(II) and nickel(II) during the processing of permanent magnets and nickel metal hydride batteries, achieving up to 99.9% purity.[26] It was shown that this IL is capable of reducing the viscosity of the di(2-ethylhexyl) 2-ethylhexylphosphonate extractant, causing increased extraction efficiency for rare earth elements such as terbium(III), europium(III), yttrium(III), and cerium(III) from waste luminophores. The extraction efficiency was reported to be up to 90% and can be attributed to synergistic effects.[27]

Furthermore, Cyphos 101 in toluene acts as an effective extractant for gold(III) from thiosulfate solutions, achieving an extraction efficiency of 99%.[28] When used undiluted, Cyphos 101 allows for the quantitative recovery of platinum(IV) and palladium(II) from an acidic leaching solution of waste catalytic converters.[29]

$[P_{66614}]$[MA], which is a modified version of Cyphos 101 with N,N,N′,N′-tetra(2-ethylhexyl)malonate anion, has been combined with the $[P_{66614}][N_{O3}]$ ionic liquid as a diluent to extract trivalent rare earth elements, including europium(III), from a nitric acid medium. The researchers investigated the europium extraction behaviour by altering several parameters such as the extractant and salting-out agent concentrations, pH, temperature, and metal content in the aqueous medium. They discovered that this ionic liquid system is effective in separating rare earth metals from transition metals that are usually coexist in magnets and luminophore lamps.[30]

Researchers have utilized tetrabutylphosphonium bis(2,4,4-trimethylpentyl) phosphinate [P4444][BTMPP] in toluene to extract lithium. The ionic liquid showed

a significantly higher extraction efficiency (94.07%) compared to the molecular analog, bis(2,4,4-trimethylpentyl)phosphinic acid. Another advantageous feature of [P_{4444}][BTMPP] is its ability to be fully regenerated and reused without any reduction in extraction properties.[31]

2.2.2 Group 5 and 6 metals of the periodic table of elements

The use of Aliquat 336 ionic liquid has been shown to be effective in extracting vanadium and molybdenum over a wide pH range. For instance, Wang et al.[32] achieved complete recovery of trace amounts of vanadium(V) from an ammonium tungstate solution by using Aliquat 336 IL in sulfonated kerosene as the extractant. The authors[32] observed the formation of a third phase when using 1 vol.% Aliquat 336 and 1 vol.% 2-octanol as a modifying agent. However, increasing the 2-octanol concentration to 5 vol.% eliminated the formation of the third phase and improved the extraction speed, came at the cost of a decrease in vanadium(V) extraction efficiency. This decrease was attributed to the inhibitory effect of 2-octanol on ILs. The authors noted the high selectivity and kinetics of this method compared to vanadium precipitation by calcium(II) salts.

A separation flow diagram using Aliquat 336 in sulfonated kerosene was developed for the separation of vanadium(V) and aluminium(III).[33] The study found that an initial pH of 0.78, an organic-to-aqueous phase ratio of 1:2, an IL concentration of 40 vol.%, and an equilibrium time of 3 min yielded a 99.06% extraction efficiency for vanadium and only 7.95% for aluminium, resulting in a separation factor β (V(V)/Al(III)) of 1221. The authors proposed that the mechanism for the extraction of vanadium(V) from shale oxalic acid leachate using Aliquat 336 involves anion exchange between the VO(C2O4)22- anion and the chloride ion in the IL:

$$2[\mathrm{R_4N^+Cl^-}]_{\mathrm{org}} + \mathrm{VO(C_2O_4)_2^{2-}}_{\mathrm{aq}} = [(\mathrm{R_3N})_2\mathrm{VO(C_2O_4)_2}]_{\mathrm{org}} + 2\mathrm{Cl^-}_{\mathrm{aq}} \qquad \text{(Reaction 2-2)}$$

8 mol dm^{-3} HCl was suggested for the back extraction of vanadium.

The authors determined that this method is environmentally safe, does not require pH control, and can extract vanadium(V) faster than systems containing inorganic acids. It is suitable for processing vanadium-bearing shale.

Additionally, Aliquat 336 diluted with kerosene can be used to recover molybdenum(VI) from an alkaline solution containing aluminum(III), copper(II), and

nickel(II).[34] By increasing the extractant concentration to 0.1 mol dm^{-3}, the molybdenum extraction efficiency was raised to 98.5%, and the process was mostly unaffected by temperature changes.

The authors[34] also noted that Aliquat 336 can be utilized for the hydrometallurgical recovery of molybdenum from spent hydrotreating catalysts. However, they did not examine separating molybdenum from other elements, such as cobalt, rhodium, platinum, palladium, and vanadium, present in the spent catalysts.

2.2.3 Imidazolium based ionic liquids for metal extraction

Transition metals can be extracted and separated using ionic liquids that are based on imidazolium cations. Corbett et al.,[35] studied a range of imidazolium based ionic liquids for the extraction of Zn^{II} and Cu^{II} from n-hexadecane based model diesel. They reported that 99.3% of Zn^{II} and 99.7% of Cu^{II} were extracted using $[C_4C_1im][OAc]$ at 100:1 fuel:IL ratio. A study involving zinc(II), cadmium(II), copper(II), and iron(III) extraction from a hydrochloric acid solution demonstrated that 1-butyl-3-methylimidazolium tetrafluoroborate [bmim][BF4] can selectively separate zinc and cadmium from iron and copper. The study also found that 1-butyl-3-methylimidazolium hexafluorophosphate ([bmim][PF_6]) and 1-octyl-3-methylimidazolium bis(trifluorom ethylsulfonyl)imide ([omim][NTf_2]) can selectively separate zinc/cadmium and zinc/iron pairs, respectively.[36]

To substitute the commonly used methyl isobutyl ketone in separating tantalum(V) from a sulfuric acid solution, imidazolium ionic liquids with a keto group in the cation, namely [EPipMIBK][NTf2] and [MImMIBK][NTf2], were employed in a liquid-liquid extraction process. These ionic liquids offer several advantages over methyl isobutyl ketone. Unlike the latter, which is highly soluble in water and poses fire and explosion risks, the ionic liquids are non-flammable, non-volatile, and have low viscosity. They exhibit poor solubility in water but dissolve readily in organic solvents such as kerosene. The extraction efficiency of tantalum using these ionic liquids reached an impressive 96%.[37]

In a separate study, researchers suggested the use of an undiluted ionic liquid, 1-ethyl-3-methylimidazolium diethyl phosphate [EMIM]-DEP, for extracting vanadium(V) from diluted oil sands. Vanadium exists in oil in the form of a porphyrin complex. To displace the VO22+ ion from the porphyrin anion, the ionic liquid was acidified with 37%

hydrochloric acid. However, the recovery of vanadium using this method was only 26%, and the authors did not provide an explanation for this outcome.[38]

2.3 Vanadium Refining Vanadium Refining

2.3.1 Slags – Vanadium refining

Direct production of vanadium from titanomagnetite ores is economically infeasible due to the low (<1 %) vanadium grade of the ores. Instead, the ores are utilised as feed for blast furnaces (BF) or direct reduction (DR) in the steel and iron industries. In the smelting process in a BF, the reduced vanadium ends up in the molten phase and the unreduced vanadium makes its way into the BF slag. Some studies used the BF slag as a feed for vanadium extraction, however, the results were not satisfying, and the BF slag was reported to contain very low vanadium content for commercial vanadium processing plants.[39,40] Meanwhile, the molten phase is exposed to a ladle furnace to oxidise the impurities, including vanadium, which ends up in the slag phase and is discarded as vanadium slag. Vanadium slag is produced in the DR technology in a very similar way to the BF technology. The vanadium oxide fraction in the vanadium-bearing slag can be as high as 20 %, which meets the requirements for commercial vanadium processing plants.[41]

There are plenty of research works dedicated to designing and developing vanadium extraction processes from vanadium-bearing slags. The majority of the research works take advantage of the roasting-assisted leaching process to generate water-soluble vanadium species, followed by separation, purification and recovery processes through different techniques to produce vanadium metal, vanadium oxides or ferrovanadium compounds. There have been recent advancements to the conventional roasting processes as well as attempts for full hydrometallurgical extraction of vanadium.

The treatment of vanadium-bearing slag and the subsequent metal separation from the leach solution of vanadium-bearing slag has not been the subject of any reviews addressing the extractive metallurgy of vanadium. Gallagan and Nikoloski, recently reviewed the extraction of vanadium from titanomagnetites and other sources, although they only briefly touched on the treatment of vanadium-bearing slags.[42] Additionally, it was not precisely stated what new and recent advancements had been

made in the extraction and treatment processes, particularly for the hydrometallurgical separation of vanadium from its competitor components.

2.3.2 Petroleum ash – Vanadium refining

Crude oils naturally contain transition metals, and are rich sources of transition metals, particularly heavy crude oils from the Orinoco and the Canadian Oil Sands which contain high V and Ni concentrations.[43] In terms of chemical structure, vanadium and nickel create organic metal complexes in crude oils, mostly in porphyrinic forms. These complexes are identified as the most objectionable and abundant materials in the organic fraction of crude oils, consequently, are the primary targets of refineries for removal. Although lighter crudes, namely sweet crudes, contain lower concentrations of impurities, as lighter crude deposits are diminishing, the industry is anticipated to move towards upgrading heavier crude feedstocks to meet the ever-increasing demands and hence, metal recovery from crude oil becomes more emphasised.[44]

Figure 2-1 depicts the combination of pyro- and hydro-metallurgical technologies that make up the entire supply chain for the various process steps necessary to achieve vanadium recovery. The former refers to steps in the process where a high temperature is used to condition the metals present in fly ash, mined ore, or spent catalyst for recovery using rotary kilns and furnaces. The term "hydrometallurgy" itself refers to the process of dissolving, extracting, and purifying desired metals using aqueous chemistry (acid, base, or water). The use of solvents, particular complexing agents, and oxidation additives, among other things, can be included in the extension of hydrometallurgical extraction of vanadium.

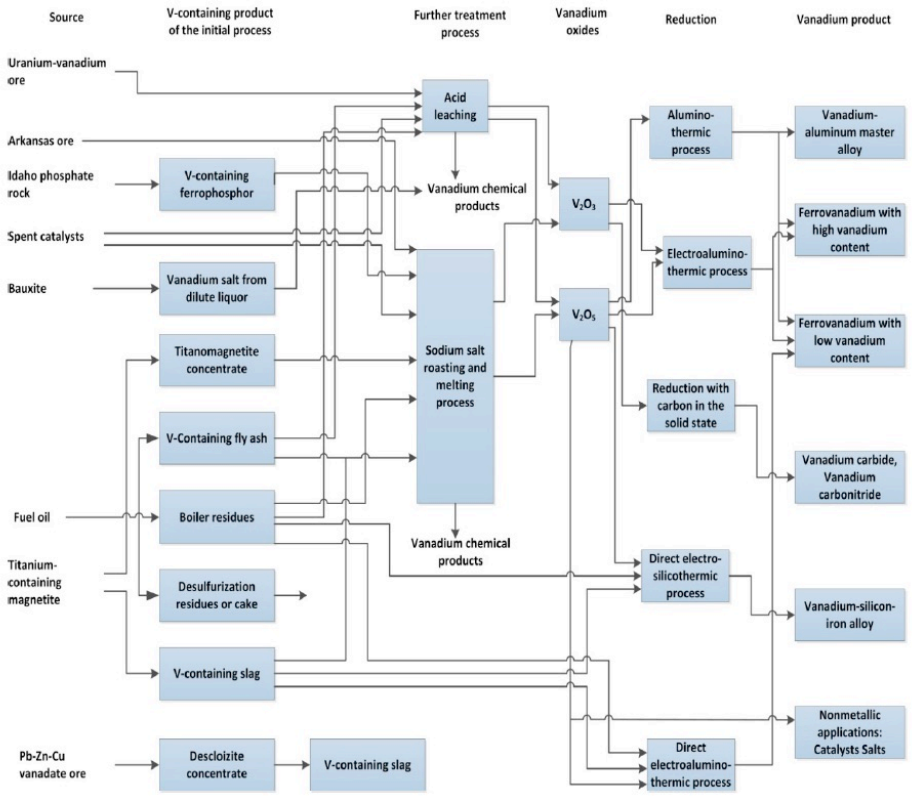


Figure 2-1. Vanadium processing paths from different raw materials.[45]

2.4 Chemical Composition of vanadium-bearing materials

2.4.1 Vanadium-bearing slag – Chemical composition

Table 2-1 shows the chemical composition of some vanadium-bearing slags from different sources. According to various research works, CaO, SiO_2, MgO, and Al_2O_3 concentrations typically vary from 2 % to 45 %, 6 % to 25 %, 1 % to 16 %, and 2 % to 10 %, respectively. Vanadium oxides chemical compositions either as V_2O_3 or V_2O_5 vary based on the different inputs into the furnaces, the effectiveness of such operations, and the intended end products. Chromium is specifically troublesome to the vanadium extraction process, suggesting that an additional metal separation technique is required to produce vanadium of high purity. During reduction smelting, titanium oxide in the titanomagnetite ore is primarily transported to the slag and is hardly reduced. However, a little amount of titanium is frequently detected in the molten metal and then removed together with vanadium during the oxygen-blowing procedure.

Table 2-1. Chemical composition of vanadium-bearing slags from different iron and steel-making plants.

Sources	Technology	Chemical compositions (wt. %)					Ref.
		V_2O_5/ V_2O_3	Cr_2O_3	FeO /Fe_2O_3	TiO_2	MnO/ MnO_2	
Panzhihua Iron & Steel	BF-BOF	8.5-14.3	2.1-4.3	32.9-42.1	11.1-12.9	5.9-9.1	46,47
Kapok Iron and Steel	BF-BOF	14.2-16.0	NA	31.9-32.3	12.0	7.6-8.7	48
Chengde Xinxin Vanadium & Titanium Chemical	BF-BOF	8.5	3.5	51.1	10.5	5.2	49
Desheng Iron and Steel Group	BF-BOF	15.2-20.8	7.7-10.6	35.3-64.5	639-8.5	5.5-7.6	41
Chengde Iron and Steel	BF-BOF	10.2-13.4	1.7-4.2	36.7-49.1	6.8-11.1	5.2-7.2	50,51
Esfahan Steel	BF-BOF	1.5-1.9	NA	17.3-17.6	1.0-1.5	4.2-4.5	52
Sichuan Weiyuan Iron & Steel	BF-BOF	14.3	4.4	24.8	7.4	8.5	53
Ma Steel	BF-BOF	3.1	NA	8.5	NA	1.5	54
Jianlong Steel	BF-BOF	15.3	12.5	26.9	8.1	7.3	55
British Steel	BF-BOF	0.8	0.2	32.0	0.3	4.5	56
CITIC Jinzhou Ferroalloy	DR-EAF	15.3	2.3	30.5	13.7	10.9	57,58
Pan Steel	DR-EAF	8.9-13.0	2.0-8.7	24.3-25.2	3.3-14.7	1.6-13.8	59
South Africa Slag	BF-BOF	21.2	3.4	35.6	10.9	3.8	56
NA: Not analysed							

2.4.1 Petroleum ash – Chemical composition

The so-called heavy oils around the world contain metals such as V, Ni, Fe, Si, and Al, as well as sulphur and sometimes Ti. Depending primarily on the characteristics of the heavy oil, processing of these heavy oils typically entails some type of thermal cracking to create a "light oil" fraction and a heavier residual oil or petroleum coke. A residual oil fraction or a by-product called petroleum coke is where the majority of the metals and part of the sulphur end up because they are still linked to the non-volatile components. Either of these fractions will produce fly ash after combustion, and the heavy metals in particular have a tendency to accumulate there. Table 2-2 shows the chemical composition of some fully oxidised (ashed) petroleum fractions. The reported compositions vary greatly. However, vanadium and nickel were the most abundant constituents of petroleum ash. The concentrations of aluminium and silicon in some of the samples were reported to affect the leaching efficiency due to the generation of a silica-alumina matrix in the solutions.[14]

Table 2-2. Chemical composition of different ashed petroleum fractions.[14]

Source	Chemical compositions (wt. %)						
	V_2O_5	NiO	Fe_2O_3	Al_2O_3	SiO_2	S	C
Amuay (Venezuela)	16.24	0.89	8.58	-	-	-	-
Canadina Petrofina	13.9	1.03	0.67	3.77	6.4	2.75	54
Long Island Lighting Co., USA	35-40	3	-	-	-	6-10	1
Long Island Lighting Co., USA	8-12	-	-	-	-	-	-
Great Canadian Oil Sands	2.49	0.84	5.5	14.6	24.8	2.16	39.8
Great Canadian Oil Sands	3.58	1.74	6.66	15.63	33.1	2.48	26
Flue Dust from Venezuelan Oil	35.28	6.01	4.8	0.5	2.5	29.94	2.84

2.1 Mineralogical characterisation of vanadium-bearing materials

2.1.1 Vanadium-bearing slag – Mineralogical characterisation

Although vanadium-bearing slags can be sourced from different processes such as ammonia production or steel production processes, the mineralogical characterisation was found to be similar. Vanadium is present in the spinel phases of chromium which

are $(Fe,Mg,Mn)(V,Cr)_2O_4$, or titanium which are $(Fe,Mn)_2(V,Ti)O_4$. In a typical spinel grain, chromium is positioned at the centre, vanadium is at the outer layer and titanium is at the edge.[59] The spinel phases are dispersed in the olivine matrix (Fe,Mg)2SiO4, fayalite matrix (Fe_2SiO_4), augite matrix ($Ca(Fe,Mg)Si_2O_6$) (minor) and the diopside matrix ($Ca(Fe,Al)_2SiO_6$) (minor).[59-62] Other than V, Ti and Cr, other elements were also found the in the spinel grain. Manganese, for example, is evenly distributed throughout the spinel grain. Magnesium and chromium are concentrated in the $MgCrO_4$ as a minor phase.[60] Due to the large quantity of limestone used during the production of iron and steel, another vanadium phase, $Ca_2V_2O_7$ has also been detected.[52] Some other oxides have also been reported, which are derived from the fluxes added to the furnaces.[63]

2.1.2 Petroleum ash – Mineralogical characterisation

Li et al.,[64] studied the effect of temperature and potassium/sodium addition on the fusion characteristics of petroleum ash containing high amounts of vanadium and nickel. They reported that vanadium was present in V_2O_3 and FeV_2O_4 phases. The rest of the minerals were present in phases such as $NiFe_2O_4$, $CaAl_2Si_2O_8$ and $AlSiO_4$. Ibrahim et al.,[65] studied the phase transformation mechanisms of heavy fuel oil ash. The sample was taken from the boiler of an electrical power plant which could be fed with different carbon-rich feedstocks and thus the reported phases might not accurately reflect the typical phases in petroleum ash. The original sample contained $FeVO_4$, VO_2, $NaVO_3.H_2O$, $VOSO_4(H_2O)_6$, ZnS, Mg_2SiO_4, $CaSiO_3$ $Na_2S_2O_5$, and $CaFeSi_2O_6$. Jia et al,[66] investigated the vanadium phases from a boiler that was using 100 % petroleum coke. They reported that vanadium in the form of vanadate was accompanied by a mixture of cations and that its general phase was described as (Mg, Ca, Na, K, Fe)-$V_2O_7.xH_2O$. The rest of the elements were present in phases such as $CaSO_4$, CaO, MgO, $Ca_2Al_2SiO_7$ and SiO_2. Rahimi et al.,[67] reported that a sample of fuel oil fly ash contained Fe_2O_3, NaV_6O_{15} and NiV_2O_6. It can be seen from the existing research works that vanadium is accompanied by cations called concomitant cations and the bulk of the vanadium species can be present in the 3+, 4+ and 5+ oxidation states.

2.2 Roasting

The feedstock materials, production rates, and technological advancements used during the iron/steel-making process all affect the vanadium contents of the vanadium-bearing slags. The commercial vanadium production from slag plants, like those at

Highveld Steel and Vanadium Corp. in South Africa, Chengde Iron and Steel Group in China, Nizhniy Tagil Iron and Steel Works in Russia, etc., do use some common features, most notably the use of the following steps: (i) salt or non-salt roasting-water leaching and (ii) ammonium polyvanadate precipitation. The roasting step is the most essential step, which is to break down the vanadium spinels, generating soluble vanadium phases such sodium metavanadate soluble in aqueous media. A flowsheet for vanadium recovery is shown in Figure 2-2, highlighting the significance of the roasting stage in the vanadium refining processes.

2.2.1 Sodium roasting technology

The first sodium salt-roasting technology was proposed by Bleecker in 1912 when the sodium salts (NaCl, Na_2SO_4 or Na_2CO_3) were added to the vanadium-bearing slag and roasted at high temperatures.[16,68] The roasting process can also be conducted in the presence of additives in the temperature range of 400 to 1000 °C. The purpose of roasting is to convert the stable vanadium spinel or matrices into leachable forms in a way that the generated phases can be readily attacked in the next step which is leaching in water, acid, alkaline or a combination of the three. Moreover, low valence vanadium such as V^{III} is oxidized by the oxygen gas to the maximal extent and subsequently transformed into soluble vanadate species. The following chemical reactions are the steps that might be involved in the roasting process. It was reported that the formation of chlorine gas could catalyze the oxidation reaction.[69]

$$4\,NaCl + O_2 \rightarrow 2Na_2O + 2Cl_2 \qquad \text{(Reaction 2-3)}$$

$$2V_2O_3 + O_2 \rightarrow 2V_2O_4 \qquad \text{(Reaction 2-4)}$$

$$4VOCl_3 + 3O_2 \rightarrow 2V_2O_5 + 6Cl_2 \qquad \text{(Reaction 2-5)}$$

$$xNa_2O + y2V_2O_5 \rightarrow xNa_2O.y2V_2O_5 \qquad \text{(Reaction 2-6)}$$

The values of x and y in Reaction 2-6 are functions of the roasting conditions. The generated Na-V-O phase is highly soluble in water or acid.

Jing et al.,[70] used Na_2CO_3 to roast the feedstock followed by precipitation using $(NH_4)_2SO_4$ which resulted in the extraction of 94.6 % of vanadium(V) and 96.5 % of chromium(VI). Zhao et al.,[71] attempted the recovery of vanadium(V) from stone coal with the following roasting additives: 6 wt % NaCl and 10 wt % Na_2SO_4. The muscovite with quartz was reacted during the roasting process and subsequently was converted

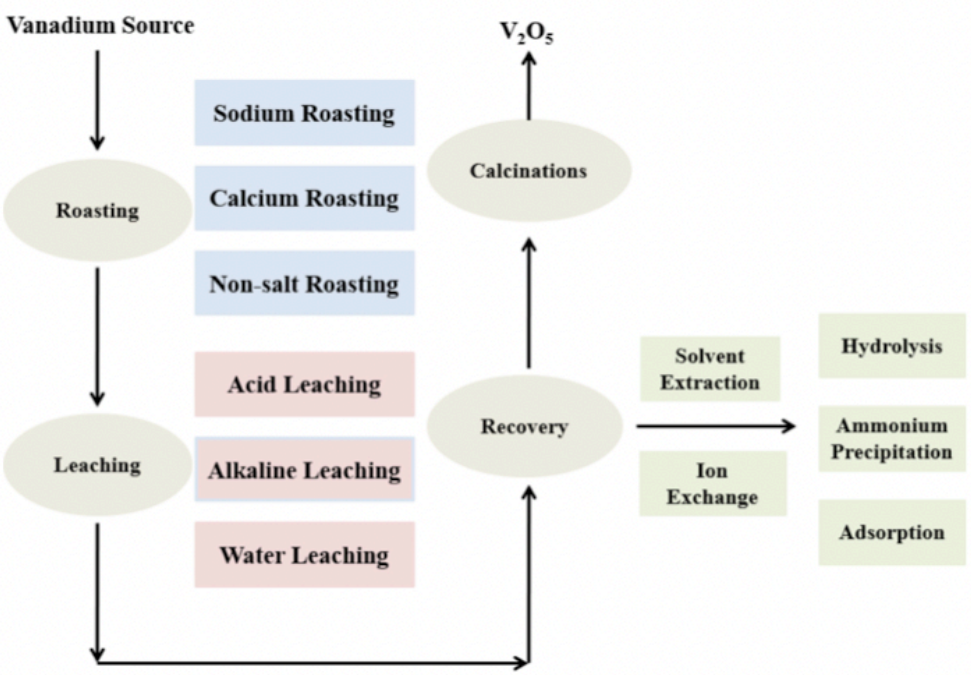


Figure 2-2. Flowsheet of vanadium recovery from a vanadium source to vanadium pentoxide.[16]

into feldspar group minerals (albite, orthoclase and anorthite). Because chromium is located at the centre of the spinels, Li et al.,[59] proposed the stepwise sodium roasting and water leaching technology through which high-chromium vanadium slag was roasted with Na_2CO_3 at 800 °C for 120 minutes. Approximately 87.9 % of the vanadium was leached out in the first step with only 6.3 % chromium extracted. After the second roasting and water leaching stage, 96.4 % of chromium along with 90.7 % of residual vanadium from the first stage were extracted to the water phase.

Although the sodium salt-roasting process might arguably provide a low production cost, this comes at the cost of severe environmental impacts due to the production of chlorine gas, and large quantities of carbon dioxide during the roasting process. The sodium salt roasting process has been prohibited in several countries including China (since 2006) which is the largest producer of vanadium.[72,73]

2.2.2 Calcium roasting technology

Due to the harmful emissions of sodium roasting technology such as SO_2 and Cl_2, a relatively cleaner process was proposed to substitute the sodium salt roasting process. In the calcium roasting technology, calcium salts such as lime or limestone or a

combination of the two are mixed with vanadium-bearing slag and ground to fine particles followed by roasting in a vertical kiln in which vanadium is converted to calcium vanadate, ready for the acid leaching step.[74-76] Alternatively, alkaline leaching may be used with carbonate or bicarbonate solutions.[77,78] The principle of the calcium roasting process can be broken down into four main steps according to the roasting temperature:

(1) The oxidation of FeO at 300 °C

$$2FeO + O_2 \rightarrow Fe_2O_3 \quad \text{(Reaction 2-7)}$$

(2) Decomposition of the iron-silica compounds within the range of 400-500 °C

$$Fe_2O_3.SiO_2 \rightarrow Fe_2O_3 + SiO_2 \quad \text{(Reaction 2-8)}$$

(3) Oxidation of the spinel phase in the hot air flow

$$Fe_2VO_4 + 2FeO + O_2 \rightarrow 2Fe_2O_3.V_2O_3 \quad \text{(Reaction 2-9)}$$

$$2Fe_2O_3.V_2O_3 + O_2 \rightarrow 2Fe_2O_3.V_2O_4 \quad \text{(Reaction 2-10)}$$

$$2Fe_2O_3.V_2O_4 + O_2 \rightarrow 2Fe_2O_3.V_2O_5 \quad \text{(Reaction 2-11)}$$

$$Fe_2O_3.V_2O_5 \rightarrow Fe_2O_3 + V_2O_5 \quad \text{(Reaction 2-12)}$$

(4) Calcium vanadate formation

$$Fe_2O_3 + V_2O_5 \rightarrow 2FeVO_4 \quad \text{(Reaction 2-13)}$$

$$2FeVO_4 + CaO \rightarrow CaV_2O_6 + Fe_2O_3 \quad \text{(Reaction 2-14)}$$

$$VO_2 + CaO \rightarrow CaVO_3 \quad \text{(Reaction 2-15)}$$

$$V_2O_5 + 3CaO \rightarrow Ca_3V_2O_8 \quad \text{(Reaction 2-16)}$$

$$3VO_2 + CaO \rightarrow CaV_3O_7 \quad \text{(Reaction 2-17)}$$

The calcined products are controlled by the kiln temperature and the Ca/V ratio.[79] The CaV_2O_6 and $Ca_3V_2O_8$ products are not soluble in water, hence an alkaline or H_2SO_4 solution must be chosen as the leaching medium. $CaCrO_4$ has a lower solubility even in acidic solutions, which is favourable for high vanadium selectivity.[80] Sometimes limestone is used in place of lime to reduce the cost of the reagent, forming compounds identical to calcium vanadate and chromate but with the production of additional CO_2. Gao et al.,[81] was able to achieve 98.29 % vanadium recovery by roasting high-chromium vanadium slag using a microwave-assisted method. The method not only decreased the particle size, which was beneficial for the acid/alkaline leaching kinetics

but also decreased the roasting time under optimal conditions. Zhang et al.,[53] investigated the roasting process with lime. They reported that the rate of heating had a considerable effect on the recovery of vanadium. Moreover, lowering the heating rate from 4 °C min^{-1} to 2 °C min^{-1} can improve the vanadium recovery efficiency by 10 % to a total of 91.46 %.

2.2.3 Non-salt roasting

The objective of this process is simply breaking down the iron-vanadium compounds which would result in the formation of acid- or alkaline-leachable species such as Mg_2VO_7 and CaV_2O_7 compounds. Hence, one requirement for such a process is vanadium-bearing slag with high Mg or Ca contents. The oxidation pathway was described by Meng et al.,[82]: (i) transformation of the vanadium spinel phases to $Fe_2O_3.V_2O_3$ during the initial time of the roasting process (0-10 min) (ii) oxidation of vanadium(III) to vanadium(IV) followed by partial reaction with MgO to produce Mg_2VO_4 until half an hour through the roasting process and (iii) generation of the highest-valence of vanadates due to further oxidation at a longer time. The next step in the non-salt roasting process is similar to that of the calcium or the sodium salt roasting processes as once the spinel or olivine phases were broken down to Mg and/or Ca -vanadium salts, vanadium could be leached out by water-leaching, acid-leaching or alkaline-leaching. The most common acid and alkaline solutions were reported as H_2SO_4 and NaOH, respectively. In the case of Ca-V-O phases however, sodium carbonate solution is the most effective solvent for leaching vanadium. [63]

2.3 Leaching

2.3.1 Water leaching

This system was only applied to sodium salt-roasted vanadium-bearing slags. The leaching reaction is shown in Reaction 2-18 to Reaction 2-20. The success of the leaching process was reported to be greatly dependent on the conversion efficiency of the sodium roasting process.[83-85] Li et al.,[59] reported 90.7 % vanadium and 96.4 % chromium extraction efficiencies through a two-step sodium roasting process which was in line with the results reported by other research works.[83-85] Other than the environmental considerations, there has been reported another particular issue with the sodium-roasting water-leaching process which is the selective separation of

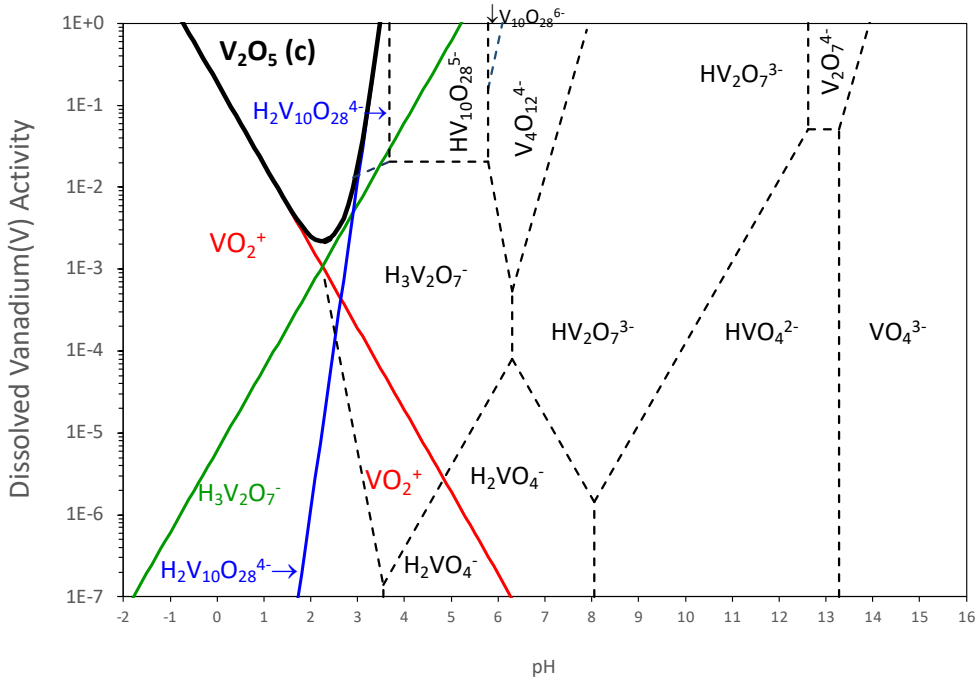


Figure 2-3. V^V activity-pH diagram for species in equilibrium with $V_2O_5.H_2O$ at 298 K, 0.1 MPa.

vanadium and chromium from the solution. Moreover, Na^+ ion recycling or recovery has been less of a concern in the literature so far.

$$NaVO_3 + H_2O \rightarrow H_2VO_4^- + Na^+ \quad \text{(Reaction 2-18)}$$

$$Na_4V_2O_7 + H_2O \rightarrow 2HVO_4^{2-} + 4Na^+ \quad \text{(Reaction 2-19)}$$

$$Na_2CrO_4 \rightarrow {CrO_4}^{2-} + 2Na^+ \quad \text{(Reaction 2-20)}$$

2.3.2 Acid leaching – Oxidative and non-oxidative

As mentioned earlier, due to the insolubility of calcium-vanadium salts, calcium roasting technology was combined with acid leaching, usually with H_2SO_4. The leached vanadium species were reported as VO_2^+, $V_{10}O_{28}^{-6}$ or other speciation determined by the pH of the solution and concentration of the dissolved vanadium as shown in Figure 2-3. The following reaction shows a typical reaction between the calcium-roasted vanadium slag and sulfuric acid at low pH.

$$Ca_3V_2O_8 + H_2SO_4 \rightarrow 3CaSO_4 + (VO_2)SO_4 + H_2O \quad \text{(Reaction 2-21)}$$

Some researchers reported enhancements in vanadium recovery yield upon addition of an oxidant. Yang et al.,[86] reported that the vanadium recovery yield was improved

from 74 % to 85 % without any influence on the selectivity for vanadium only by the addition of 2 % $KClO_3$ to the leach solution. Zhi-Gan et al.,[87] reported that the addition of an oxidant to the leach solution was able to improve the leaching efficiency from 14 % to 73 %. Tian et al.,[88] also reported a vanadium leaching efficiency of 96 % using microwave and 0.4 MPa oxygen pressure while only 46 % was achieved using electrical heating with all other experimental conditions being held constant. Different reports suggested that the addition of oxidant not only improved vanadium extraction yield but also reduced the amounts of leaching reagents.[87,88] Liu et al,[89] used electro-oxidation technology to increase the leaching efficiency of converter vanadium slag in an acidic medium; at the ideal leaching conditions, a high leaching efficiency (> 70 %) was achieved. Li et al.,[90] discovered that at an oxygen partial pressure of 1.2 MPa and a reaction temperature of 150 °C - 180 °C, the leaching efficiency of vanadium exceeded 90 % during the two-stage counter-current leaching technique. They subsequently reported that the leaching kinetics followed the shrinking core model with slight modifications in which the rate-controlling steps were both the interfacial transfer and the diffusion of reactant through the reactant sites.

2.3.3 Alkaline leaching – Oxidative and non-oxidative

The metal oxides of the following elements: Fe, Al, Mg in vanadium-bearing slags were reported to have high solubility in an acidic medium. The aforementioned elements were troublesome in the leaching process because they could leach out along with vanadium and thus were able to make an extensive amount of impurities in the leach solution which were difficult to separate effectively.[91] Sodium-vanadium or calcium-vanadium phases generated in roasting processes could also be leached out in an alkaline medium as shown in the following reactions:

$$Ca_3V_2O_8 + 3Na_2CO_3 \rightarrow 3CaCO_3 + 2Na_3VO_3 \qquad \text{(Reaction 2-22)}$$

$$Na_2O.V_2O_5 + 4NaOH \rightarrow 2Na_3VO_4 + 2H_2O \qquad \text{(Reaction 2-23)}$$

The sub-molten salt (SMS) technology has been recently developed to simultaneously oxidise and convert partially oxidised vanadium to soluble vanadium salts in a more environmentally friendly manner. Vanadium-bearing slags were exposed to highly alkaline solutions of NaOH, or KOH mixed with $NaNO_3$ in 3:1 ratio at a temperature of 200-400 °C. Reaction 2-24 shows a typical reaction involved in the SMS process. Liu et al.,[92] achieved a vanadium leaching efficiency of 93.7 % using the SMS process

under optimal conditions. The apparent activation energy was reported to be 98.02 kJ mol^{-1} and the extraction kinetics followed the unreacted shrinking core model. Wei et al,[93] studied the dissolution kinetics of lab-grade vanadium(III) oxide in an alkaline-oxygen system. The dissolution process was reported to follow the shrinking core model and it is independent of agitation speed above 800 rpm and sodium hydroxide concentration above 1 mol dm^{-3}. Over 90 % of the vanadium(III) oxide was converted to V_2O_5 under the following reaction conditions: 2 mol dm^{-3} NaOH concentration, 1000 rpm stirring speed, 500 kPa oxygen partial pressure and 86 μm particle size.

$$2FeO.V_2O_3 + 12NaOH + 5NaNO_3 \rightarrow$$

$$5NaNO_2 + 2Fe_2O_3 + 6H_2O + 4Na_3VO_4 \qquad \text{(Reaction 2-24)}$$

Peng et al,[94] investigated Alkaline-hydrogen peroxide and alkaline-electro-oxidation technologies to enhance vanadium recovery. They reported that the electro-oxidation technology was an efficient way to increase the extraction yield of vanadium(V). They also concluded that hydrogen peroxide can be used to intensify the leaching process and to reduce the apparent activation energy.

Liu et al.,[95] Performed a very similar experiment and they reported that the extraction yield was improved by 3.73 % at a current density of 1000 A m^{-2}, 4:1 cm^{-3} g^{-1} liquid-to-solid ratio, 80 °C temperature and 40 min leaching time.

2.4 Vanadium separation and purification techniques

One of the main disadvantages of the hydrometallurgical extraction process of vanadium is the undesirable co-extraction of other metal ions in the aqueous phase. The impurities type can be a large range depending on the pH, the nature of the feedstock and the leaching reagent type. Some interfering elements are chromium, silicon, phosphorous and aluminium. A wide range of purification and separation techniques has been reported in the literature. Following the purification process, vanadium compounds/oxides are separated typically in a solid form. Herein, different methodologies are described most of which produce V_2O_5 as the final product.

2.4.1 Desilication

Soluble silica such as sodium silicate interferes with both the filtration of leach liquor and the subsequent purification processes such as solvent extraction.[49] It was suggested to perform desilication by alkaline leaching prior to target metal extraction. However, this was described to be unfavourable from both economic and sustainability points of view because of the requirements for additional processing units and possible loss of vanadium if co-extracted in the desilication process. The desilication process has been utilised by some vanadium refining plants in Mustavaara, Finland[96], Rhovan, South Africa[97], Windimurra, Australia[98], etc. The basic principle of the desilication process is to co-precipitate the soluble silica with aluminium at pH 3.0-3.5 as silica-aluminium hydrates, as shown in Reaction 2-25. The neutralisation precipitation path typically takes a long time. Queneau and Berthold reported that adding a flocculating agent generates a bridge between the colloidal particles which could result in a faster precipitation rate while avoiding co-precipitation of vanadium(V). The results showed a combination of film separation and flocculation techniques and reported enhancements in the removal of silicon while the precipitation time was shortened to 30 minutes.[99]

$$\mathrm{Si-OH + Al-OH \rightarrow (Si-O-Al).xH_2O} \qquad \text{(Reaction 2-25)}$$

Zhang et al,[99] reported a desilication process through a combination of neutral depositing with solvent extraction. They reported a highly efficient method for removing silicon using the following procedure: The solution pH was adjusted to 9.5 to remove silicon partially, then vanadium(V) and silicon (IV) were extracted in the organic phase by contacting the aqueous solution with 18.5 % N235 (a tertiary amine) + 8.5 % Octanol + 73 % sulfonate kerosene. Silicon was stripped using a sodium carbonate solution at pH 10. About 99.6 % silicon removal was achieved in this method.

2.4.2 Dephosphorisation

Phosphorous forms stable heteropoly acids in the presence of ammonium and vanadium ions. Researchers have used magnesium, aluminium and calcium salts in order to eliminate phosphonium ions. In particular, magnesium salts were used in the pH range of 9.5-11.0 at 45 °C (see Reaction 2-26 and Reaction 2-27). The optimum conditions in the case of calcium salts were (i) pH of 8-9 and temperature of 80-95 °C that left behind products such as $Ca_3(PO_4)_2$, $Ca_5(PO_4)_3OH$, $CaHPO_4$, $CaHPO_4.2H_2O$

and $Ca_4H(PO_4)_3.2.5H_2O$.[100] In the case of other +3 cations such as iron(III) or aluminium(III), the process was operated in a lower pH range such as 5.0-7.0 to obtain products of $Fe_x(OH)_y(PO_4)_z$ or $Al_x(OH)_y(PO_4)_z$. Vanadium concentration in the leach liquor during the dephosphorization process plays a vital role in the overall vanadium(V) recovery yield. For example, Song et al.,[101] reported that vanadium(V) concentration must be kept around 19-22 g dm^{-3} in order to avoid the co-precipitation of vanadium as $Ca_{10}(PO_4)_{6-x}(VO_4)x(OH)_2$ in the dephosphorization process with Ca^{2+} ions. It was suggested that the pH should be carefully controlled to avoid the generation of dihydric phosphate and hydrophosphate as they exhibit higher solubility than phosphate.

$$Mg^{2+} + HPO_4^{2-} + xH_2O \rightarrow MgHPO_4.xH_2O \qquad \text{(Reaction 2-26)}$$

$$Mg^{2+} + PO_4^{3-} + xH_2O \rightarrow Mg_3(PO_4).xH_2O \qquad \text{(Reaction 2-27)}$$

2.4.3 Precipitation by hydrolysis

As mentioned earlier, vanadium(V) exists in the form of different species according to pH and log of the total vanadium concentrations (see Figure 2-3). For highly acidic solutions containing dissolved V^V species, the solution pH is adjusted to 2-4 by dilution or hydroxide salt addition. As a result, the oxovanadium ions such as decavanadate ($V_{10}O_{28}^{6-}$) undergo hydrolysis to form precipitation (red cake)[16], ideally at high temperatures as shown by Reaction 2-28.

$$6Na_4H_2V_{10}O_{28} + 7H_2SO_4 + nH_2O \rightarrow$$

$$5Na_2V_{12}O_{31}.nH_2O + 7Na_2SO_4 \qquad \text{(Reaction 2-28)}$$

Lee et al.,[63] reported that over 98 % of the vanadium could be recovered using this method. However, there is a significant disadvantage to this method. According to Peng,[16] vanadium recovery by hydrolytic precipitation left behind a red cake which contained a variety of impurities and the vanadium content was only 85 %, with the majority of the impurities being sodium. Further treatments such as ammonia rinsing were required to obtain high-content vanadium oxides.

2.4.4 Ammonium salt precipitation

This is by far the most widely used method in the vanadium refining industry. This method can be applied to all water/acid/alkaline systems. Wen et al.,[102] investigated vanadium leaching in $(NH_4)_2SO_4$-H_2SO_4 synergistic system and NH_4^+ recycle. Upon

adjusting the pH of the vanadium(V) solution to 1.8-3 using ammonium salts such NH_4Cl or $(NH_4)_2SO_4$, the vanadium polymer ions were precipitated as follows:

$$H_2V_{10}O_{28}{}^{6-} + 10NH_4^+ + 8H^+ \rightarrow$$
$$5(NH_4)_2V_6O_{16} \downarrow + 4H_2O \qquad \text{(Reaction 2-29)}$$

While in the alkaline medium, Xiong et al.,[103] reported that addition of an ammonium salt resulted in the precipitation of ammonium metavanadate (AMV) within the pH range of 8-9 and the temperature range of 80-90 °C as expressed in the following equation:

$$H_2VO_4{}^- + NH_4^+ \rightarrow NH_4VO_3 \downarrow + H_2O \qquad \text{(Reaction 2-30)}$$

Shi and Wang[104] reported that the solubility of NH_4VO_3 was related to the NH_4Cl concentration: 2.490, 0.026 and 0.006 g NH_4VO_3 in g^{-1} H_2O in the presence of 0.210, 2.540 and 4.470 g dm^{-3} NH_4Cl. The final product, V_2O_5, was achieved by calcining the AMV at 550 °C. In the vanadium refining industry, the calcination process is carried out in a kiln, which produces high purity vanadium pentoxide (over 99.5 %). Some typical reactions involving in the calcination process are shown below:

$$(NH_4)_2V_6O_{16} \rightarrow 3V_2O_5 + 2NH_3 + H_2O \qquad \text{(Reaction 2-31)}$$

$$2\ NH_4VO_3 \rightarrow V_2O_5 + 2\ NH_3 + H_2O \qquad \text{(Reaction 2-32)}$$

Zhang et al.,[103] studied the AMV process and the ammonium salt precipitation process in acidic solutions, from an stripping solution. They concluded that the precipitation process was less complicated in alkaline media, while the purity was higher in acidic media. The dissolved sodium had a negligible effect on the precipitation efficiency while dissolved phosphorus had a considerable effect in an acidic medium.

2.4.5 Adsorption

This method is not particularly used to recover vanadium(V) as a saleable product but rather is used in wastewater treatment, due to high efficiency, ease of regeneration of the adsorbents and simple operation. Melamine was reported to have great performance for adsorbing vanadium, presumably due to the interaction of vanadium(V) with the three free amino groups and three aromatic nitrogen atoms in the structure of melamine. The adsorption capacity of melamine was reported to be approximately 1429 mg g^{-1} and the adsorption kinetics were well fitted by the pseudo-

second-order kinetic model of Langmuir and Freundlich. Zhu et al.,[105] studied the adsorption performance of vanadium(V) on natural montmorillonite and kaolinite. The adsorption kinetics also followed the Langmuir model and the vanadium(V) ions had low affinity for natural montmorillonite and kaolinite function groups with the maximum adsorption capacities being 0.98 mg g^{-1} and 0.78 mg g^{-1}, respectively.

2.4.6 Solvent extraction

There are a large number of researchers who have focused on vanadium (mostly vanadium(V)) recovery from aqueous solutions using solvent extraction with a wide range of extractants. The extractants were trialkylamine (N235)[106-108] di(2-ethylhexly) phosphoric acid (D2EHPA)[109-112], 2-ethylexyl phosphoric acid mono 2- ethylexhyl ester (EHEHPA)[113], tri- butyl-phosphate (TBP)[114], bis(2,4,4-trimethylpentyl) phosphoric acid (CYANEX 272)[115], and trica- pryl-methyl ammonium nitrate (A336).[116,117]

The following vanadium species can be detected within the pH range of 0 to 4: VO_2^+, $VO_2SO_4^-$, $H_2V_{10}O_{28}^{4-}$ and $HV_{10}O_{28}^{5-}$. It was reported[118] that N235 was able to successfully extract oxovanadium anions through the following ion-exchange-type extraction reactions:

$$2[\mathrm{R_3N}]_{\mathrm{org}} + \mathrm{H_2SO_4} \rightarrow [\mathrm{R_3NH}]_2^+(\mathrm{SO_4})^{2-}{}_{\mathrm{org}} \qquad \text{(Reaction 2-33)}$$

$$[\mathrm{R_3NH}]_2^+(\mathrm{SO_4})^{2-}{}_{\mathrm{org}} + 2\mathrm{VO_2SO_4^-} \rightarrow$$

$$2[\mathrm{R_3NH}] + \mathrm{VO_2SO_4^-}{}_{\mathrm{org}} + 2\mathrm{SO_4^-} \qquad \text{(Reaction 2-34)}$$

$$[\mathrm{R_3NH}]_2^+(\mathrm{SO_4})^{2-}{}_{\mathrm{org}} + \mathrm{H_2V_{10}O_{28}^{4-}} \rightarrow$$

$$[\mathrm{R_3NH}]_4^+\ \mathrm{H_2V_{10}O_{28}^{4-}}{}_{\mathrm{org}} + 2\mathrm{SO_4^-} \qquad \text{(Reaction 2-35)}$$

$$[\mathrm{R_3NH}]_2^+(\mathrm{SO_4})^{2-}{}_{\mathrm{org}} + 2\mathrm{HV_{10}O_{28}^{5-}} \rightarrow$$

$$2[\mathrm{R_3N}]_5^+\ \mathrm{HV_{10}O_{28}^{5-}} \qquad \text{(Reaction 2-36)}$$

Vanadium(V) that was extracted in the organic phase was stripped in multi-stage counter-current process using concentrated NaOH solutions, and was then precipitated as AMV according to Reaction 2-32. Xiong et al., studied the selective extraction process of vanadium(V) with P507 and N235 and reported that approximately 95 % of vanadium(V) was extracted and the impurities remained in the solution after performing only one stage extraction. The reaction conditions were: 10-

minute contact time, initial pH of 1.7, organic to the aqueous phase of 1:2 and temperature 25 °C. Wen et al.,[119] investigated the extraction of various vanadium(V) species by primary amine. It was revealed that the extraction mechanism of vanadium(V) with amines was similar to that of CO_2 adsorption that is two hydrogen atoms and one nitrogen atom in -NH_2 group combined with one hydrogen atom and two oxygen atoms in the oxovanadium species ($H_xV_yO_z$) as N-H and O-H during the extraction process. Nguyen and Lee.,[120] studied the liquid-liquid extraction systems containing 5,8- diethyl-7-hydroxydodecane-6-oxime (LIX 63) and 2-ethylexyl hydrogen 2-ethylhexyl phosphonate (PC 88A) to selectively separate vanadium(V) from sulfate solutions under initial pH 1.2-6. It was revealed that the extraction process was highly dependent on the solution pH when LIX 63 was used in a way that the extraction yield dropped from 98 % to 20 % when the equilibrium pH was increased from 2.5 to 3.7. In the case of PC 88A, the extraction yield was increased from nil to 87 % as the equilibrium pH increased from 1.4 to 3. A further 14 % extraction yield was achieved from 83 % to 97 % when the extractant concentration increased from 0.05 to 1 mol dm^{-3}. Kim et al.,[121] studied the extraction process of vanadium(V) with a mixture of Alamine-336 and tri-butyl phosphate in 20 and 5 v/v %, respectively. It was revealed over 99 % of vanadium(V) was stripped in a two-stage extraction process at pH 1.25. The extract was then further processed with ammonium hydroxide to recover AMV as described in Reaction 2-32. The AMV was calcined to V_2O_5 and the purity of the final product was 98.4 %.

2.4.7 Ion exchange

The ion exchange process in principle is similar to the liquid-liquid extraction process with the difference being the extractants are solids such as resins. Zeng et al.,[122] studied the ion exchange kinetics of vanadium(V) on the weak base D314 resin. The adsorption mechanism was described as:

$$R_3N + HCl \rightarrow (R_3NH)Cl \quad \text{(Reaction 2-37)}$$

$$4(R_3NH)Cl + H_2V_{10}O_{28}^{4-} \rightarrow (R_3NH)_4.H_2V_{10}O_{28} + 4Cl^- \quad \text{(Reaction 2-38)}$$

$$5(R_3NH)Cl + H_2V_{10}O_{28}^{5-} \rightarrow (R_3NH)_5.H_2V_{10}O_{28} + 5Cl^- \quad \text{(Reaction 2-39)}$$

$$6(R_3NH)Cl + H_2V_{10}O_{28}^{6-} \rightarrow (R_3NH)_6.H_2V_{10}O_{28} + 6Cl^- \quad \text{(Reaction 2-40)}$$

The ion exchange process was stopped when the vanadium(V) concentration in the effluent reached 0.05 g dm^{-3}. The loaded resins were stripped using concentrated NaOH solutions as shown below:

$$(R_3NH)_4.H_2V_{10}O_{28} + 10NaOH \rightarrow 4R_3N + 10NaVO_3 + 8H_2O \quad \text{(Reaction 2-41)}$$

$$(R_3NH)_5.H_2V_{10}O_{28} + 10NaOH \rightarrow 5R_3N + 10NaVO_3 + 8H_2O \quad \text{(Reaction 2-42)}$$

$$(R_3NH)_6.H_2V_{10}O_{28} + 10NaOH \rightarrow 6R_3N + 10NaVO_3 + 8H_2O \quad \text{(Reaction 2-43)}$$

The vanadium(V) in the products of the above reactions were further treated to AMV through Reaction 2-32. The overall vanadium(V) recovery was over 99 %. Li et al.,[61] compared the solvent extraction technology and the ion exchange technology for vanadium(V) recovery from sulfuric acid media. It was revealed that vanadium(V) extraction kinetics favoured the ion exchange technology whereas vanadium(IV) extraction kinetics favoured the solvent extraction technology. Five different ion exchange resins were tested, from which ZGA414 resin showed the highest adsorption efficiency, about 99.9 % of vanadium(V) was extracted at pH 2.5. In the same study, it was shown that through a five-stage counter-current extraction process, 99 % of the vanadium(IV) in the aqueous phase was transferred to the organic phase containing 15 % (v/v) D2EHPA and 5 % (v/v) TBP with the organic to aqueous volume ratio of 1.0. Zhu et al.,[123] studied the separation characteristics of vanadium(V) in red mud by 201, D314 and 717 resins. It was revealed that over 99 % vanadium(V) was recovered from a hydrochloric acid solution regardless of the resin type. Each resin had a unique feature, resin D201 performed better in a strongly acidic medium with the highest loading per unit mass D201, and resin 717 showed the fastest adsorption rate in a weak acidic medium.

2.4.8 Adsorption using ionic liquids

Hu et al.,[124] studied the selective separation of vanadium(V) and chromium(VI) using ionic liquids. They investigated a range of imidazolium-based hydrophobic ionic liquids and reported that $[C_8mim][PF_6]$ exhibited satisfactory extraction behaviour for vanadium(V) and weak extraction for Cr(VI). The extraction behaviour was found to be

strongly dependent on the acidity of the aqueous phase and the highest separation factor (one distribution ratio divided by another) between vanadium(V) and chromium(VI) was found to be 100.6 at pH 3.5. The extraction mechanism was proposed to be the anion exchange between the oxovanadium species and PF_6^-. The extracted vanadium(V) in the ionic liquid phase was stripped using KPF_6 solutions. In the aforementioned process, the ionic liquid regeneration has yet to be addressed. Singh et al.,[125] investigated the extraction behaviour of vanadium(V) from a sulphate medium in an organic mixture of Cyphos IL 102 (trihexyl(tetradecyl)phosphonium bromide) diluted in toluene. They reported that the IL had a loading capacity of 16.3 mM vanadium(V) per 5 mM IL owing to the interaction of the polyoxovanadium species with the ionic liquid. Over 99 % vanadium(V) recovery was obtained in two counter-current stages at A/O of 2:1 and then A/O of 4:1, respectively. Highly pure V_2O_5 was achieved using this method which can be used for speciality applications such as smart windows and optical filters. Zhao et al.,[116] used pure ionic liquid [A336][NO_3] plus [RNH_3][NO_3] for the selective extraction of vanadium(V) from an aqueous solution containing chromium(VI). Compared to [A336][NO_3] alone, the distribution ratio of vanadium(V) was almost doubled and the separation coefficients of vanadium(V) to chromium(VI) were increased from 10 to 35 in the mixture of [A336][NO_3] and [RNH_3][NO_3] when the solution pH was 9.0. The extraction mechanism was described by the anion exchange between NO_3^- and $V_4O_{12}^{4-}$

2.4.9 Membrane electrolysis

Membrane electrolysis was utilised by Pan et al.,[126] to increase the V/Na ratio in leach liquor. The process was identical to the Chlor-alkali process with the difference being chloride anions were substituted by vanadate anions. The membrane electrolysis of sodium vanadate ($NaVO_3$) decreased the sodium content in the anode chamber and increased the pH in the cathode chamber due to the formation of NaOH. The pH in the anode chamber was simultaneously decreased which resulted in the formation of different oxovanadium species, depending on the pH, which is a function of time for batch electrolysis. They reported that $V_xO_y^{n-}$ could be converted to ammonium-V_2O_5 compounds using the ammonium metavanadate and ammonia system shown below:

$$2NH_4VO_3 + 4VO_3^- + 4H^+ =$$

$$(NH_3)_2.3V_2O_5.H_2O \downarrow + 2H_2O \qquad \text{(Reaction 2-44)}$$

$$2NH_3.H_2O + 2VO_3^- + 2H^+ =$$

$$(NH_3)_2.V_2O_5.H_2O \downarrow + 2H_2O \qquad \text{(Reaction 2-45)}$$

It was revealed that the ammonium metavanadate system (Reaction 2-44) showed higher precipitation yields (66.36 %) compared to the ammonia system (Reaction 2-45) which precipitated 38.76% of the vanadium(V) from the aqueous V_xOyn^- phase. Fang et al.,[127] used bipolar membrane electrodialysis (BMED) to purify vanadium(V) from a solution of $NaVO^3$.The optimum condition was pH 12 at which that $V_2O_7^{4-}$ species were transported through the membrane. The rest of the optimum conditions were reported as 30 mA cm^{-2} current density, 0.3 mol dm^{-3} $NaVO_3$ concentration, volume ratio between acid and salt compartments of 1:2 under which the vanadium(V) concentration in the acid chamber reached to 0.168 mol dm^{-3}, which corresponded to 17.29 % conversion. The specific electrical energy consumption was 13.52 kW h kg^{-1} V_2O_5 and the purity of the precipitate was 98.05 %.

Researchers often fail to address the fact that the leach liquor of sodium metavanadate has to be obtained from a sodium-roasting process, which produces toxic gasses such as Cl_2 and SO_2. The sodium-salt roasting process, as mentioned previously, has been prohibited in several countries, including China (since 2006), which is the largest producer of vanadium.[72,73] Moreover, the vanadium(V) selectivity of sodium-vanadium systems has major challenges such as the co-extraction of silicon(IV) and aluminium(III) at high pH.

2.5 Vanadium recovery from petroleum ash

Since the metal oxide types and phases of petroleum ash are different to those of the primary source of vanadium i.e., vanadium-bearing slags, the salt roasting process might be skipped, and direct leaching may be used instead in commercialised vanadium refining processes.

2.5.1 The SOTEX process

The SOTEX process shown in Figure 2-4 was one of the commercialised processes that directly used ash and soot residues as feedstock for vanadium refining without further chemical modifications to the ash. The process[128] starts with a primary wash, designed to remove water-soluble salts such as magnesium. This wash could potentially decrease the acid consumption in the sulfuric acid leaching step.

The solubility of vanadium during the primary wash was reported to be very low, and the nickel dissolution was negligible. The washed feedstock is then sent to the leaching reactors in which the redox potential is controlled by SO_2 in addition to keeping the vanadium in its tetravalent state. In the next step, the solution, which mostly contains V^{IV}, Fe^{II} and Ni^{II} is contacted with an organic phase containing 20 % di(2-ethylhexyl)-phosphoric acid and 15 % tributyl phosphate in kerosene. Iron(II) and vanadium(IV) are transferred to the organic phase whereas nickel(II) stays in the aqueous phase and is recovered as nickel ammonium sulfate. The selective separation of vanadium(IV) is achieved by stepwise washing the organic phase with different concentrations of sulfuric acid. The extracted vanadium(IV) is stripped using 1.5 mol dm^{-3} sulfuric acid. In the final stripping stage, a highly concentrated sulfuric acid solution is used to strip iron(II). The vanadium(IV)- rich solution is oxidised to vanadium(V) using an oxidising agent such as hydrogen peroxide. Subsequently, ammonia is introduced to the solution to precipitate ammonium polyvanadate (APV). The APV slurry is thickened, filtered and washed with fresh water. The thick APV filter cake is dried and subsequently calcined to V_2O_5. The plant however was shut in 1985.[128]

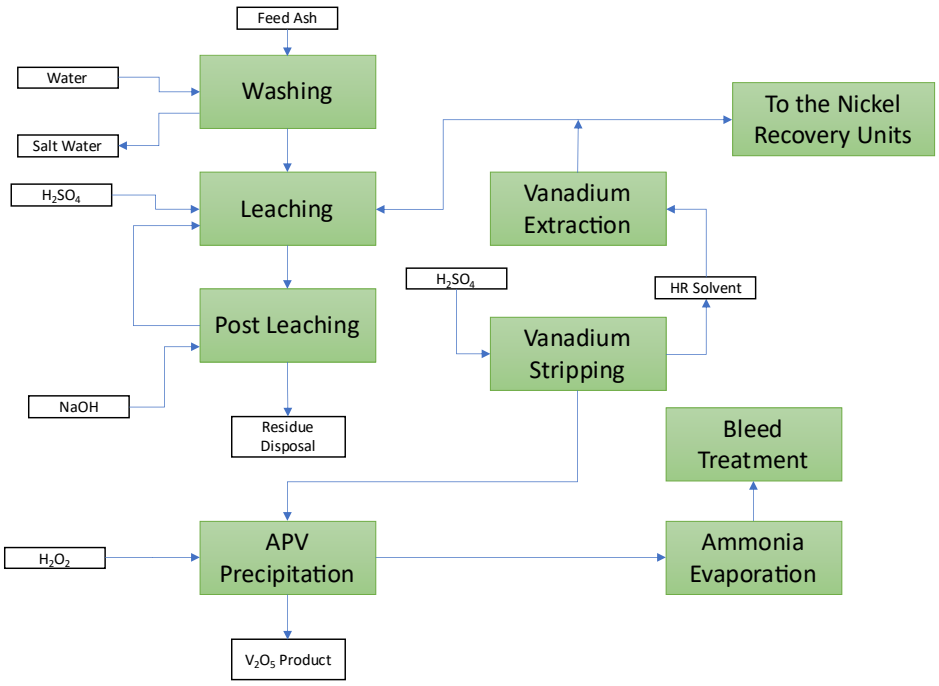


Figure 2-4. Process flow diagram of the SOTEX process for the extraction of vanadium and nickel from soot and flue ash.

Navarro et al.,[129] investigated the leaching kinetics of vanadium(V) from a petroleum ash (oil fly ash) sample by leaching, precipitation and solvent extraction. They reported that acidic leaching was highly efficient for vanadium recovery, however, alkaline leaching was considerably more selective for vanadium(V) recovery. Figure 2-5 shows the steps involved in the experimental setup. About 61 % vanadium(V) extraction yield and 49 % aluminium(III) extraction yield were achieved using a sodium hydroxide solution maintained at pH 12. Solvent extraction was performed with an extractant containing Aliquat, kerosene and isodecanol. Over 99 % of the vanadium(V) and 24 % of the aluminium(III) were transferred to the organic phase. The aqueous phase was treated with chitosan to remove 70 % of the vanadium(V). The organic phase was contacted with a mixture of ammonium hydroxide and ammonium chloride both had the same concentration, 1.5 mol dm^{-3}. About 48 % of the vanadium(V) was recovered from the organic phase while aluminium(III) was not stripped.

Alternatively, the leach liquor was treated by precipitation in a two-step process. The leachate was first neutralised to pH 8 as a result of which almost 100 % of aluminium(III) was precipitated with a negligible loss in vanadium(V). Then, ammonium polyvanadate was precipitated at pH 5 using NH_4Cl and sulfuric acid. About 99 % of

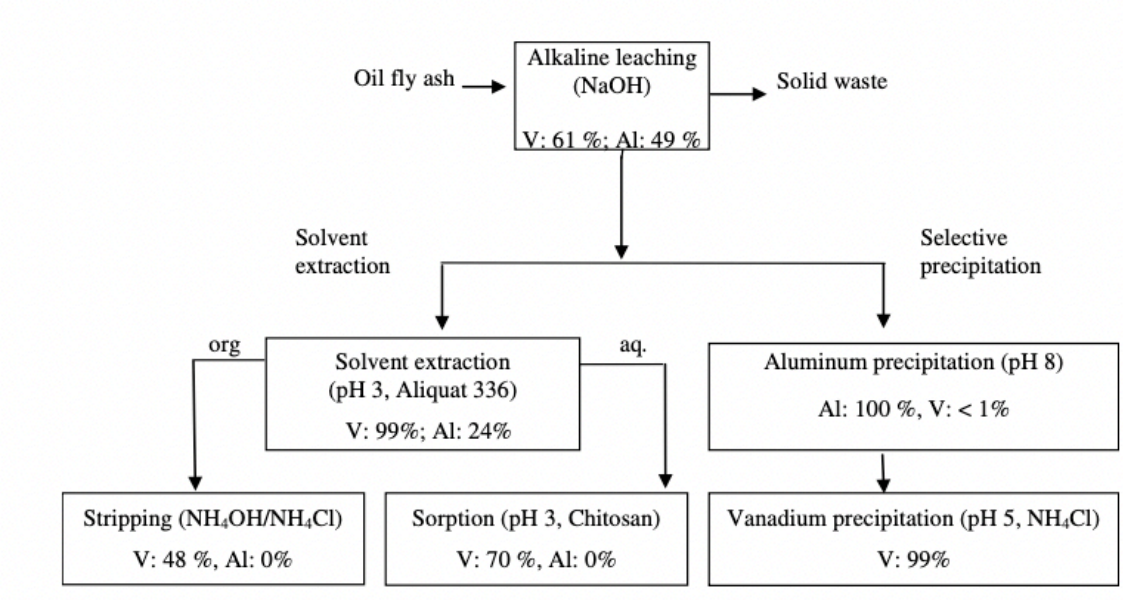


Figure 2-5. Oil fly ash treatment using different techniques.[129]

the vanadium was recovered. The overall recovery yield of vanadium(V) was 59.8 % if the selective precipitation method was used.

Rahimi et al., investigated ultra-sound assisted leaching of vanadium from petroleum ash (fuel-oil fly ash) using lemon juice (i.e. citric acid). The ash mostly contained Fe_2O_3, NaV_6O_{15} and NiV_2O_6. Hydrogen peroxide was used for the reductive dissolution of vanadium ash shown in Reaction 2-46. About 88.7 % of the total vanadium in the sample was leached out under the optimal condition: 27.9 % lemon juice, 10 % H_2O_2, S/L ratio of 0.01 % and ultrasound power of 159 W.

$$8H_3C_6H_5O_7 + NiV_2O_6 + H_2O_2 \rightarrow$$

$$Ni^{2+} + 2V^{3+} + 8H_3C_6H_5O_7 + 5H_2O + 3/2O_2 \qquad \text{(Reaction 2-46)}$$

2.6 Comparison of different extraction methods of vanadium and discussion

Vanadium ores are not commonly found in nature, which has led to the exploration of diverse sources for vanadium extraction. One such source is vanadium-bearing titanomagnetite reserves, which are widely utilised for this purpose. Another reliable primary source of vanadium at least in China is stone coal, due to the high demand for vanadium and the significant number of reserves. Mineral processing operations are typically employed for the beneficiation of titanomagnetite ores. However, the extraction of vanadium concentrate from stone coal is challenging, as the complex structure of stone coal and its low vanadium grade result in low vanadium recovery rates. Thus, researchers are focused on developing methods to improve vanadium recovery from stone coal.

Table 2-3 summarises different metallurgical methods for vanadium extraction. The production of fine-grade vanadium pentoxide through the traditional sodium roasting-water leaching process is a selective, industrial, economical, and mature method. This process is characterized by its stable operation and high recovery rate of vanadium, which makes it a popular choice for vanadium production. However, the sodium roasting-water leaching process is associated with environmental pollution, including the release of corrosive gases and the generation of large volumes of high-alkali wastewater. This poses a significant threat to the development of the vanadium industry. To address these issues, alternative technologies have been proposed for the efficient and clean production

of vanadium pentoxide. However, these alternative processes have their own limitations, and their industrial development will be challenging due to the complex extraction characteristics involved. Therefore, significant investment and research are required to develop these processes for industrial-scale production.

Compared to the commonly used sodium roasting-water leaching process for extracting vanadium from vanadium converter slag, the calcification roasting process has significant advantages in terms of environmental friendliness, cost of roasting additives, and reutilization of tailings. After undergoing calcification roasting, the vanadium spinel present in the vanadium converter slag is transformed into calcium vanadate, which can be extracted using either carbonation leaching or sulfuric acid leaching methods.

Titanomagnetite treatment does not involve the use of alkaline or acid leaching methods. Although acid leaching with sulfuric acid reagent has been efficient in extracting vanadium from uranium-vanadium ores, fly ashes, and boiler ashes, it has not been widely used in titanomagnetite processing. On the other hand, alkaline leaching, which is known to have higher selectivity compared to acid leaching, has been used less frequently in vanadium extraction and has mainly been applied to high lime uranium-vanadium ores using sodium carbonate, as well as fly ash, boiler ash, and spent catalysts with sodium hydroxide.

Vanadium extraction processes typically result in impure leach liquors that require purification. Currently, chemical precipitation is commonly used for leach liquor containing simple impurities obtained through the sodium roasting-water leaching process, due to its simplicity and lower cost. However, for complex or dilute solutions from stone coal and spent catalyst, solvent extraction or ion exchange methods are commercially used. Despite these purification methods, challenges remain in the purification of leach liquors obtained from new vanadium extraction processes.

To the best of the author’s knowledge, the only commercialised and fully hydrometallurgical process that uses petroleum ash as the feedstock was the SOTEX process. The plant however was shut in 1985 and no documents were published discussing the reasons. Some pyrometallurgical techniques have been commercialised with slight modifications to the process according to the nature of the

feedstock. By far, the process of salt roasting-water leaching followed by ammonium metavanadate precipitation is the most common technique used in the vanadium refining industry. The major challenges remained to be addressed, which are (i) low to moderate vanadium recovery yield (ii) energy-intensive processes (iii) emission of toxic gases such as Cl_2 and SO_2 which are hazardous at small levels (iv) low to moderate selectivity (v) CO_2 production (vi) production of tailings and undesired by-products. Hence, for the purpose of satisfying the world's ever-increasing demand for vanadium while having the minimum impact on the environment, some fundamental modifications have to be applied to the vanadium refining industry. Ionic liquids (ILs) which are frequently known as 'designer solvents' could help addressing the aforementioned challenges.

Table 2-3. A comparison of different metallurgical methods for extracting vanadium from vanadium-bearing slag.[130]

Metallurgical treatments	Environmental impact	Economic impact				
		Recovery rate	Selectivity	Reagent cost	Energy consumption	Special investment
Roasting-assisted leaching						
Sodium roasting	High	High	Low	Medium	High	Scrubbing gas system, kiln
Calcium roasting	Fairly high	Fairly high	Hig.h	Medium	High	Scrubbing gas system, kiln
Molten salt	Medium	High	Low	Fairly high	Medium	Scrubbing gas system, kiln
Mechanical activation	High	High	Not specified	Not specified	Fairly high	Milling circuit, dust collector
Microwave assistance	Fairly high	High	Not specified	Not specified	Fairly high	Microwave radiator
Leaching						
Ultrasound assistance	Medium	High	Not specified	Not specified	Fairly high	Ultrasonic transducer
Bioleaching	Low	Low	Fairly high	Low	Medium	Storage tank for growing microorganism
Sub-molten salt	Fairly high	High	Low	High	Medium	Autoclave
Pressure leaching	High	High	Low	High	Medium	Autoclave
Electrooxidation	Fairly high	High	Low	Medium	Fairly high	Electrodes
Urea leaching	Medium	Low	Lack info.	Medium	Low	Not specified
Chelating leaching	Medium	Medium	Low	High	Medium	Not specified
Surface control-assisted leaching	Medium	Medium	Medium	High	Medium	Not specified

3. Gasifier ash characterisation, vanadium(V) extraction kinetics and reaction mechanism

3.1 Introduction

Liquid-solid heterogeneous reaction systems have gained particular attention in hydrometallurgical and chemical processes in order to comply with sustainability and circular economy goals. Such hydrometallurgical extraction of metal oxides from industrial by-products or so-called industrial waste involves a heterogeneous mixture of reactants. Depending on the analyte of interest, semi-hydrometallurgical techniques may also be employed for the pre-treatment. For example, vanadium-bearing combustion residues (such as gasifier ash, steel slag and petcoke ash) are pre-treated by roasting the ash with sodium carbonate, resulting in the formation of water-soluble sodium vanadate ($NaVO_3$).[131] The key is the careful selection of the cation to minimize side reactions by which water-soluble impurities are formed. The other frequently used process to extract vanadium oxide materials is the direct leaching process in either highly acidic or highly basic conditions, or a combination of the two. Hydrometallurgical extraction of vanadium has long remained a challenge due to the oxyanionic character of the vanadate ions which form vanadate salts with the concomitant cations, defined as the elements co-existing in the vanadium phase i.e. Ca^{II} and V^{V} make Ca-V-O phases which are thermodynamically stable at a given pH.[132] Regardless of the extraction route, the conventional process to purify vanadium(V) is to use an ammonium salt as the precursor to precipitate ammonium polyvanadate, followed by the calcination of the solids to produce V_2O_5.[17]

3.1.1 Tetramethylammonium hydroxide as the leaching and the extractant agent

Quaternary ammonium salts such as Aliquat 336 in organic medium have been shown to be effective in the selective removal of vanadium from and aqueous solution.[32] It was established in this part of the research that quaternary ammonium hydroxide solutions such as tetramethylammonium hydroxide dissolve V^{V} selectively, leaving behind the most abundant elements which are commonly found in ash, such as silicon and aluminium ions in the precipitate.

Tetramethylammonium hydroxide is the simplest quaternary ammonium salt and is highly soluble in water. The solubility in water was reported to be 34.6 kg parts of tetramethylammonium hydroxide in 100 parts of solution at 15 °C.[133] The solubility can increase up to 100 g per 100 cm^3 at 20 °C. The melting point of the solid salt is ranging

from 63-70 °C and the boiling point of the pentahydrate salt is 102 °C. The vapour pressure at 25 °C is approximately 2.1 kP at room temperature and the physical appearance can be described as liquid, colourless with a slight amine odour.[134] The high pH (> 13) of the ionic liquid is desirable for the extraction of vanadium where it acts as both the leaching and the extractant agent, moreover, the hydroxide anion can be readily regenerated via electrochemical reactors which was one of the main motivations to use this ionic liquid. Tetramethylammonium vanadate, contrary to ammonium metavanadate, is highly soluble at high pH and in alcohols, forming highly concentrated vanadium(V) solutions with exceptionally high purity in both solvents.

3.1.2 Chapter objective

The initial objective in this section was to focus on understanding the chemical interaction between TMA^+, V^V and a range of concomitant cations at different pHs, enabling 'extractable' and 'unextractable' vanadium(V) oxide to be identified. Ultimately, a broader study was conducted to predict the extractability of vanadium(V) from a broader range of feedstocks with TMA^+ salts if the vanadium(V) phase is identified in the sample.

Determination of the hydrometallurgical extraction kinetics is of great importance for the fundamental interpretation of the nature of the process. Having a good understanding of the extraction mechanism and information on the overall mass transfer rate in a defined system enables prediction of inhibitions and enhancements in the rate of extraction. In a broader picture, the overall reaction rate is suggested to be limited by one of the following steps: diffusion of reactants through a thin liquid film, diffusion through the solid particles of ash, chemical reaction of unreacted materials on the surface of the core, or diffusion of the reactants through a newly formed product layer. To determine the rate-controlling step and the kinetic parameters of vanadium(V) dissolution from vanadium-bearing materials, the experimental data were used to determine the best fit model.

The objectives of this part of the project were to:

- Characterise the ash sample in the context of giving insights to the extraction kinetics behaviour and yield
- Conduct control experiments with lab-grade chemical reagents to study the dissolution of vanadium(V) in the presence of concomitant cations, potentially

leading to better understanding the hydrometallurgical behaviour of vanadium(V) extraction

- Describe a mechanism by which the overall rate of reaction is controlled
- Provide a mathematical model to predict the leaching kinetics.

3.2 Methodology

3.2.1 Leaching experiments

The ash sample was supplied by Shell Global Solutions International BV from Shell's Pernis refinery in Rotterdam, the Netherlands. The ash sample used in this study will be referred to as the gasifier ash which was taken from the Soot Ash Removal Unit (SARU).

The vanadium(V) leaching experiments were conducted using tetramethylammonium hydroxide (TMA^+OH^-) in a 250 cm^3 single-necked round bottom flask. In a typical experiment, 200 cm^3 of a TMA^+OH^- solution (0.95-2.78 mol dm^{-3}) was poured into the round bottom flask. This was then placed onto an aluminium heating block on a hotplate and was wrapped with a sheet of cotton insulator. The TMA^+OH^- solution temperature was allowed to reach the set temperature while being stirred using a PTFE-coated stirrer bar. Once the set temperature was reached, specific amounts of the gasifier ash and the additive were introduced to the solution. The studied variables were liquid-to-solid ratio (5 – 10 cm^{-3} g^{-1}), ionic liquid concentration (0.95 – 2.78 mol dm^{-3}) , temperature (60 – 90 °C) , additive concentration (0.055 – 0.221 mol dm^{-3}), and reaction time. The maximum reaction temperature of 90 °C was chosen to avoid TMA^+OH^- decomposition. It was reported that the ionic liquid starts to decompose above 130 °C.[135]

For the kinetics analysis, samples of approximately 3 cm^3 of the suspension were taken at different intervals using syringes. The wide bore needle was then replaced with a 0.22 µm syringe filter and the vanadium-loaded TMA^+OH^- solution was filtered into a 4 cm^3 vial, ready to be diluted for subsequent measurements by inductively coupled plasma mass spectrometry.

At the end of the extraction time, the resulting suspension was then transferred into a 50 cm^3 centrifuge tube. The suspension was centrifuged for 30 min at 4 000 rpm. The solid phase was separated from the V^V loaded TMA^+OH^- solution phase by simply decanting the upper phase into a glass vial. Since the leached vanadium(V) was

soluble in methanol and the rest of the residue was essentially insoluble in methanol, the residual solid phase was resuspended in 30 cm^3 methanol in the same centrifuge tube and the suspension was mixed using a vortex shaker. The suspension was centrifuged for 10 min and the solids were recovered by decanting the supernatant liquid phase. This was repeated twice to ensure the majority of the methanol-soluble vanadium(V) complex was removed from the residue. The solids were again suspended in methanol, but this time the slurry was vacuum filtered through two filter papers on a porcelain Büchner funnel and was rinsed with fresh methanol for the final step. The cake was dried in a vacuum oven at 60 °C overnight. The following day, the mass of the residue was recorded for mass balance analysis.

3.2.2 Inductively coupled plasma mass spectrometry

The elemental composition of the ash was analysed by Inductively Coupled Plasma Mass Spectrometry (ICP-MS; Agilent 7900). The technique ionizes elements via an extremely hot plasma created by argon gas. The sample ions are then identified based on the mass-to-charge ratio. In the mass spectrometer, the magnitude of the signal sent by the detector determines the relative concentration of the corresponding ions in the reference solutions. The advantage of this technique was the simultaneous precise determination of multiple metal ions in the same sample in a short period, approximately 4 minutes per sample. The major drawbacks were the time-consuming sample preparation steps and the volume of aqueous waste, as described below.

A triple $Sc^{III}/Y^{III}/Ir^{III/IV}$ solution was used as an internal standard to correct instrumental drift. The multi-element standard solution and the samples were diluted by a carrier solution with the same solution matrix as the ICP-MS internal solution. This carrier solution was prepared from 69 % nitric acid and 37 % hydrochloric acid, both for ultra-trace elemental analysis purchased from Fisher Scientific. The carrier solution was always made on the day of analysis by diluting the aforementioned concentrated nitric acid and the hydrochloric acid solutions using ultra-pure water to 2 vol% and 0.5 vol%, respectively. The calibration curves were prepared according to the following procedure: 1, 0.75, and 0.5 cm^3 of the certified Multielement Standard Solution 5 for ICP, which was purchased from Sigma Aldrich, were each diluted in 10 cm^3 volumetric flasks to make the reference solutions of R1, R2 and R3, respectively. Subsequently, 3 cm^3 of R1, 2 cm^3 of R2 and 1 cm^3 R3 were each diluted in 10 cm^3 volumetric flasks,

making the reference solutions of R4, R5 and R6. The seventh reference solution, R7, was the blank carrier solution.

The maximum theoretical concentration of the elements in the post-reaction vanadium(V)-rich solution could be determined simply by dividing the total concentration of the corresponding element, such as vanadium(V) in the ash, by the leaching solution volume. This was important to determine the minimum dilution factor (fold) required to dilute the post-reaction solution to concentrations below 1 μg cm^{-3}, which is common practice in this laboratory. For example, when the liquid-to-solid ratio was 10:1 cm^3 g^{-1}, 0.5 cm^3 of the sample was diluted in a 100 cm^3 volumetric flask to make the first fold (F1). Exactly 0.5 cm^3 of F1 was pipetted into another 100 cm^3 volumetric flask to make the second fold (F2). The resulting solution was filtered using a 0.22 μm syringe filter into a 10 cm^3 falcon tube ready for ICP analysis. The elemental analysis was conducted in triplicates and the average concentration was used to calculate the extraction yield shown below:

$$\gamma = \frac{V_{TMAH+V^V}\, C_{V^V}}{m_{ash} x_{V,ash}} \qquad \text{(Equation 3-1)}$$

Where γ represents the extraction yield, V_{TMAH+V^V} the volume of the vanadium(V) rich solutionin (dm^3), m_{ash} the mass of the gasifier ash (g), $x_{V,ash}$ the vanadium(V) fraction the gasifier ash (g g^{-1}) in and C_{V^V} the measured concentration of the vanadium(V) in the leach solution in (g dm^{-3}).

3.2.3 Microwave digestion

The ash samples were digested in a closed vessel according to the U.S. Environmental Sampling and analytical Method 3051A: Microwave Assisted Acid Digestion of Sediments, Sludges, and oils, with some slight modifications.[136] In a typical experiment, 50.0 ± 1.0 mg of the ash was weighed on a polystyrene weighing boat. Using a pipette, the solids were then washed into a 110 cm^3 iPrep™ Teflon digestion vessel with 9 cm^3 concentrated nitric acid (69 %, Ultra-Trace Elemental Analysis, Fisher Scientific) and 3 cm^3 hydrochloric acid (37 %, Ultra-Trace Elemental Analysis, Fisher Scientific). The vessels were fully sealed with Teflon caps and introduced to the microwave for the closed digestion process: 300 W at 83 % power for 5 min, 600 W at 66 % power for 5 min and 1200 W at 58 % power for 6 min. The target temperature was set at 180 °C. The vessels were left cooling inside the microwave for one hour for

safety reasons followed by three hours resting inside a ventilated fumehood. The caps were carefully loosened in a fume hood using special tools, allowing for nitrous oxide gas to purge. The caps then were opened fully, the contents of each vessel were transferred into 100 cm^3 volumetric flasks, and the volume was made up to the mark with the carrier solution. Then, the flasks were shaken, and the resulting solutions were filtered using 0.22 µm pore size syringe filters. 0.5 to 1 cm^3 of each of these solutions were diluted further in 100 cm^3 volumetric flasks to be ready for ICP-MS analysis. Certified sewage sludge was also digested separately from the ash, to assess the quality of the microwave-assisted digestion procedure.

3.2.4 Thermogravimetric analysis

Thermogravimetric analysis (TGA) is a technique for determining specific properties of materials that have lost or gained mass owing to decomposition, oxidation, or the loss of volatile components such as moisture. The TG 209 F1 Libra integrated with the 403 Aëolos Quadro quadrupole mass spectrometer was used for thermogravimetric analysis (TGA) of the as-received gasifier ash. The technique was predominantly used in this project to detect and trace the 'volatile' matter such as moisture, carbon residue and sulphur residue of the ash.

Approximately 45 mg of the sample was placed in an Al_2O_3 crucible, and it was introduced carefully to the instrument. The initial temperature was set as 30 °C, the thermal ramp rate was set as 7 °C min^{-1} and the final temperature was set to 900 °C. The nitrogen and air flowrates were set at 40 and 20 cm^3 min^{-1}, respectively, creating a mildly aggressive oxidative environment in the chamber. Heating and cooling rates, maximum and minimum temperatures, and dwell temperature and time were all regulated automatically. It was possible to obtain plots of differential thermal analysis, DTA (dT/dt versus temperature or time), thermogravimetry, TG (mass vs. temperature or time), derivative thermogravimetry, DTG (dM/dt versus temperature or time).

3.2.5 Density measurements

The density of the post-leaching TMA^+OH^- solution changed due to the dissolution of vanadium(V). Hence, the ICP measurements required corrections according to the vanadium(V) concentration in the final leach solution. A calibration line was constructed in the following manner: the density of a range of vanadium(V) concentrations was measured while keeping the ionic liquid concentration constant at

2.78 mol dm^{-3} TMA^+OH^-. The apparatus was a Mettler-Toledo DM40 density meter; the measurements were conducted at 20 °C which was similar to the lab temperature during the preparation of the ICP-MS samples.

3.2.6 X-ray diffraction

The diffraction patterns of the solid powders were obtained using a PANalytical X'Pert Pro multipurpose diffractometer (Cu K radiation). The equipment was used at room temperature, in the reflection mode, with a current of 30 mA and a voltage of 40 kV. The samples were scanned at angles ranging from 7 to 90° 2-theta. The X'pert high score software was used to identify the materials based on the XRD chromatogram patterns.

3.2.7 X-ray photoelectron spectroscopy

The X-ray photoelectron spectroscopy measurements were conducted using a Thermo Fisher K-Alpha+ High-throughput X-ray Photoelectron Spectrometer. For a homogeneous sample, high-resolution spectra could be obtained for the major elements, as well O1s and C1s in the corresponding samples. Therefore, the samples were ground to fine dust prior before the experiment to increase the homogeneity. A sufficient amount of the sample was dusted onto a 2x2 mm^2 carbon tape and flattened onto a sample holder using the back of a spatula.

The emitted photoelectrons were collected by the detector under ultra-high vacuum conditions. Each element in the ash has a unique binding energy that corresponds to the atomic orbital from which the photoelectron was emitted. As a result, a package of characteristic peaks for each element appeared in the XP spectrum. The registered databases were utilised to relate the emitted photoelectrons of a sample to a reference compound. It is crucial to understand that inelastically scattered photoelectrons cause a solid-state specimen to generate a background in the XP spectrum. Hence, the first step was the subtraction of the background to determine the stoichiometry of the elements from experimental spectra.

The area ratio of XP spectrum peaks of elements in a sample can be utilised to estimate the stoichiometry of the corresponding elements or oxides of an element. The typical formula for the peak area of an experimental spectrum is: [137]

$$\alpha = nf\sigma y\theta\lambda AT_{ef} \qquad \text{(Equation 3-2)}$$

where α represent the number of photoelectrons, n the concentration of the atoms in cm^{-3}, f the x-ray flux in photons cm^{-2} , σ the cross-section for of photoelectron in the target atomic orbital in cm^2, y the photoelectronic process efficiency for normal photoelectron energy formation, θ the angular efficiency factor for the instrumental arrangement, λ the photoelectrons mean free path in the sample, A the area (cm^2) of the sample from which photoelectrons are detected and T_{ef} the detection efficiency for electrons emitted from the sample.

The stoichiometry ratio of two elements of interest for example A and B could be determined from the area of the peaks resulting from a laboratory X-ray tube:

$$\frac{n_A}{n_B} = \frac{\alpha_A/\sigma_A y_A \lambda_A T_A}{\alpha_B/\sigma_B y_B \lambda_B T_B} = \frac{\alpha_A/S_A}{\alpha_B/S_B} \qquad \text{(Equation 3-3)}$$

Where S represents the sensitivity factor tabulated in literature.[137]

The area ratio of the overlapping peaks in the $V2P3_{3/2}$ region was utilised to estimate the stoichiometry of vanadium in different oxidation states. If the peaks in the $V2P3_{3/2}$ region are utilised, the sensitivity factor ratio is unity. Hence, Equation 3-3 can be written exclusively for vanadium oxides in the $V2P3_{3/2}$ region as:

$$\frac{n_{V^V}}{n_{V^{IV}}} = \frac{\alpha_{V^V}}{\alpha_{V^{IV}}} \qquad \text{(Equation 3-4)}$$

The above equation implies that the atomic mass of vanadium(V) to vanadium(IV) can be calculated simply from the area ratio of the corresponding overlapping peaks in the $V2P3_{3/2}$ region.

3.2.8 XRF

The bulk atomic compositions of the as-received ash and the post-leaching residue were determined by X-ray fluorescence in a PANalytical Epsilon 3^{XLE} EDXRF spectrometer. This rapid, non-destructive technique was implemented predominately to obtain a quick survey of the elemental composition of the gasifier ash.

In a typical experiment, 2-3 g of sample was placed in the provided plastic tubes with a thin film bottom cover. The sample was subsequently flattened using a plastic flat-bottom pestle to ensure uniform distribution of materials. In the case of a liquid sample, just enough sample was poured onto the tube to cover the film. The measurements were conducted at a current of 30 mA and a voltage of 40 kV.

3.3 Results and Discussion

It was established that a tetramethylammonium hydroxide solution can extract up to 83 % of the total vanadium from the gasifier ash. The determining variables were found to be the reaction time, temperature, quaternary ammonium hydroxide concentration, liquid-to-solid ratio and oxidising agent concentration. The reaction kinetics data were fitted in four different models. The fourth model, an alternative variant of the shrinking core model, appeared to be the best fit to account for both the interfacial transfer from the liquid phase to the solid phase and then diffusion of the materials across the product layer. The model was modified further to account for the reaction variables with the most impact on the vanadium(V) extraction yield in the following form: $k = k_0[TMAH]^a\,[NaClO_2]^b\left[\frac{L}{S}\right]^c e^{\frac{-E_a}{RT}}$. The exponents a, b and c were evaluated by plotting the natural logarithm of the rate constants versus the natural logarithm of the corresponding manipulated variable at fixed other conditions.

3.3.1 Gasifier ash characterization

Characterization of the gasifier ash was carried out on the as-received sample with no further processing.

3.3.1.1 Elemental analysis of the gasifier ash

Table 3-1 reports the chemical analysis for the gasifier ash measured by ICP MS whose typical calibration curve is shown in Figure 3-1. The first three major elements in the gasifier ash were V, Ni and Fe with concentrations of 38.32 %, 12.34 % and 5.09 %, respectively. The gasifier ash sample contained relatively high fraction of vanadium compared to other feedstocks such as vanadium slag with 5 %, and ammonia slag with 7 % V content.[132,138] The sulphur and phosphorous contents in Table 3-1 were determined from their relative concentrations determined by the XRF measurements. The compositional analysis was done also on the basis of the most stable oxide form to estimate the oxygen content and to close the mass balance; the oxygen content of the gasifier ash was 37.5 %. The error in the sum of the metal oxides percentages was less than 2%, which was reasonable and could have been due to the presence of less common, mixed oxide phases such as Ni-V-O or Fe-V-O materials, or partially oxidised materials.

Table 3-1. Composition of the gasifier ash measured by ICP-MS

Major elements	**Elemental composition / wt%**	**Composition based on the most stable oxide / wt%**	**Minor elements**	**Composition / mg kg^{-1}**
V	38.32	68.41	P	849
Ni	12.34	15.7	Mn	414
Fe	5.09	7.28	Cr	383
Ge	2.15	3.1	Si	290
Ca	1.17	1.64	Pb	273
Na	0.92	2.48	Ga	200
Zn	0.66	0.82	Sr	189
K	0.42	0.51	Cu	186
Mo	0.42	0.32	Li	108
Al	0.25	0.47		
S	0.23	0.46		
Co	0.18	0.08		
Mg	0.17	0.28		
Ba	0.16	0.18		
SUM	62.48	101.72		

Table 3-2. Composition of the volatile contents of the gasifier ash measured by XRF

Major Compound	**Composition / wt%**	**Minor compound**	**Composition / mg kg^{-1}**
V_2O_5	73.5	Cl	222.9
SO_3	0.74		
P_2O_5	0.25		

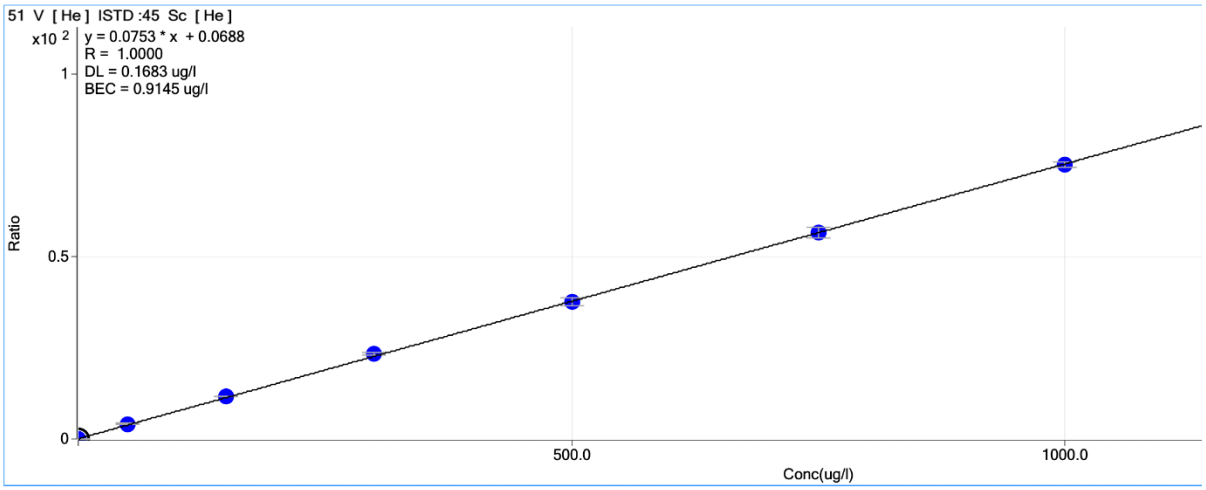


Figure 3-1. Typical ICP-MS calibration line for vanadium.

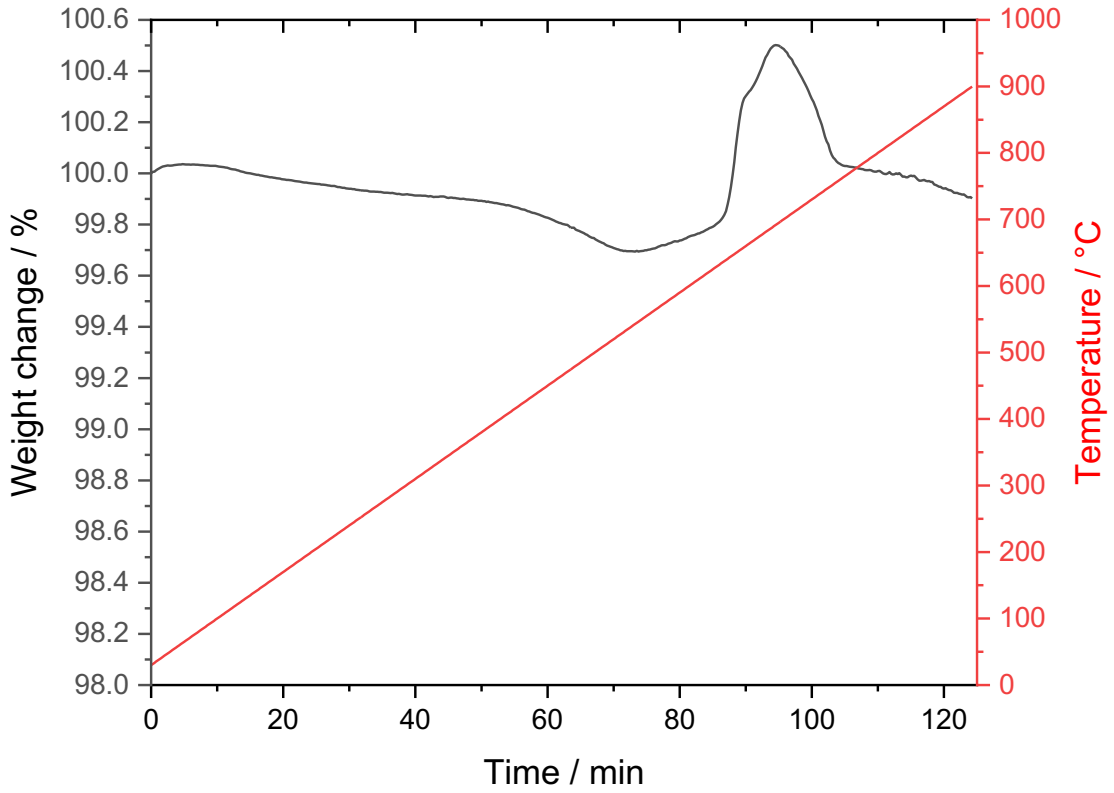


Figure 3-2. TGA data for the as-received SARU sample.

3.3.1.2 TGA analysis

Figure 3-2 illustrates thermogravimetric data for the gasifier ash heated in air from 30 °C to 900 °C at the rate of 7 °C min^{-1}. The sample weight stayed relatively stable up to ca. 150 °C, indicating the adsorbed moisture content was negligible. As the temperature was increased to 350 °C, the sample weight decreased by 0.2 % which was probably due to the decomposition of hygroscopic materials, i.e. the decomposition of water in Ca-V-O in Figure 3-5 . The combination of the results from the compositional analysis from **Error! Reference source not found.** and the vanadium oxidation state composition from Figure 3-58, implies that the ash consisted of 5.25 % V^{IV}. As a result, the oxygen mass required for the V^{IV} to oxidise to V^{V} was approximately 0.82 %. This was comparable with the mass gain from the TGA minimum at 550 °C to the maximum at 690 °C, going from -0.31 % to +0.55 % (0.86 % total mass gain). To investigate the chemical reaction at the corresponding temperature, 5 g ash was placed in a porcelain crucible and subsequently heated to 700 °C for 2 h in a muffle furnace. After cooling, a shiny metal-like lump appeared in the crucible with a significantly smaller volume than the starting materials. The metal oxide materials had been sintered to compounds such as Ni-Fe-V-O material (Figure 3-7) which lead to negligible extraction yield at the mild extraction conditions using TMAH.

3.3.1.3 Physical properties of the gasifier ash

shows some physical properties of the as-received gasifier ash. The mean particle size appeared to be 35 µm, which was suitably small to carry out the leaching experiments without further grinding. The density of the ash was relatively large with respect to water, so particles were not expected to float during the leaching experiment.

Figure 3-3 shows the particle size distribution (PSD) and the cumulative volume percentage for the as-received gasifier ash. The mean and the median particle sizes were found to be about 35.0 µm and 22.3 µm, respectively. The wide particle size distribution had d(0.1) and d(0.9) of 7.6 µm to 69.2 µm, respectively. The PSD analysis suggested that the ash did not contain large aggregates which would have been

required to be broken down into finer particles for the leaching experiments. The study of particle size distribution effect was eliminated from this project, due to: (i) simplification of the mathematical equation for the kinetic model, and (ii) reluctance to further chemical or physical processing of the gasifier ash prior to leaching.

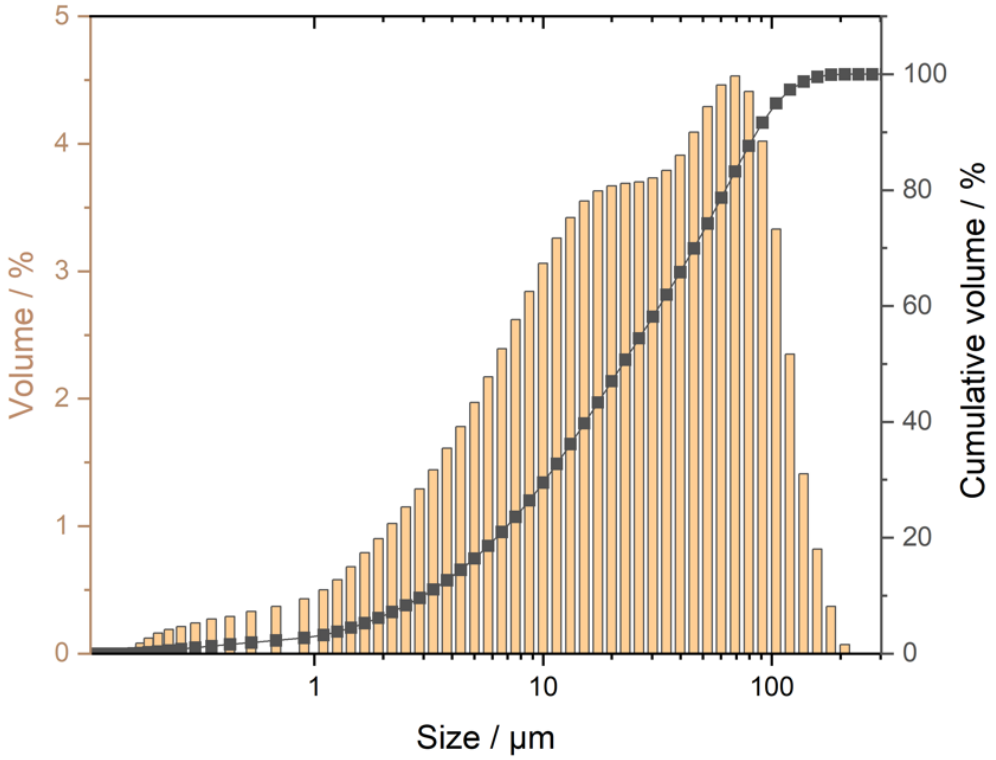
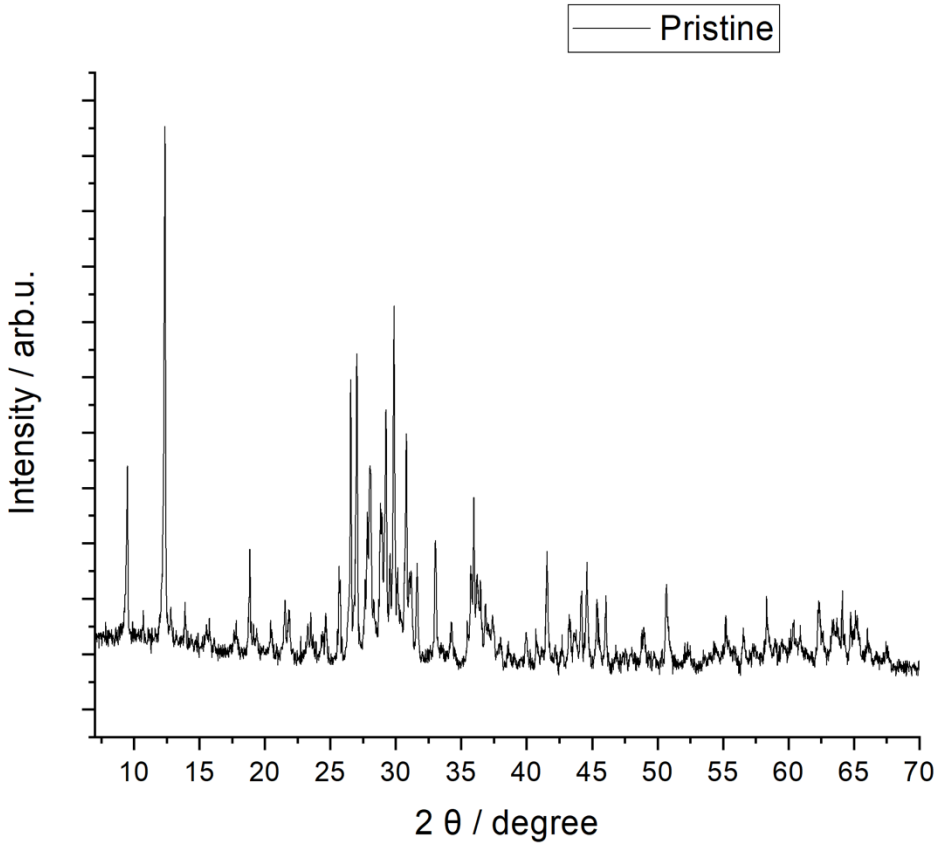


Figure 3-3. Particle size distribution for the as-received gasifier ash.

Table 3-3 physiochemical characterisation of the as-received gasifier ash.

Property	gasifier ash
Mean size / µm	35.0
d(0.5) / µm	22.3
Bulk density / g cm^{-3}	0.98
Specific gravity	2.38
Specific surface area / m^2 g^{-1}	0.934
pH of zero potential	4.3
Volatile mass %	0.31


Pristine
Intensity / arb.u.
10 15 20 25 30 35 40 45 50 55 60 65 70
2 θ / degree

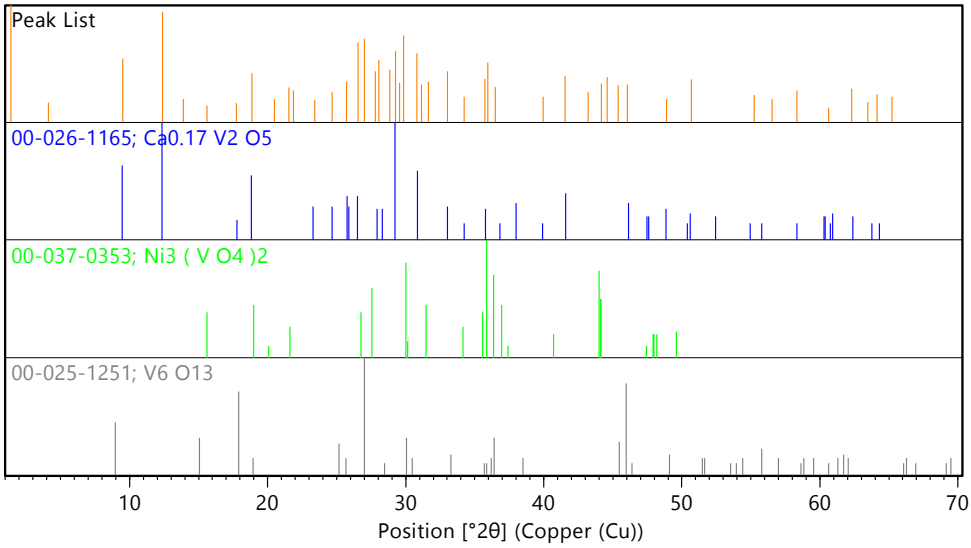

Peak List
00-026-1165; Ca0.17 V2 O5
00-037-0353; Ni3 (V O4)2
00-025-1251; V6 O13
10 20 30 40 50 60 70
Position [°2θ] (Copper (Cu))

Figure 3-4. X-ray diffraction pattern for the as-received gasifier ash and the identified phases.

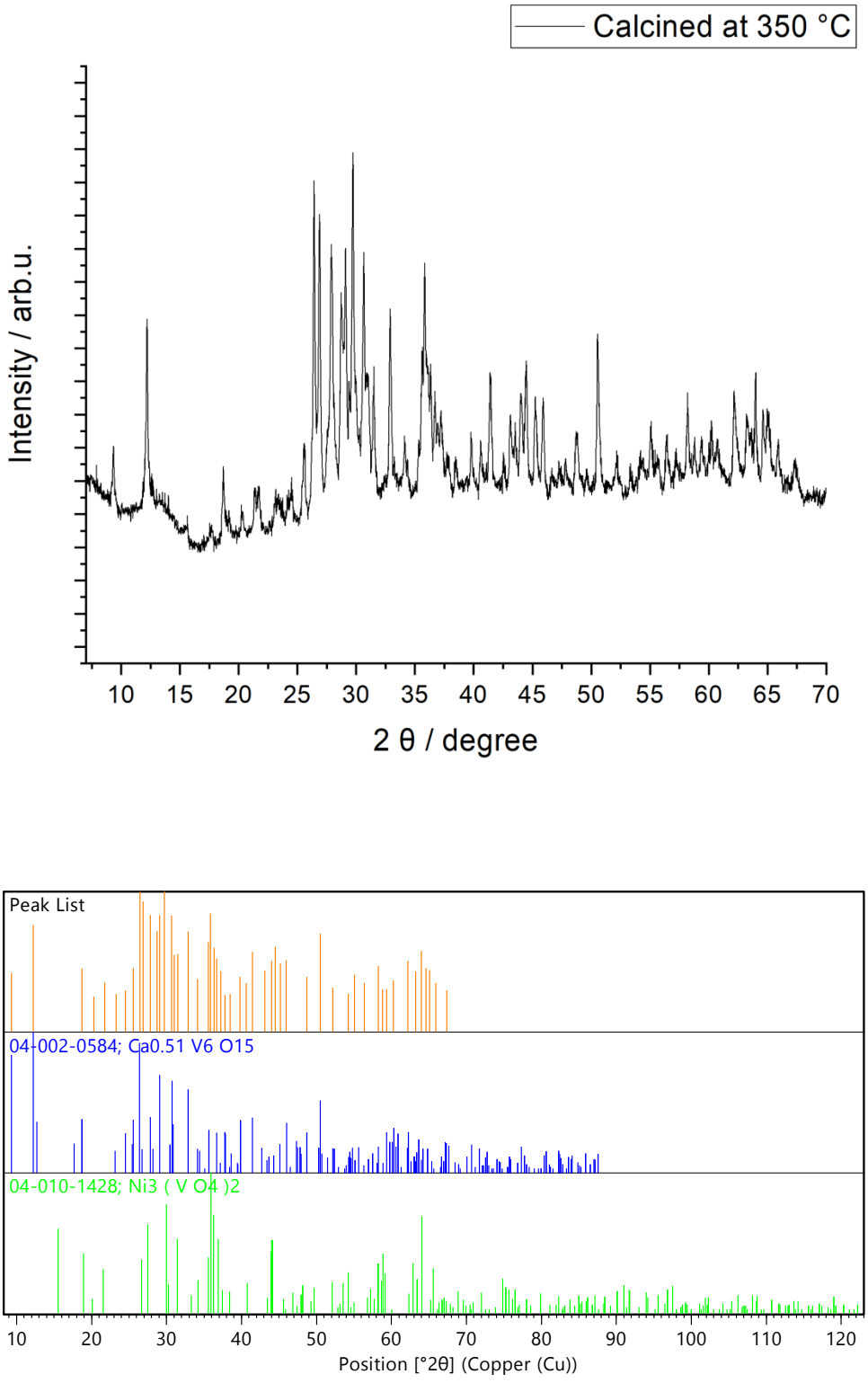
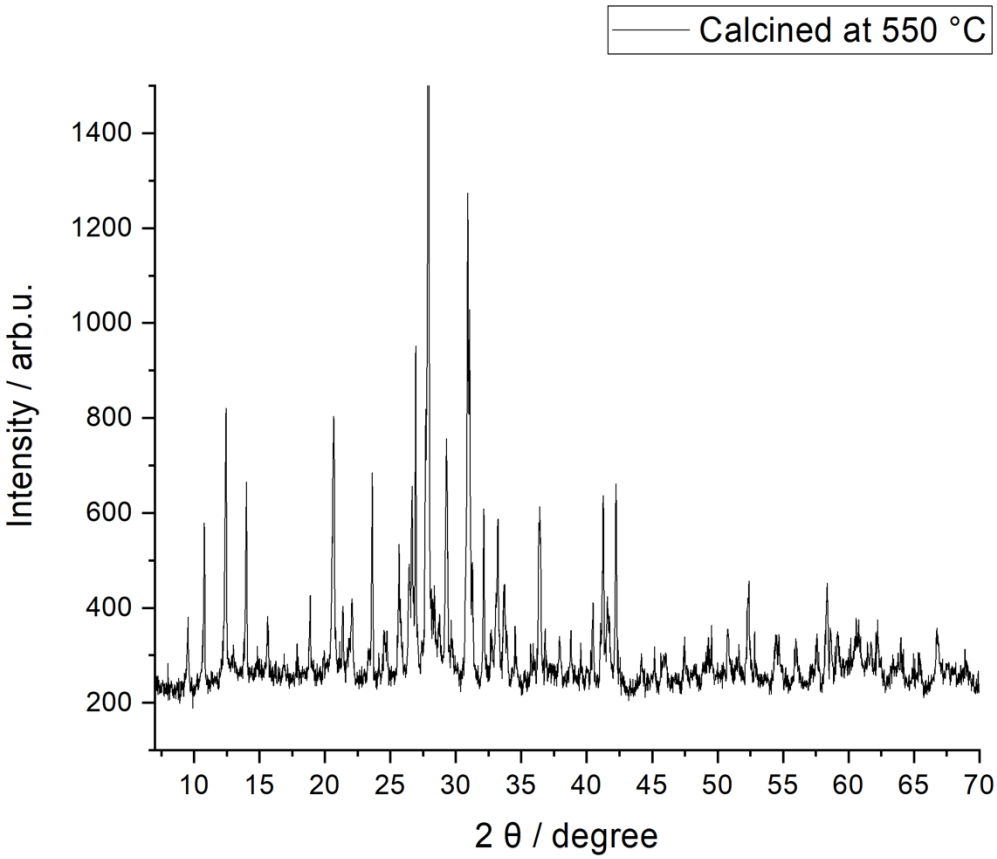


Figure 3-5. X-ray diffraction pattern for the calcined gasifier ash at 350 °C



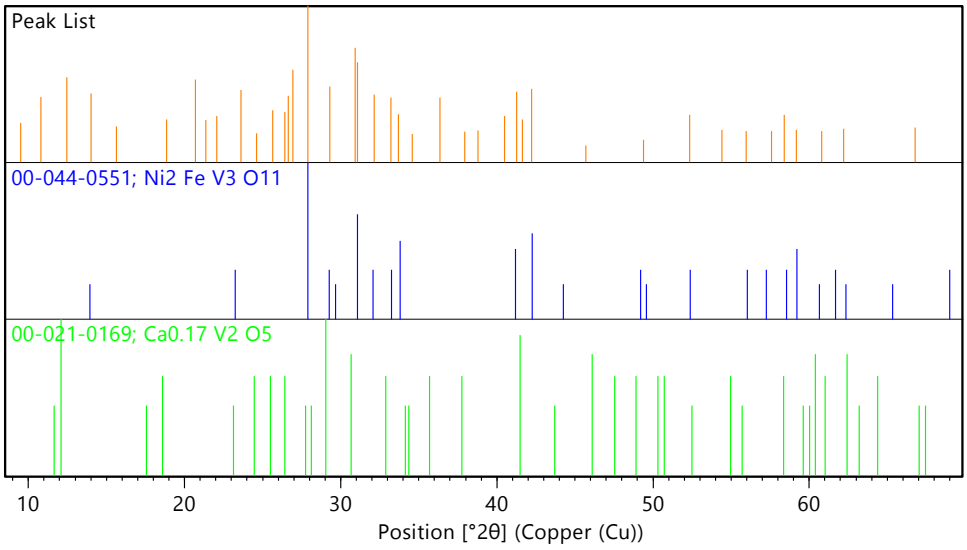


Figure 3-6. X-ray diffraction pattern for the calcined gasifier ash at 550 °C

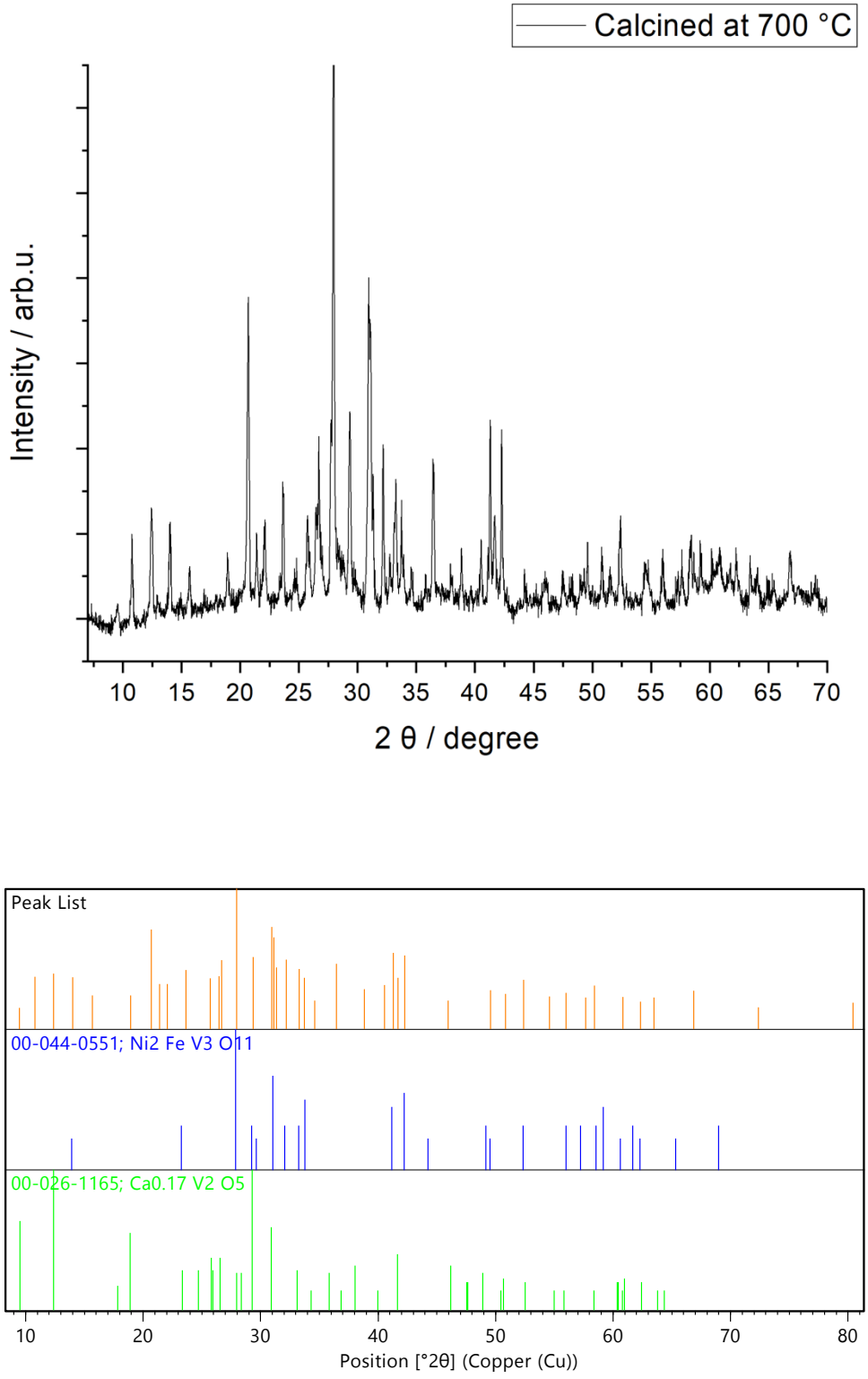


Figure 3-7. X-ray diffraction pattern for the calcined gasifier ash at 700 °C

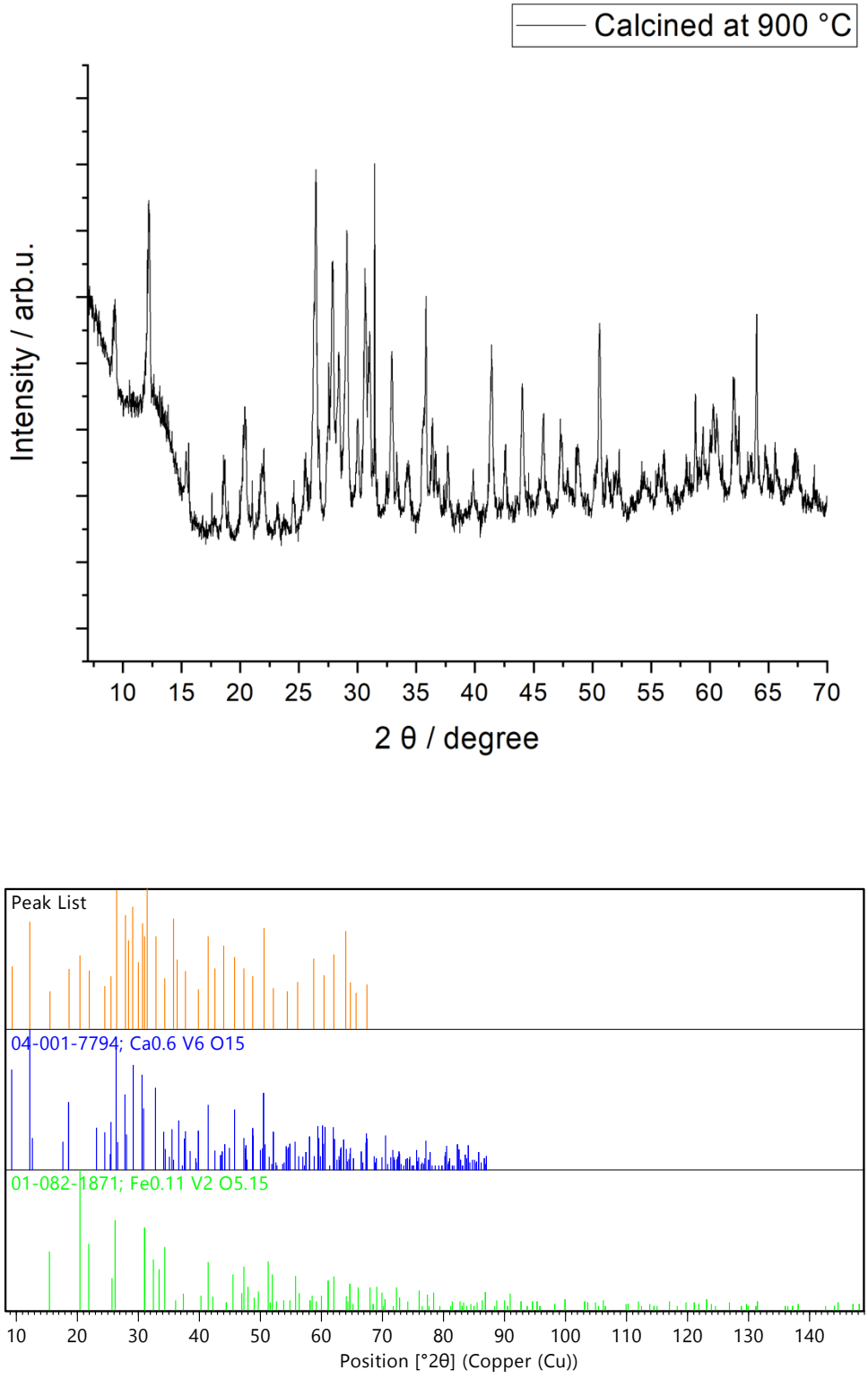


Figure 3-8. X-ray diffraction pattern for the calcined gasifier ash at 900 °C

3.3.1.4 XRD analysis of the as-received gasifier ash sample

The combination of X-ray fluorescence and ICP-MS techniques revealed that there were over 20 oxidised elements in the as-received gasifier ash. The exact identification of the phases and their crystalline structure seem to be impractical using the X-ray diffraction technique alone, due to the overlapping peaks and the embedded small intensity peaks in broad amorphous patterns, or simply being lost in noise due to their extremely low intensity relative to the major peaks.

Figure 3-4 shows the XRD pattern of the as-received gasifier ash and the identified phases. The XRD peak position and the relative intensities obtained from the gasifier ash were significantly comparable to those obtained by Romanovskaia et al. for the $Ca_{0.17}V_2O_5$ and V_2O_5 phases.[139] The XRD pattern for the post-extraction residue (Figure 3-57(a)) shows that the $Ni_3V_2O_8$ phase clearly remained in the residue and was not extractable under the experimental conditions. The presence of the NiV_2O_6 phase was previously reported in a petroleum ash sample.[140] The Ni-V-O phase was also identifiable in the as-received gasifier ash in Figure 3-4. Hence, the crystallographic phases in the gasifier ash were identified as $Ca_{0.17}V_2O_5$, V_2O_5 and $Ni_3V_2O_8$. Note that the $Ca_{0.17}V_2O_5$ phase or in general, $M_xV_2O_5$ phases contain mixed vanadium oxides, where M is the concomitant cation and x is a stoichiometric coefficient. It was also possible that the gasifier ash contained various $M_xV_2O_5$ crystals, but what is most important to understand from the XRD analysis is that the gasifier ash contained low oxidation state vanadium oxides and the unextractable Ni-V-O compound under the experimental conditions.

3.3.1.5 Distribution of the mixed vanadium oxides

X-ray photoelectron spectroscopy was another technique, that was used to further investigate the oxidation state of the vanadium-bearing materials in the gasifier ash. Each element in the ash has a unique binding energy that corresponds to the atomic orbital from which the photoelectron is emitted. As a result, a package of characteristic peaks for each element appears in the XP spectrum. The registered databases were utilised to relate the emitted photoelectrons of a sample to a reference compound. The XP spectra of various reference vanadium oxides for the determination of vanadium oxidation state were studied broadly in the literature. Table 3-4 shows the summary of

the binding energy (BE) reference data reported in the literature.[141-144] Commonly, the ΔBE data is very consistent for V^{V} in various references, but data for V^{IV} and V^{III} are scattered widely. Despite this, the V^{IV} component in the $V2p_{3/2}$ peak always has a higher BE and a narrower width than that for V^{III}.

Figure 3-9 shows the original XPS scan and the fitted model for the $V2P_{3/2}$ region for the as-received gasifier ash. It consists of two peaks centred at around 517.48 and 516.28 eV. From data in Table 3-4, it is clear that these two peaks correspond to V^{V} and V^{IV}, respectively. The fact that the peaks corresponding to the V^{V} and V^{IV} were well separated can be utilised to estimate the average oxidation state or to determine the relative amount of atoms in each oxidation state. Equation 3-4 was utilised to calculate the area ratio of the $V2p_{3/2}$ V^{V} curve to $V2p_{3/2}$ IV^{V}. The area ratio was found to be 5.788, implying that the ratio of the $V2p_{3/2}$ V^{V} to the fitted scan was 0.853 and the area ratio of the $V2p_{3/2}$ IV^{V} to the fitted scan was 0.147. In other words, the as-received gasifier ash contained 85.3 % V^{V} and 14.7 V^{IV}. Herein, it was revealed by the XRD analysis that the gasifier ash contained low oxidation state vanadium oxides in the form of $M_xV_2O_5$ and XPS analysis was used to quantify the amounts of the low oxidation state vanadium oxide phase.

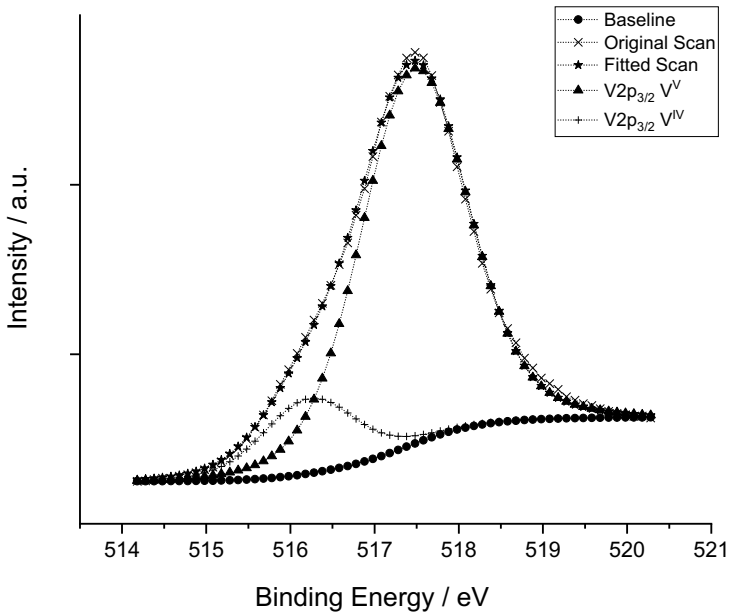


Figure 3-9. XP spectra for $V2P_{3/2}$ region. The peak positions extracted from the fitted scan suggest the presence of V^{V} and V^{IV} in the as-received SARU.

Oxide	Ox.St.	BE of Ref. Peak, eV	BE (O1S), / eV	BE (V2P3/2), / eV	FWHM (V2P3/2), / eV	ΔBE (O1s-V2p3/2), / eV	Reference
V_2O_5	5	FE of Sample holder	529.8	516.9	1.6	12.9	[144]
VO_2	4		529.9	516.2	3.2	13.7	
VO_2	4		529.7	515.9	4.1	13.8	
V_2O_3	3		530.1	515.7	4.2	14.4	
V_2O_3	3		530.3	515.9	3.8	14.4	
V_2O_5	5	Au4f/C1s 84.0/285	530	517.2	1.2	12.8	[141]
VO_2	4		530	516	2.0	14	
V_2O_3	3		530	515.85	4.0	14.15	
V_2O_5	5	O1s 329.8/530.0	529.8	517.0	1.3-1.4	12.8	[143]
V_6O_{13}	5,4		530	516.5	3.4	13.5	
VO_2	4		530	515.65	4.0	14.35	
V_2O_3	3		530	515.15	4.8	14.85	
V_2O_5	5	FE of Au	530	517.1	1.1	12.9	[142]
VO_2	4		530.1	516.2	2.5	13.9	
V_2O_3	3		530.2	515.6	3.5	14.6	

3.3.1 Concomitant cations effect vs. pH– Control experiments

Over 20 elements were identified in the gasifier ash (see Table 3-1). It was nearly impossible to identify all the phases, due to the overlapping peaks in the XRD diffractogram, so it was challenging to predict the reaction mechanism by which vanadium(V) was extracted. Moreover, the interaction between the TMA^+OH^- solvent and the abundant cationic species must be established in order to expand the application to other vanadium-bearing feedstocks. To address the aforementioned

Table 3-4 Summary of the XPS reference data for vanadium with various oxidation states

challenges, the following control experiments were conducted using lab-grade reagents for each pair of V and Al, Ca, Fe, Mn, Na, Ni or Si, where ammonium metavanadate particles were suspended in aqueous solutions of the nitrate metal salts. For the case of Si, lab-grade silica (SiO_2) was used to identify its solubility at the set conditions. The solution pH was modified to 2, 6 and 13 with TMA^+OH^- solutions and dilute nitric acid and the solids were separated and treated with methanol to remove the soluble phase. The treated precipitates were heat-treated at 700 °C for two hours to enhance the crystallinity of the precipitated phases before X-ray diffraction measurements.

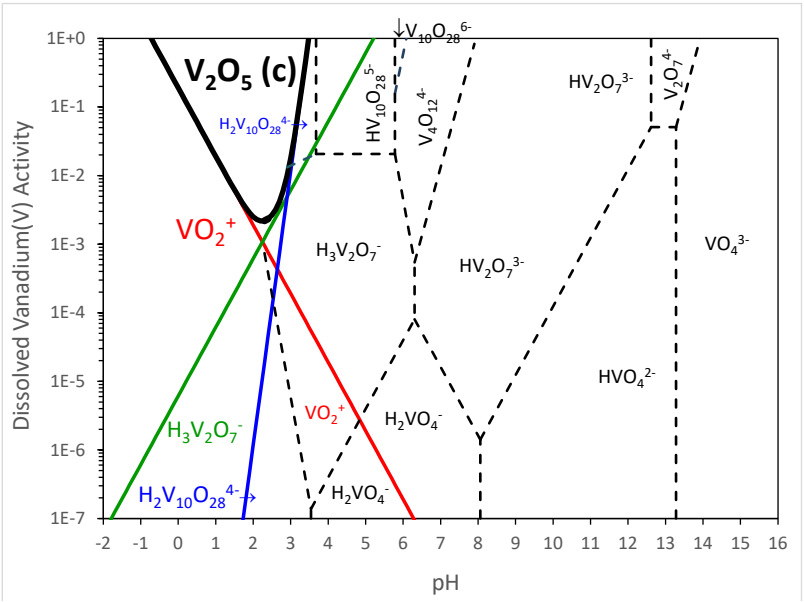
Figure 3-11 to Figure 3-50 show the uncalcined and the calcined XRD diagrams of the precipitates at different pH and the presence of different concomitant cations. Table 3-5 shows the crystallographic phases identified in the calcined precipitates. Note that the identified phases hardly match the detected peaks in the uncalcined precipitates when pH = 2. This is due to the co-precipitation of the tetramethylammonium cations along with the vanadium species which will be explained in Chapter 4.

The results gave significant insights for the interaction of multiple species in aqueous solutions. Although Fe^{III}, Mn^{II} and Na^{I} are known to be soluble at pH 2, these cations co-precipitated with vanadium(V). Similarly, vanadium(V) coprecipitated with Al^{III}, Fe^{III}, Mn^{III} and Ni^{II} at pH 6. Further increase in pH with addition of TMA^+OH^- solutions, demonstrated that Na^+ was the only cation that did not precipitate at pH 13, indicating that sodium could be a problematic impurity in the vanadium(V) purification process. Rather interestingly, $Al(OH)_3$ was precipitated, and SiO_2 remained insoluble at pH 13, whereas if NaOH (aq) was used, they would have been completely solubilised. This can be explained by the chemistry of Si^{IV} and A^{III}, in that the two elements react with sodium ions in aqueous solutions, making ionic solutions. In the case of ammonium ions however, Si^{IV} and A^{III} do not react to make weak ionic and hydrogen bonds like ammonium ions do with V^V in NH_4VO_3.[145-147] It can be thought that TMA^+ ions behave in the same way as NH_4^+ ions in terms of chemical interactions. Nevertheless, the solubility of V^V ions was found to be considerably higher in concentrated TMA^+OH^- than in concentrated $NH_4^+OH^-$ solutions, According to Smrčok et al.,[146] 'the ammonium

ions link to the $[VO_4]\infty$ chains through one linear, one bifurcated and two trifurcated N-H...O hydrogen bonds'. Hypothetically and relatively speaking, TMA^+ ions are very large that inhibit the formation of the links which make polyvanadate ions thereby inhibiting precipitation of vanadium(V) as metavanadate.

Ca^{II} and vanadium(V) had rather complicated behaviour at pH 13 where $Ca_7V_4O_{17}$ and CaO were both present in the precipitate. The results suggest that the feedstock must

(a)



(b)

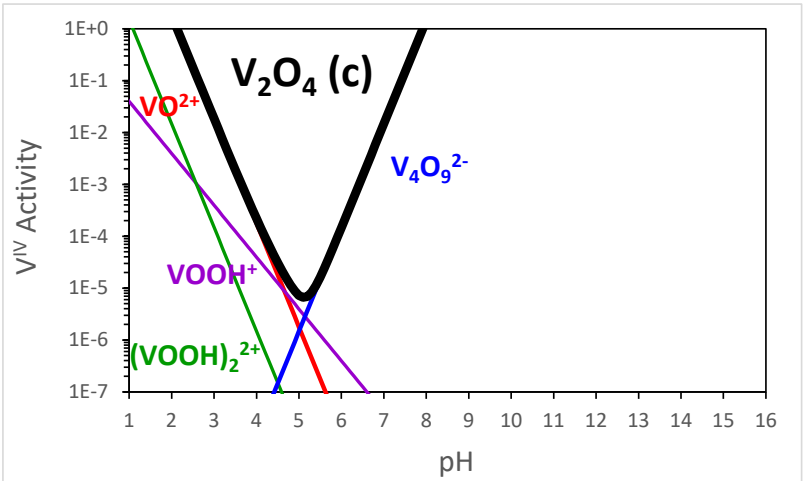


Figure 3-10. (a), top, (reprinted Figure 2-3) V^V activity-pH diagram for species in equilibrium with V_2O_5 (b),bottom, V^{IV} activity-pH diagram for species in equilibrium with V_2O_4 ; at 298 K, 0.1 MPa. These calculations omitted consideration of the presence of TMA^+ ions.

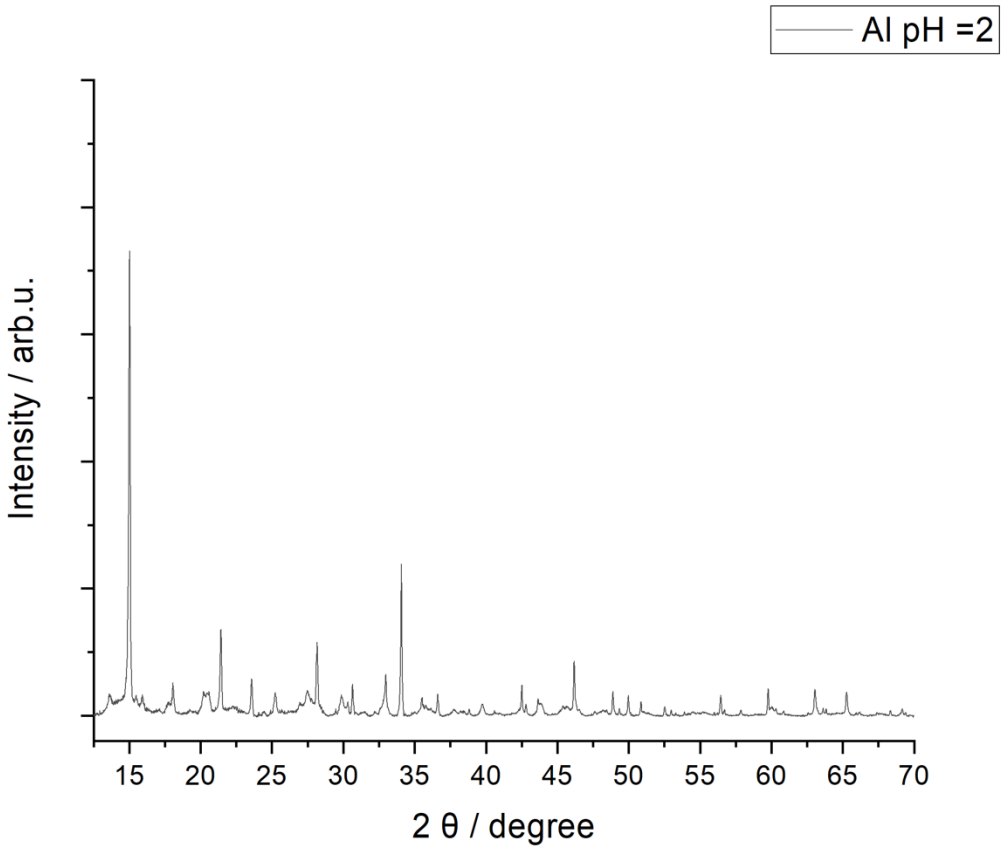
go through a calcium removal process if contained high calcium concentrations, before undergoing vanadium(V) extraction with concentrated TMA^+OH^-. Note that in phases such as NaV_6O_{12} which contained mixed vanadium oxides, the vanadium(V) from the precipitated $HNaV_6O_{16}$ went through self-reduction at 700 °C.

The above results provide insights towards understanding the correlations between the vanadium(V) species and Al, Ca, Fe, Mn, Na, Ni or Si ions in hydrometallurgical systems that use TMA^+OH^- as the extracting solutions and feedstocks such as gasifier ash. To be specific for this study, the control experiments revealed that Ni-V-O phase was stable at pH 13 when TMA^+OH^- solutions were used as the leaching solvent.

Table 3-5. Crystal structure of the phases identified in the precipitates vs. pH 2, 6 and

Coexisting Cation	**Product Phase**		
	pH 2	pH 6	pH 13
(I) Al	V_2O_5	$AlVO_4$	Al_2O_3 (amorphous)
(II) Ca	V_2O_5	V_2O_5	CaO, $Ca_7V_4O_{17}$
(III) Fe	$FeVO_4$	$FeVO_4$	Fe_2O_3
(IV) Mn	MnV_2O_6	MnV_2O_6	Mn_2O_3
(V) Na	NaV_6O_{12}	V_2O_5	No Precipitation
(VI) Ni	V_2O_5	NiV_2O_6	NiO, $Ni_3V_2O_8$
(VII) Si	V_2O_5, SiO_2	SiO_2	SiO_2

13 with a combination of vanadate ions and various concomitant cations after calcination in the muffle oven.



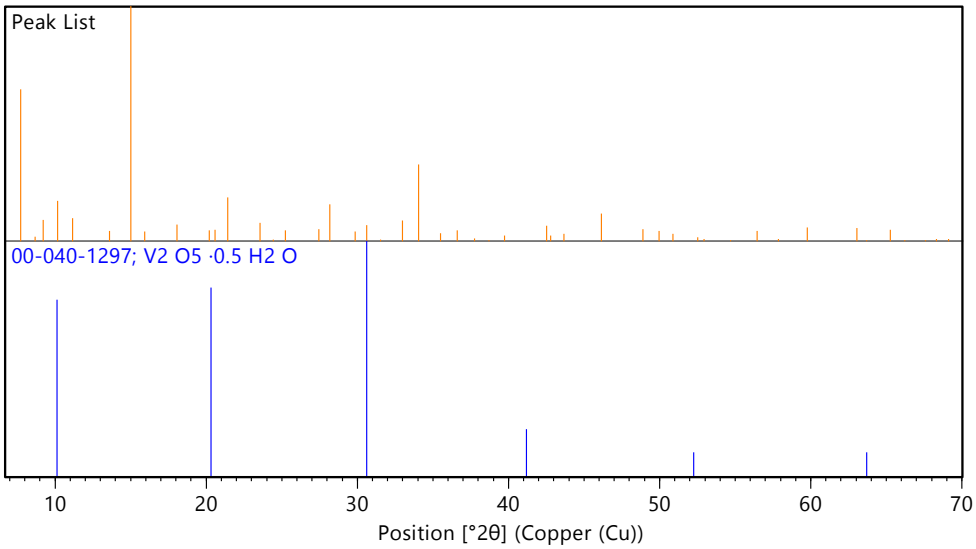


Figure 3-11. XRD diagram of the precipitate in the presence of TMA^+ cations vs. the shown pH and the concomitant cation.

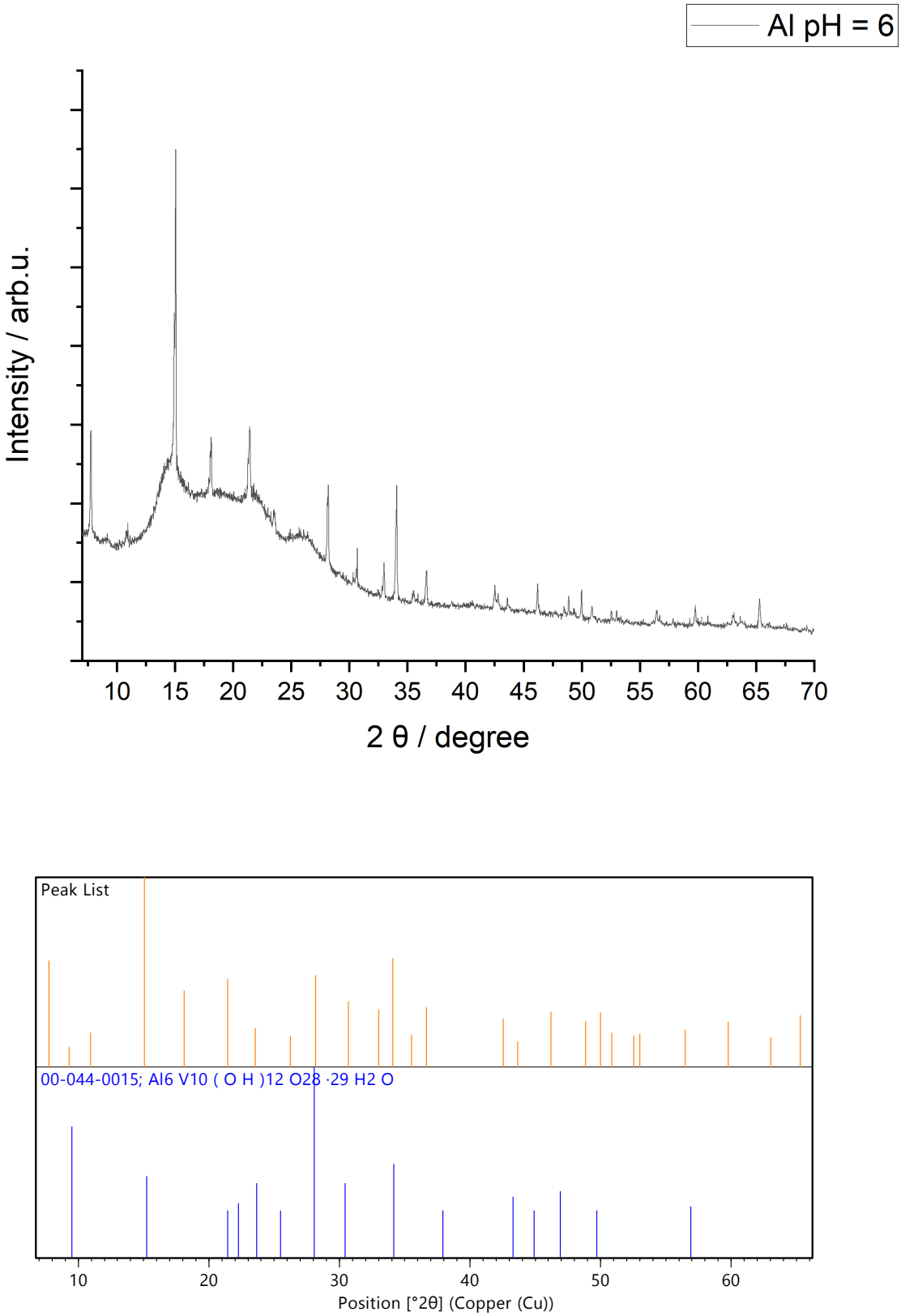


Figure 3-12. XRD diagram of the precipitate in the presence of TMA^+ cations vs. the shown pH and the concomitant cation.

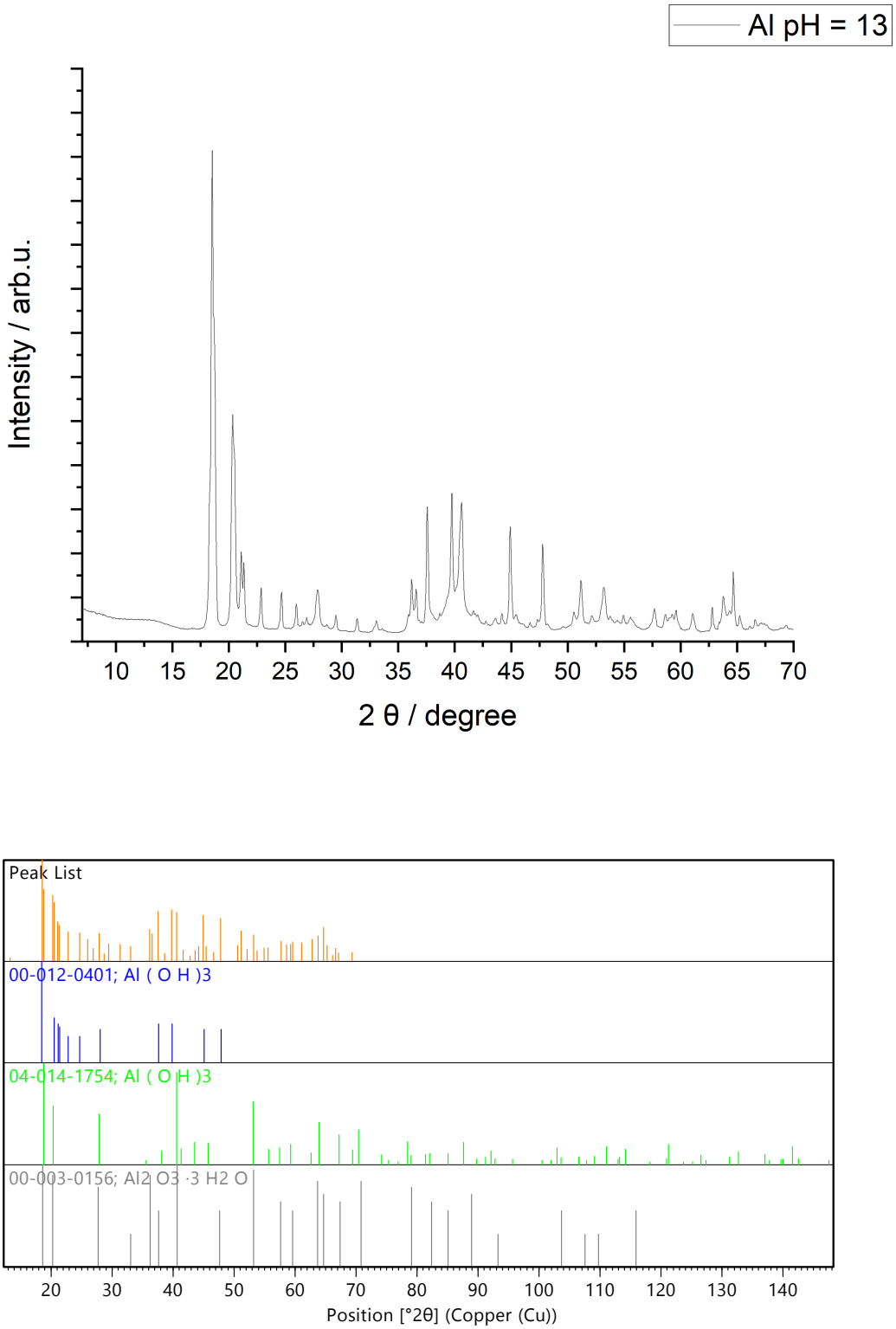


Figure 3-13. XRD diagram of the precipitate in the presence of TMA^+ cations vs. the shown pH and the concomitant cation.

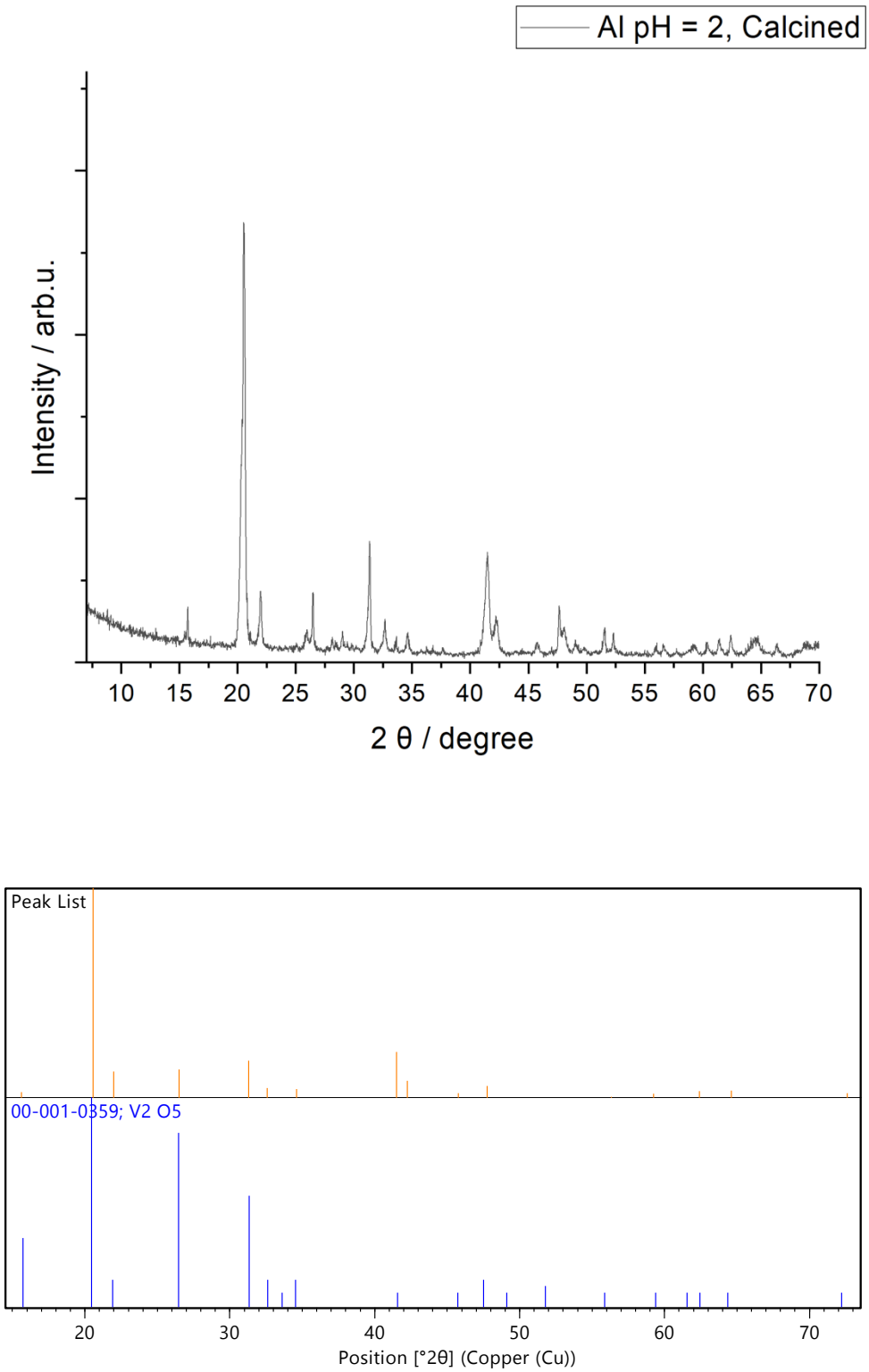


Figure 3-14. XRD diagram of the precipitate in the presence of TMA^+ cations vs. the shown pH and the concomitant cation.

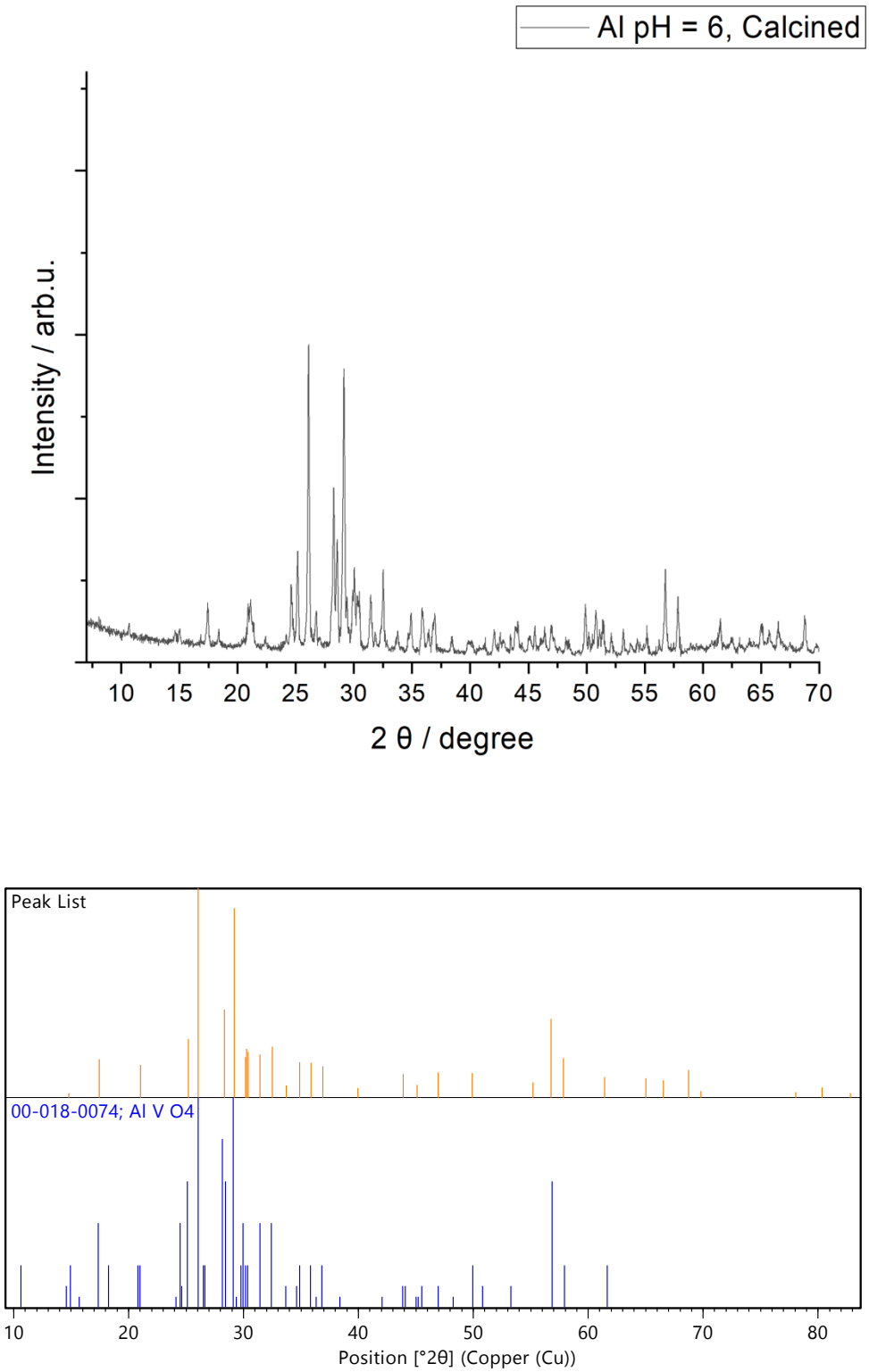


Figure 3-15. XRD diagram of the precipitate in the presence of TMA^+ cations vs. the shown pH and the concomitant cation.

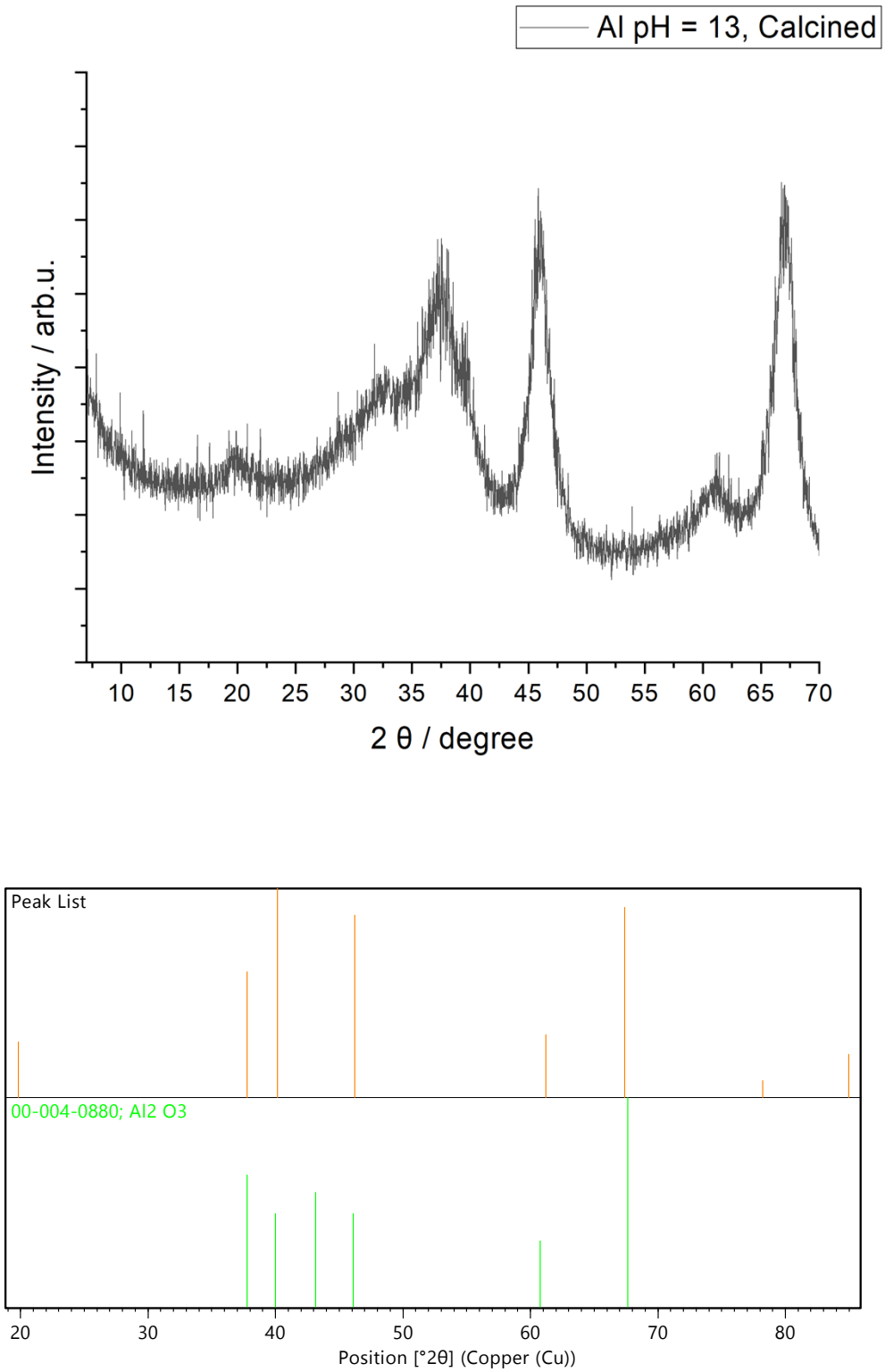


Figure 3-16. XRD diagram of the precipitate in the presence of TMA^+ cations vs. the shown pH and the concomitant cation.

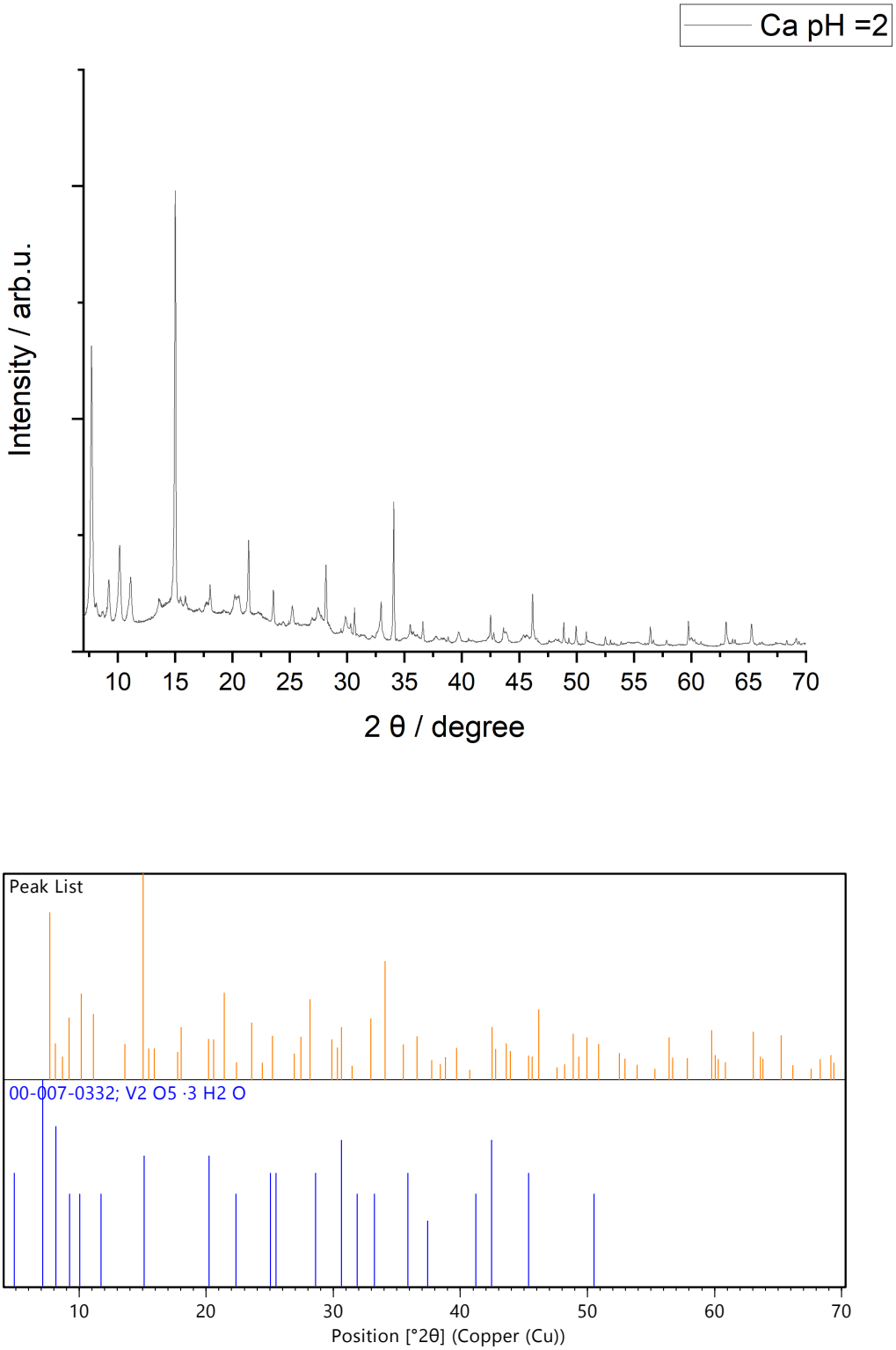


Figure 3-17. XRD diagram of the precipitate in the presence of TMA^+ cations vs. the shown pH and the concomitant cation.

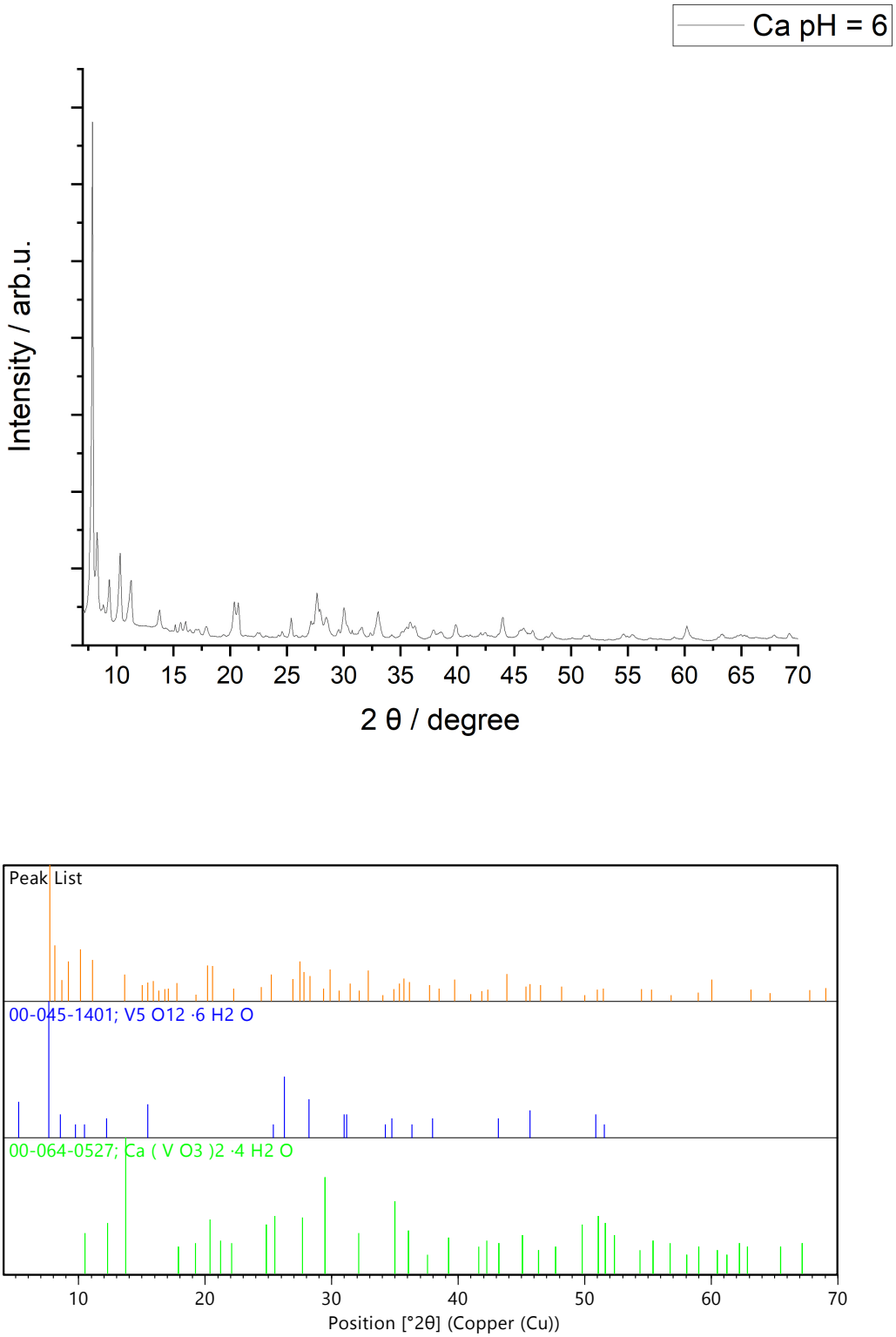


Figure 3-18. XRD diagram of the precipitate in the presence of TMA^+ cations vs. the shown pH and the concomitant cation.

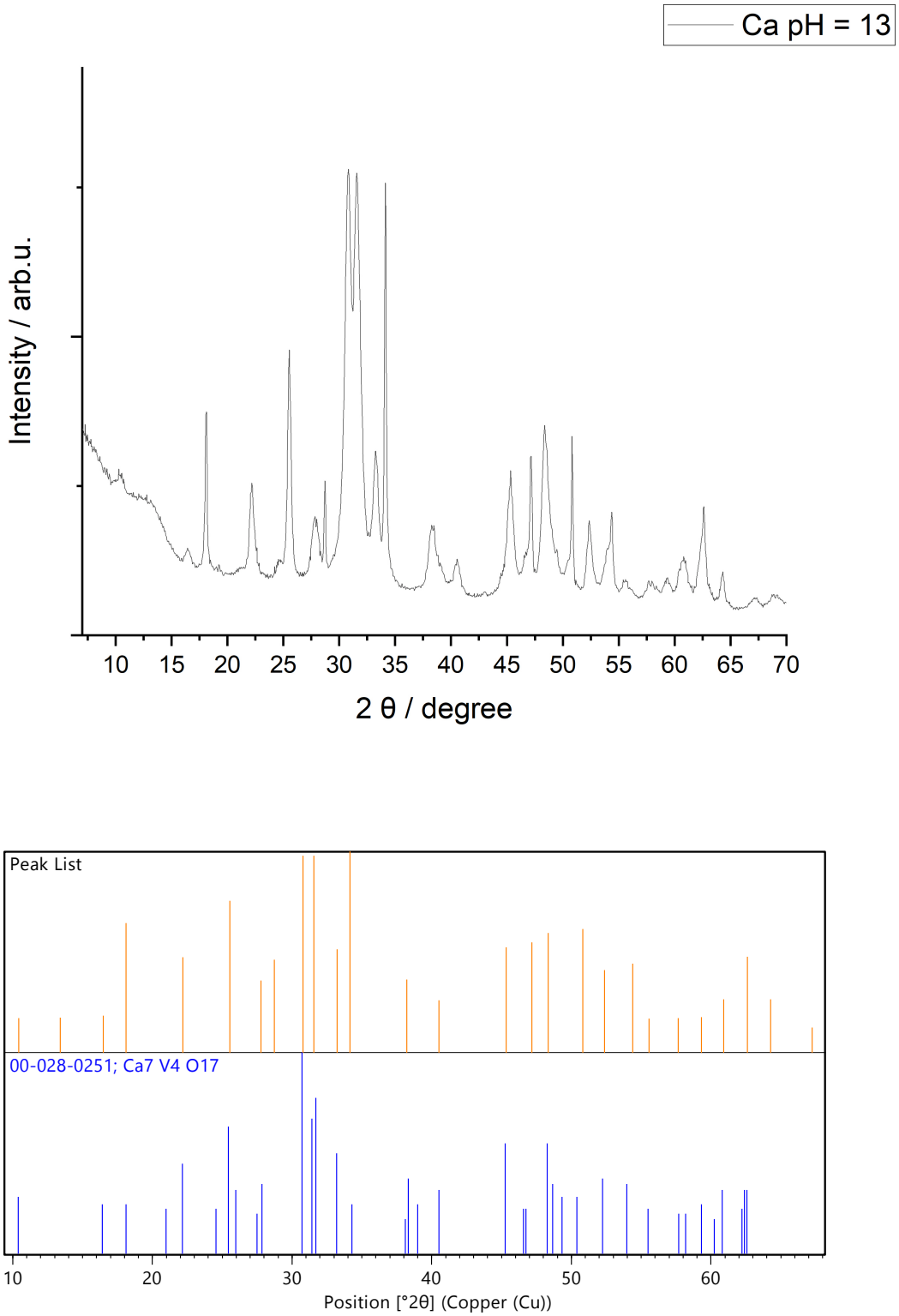


Figure 3-19. XRD diagram of the precipitate in the presence of TMA^+ cations vs. the shown pH and the concomitant cation.

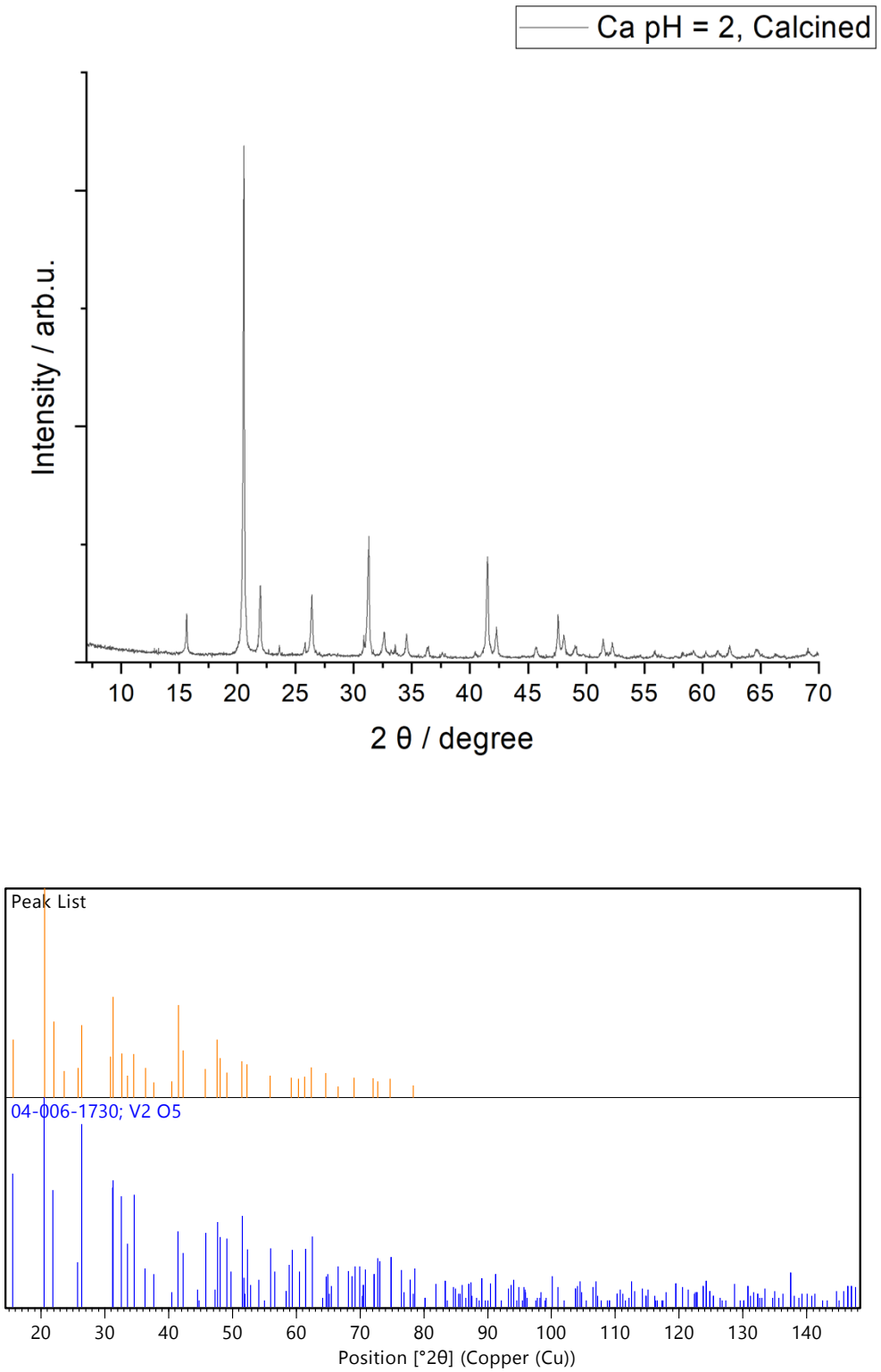


Figure 3-20. XRD diagram of the precipitate in the presence of TMA^+ cations vs. the shown pH and the concomitant cation.

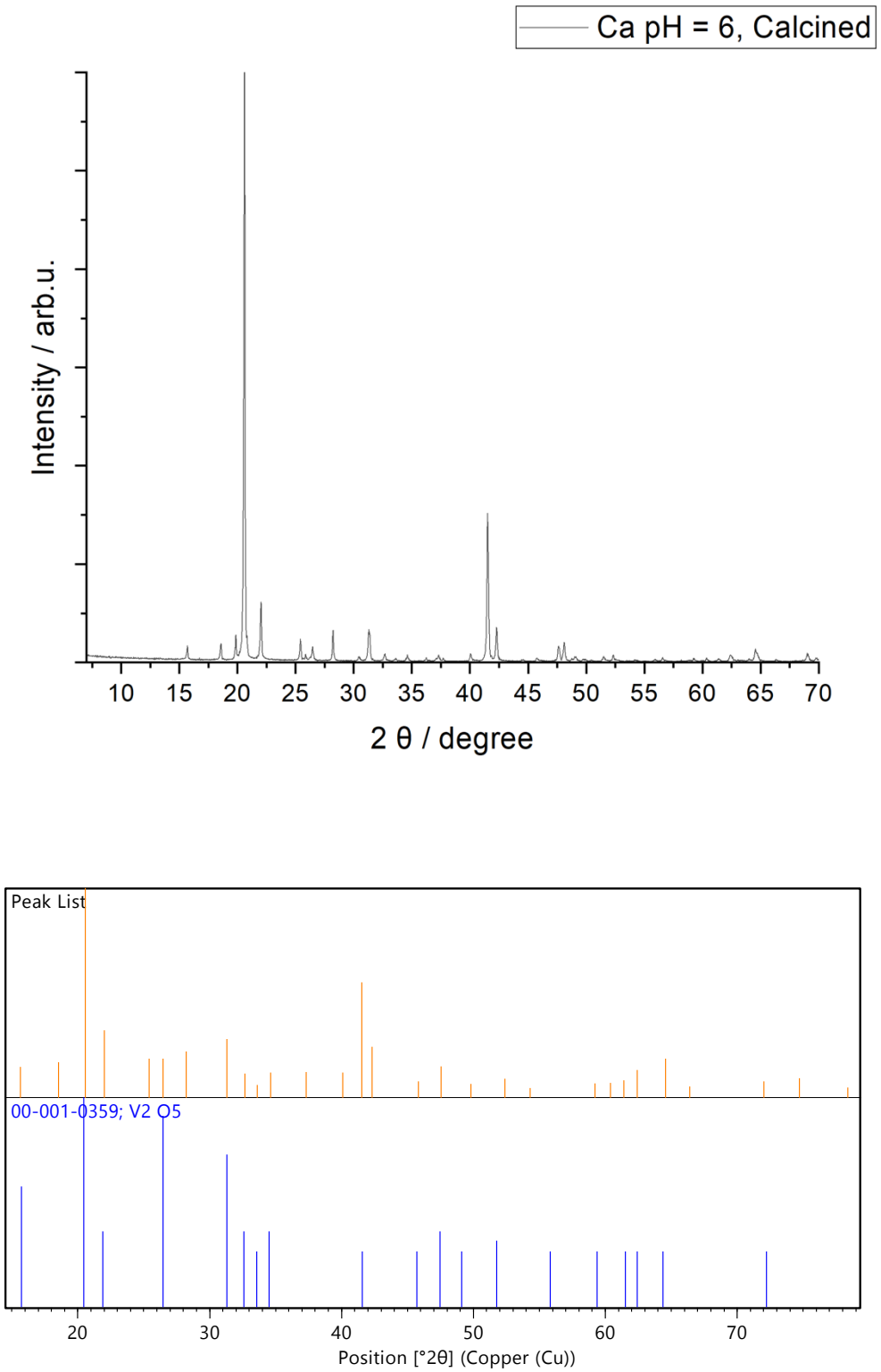


Figure 3-21. XRD diagram of the precipitate in the presence of TMA^+ cations vs. the shown pH and the concomitant cation.

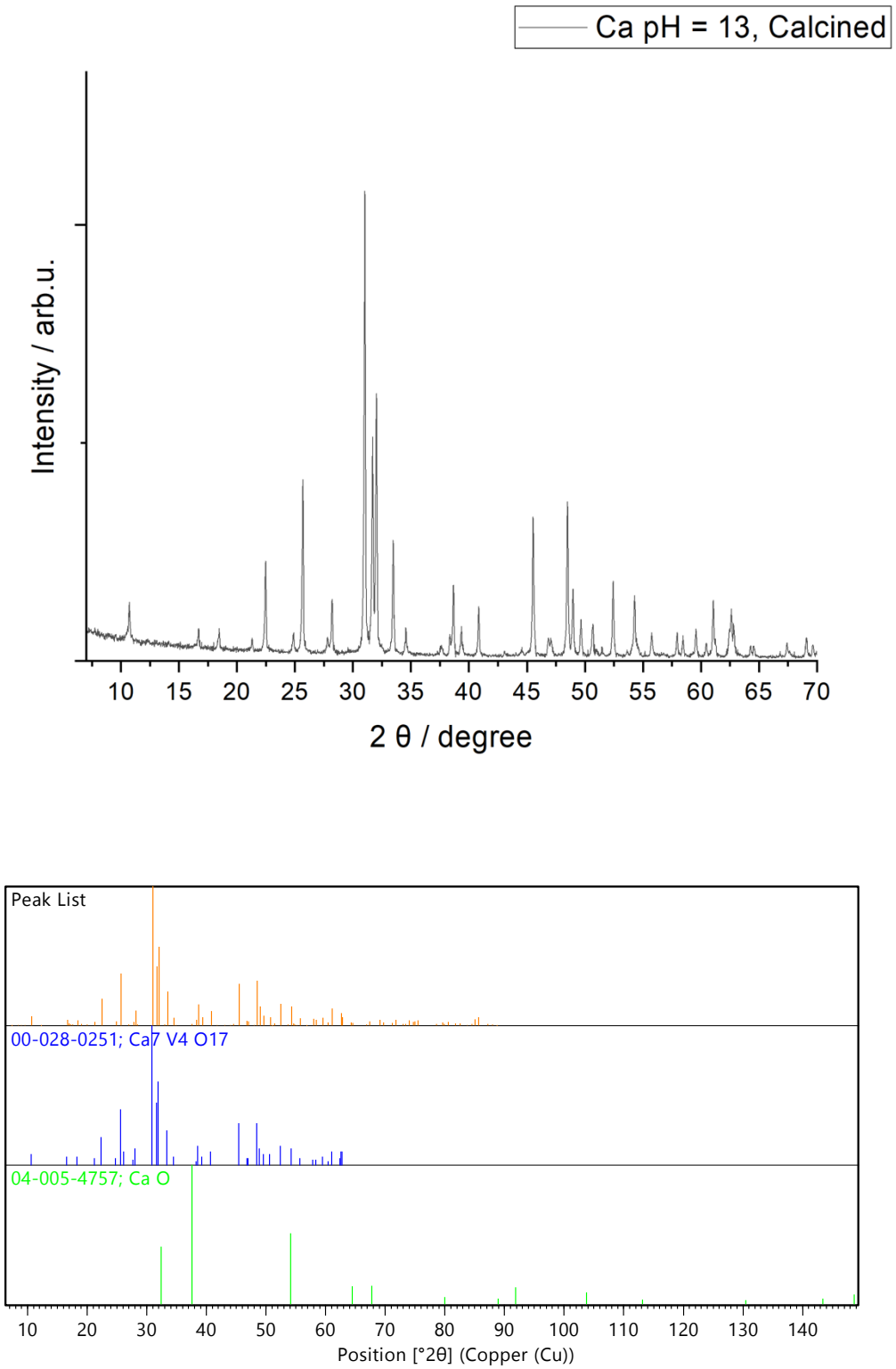


Figure 3-22. XRD diagram of the precipitate in the presence of TMA^+ cations vs. the shown pH and the concomitant cation.

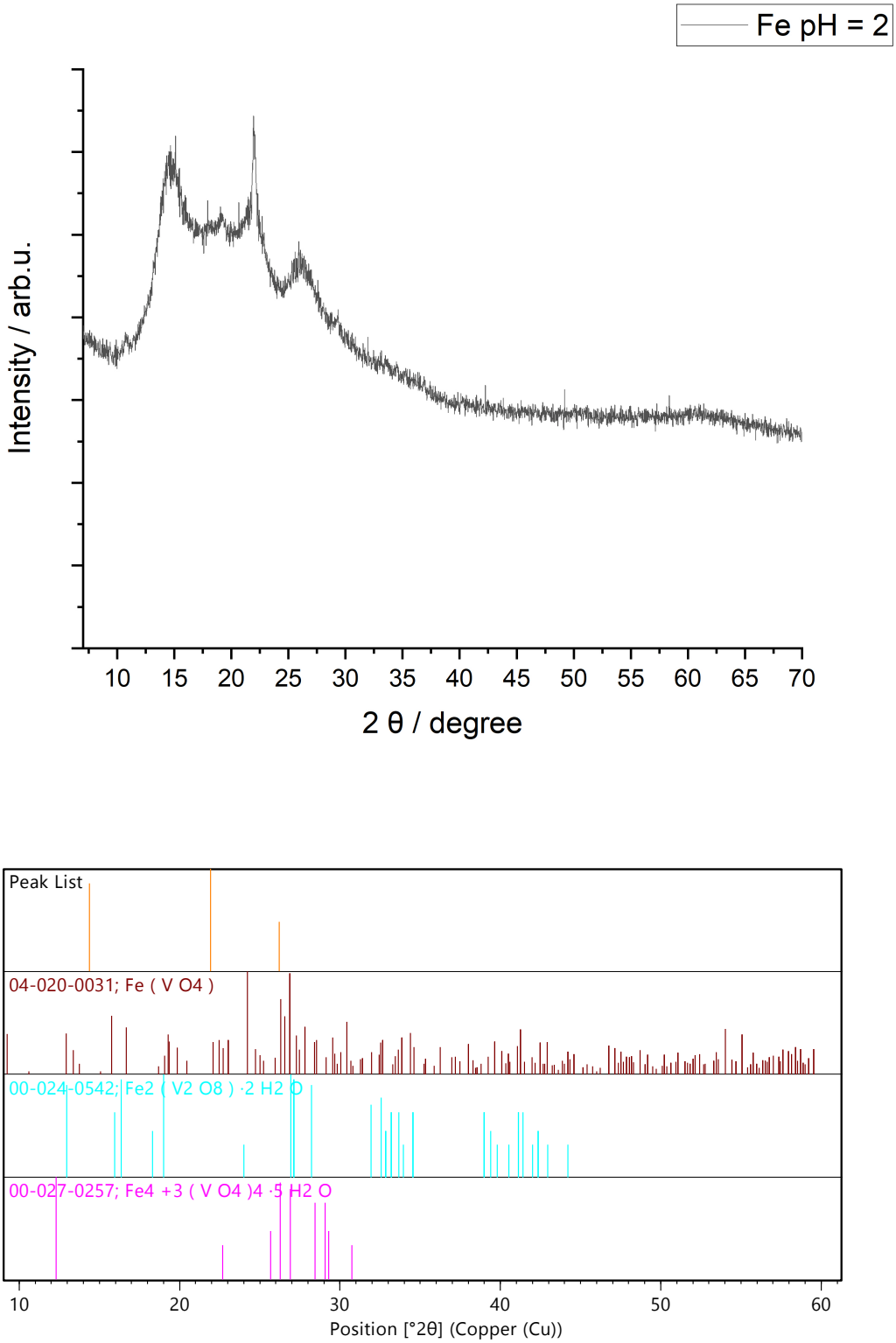


Figure 3-23. XRD diagram of the precipitate in the presence of TMA^+ cations vs. the shown pH and the concomitant cation.

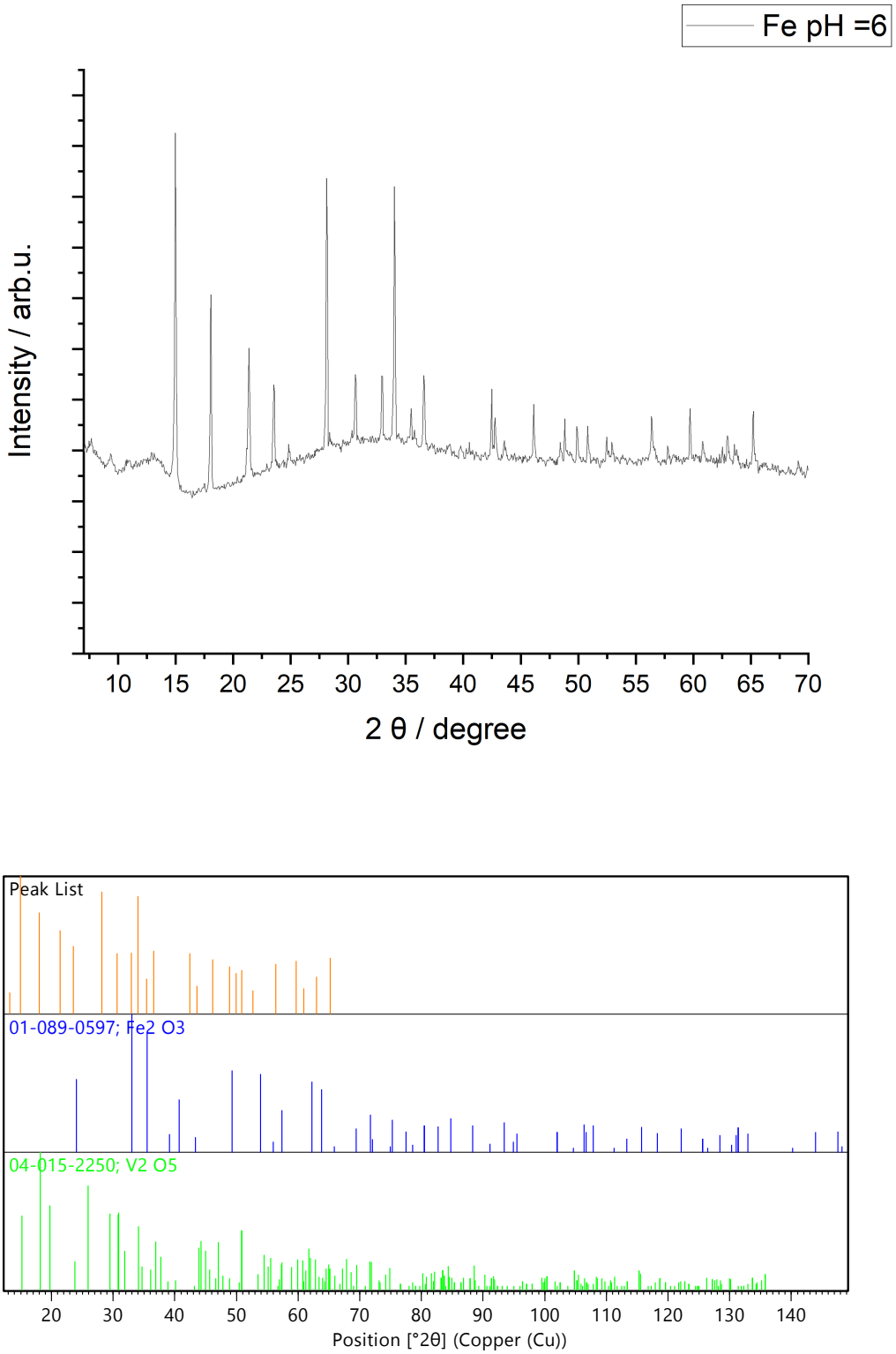


Figure 3-24. XRD diagram of the precipitate in the presence of TMA^+ cations vs. the shown pH and the concomitant cation.

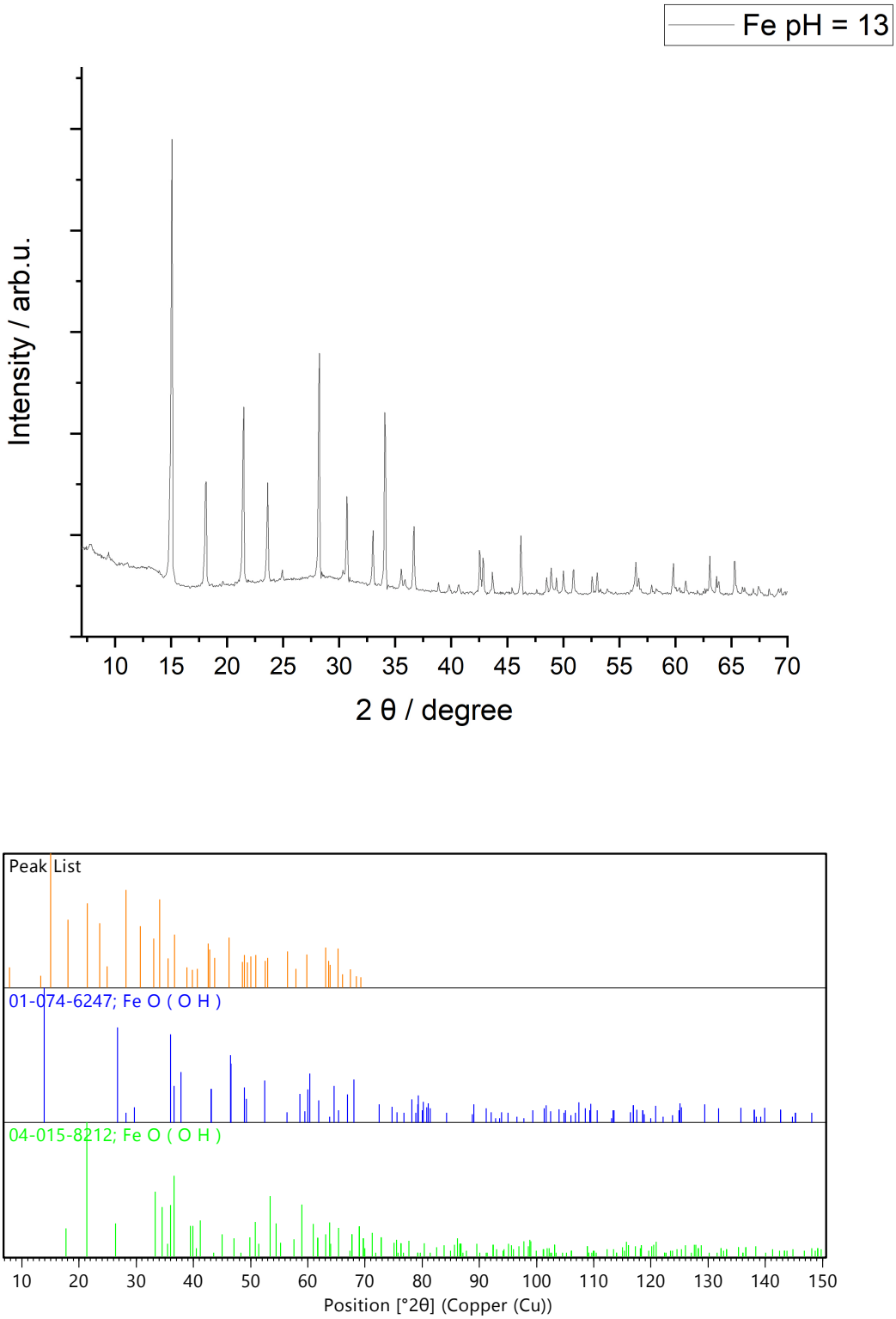


Figure 3-25. XRD diagram of the precipitate in the presence of TMA^+ cations vs. the shown pH and the concomitant cation.

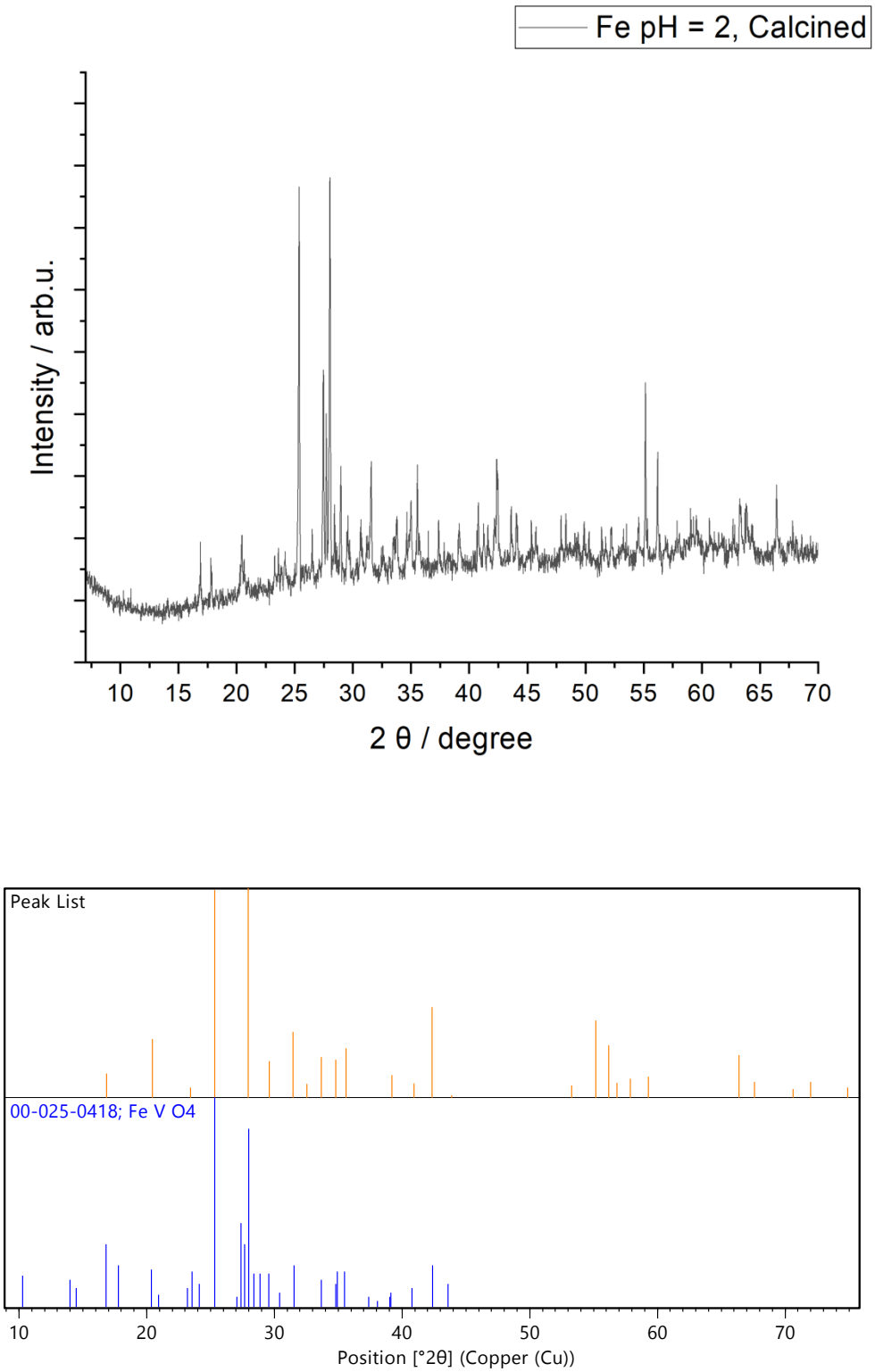


Figure 3-26. XRD diagram of the precipitate in the presence of TMA^+ cations vs. the shown pH and the concomitant cation.

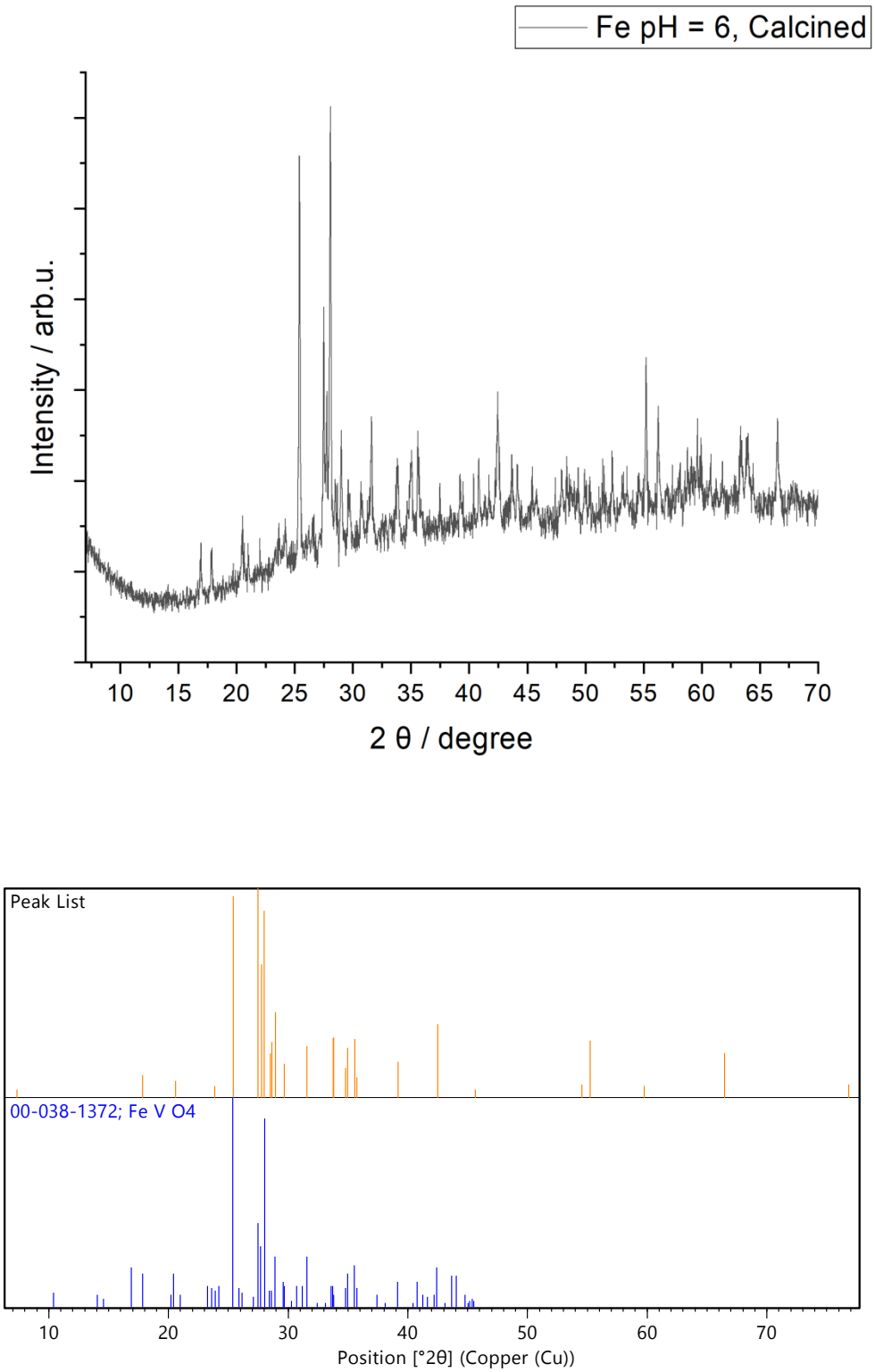


Figure 3-27. XRD diagram of the precipitate in the presence of TMA^+ cations vs. the shown pH and the concomitant cation.

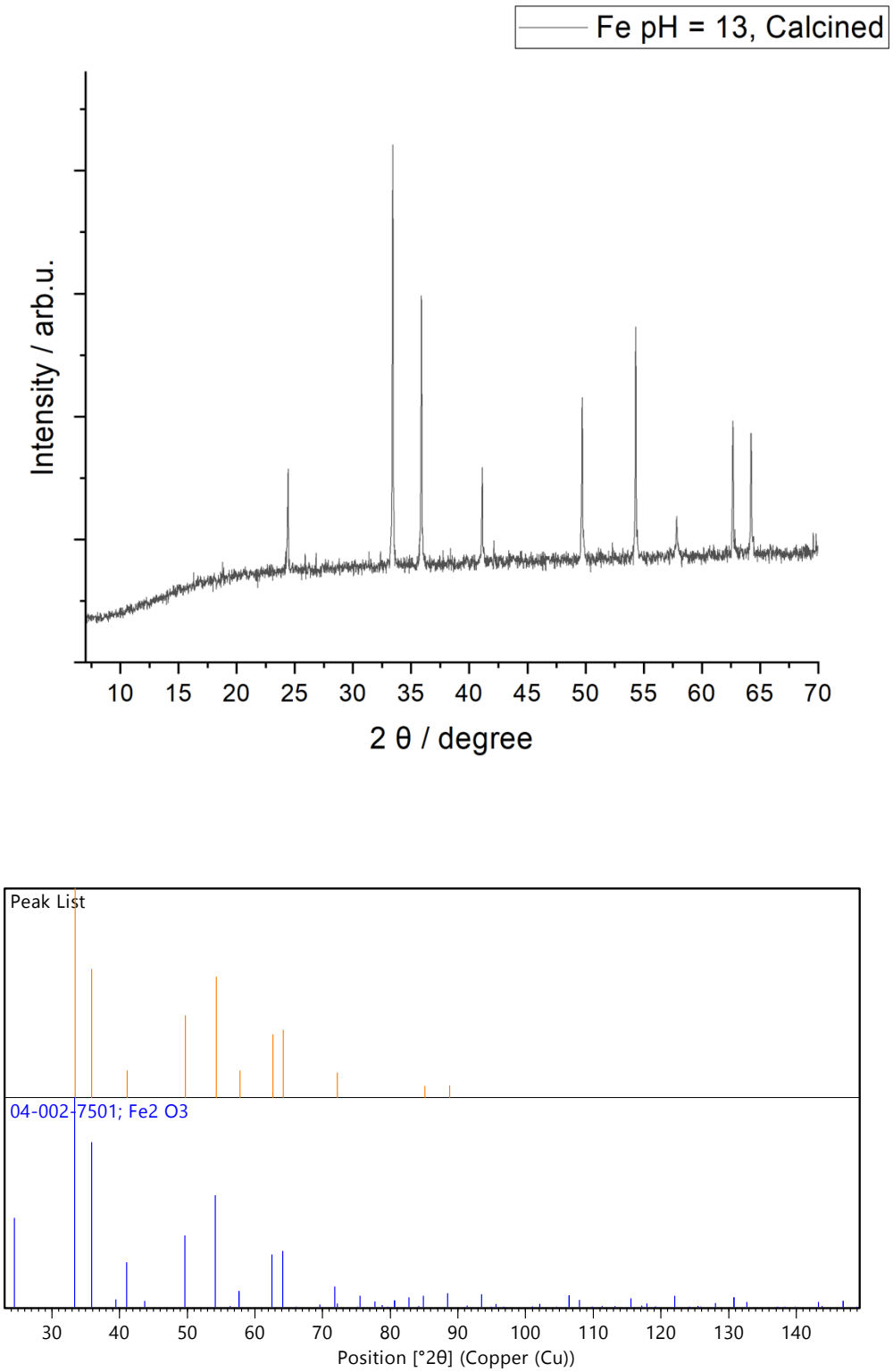


Figure 3-28. XRD diagram of the precipitate in the presence of TMA^+ cations vs. the shown pH and the concomitant cation.

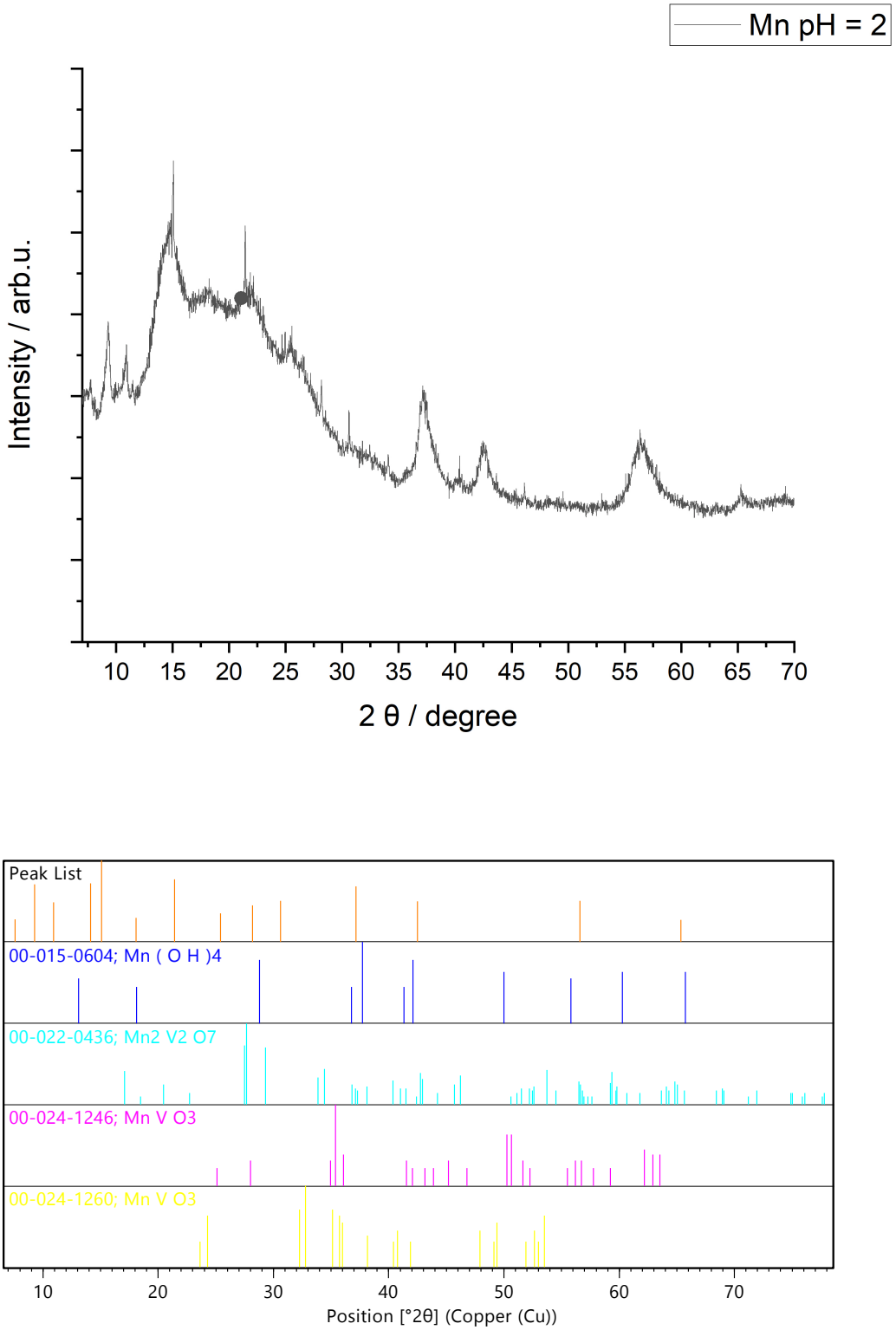


Figure 3-29. XRD diagram of the precipitate in the presence of TMA^+ cations vs. the shown pH and the concomitant cation.

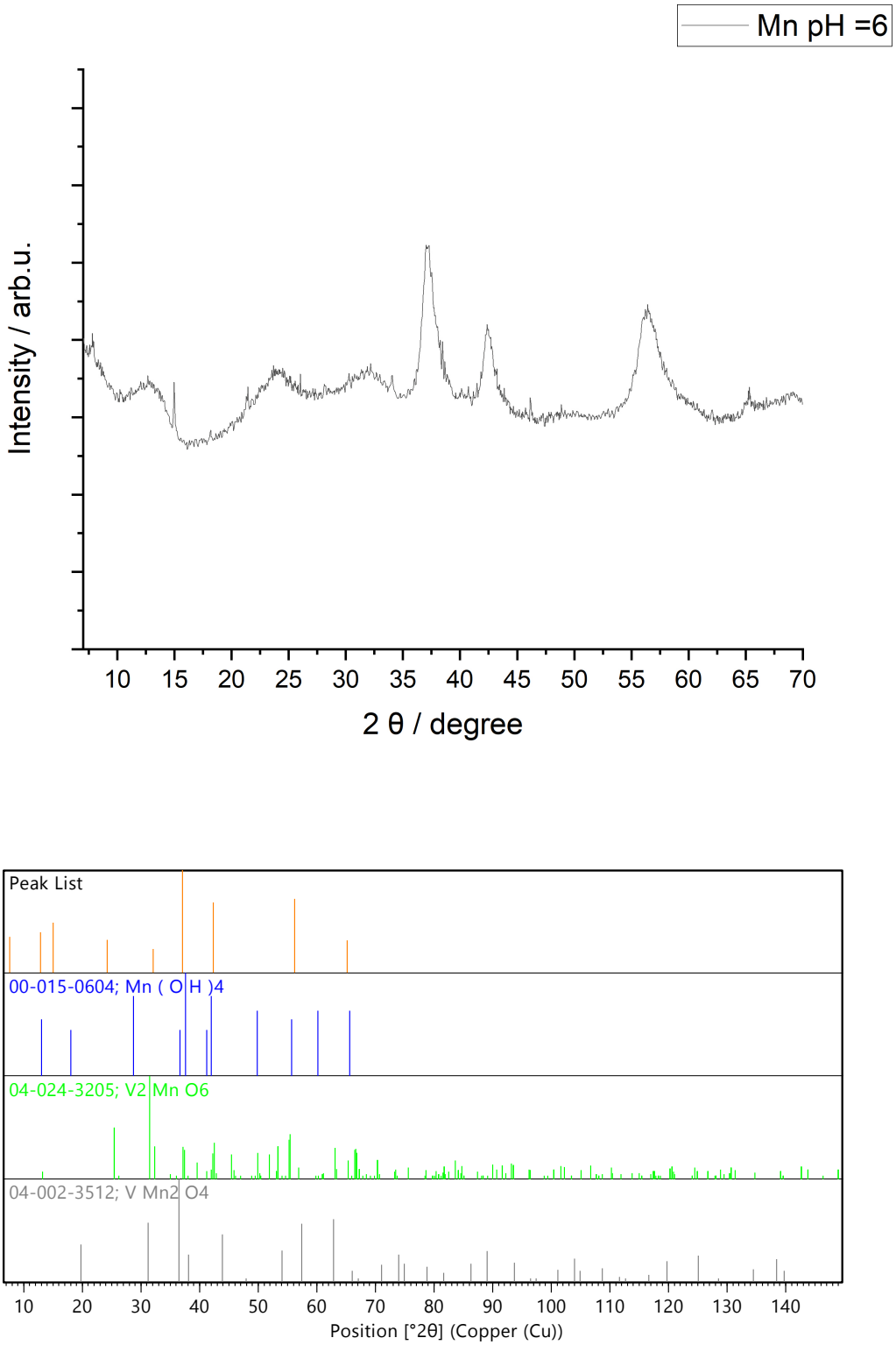


Figure 3-30. XRD diagram of the precipitate in the presence of TMA^+ cations vs. the shown pH and the concomitant cation.

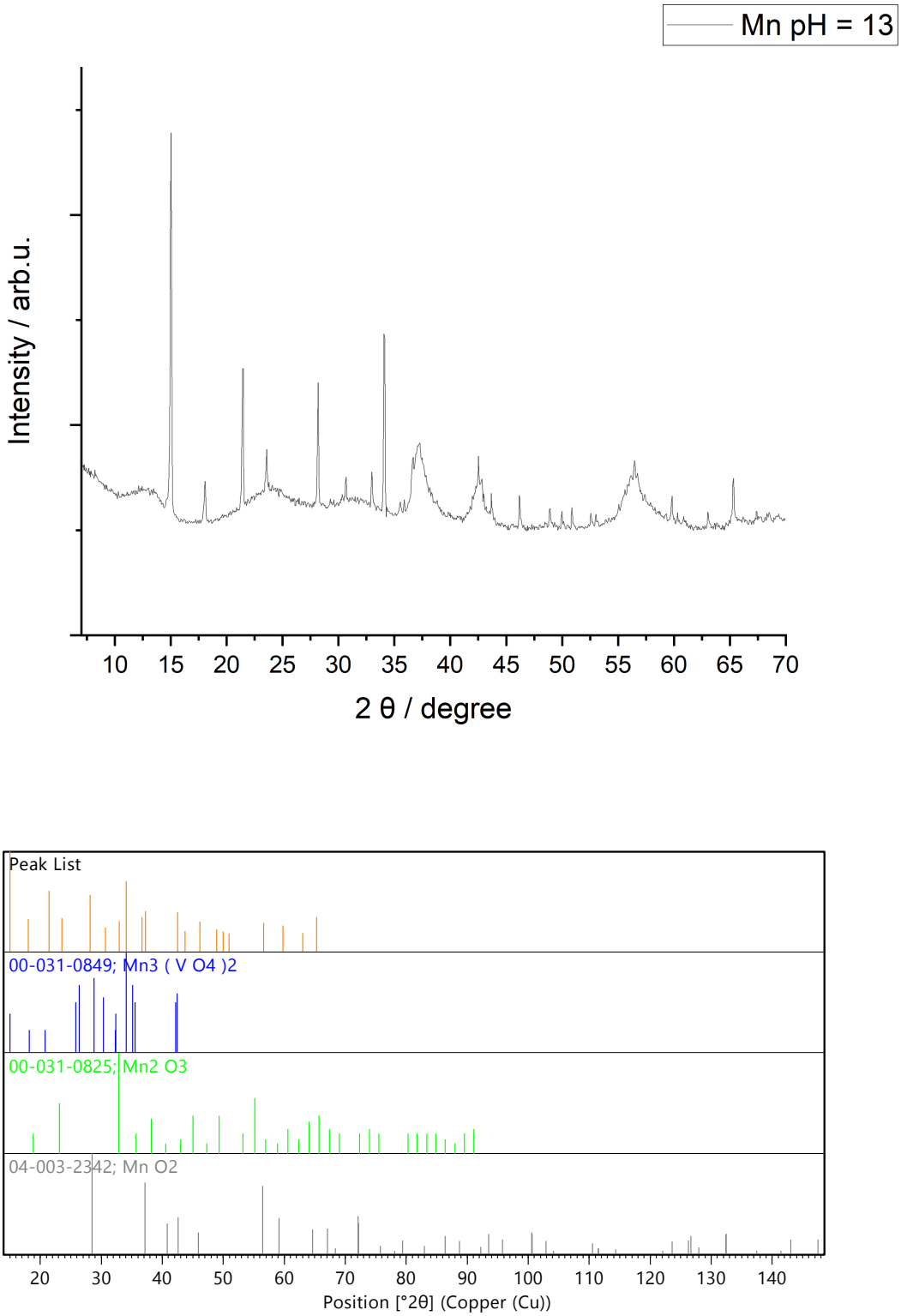


Figure 3-31. XRD diagram of the precipitate in the presence of TMA^+ cations vs. the shown pH and the concomitant cation.

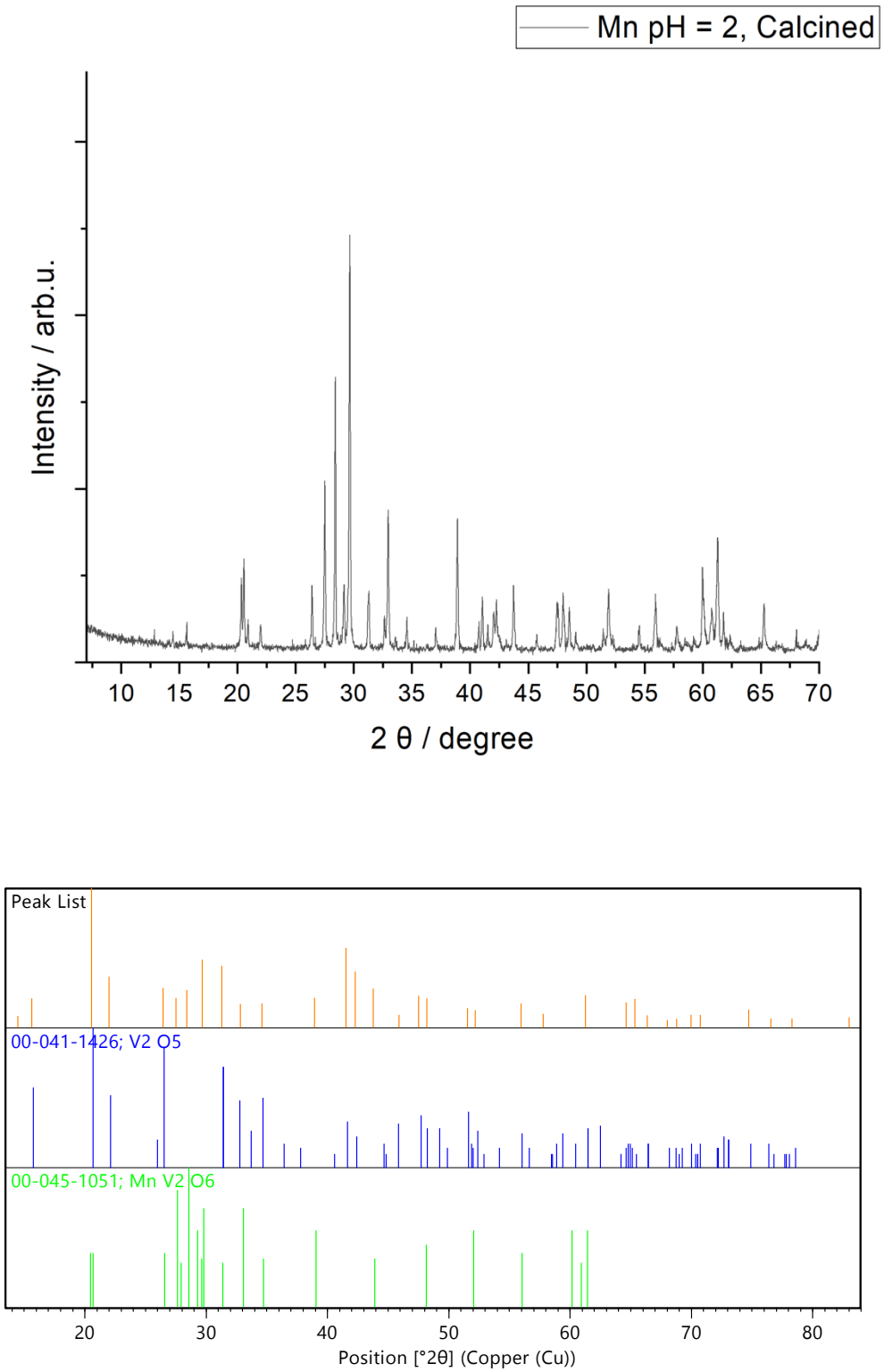


Figure 3-32. XRD diagram of the precipitate in the presence of TMA^+ cations vs. the shown pH and the concomitant cation.

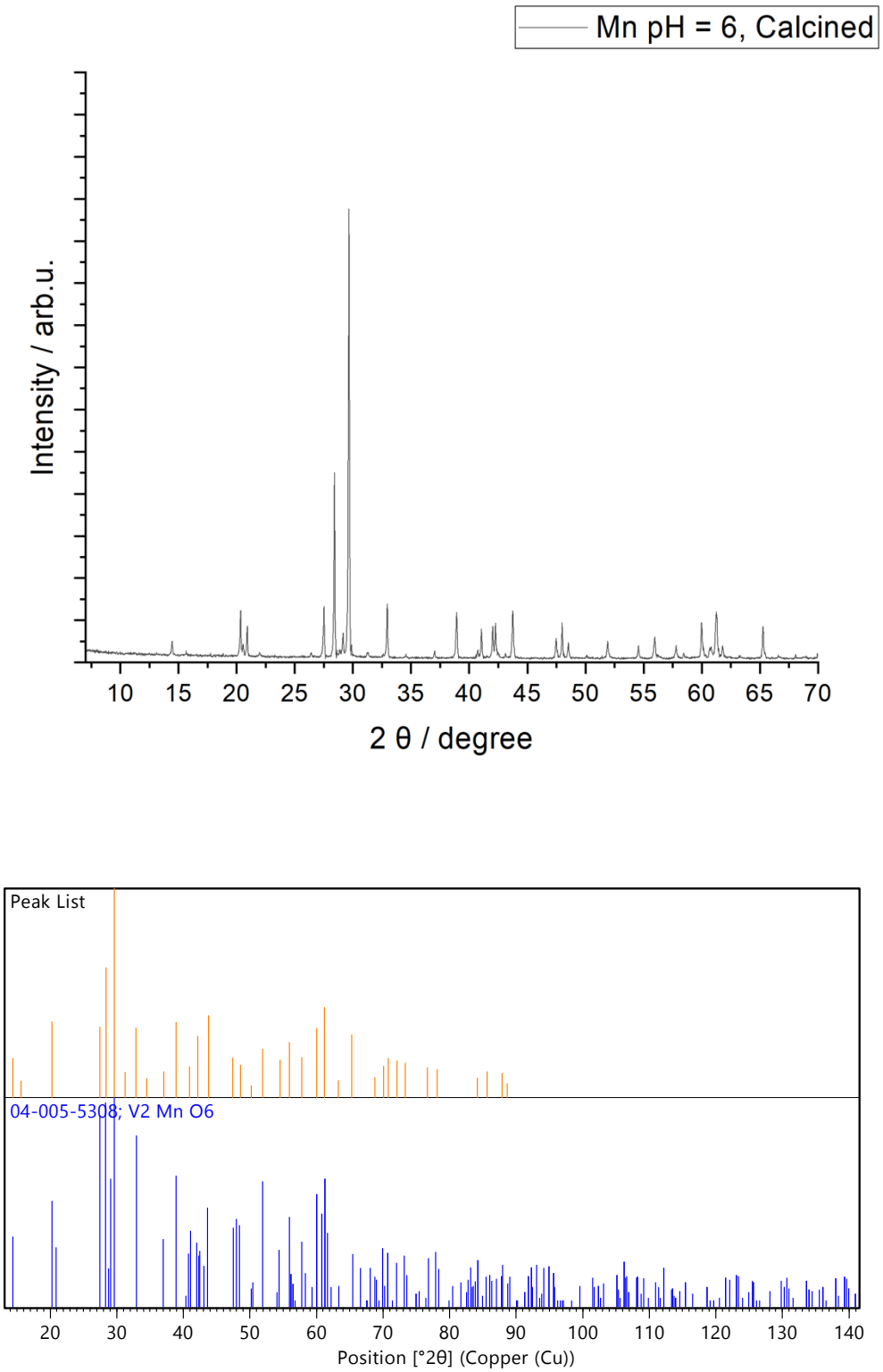


Figure 3-33. XRD diagram of the precipitate in the presence of TMA^+ cations vs. the shown pH and the concomitant cation.

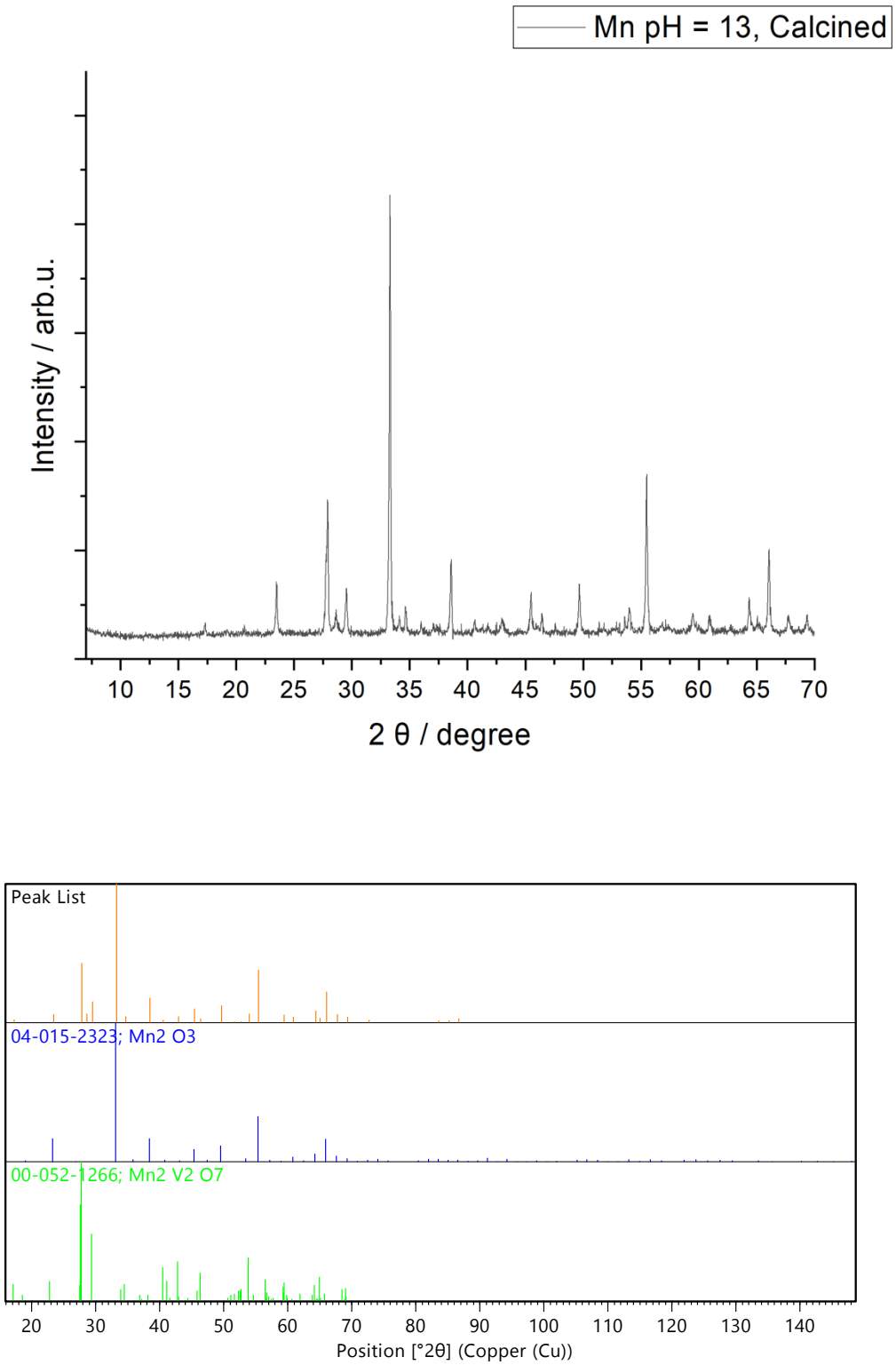


Figure 3-34. XRD diagram of the precipitate in the presence of TMA^+ cations vs. the shown pH and the concomitant cation.

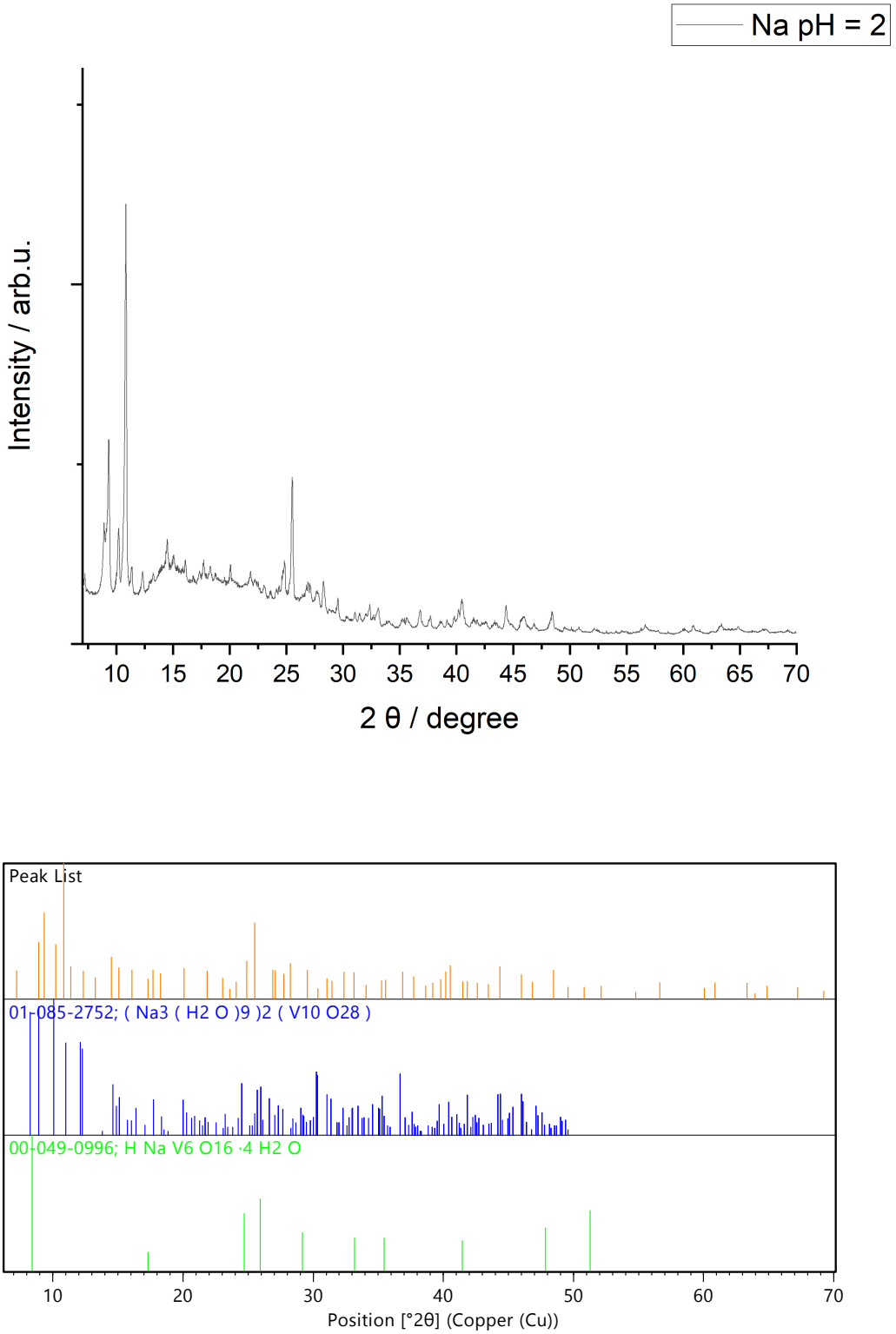


Figure 3-35. XRD diagram of the precipitate in the presence of TMA^+ cations vs. the shown pH and the concomitant cation.

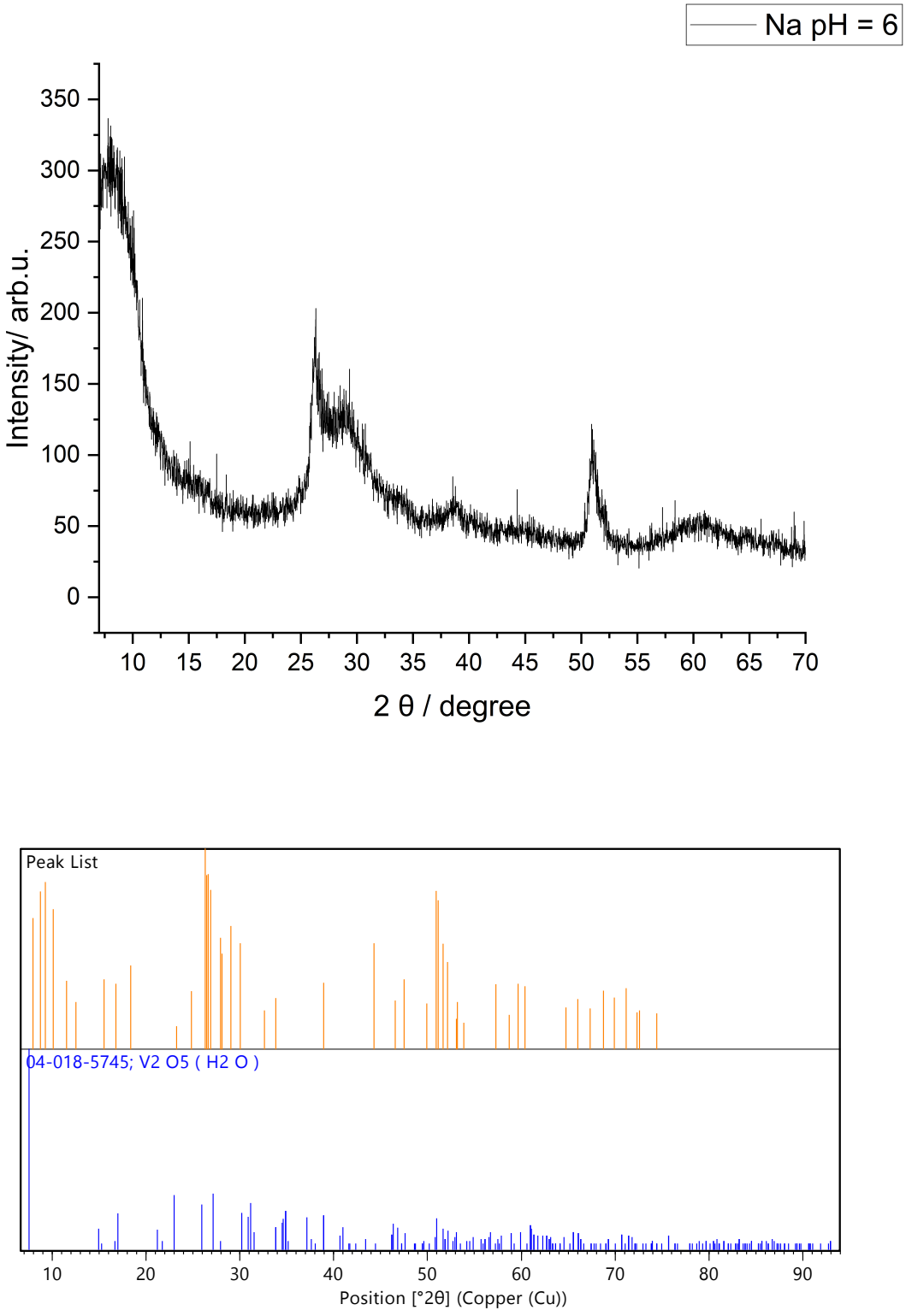


Figure 3-36. XRD diagram of the precipitate in the presence of TMA^+ cations vs. the shown pH and the concomitant cation.

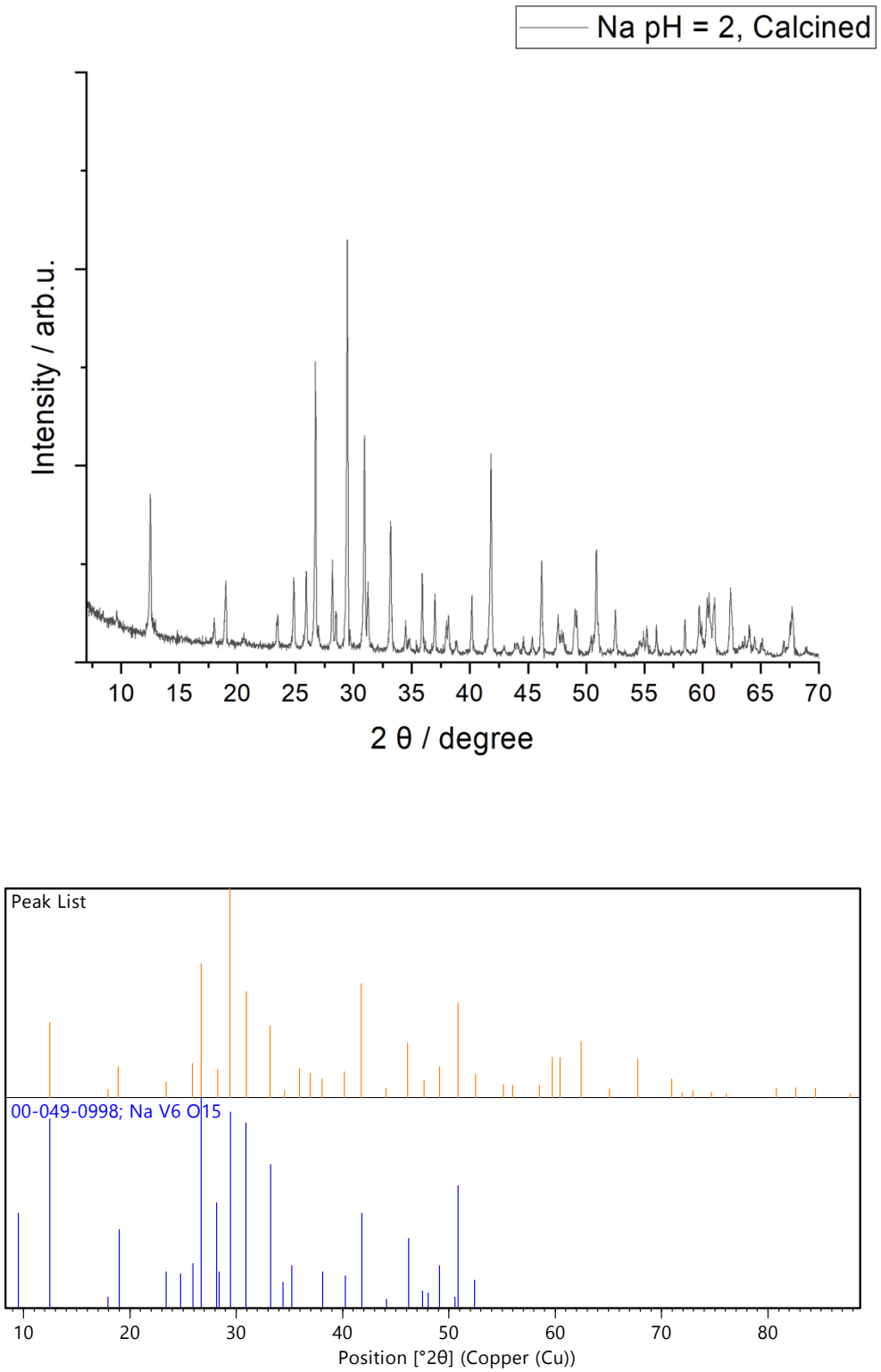


Figure 3-37. XRD diagram of the precipitate in the presence of TMA^+ cations vs. the shown pH and the concomitant cation.

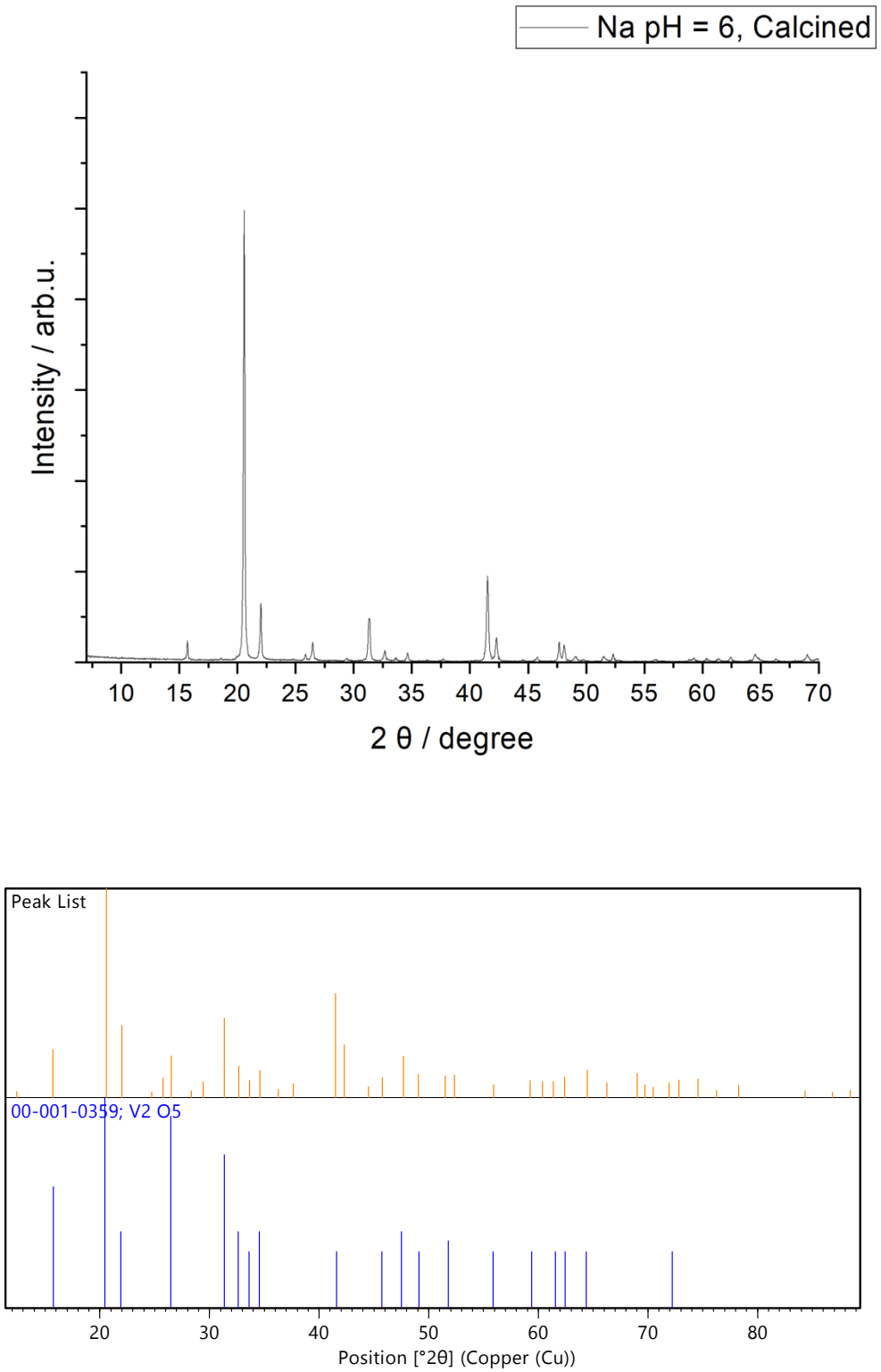


Figure 3-38. XRD diagram of the precipitate in the presence of TMA^+ cations vs. the shown pH and the concomitant cation.

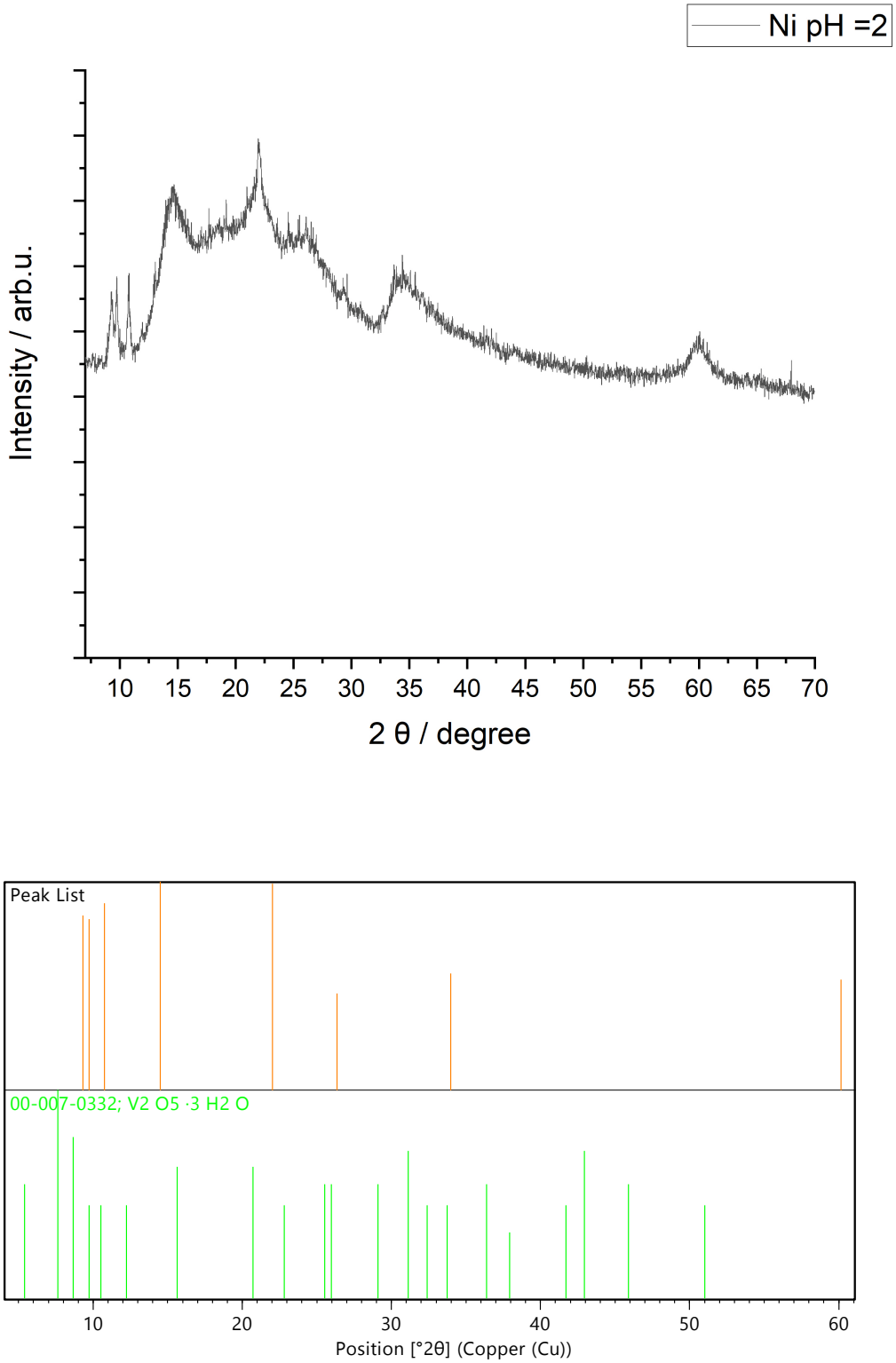


Figure 3-39. XRD diagram of the precipitate in the presence of TMA^+ cations vs. the shown pH and the concomitant cation.

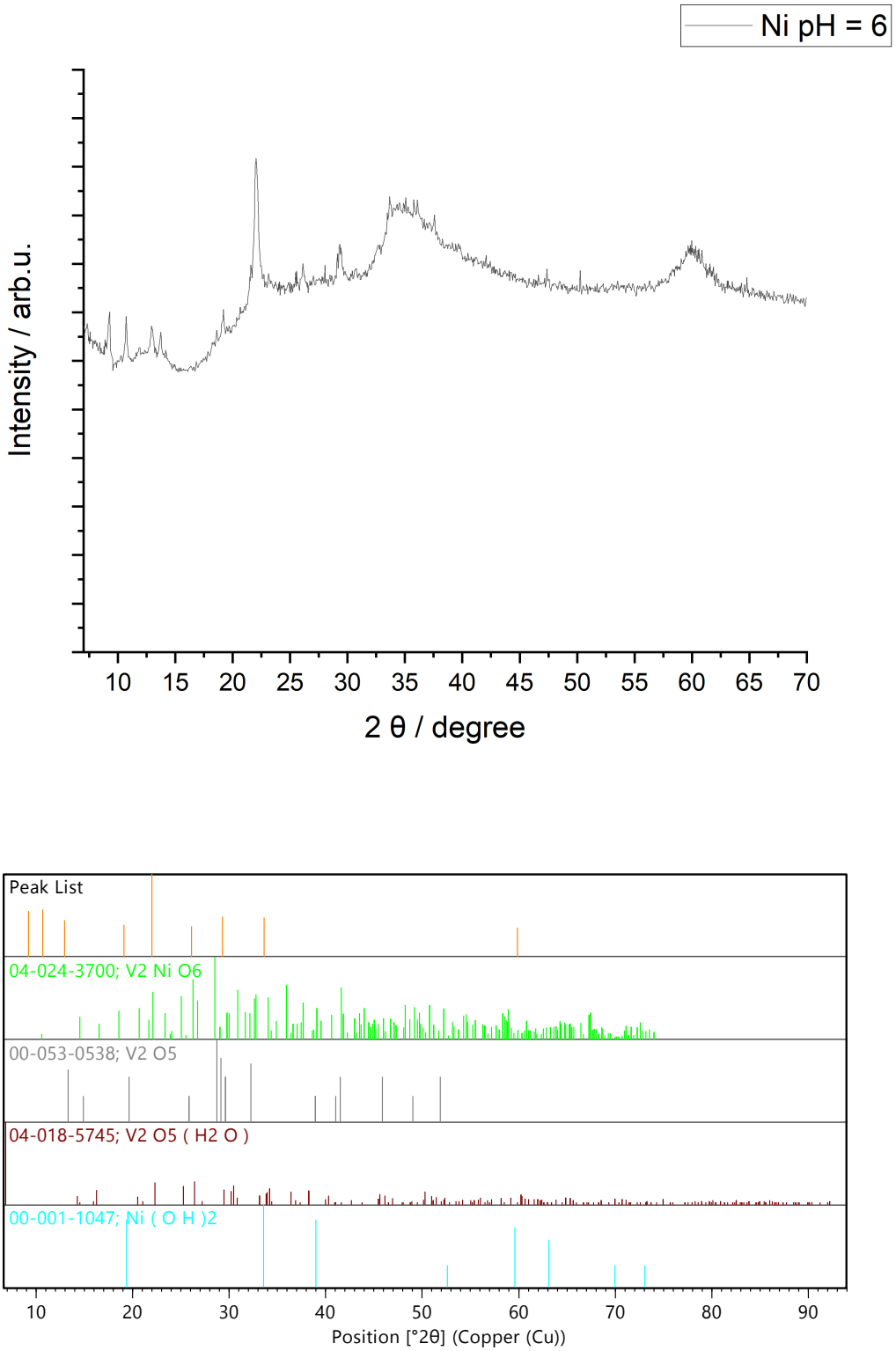


Figure 3-40. XRD diagram of the precipitate in the presence of TMA^+ cations vs. the shown pH and the concomitant cation.

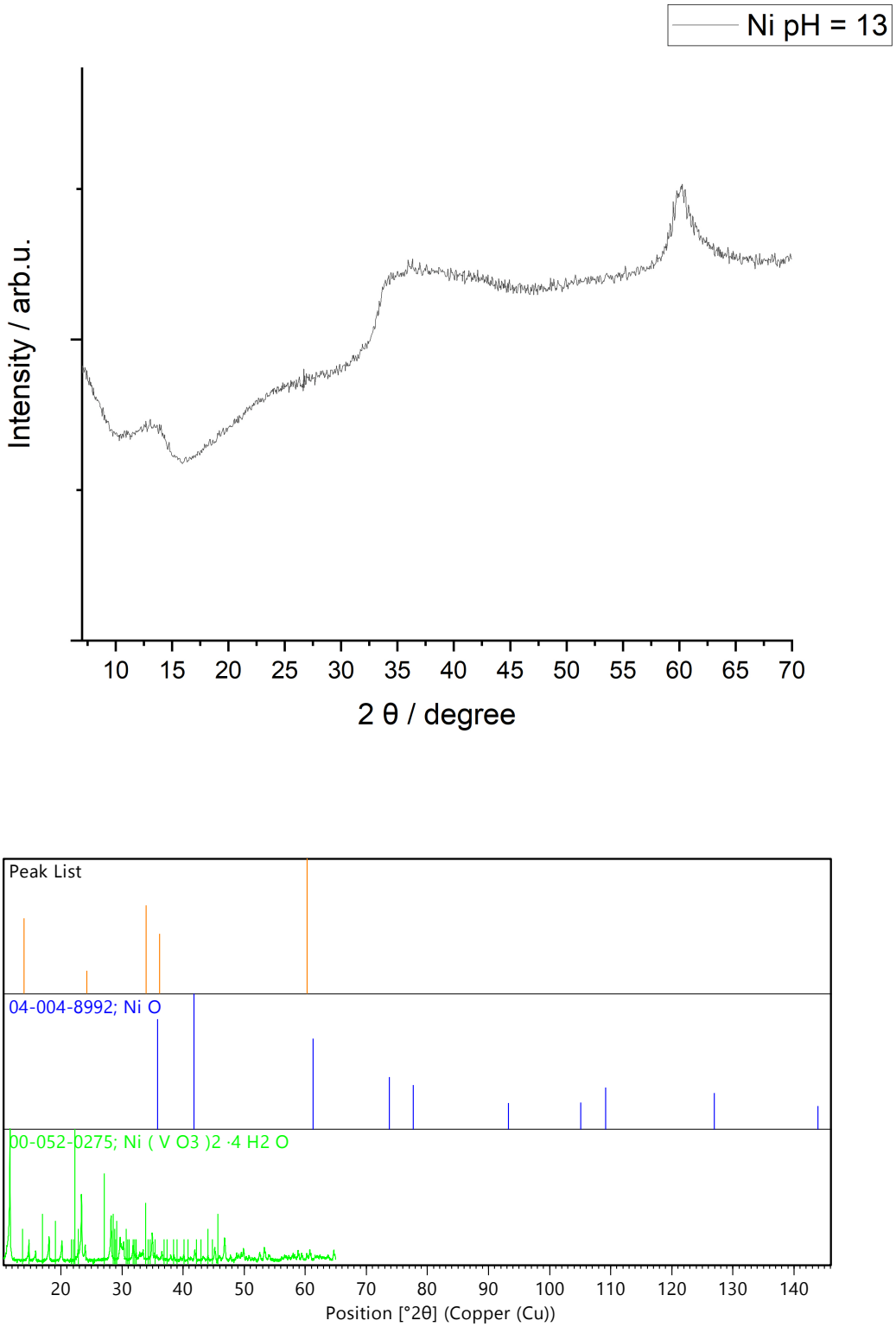


Figure 3-41. XRD diagram of the precipitate in the presence of TMA^+ cations vs. the shown pH and the concomitant cation.

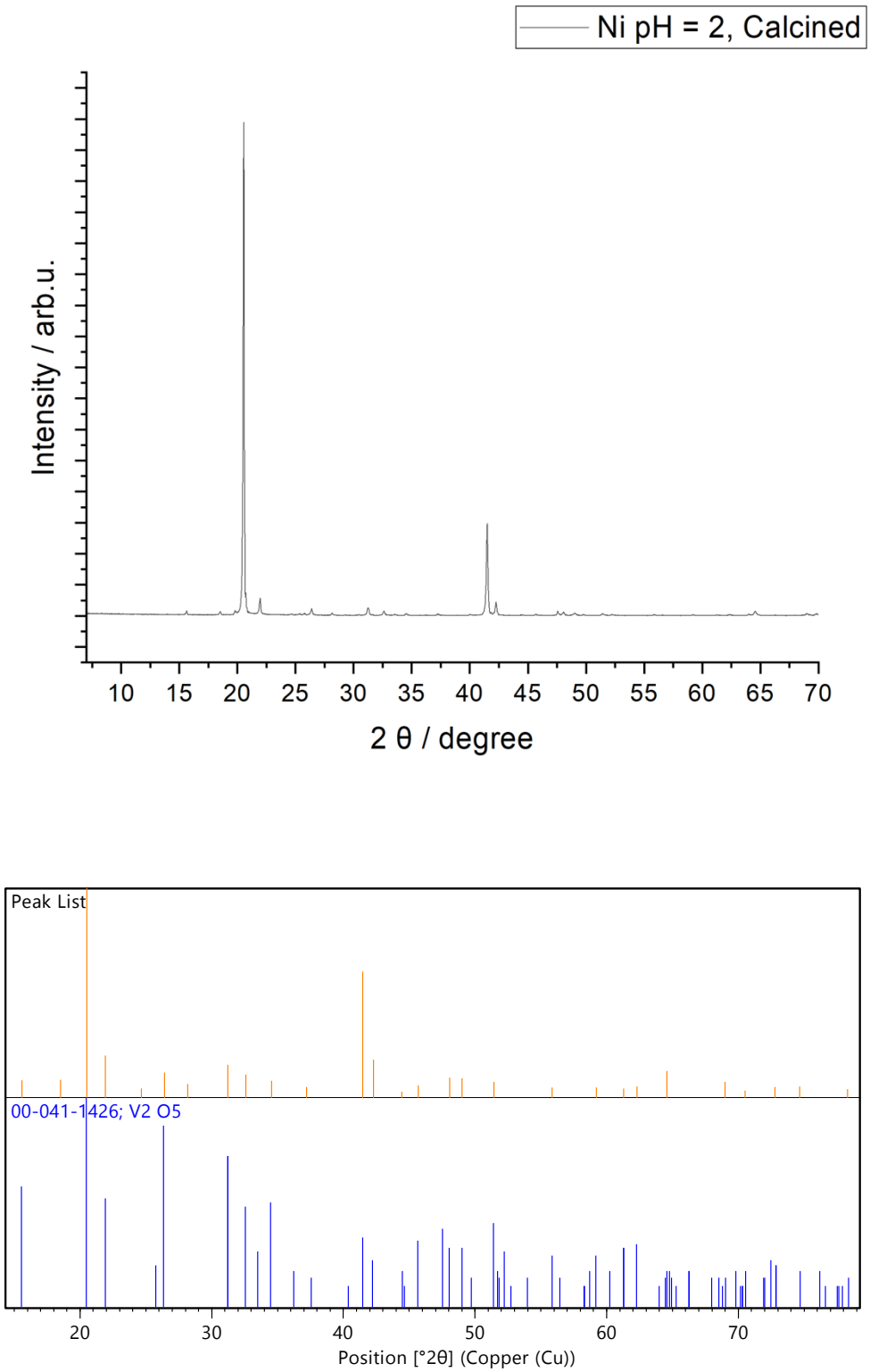


Figure 3-42. XRD diagram of the precipitate in the presence of TMA^+ cations vs. the shown pH and the concomitant cation.

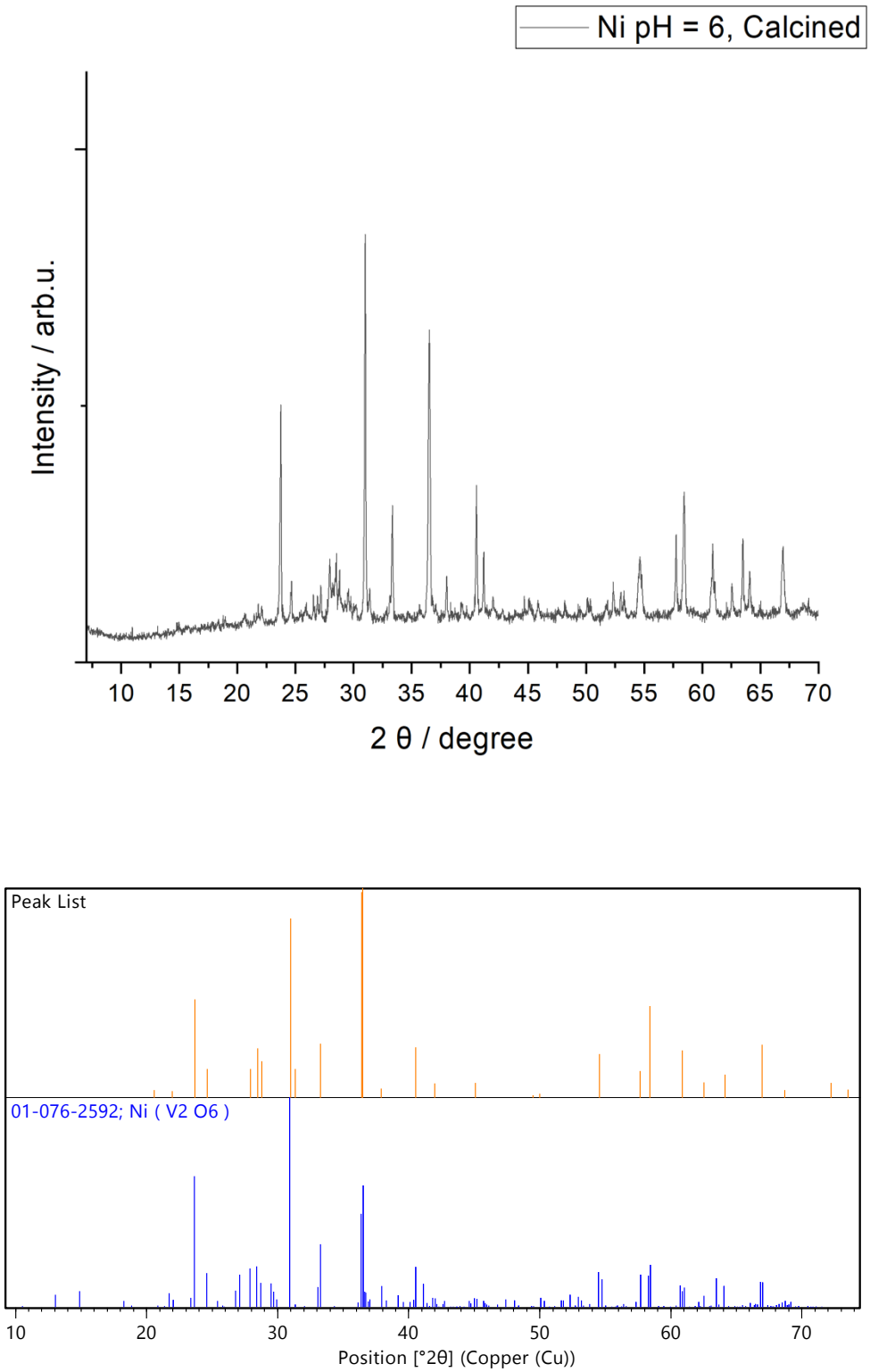


Figure 3-43. XRD diagram of the precipitate in the presence of TMA^+ cations vs. the shown pH and the concomitant cation.

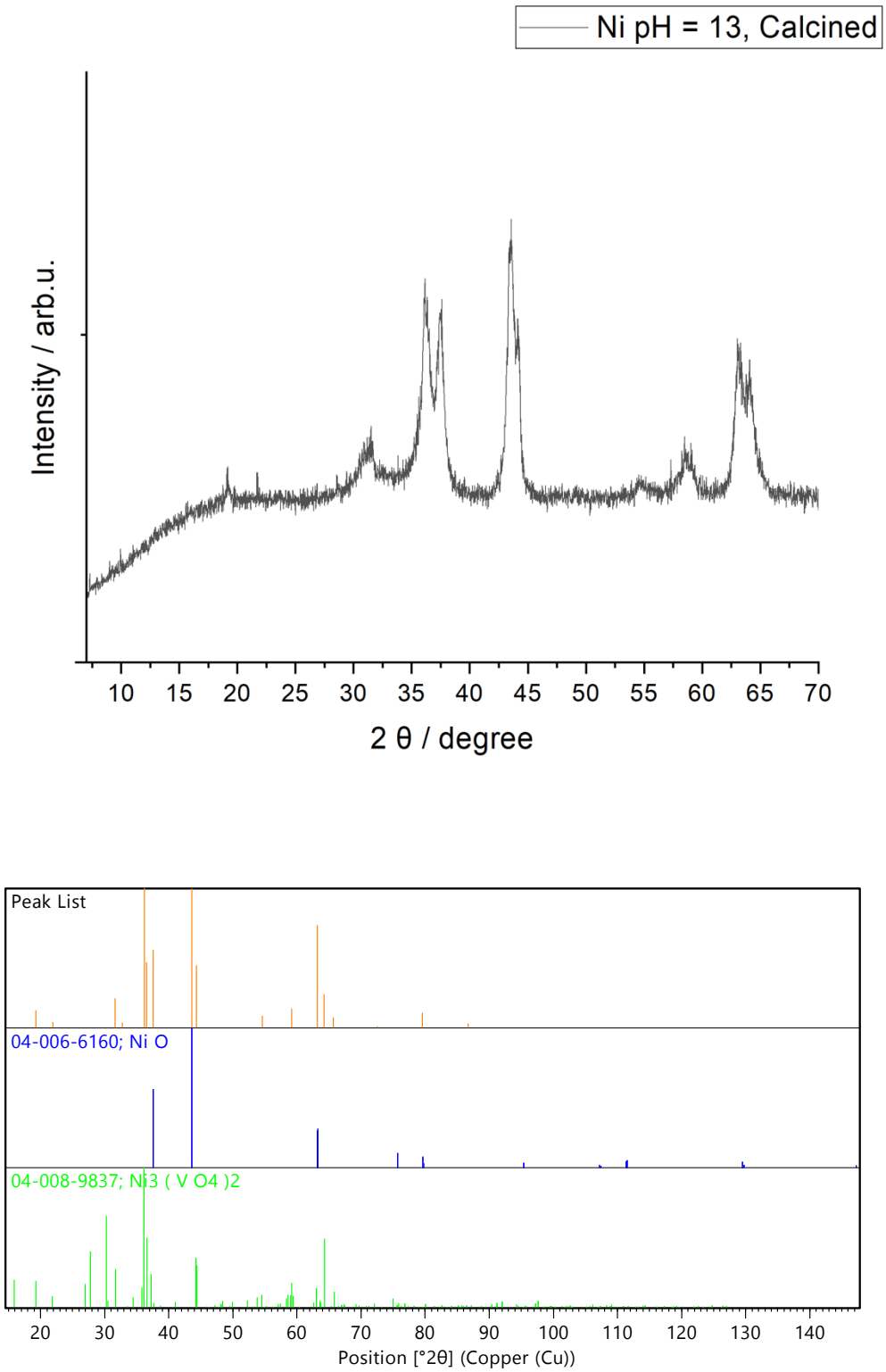


Figure 3-44. XRD diagram of the precipitate in the presence of TMA^+ cations vs. the shown pH and the concomitant cation.

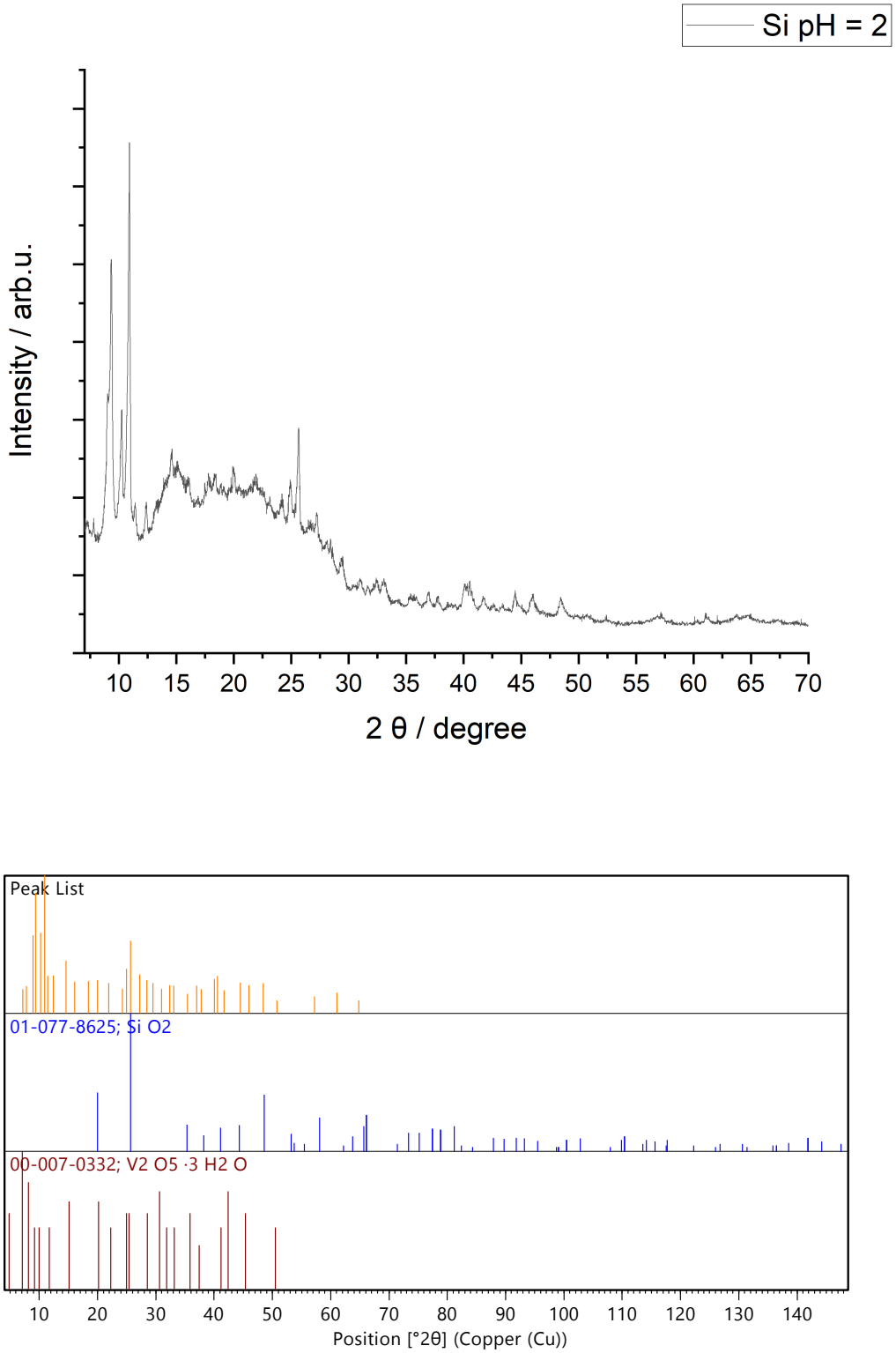


Figure 3-45. XRD diagram of the precipitate in the presence of TMA^+ cations vs. the shown pH and the concomitant cation.

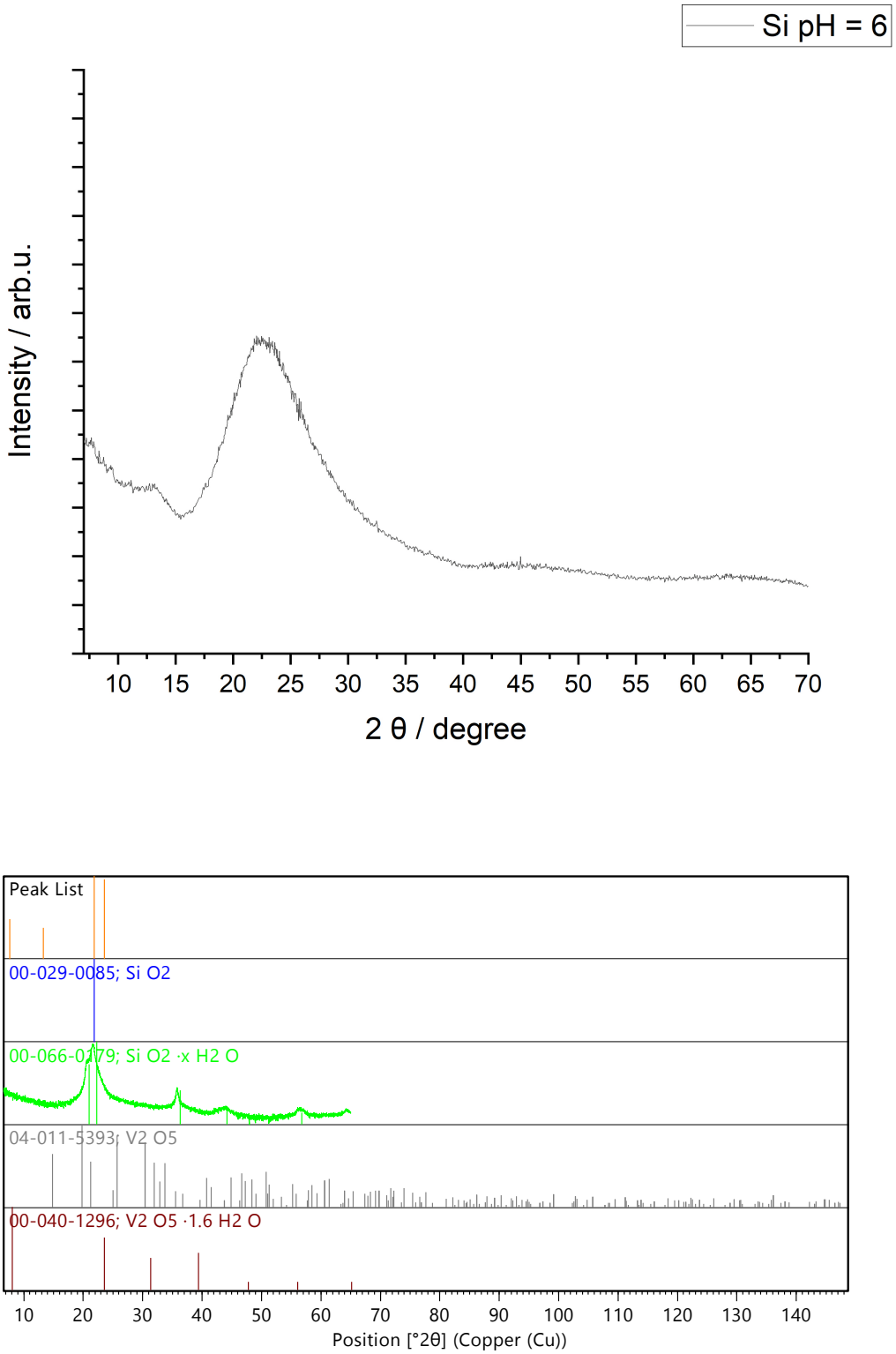


Figure 3-46. XRD diagram of the precipitate in the presence of TMA^+ cations vs. the shown pH and the concomitant cation.

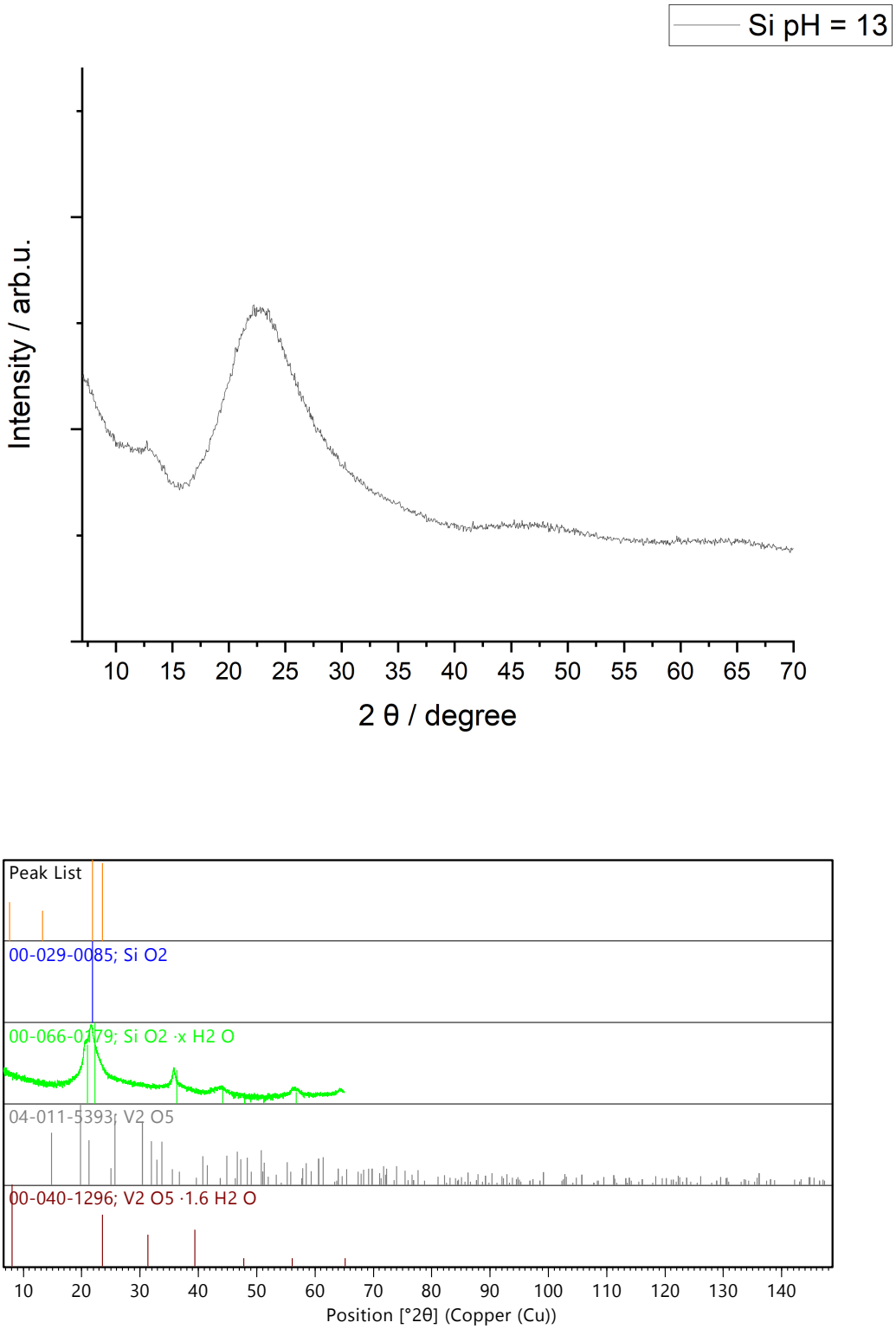


Figure 3-47. XRD diagram of the precipitate in the presence of TMA^+ cations vs. the shown pH and the concomitant cation.

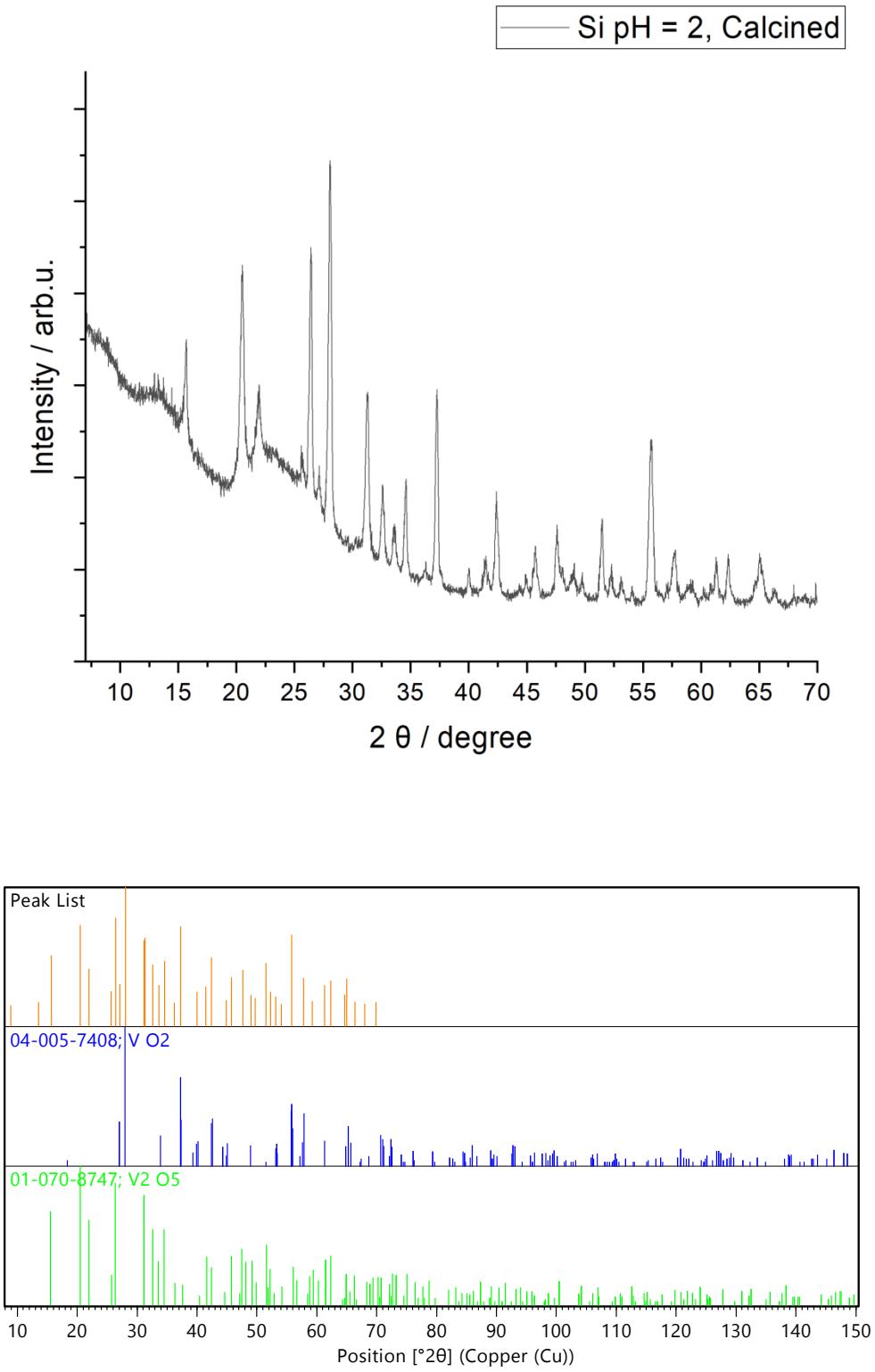


Figure 3-48. XRD diagram of the precipitate in the presence of TMA^+ cations vs. the shown pH and the concomitant cation.

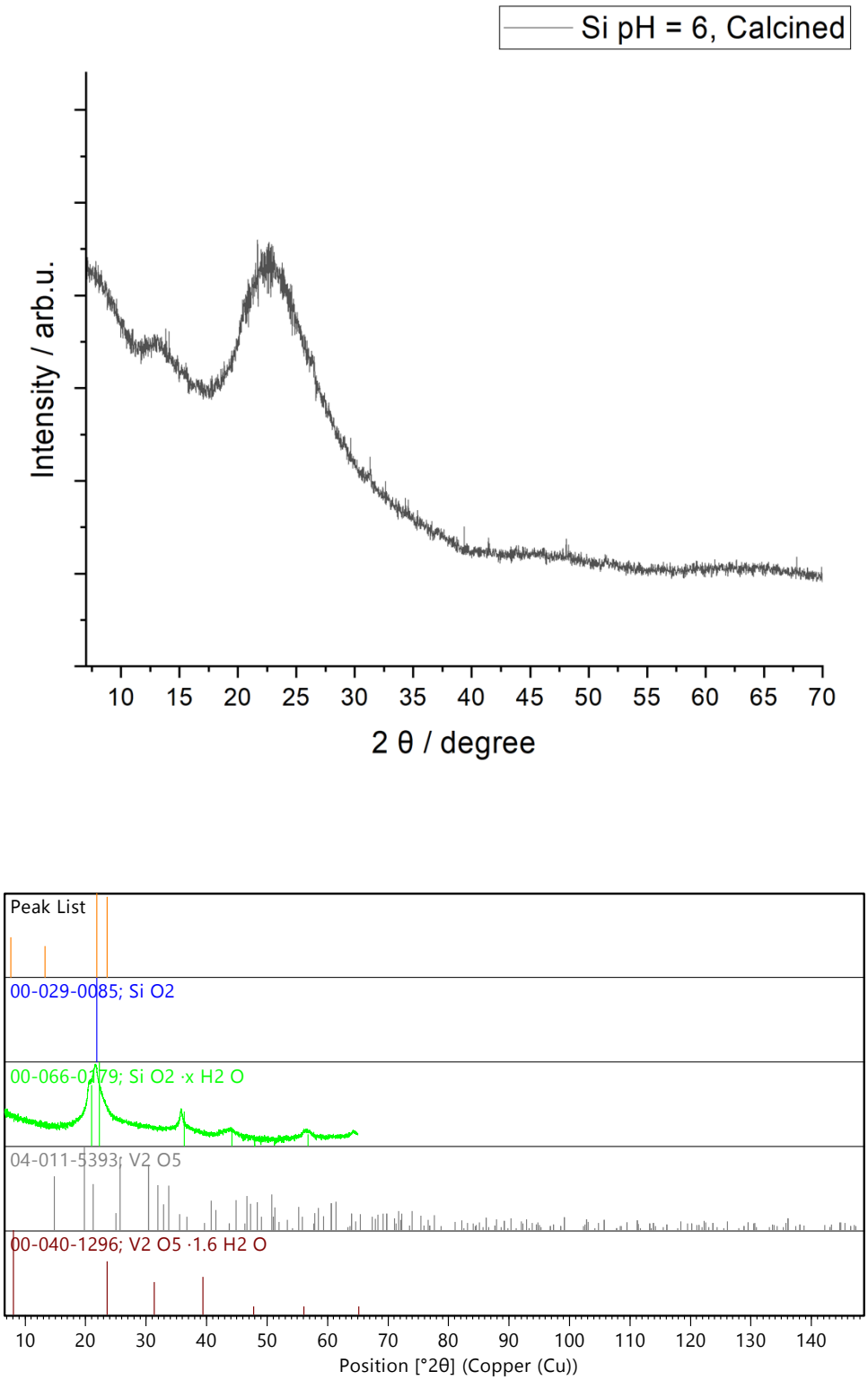


Figure 3-49. XRD diagram of the precipitate in the presence of TMA^+ cations vs. the shown pH and the concomitant cation.

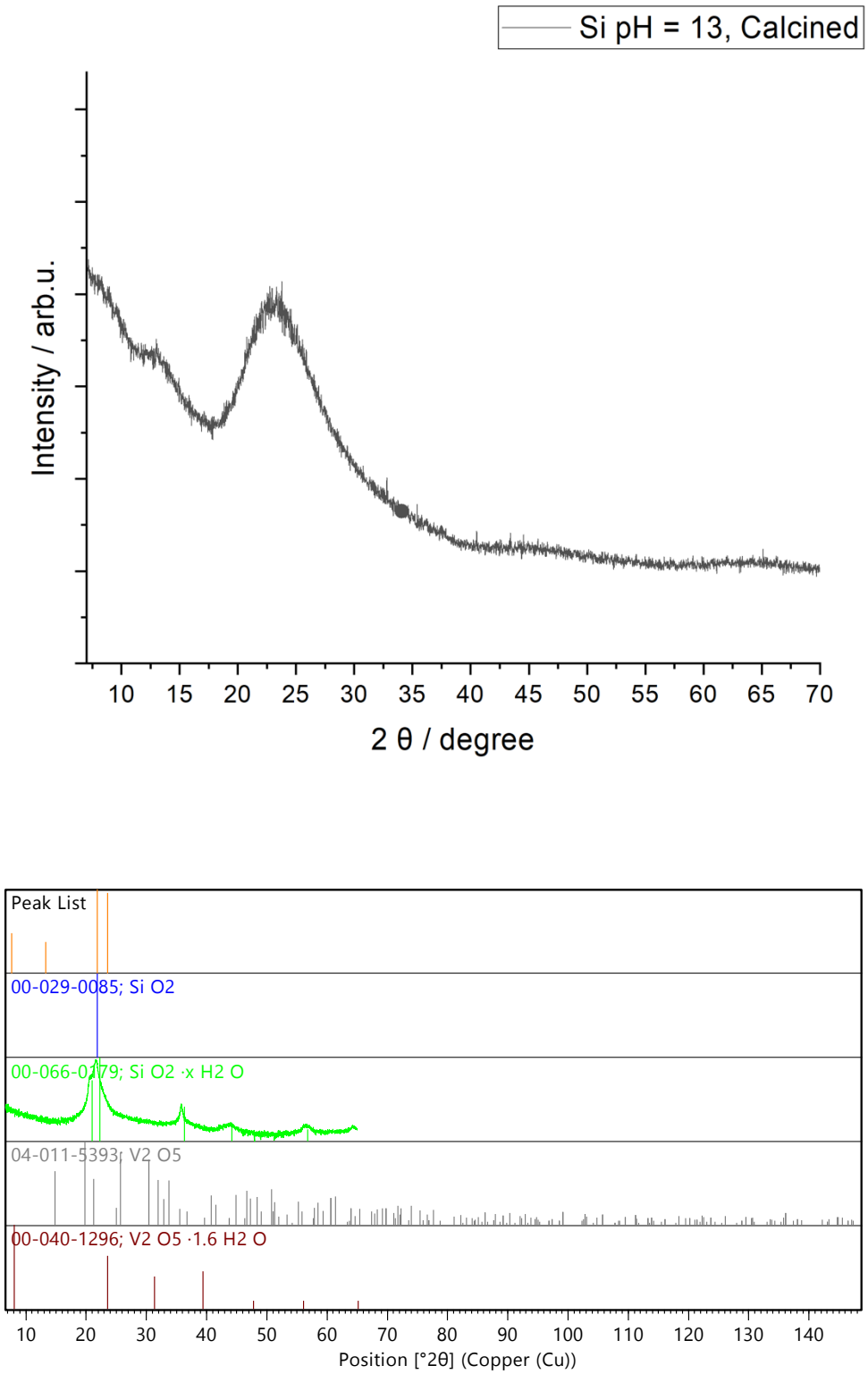


Figure 3-50. XRD diagram of the precipitate in the presence of TMA^+ cations vs. the shown pH and the concomitant cation.

3.3.2 Preliminarily leaching experiments

Preliminary experiments were conducted to screen the most impactful variables such as reaction temperature, tetramethylammonium hydroxide concentration and others. The ultimate goal was to define a range for each of the variables for the leaching experiments.

3.3.2.1 Effect of temperature – Preliminary experiments

Figure 3-51 shows the extraction yield versus time for the upper range and the lower range temperature of the leaching experiments. As a result of increasing the reaction temperature from 50 °C to 90 °C, the extraction yield was promoted by approximately 10 % at a given time. The increase in the extraction yield was expected, as it has been reported frequently in the literature that vanadium(V) extraction yield was enhanced with increasing temperature due to the increase in the rate of the chemical reaction.[148] However, the literature appears to have ignored the effect of temperature on the diffusion rate of materials through the inert/unreactive particles as will be discussed in section 3.3.6 Kinetics study.

3.3.2.2 Effect of TMA^+OH^- concentration – Preliminary experiments

Figure 3-52 shows the extraction kinetics data obtained from leaching the as-received gasifier ash with various TMA^+OH^- concentrations, while keeping the liquid-to-solid ratio, the reaction temperature and the reaction time constant. The vanadium(V) purity was calculated among the studied elements by ICP-MS. At zero TMA^+OH^- concentration, ultrapure water used as the leaching solution resulted in only 0.2 % vanadium(V) extraction yield and 17 % vanadium(V) purity. There was a significant increase in both parameters when the leaching solution was changed from ultrapure water to 0.9 mol dm^{-3} TMA^+OH^-. The vanadium(V) purity stayed around 98 % for 1.5 mol dm^{-3} TMA^+OH^- onwards, with no significant changes on increasing the ionic liquid concentration. However, there was a steady increase in the extraction yield with increasing TMA^+OH^- concentration, reaching a maximum of 38.7 % at the commercially available 2.78 mol dm^{-3} TMA^+OH^- concentration.

3.3.2.3 Effect of liquid-to-solid ratio – Preliminary experiments

The commercial TMA^+OH^- solution was available at the concentration of 25 wt% (or 2.78 mol dm^{-3}) in water or methanol. At high pH (i.e. > 14) vanadium(V) generates oxyanion species, in the case of tetramethylammonium hydroxide, $TMA_3^+VO_4^-$ was formed as the product. One way to partially overcome the concentration limitation was to increase the liquid-to-solid ratio which increased the number of reactants and diluted the product concentration, helping the chemical reaction towards completion. Also, the external diffusion resistance could become negligible at high liquid-to-solid ratios, so the intraparticle diffusion resistance should become the limiting factor in the reaction kinetics, which will be discussed in detail in section **3.3.6 Kinetics study**

Figure 3-53 shows the effects of the liquid-to-solid ratio and the TMA^+OH^- concentration on vanadium(V) extraction yields. The liquid-to-solid ratio was set as 5 $cm^3\ g^{-1}$, 10 $cm^3\ g^{-1}$ and 15 $cm^3\ g^{-1}$, and the TMA^+OH^- concentration was set as the stock solution concentration, which was 2.78 mol dm^{-3}, half of the stock solution concentration (1.39 mol dm^{-3}) and a third of the stock solution concentration (0.92 mol dm^{-3}), while keeping other reaction conditions constant. As can be seen from Figure 3-53, the vanadium(V) extraction yield was nearly independent of the liquid-to-solid ratio between 5 to 15 $cm^3\ g^{-1}$, as the variations were within the experimental error.

The vanadium(V) extraction yield was improved by using the 2.78 mol dm^{-3} TMA^+OH^- solution, where approximately 57 % of the vanadium in the solids leached out in the solution at a liquid-to-solid ratio of 10 $cm^3\ g^{-1}$. The vanadium(V) extraction yield for the liquid-to-solid ratio of 5 $cm^3\ g^{-1}$ and 2.78 mol dm^{-3} TMA^+OH^- concentration was 3 % lower than that of 10 $cm^3\ g^{-1}$ and there was hardly a change in the yield from 10 $cm^3\ g^{-1}$ to 15 $cm^3\ g^{-1}$. Moreover, the 5 $cm^3\ g^{-1}$ liquid-to-solid ratio made a slurry-like suspension, which caused difficulties in the separation of the residue and the leachate. Thus, it was decided to use the 10 $cm^3\ g^{-1}$ liquid-to-solid ratio for the leaching kinetics experiments unless otherwise stated.

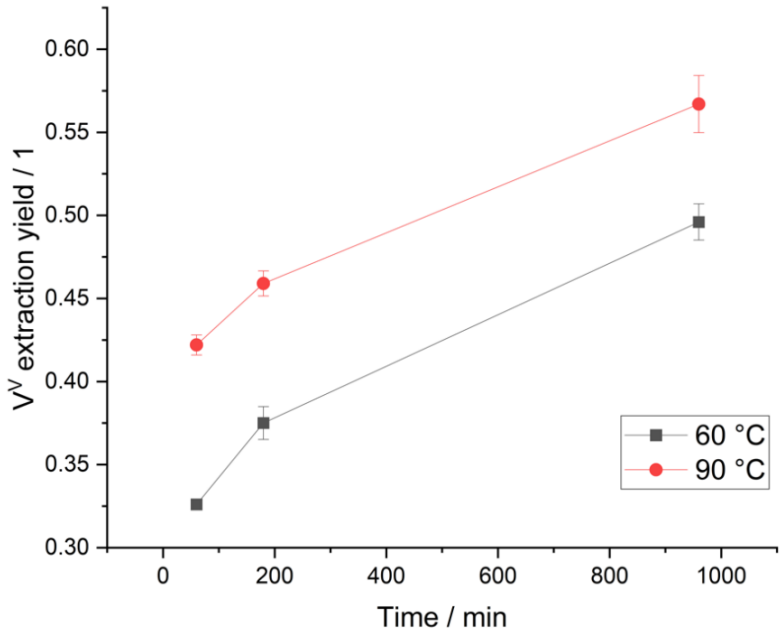


Figure 3-51. Preliminarily data for the time dependence of vanadium(V) extraction from the gasifier ash: Effect of reaction temperature. 550 rpm, 5 $cm^3\ g^{-1}$ and 2.78 mol dm^{-3} TMA^+OH^- concentration.

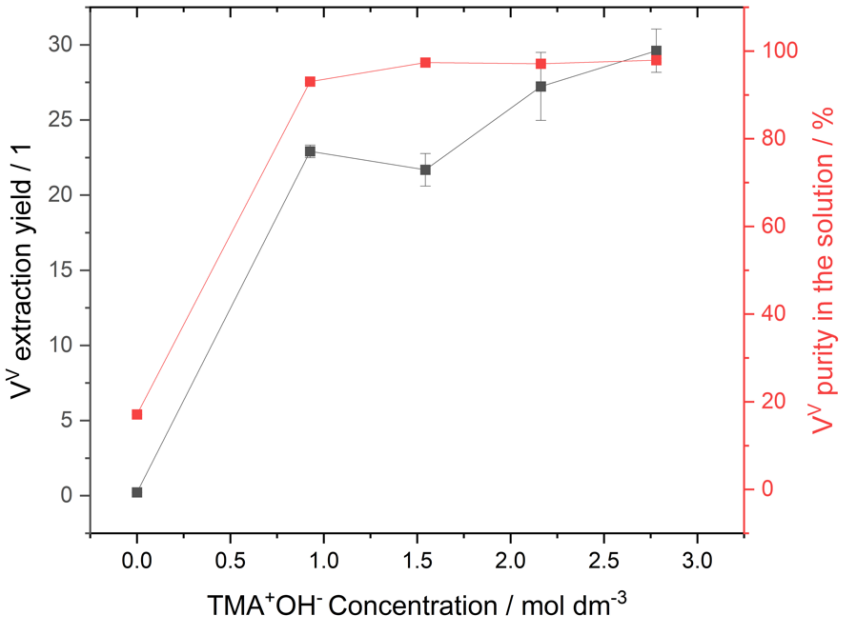


Figure 3-52. Effect of TMA^+OH^- concentration on vanadium(V) extraction yield and purities. 550 rpm, 5 $cm^3\ g^{-1}$, 180 min reaction time, 50 °C reaction temperature and 2.78 mol dm^{-3} TMA^+OH^- concentration.

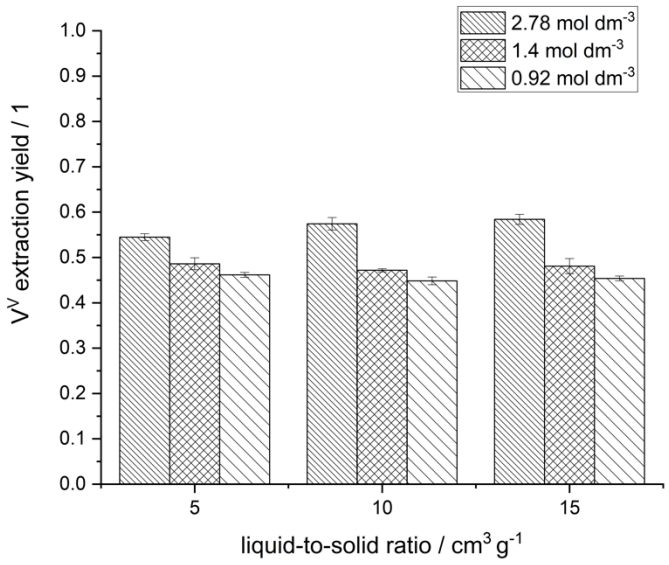


Figure 3-53. Effects of TMA^+OH^- concentration and liquid-to-solid ratio on vanadium(V) extraction yield. 550 rpm, 90 °C reaction temperature, 960 min reaction time and zero mol dm^{-3} $NaClO_2$.

3.3.2.4 Effect of reaction time – Preliminary experiments

Figure 3-54 shows the time dependence of vanadium(V) extraction yields during seven days of leaching under the following reaction conditions: reaction temperature of 90 °C, liquid-to-solid ratio of 10 cm^3 g^{-1} and TMA^+OH^- concentration of 2.78 mol dm^{-3}.

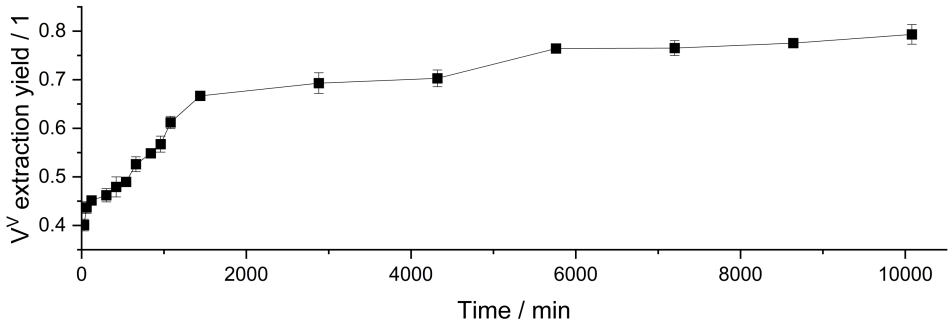


Figure 3-54. Effect of leaching time on the vanadium(V) extraction yield. 550 rpm, 10 cm^3 g^{-1}, 90 °C reaction temperature and 2.78 mol dm^{-3} TMA^+OH^- concentration.

The seven-day leaching experiment was designed to eliminate the effect of internal and external diffusion of materials which ultimately helped to find the equilibrium extraction yield of vanadium(V). As can be seen from Figure 3-54, an initially fast reaction rate was followed by a much slower phase, with the vanadium(V) extraction yield reached approximately 70 % after one day. At increased times the vanadium(V) extraction yields increased only slightly. The increases in vanadium(V) extraction yield from day 5 to day 6, and day 6 to day 7 were ca. 1%, indicating that the vanadium(V) extraction yield became limited at ca. 80 %. The residue at the end of the experiment had a deep green-ish colour and its consistency was like sticky oil paint. The remaining vanadium(V) phase which was identified by XRD (see Figure 3-57 (a) and (b)) to be a Ni-V-O phase was thermodynamically stable at the tested experimental conditions. This is in line with the results explained in section 0 where it was shown by the control experiments that the Ni-V-O phase was thermodynamically stable at high pH.

Every 100 g ash contained 12.34 % Ni, which is equivalent to 0.21 mols of Ni. The stoichiometric ratio of vanadium to nickel is 2 to 3 in $Ni_3V_2O_8$ so there had to have been at least 0.14 mols of vanadium 'locked' in this Ni-V-O phase, equivalent to 7.14 g V in 100 g ash. The ratio of vanadium in the Ni-V-O phase to the total vanadium in the gasifier ash (38.32 g V in 100 g ash) is 19 %. On the other hand, it was shown that the equilibrium extraction yield of vanadium(V) was approximately 80%. Therefore, it can be said that it is somewhat likely that almost all the remaining vanadium in the residue was in the Ni-V-O phase and was not extracted as also indicated by Figure 3-57 (a) and (b).

3.3.2.5 Effect of oxidising agent - Preliminary experiments

As explained in the previous section, the reaction time was intentionally set to be long to eliminate mass transfer effects i.e., leaving enough time for the reactants to meet the vanadium sites. The solid reactants and the liquid reactants reached an equilibrium and the remaining vanadium in the solid phase was theorised to be in a thermodynamically stable phase, so no longer reacted. On the other hand, the XPS analysis showed that there were mixed vanadium-metal oxides in the as-received gasifier ash. The appearance of low-oxidation state vanadium oxide can be attributed to the reducing nature of the gasification unit. The intercalation of the concomitant

cations within the vanadium pentoxide caused a partial reduction in the oxidation state of vanadium(V) atoms in the network; syntheses of such phases has been reported.[149,150]

Due to the existence of lower oxidation state vanadium oxide materials, the experimental conditions in Figure 3-53 were repeated, but with the oxidising agent sodium chlorite added as powder to produce a concentration of 0.221 mol dm^{-3} $NaClO_2$ (20 g dm^{-3}) in the leach solution.

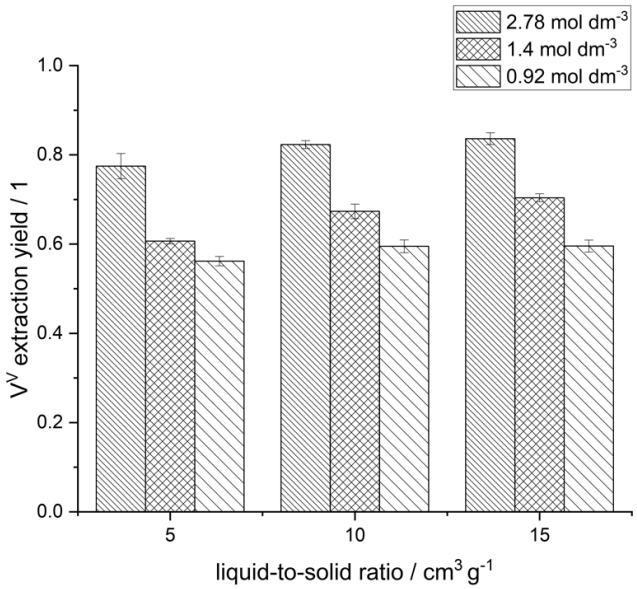


Figure 3-55. Effect of TMA^+OH^- concentration and the liquid-to-solid ratio on the vanadium(V) extraction yield. 550 rpm, 90 °C reaction temperature, 300 min reaction time, and 0.221 mol dm^{-3} $NaClO_2$.

Figure 3-55 shows that the leaching kinetics increased in 2.78 mol dm^{-3} TMA^+OH^- solution relative to lower concentrations, with ca. 82 % of the vanadium(V) dissolved at a liquid-to-solid ratio of 10 cm^3 g^{-1}. Increasing the solid to the liquid ratio by 50 %, to 15 cm^3 g^{-1} increased the vanadium(V) extraction yield only slightly, and within experimental error. Although addition of $NaClO_2$ had almost no effect on the limiting extraction yield of vanadium(V), it increased the reaction kinetics greatly, causing the reaction to reach limiting extraction yield in 300 min, rather than ca. 7 days in the absence of oxidant, as described in 3.3.2.4. Figure 3-55 also shows that liquid-to-solid

ratio had a minimal effect on the extraction kinetics, whereas the effect of TMA^+OH^- concentration was much more pronounced.

Figure 3-56 shows the effect of oxidant type on the leaching behaviour of vanadium(V). It is evident that when $NaClO_2$ was used as the oxidising agent, the limiting extraction yield of vanadium(V) was obtained in 300 min, because a further 120 min reaction time from 300 min to 420 min did not affect the extraction yield. For the case of $NaClO_3$, significant improvements were achieved compared to when no additives were introduced to the solution (as-received bars). The oxidative extraction kinetics with $NaClO_3$ however was slightly slower than that of the $NaClO_2$ case. For the case of H_2O_2, the experiments were conducted while the flasks were open to the atmosphere in the fume hood to avoid pressure build up. The vanadium content in the residue was analysed in this case to avoid error due to the volume change during the reaction. Addition of H_2O_2 also increased the extraction kinetics but slowed down from 300 min to 420 min, presumably due to the decomposition of hydrogen peroxide to H_2 and O_2

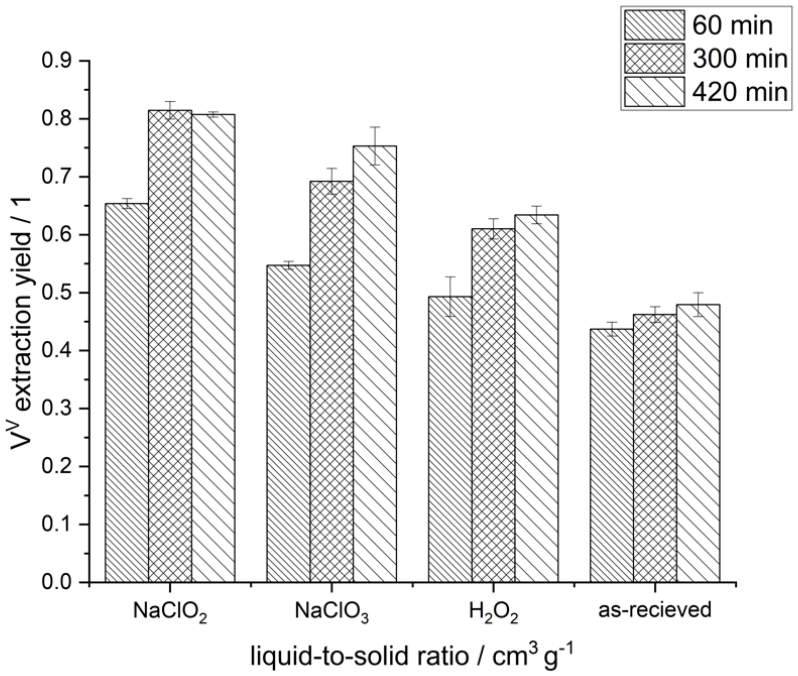


Figure 3-56. Effect of oxidising agent and time on the vanadium(V) extraction yield. 0.221 mol dm^{-3} for both $NaClO_2$ and $NaClO_3$ concentrations, and 1:5 v/v 30% H_2O_2 in the solution; 550 rpm, 90 °C reaction temperature, 2.78 mol dm^{-3} TMA^+OH^- concentration.

before reacting with partially oxidised vanadium sites. Owing to the above findings, $NaClO_2$ was used in this project for the oxidative leaching of partially oxidised vanadium in the gasifier ash.

3.3.2.6 Vanadium(V) dissolution reaction - with oxidant

It was shown in section 3.3.1 that the gasifier ash contained mixed vanadium oxides of V^{V} and V^{IV}. The oxidative dissolution of vanadium(IV) oxide from the gasifier ash using tetramethylammonium hydroxide solutions can be explained by the following reaction sequence:

Oxidation

$$2\,V_2O_4(c) + 2\,H_2O \rightarrow\ V_2O_5 + 4\,e^- + 4\,H^+ \qquad \text{(Reaction 3-1)}$$

Reduction

$$ClO_2^- + 4H^+ + 4e^- \rightarrow Cl^- + 2H_2O \qquad \text{(Reaction 3-2)}$$

Overall

$$2\,V_2O_4(c) + {ClO_2}^- \rightarrow 2\,V_2O_5(c) + Cl^- \qquad \text{(Reaction 3-3)}$$

V_2O_5 dissolution

$$2V_2O_5(c) +\ 12\,TMA^+OH^- \rightarrow 4\,[TMA]_3\,[VO_4] + 6\,H_2O \qquad \text{(Reaction 3-4)}$$

According to the Nernst equation:

$$E_{ClO_2^-/Cl^-}(SHE)/V =$$

$$1.6132 - 0.0592pH + 0.0148\log\left[\frac{ClO_2^-}{Cl^-}\right] \qquad \text{(Equation 3-5)}$$

Hence, at pH 14 and standard conditions, E (SHE) / V = 0.785

$$E_{V_2O_5/V_2O_4}(SHE)/V = 0.7067 - 0.0592pH \qquad \text{(Equation 3-6)}$$

The E-pH diagram (Figure 4-6) predicts that neither V_2O_5 nor V_2O_4 are stable at high pH, at which both should dissolve spontaneously. However, note the presence of e.g., V_6O_{13} (oxidation state 4.3), also unstable at high pH but a possible intermediate in oxidative dissolution of V_2O_4.

3.3.2.7 Vanadium(V) dissolution reaction - without oxidant

The seven-day extraction kinetics data without the use of an oxidant is depicted in Figure 3-54. It is interesting to note that after one day of leaching with no additives, the

extraction yield was increasing slowly towards the limiting extraction yield of vanadium(V) and reached ca. 80 % after 7 days, implying slow oxidation of the low oxidation state vanadium oxide materials by presumably the only oxidant source, dissolved oxygen in the reaction mixture. A similar phenomenon was studied by Morgan and Lahav[151] who reported that the spontaneous chemical oxidation of iron(II) to iron(III) was a strong function of pH. The slowest step was reported to be the formation of radicals of $O_{2\bullet(aq)}^{-}$ because it is the most endergonic process.

Oxidation

$$2\,V_2O_4(c) + 2\,H_2O \rightarrow\ 2V_2O_5 + 4\,e^- + 4\,H^+ \qquad \text{(Reaction 3-5)}$$

Reduction

$$O_2 + 2H_2O + 4e^- \rightarrow 4OH^- \qquad \text{(Reaction 3-6)}$$

Overall

$$2\,V_2O_4(c) + O_2 \rightarrow\ 2\,V_2O_5 \qquad \text{(Reaction 3-7)}$$

V_2O_5 dissolution

$$V_2O_5 +\ 6\,TMA\,OH \rightarrow 2[TMA]_3\,[VO_4] + 3H_2O \qquad \text{(Reaction 3-4)}$$

3.3.3 Vanadium oxide phase determination in the residue

One of the properties of tetramethylammonium vanadate (TMAV) is its high solubility in alcohols such as methanol which is an uncommon feature in inorganic chemistry. This allows for the maximum elimination/recovery of the leached vanadium(V) from the post-reaction residue. The solubility in alcohols is beneficial for the industrialisation of such processes, due to allowing for maximum recovery of the valuable cation (TMA^+) while allowing for safe disposal of the filter cake. The high solubility of TMAV in methanol had also a crucial application in this study. The post-reaction residue was repeatedly washed with methanol to remove the left-over TMA^+OH^- /TMAV with minimal to virtually zero loss of the metal oxides that would have occurred if water was used instead. This allowed identifying the vanadium phase that was not extracted under the experimental conditions.

Figure 3-57(a) shows the XRD pattern of the methanol-treated residue which was recovered after 7 days of leaching i.e., no additive was added and Figure 3-57(b) shows the XRD pattern of the methanol-treated residue which was recovered from the

oxidative leaching experiments i.e., $NaClO_2$ was used as an oxidising additive. Note that the extraction yields in both conditions were approximately equal to the theorised equilibrium (ca. 80 % V^V) extraction yield. The XRD patterns in Figure 3-57 (a) and (b) revealed that the extraction yields in both conditions reached an equilibrium because

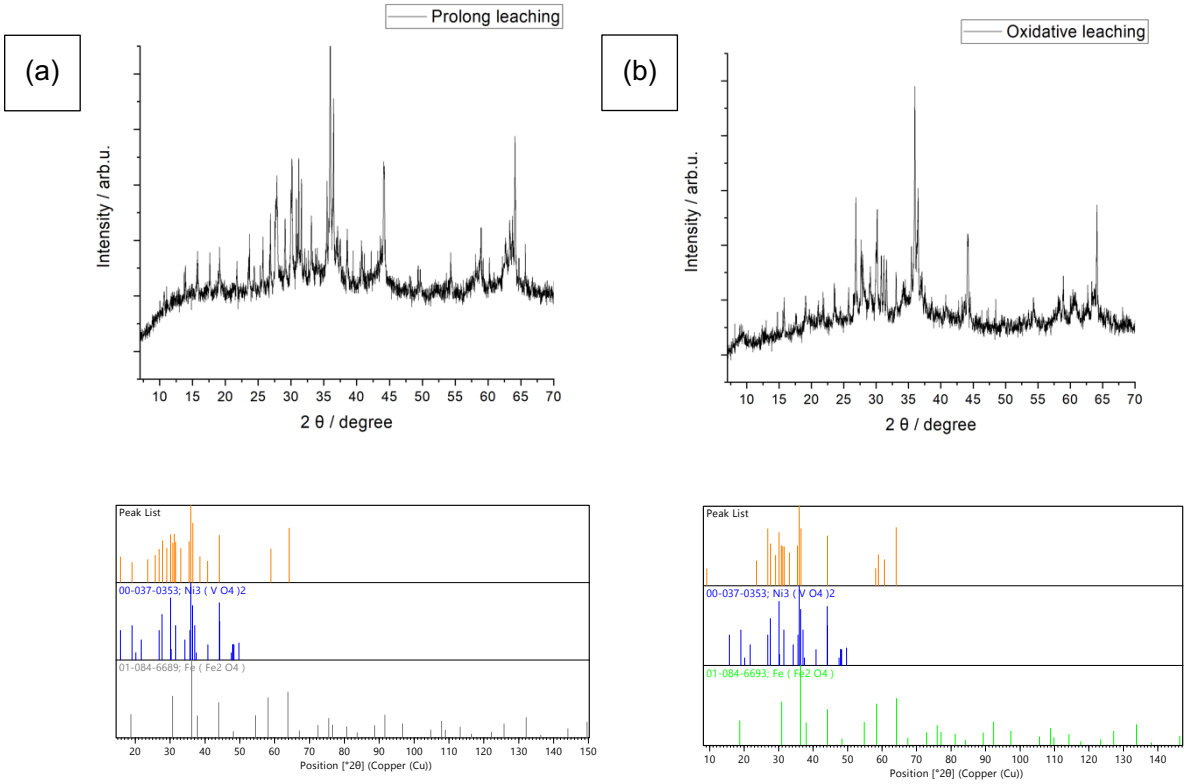


Figure 3-57. X-ray diffraction pattern for the post-extraction solids (a), left, with no additives and 7 days leaching time, and (b),right with 0.221 mol dm^{-3} $NaClO_2$ and 300 min leaching time. Both experiments were conducted under the following conditions: 550 rpm, 10 cm^3 g^{-1}, 90 °C reaction temperature and 2.78 mol dm^{-3} TMA^+OH^- concentration.

the extraction of vanadium(V) from the Ni-V-O phase was not thermodynamically feasible at the given reaction conditions. This is in line with the pH vs. metal ion species in the control experiments explained in 0

3.3.4 Extractable and non-extractable vanadium oxide fraction

X-ray diffractograms for the as-received gasifier ash (see section 3.3.4) confirmed the presence of $M_xV_2O_5$ phases. The following equation was used to calculate the apparent oxidation state of vanadium in that phase:

$$(\nu_O \times z_O) + (\nu_V \times z_V) + (\nu_M \times z_M) = 0$$

ν_M has a wide range; if a value of 0.33 is assumed for an alkali metal, then:

$$(5 \times (-2)) + (z_V \times 2) + (0.33 \times 1) = 0$$

$$z_V = 4.835 \qquad \text{(Equation 3-7)}$$

where z represents the oxidation number and ν is the stoichiometry parameter.

The apparent oxidation number $z_V = 4.835$, is non integer, but in reality, the vanadium in such phases exists as mixed oxides of integers: V^{II}, V^{III}, V^{IV} and V^{V}. The peaks' positions in the XP spectrum (Figure 3-9) revealed that the surface of the particles in the as-received gasifier ash consisted of V^{IV} and V^{V}; hence, Equation 3-7 can be expanded to the following equation:

$$z_V = (n_{V^V} \times z_{V^V}) + (n_{V^{IV}} \times z_{V^{IV}}) = 4.835$$

$$n_{V^V} + n_{V^{IV}} = 1$$

$$n_{V^{IV}} = 1 - n_{V^V}$$

Where n represents the mole ratio of the corresponding oxidation state.

Substituting for $n_{V^{IV}}$:

$$\left(n_{V^V} \times 5\right) + \left(\left(1 - n_{V^V}\right) \times 4\right) = 4.835$$

$$n_{V^V} = 0.835$$

$$n_{V^{IV}} = 0.165$$

The detected $M_xV_2O_5$ peaks in the as-received XRD spectrum (**Error! Reference source not found.**) vanished from the post-extraction XRD spectrum (Figure 3-57 (a) and (b)). On the other hand, by comparing the pre- and post-extraction diffractograms, 17 % of the total vanadium in the as-received gasifier ash was in the form of unextractable Ni-V-O, leaving 83 % extractable mixed vanadium oxides in phases such as $M_xV_2O_5$ or V_2O_5. In order to calculate the fraction of V^{IV}, the limiting extraction yield of vanadium(V) (i.e. the extractable fraction) was multiplied by $n_{V^{IV}}$ which was

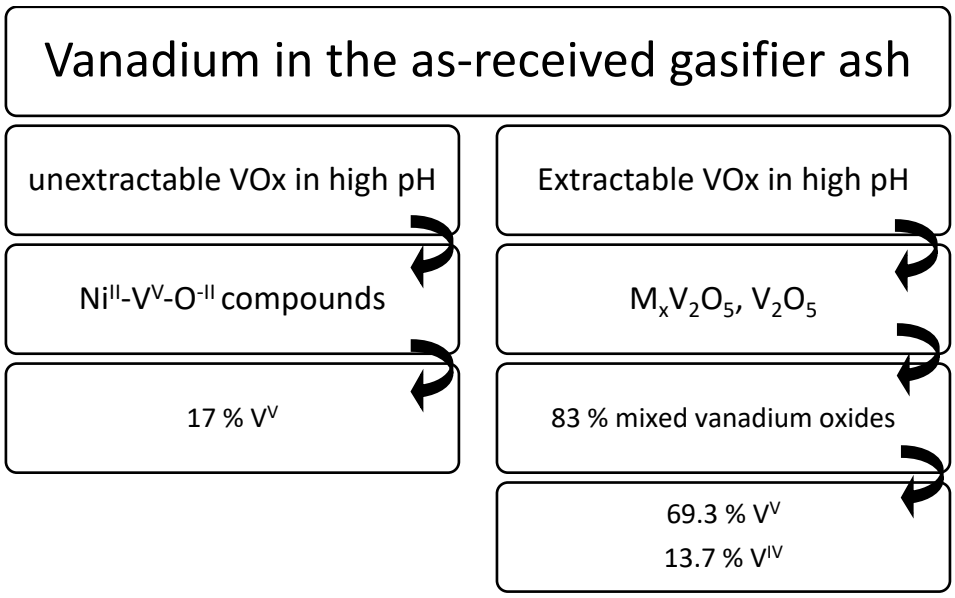


Figure 3-58. Vanadium oxidations states breakdown in extractable and unextractable phases.

estimated above. This analysis can be summarised in Figure 3-58, which shows a breakdown of the extractable and unextractable fractions of the total vanadium in the as-received gasifier ash with their respective oxidation number. It was found that 86.3 % (69.3 % +17 %) and 13.7 % of the vanadium oxides in the as-received gasifier ash were V^{V} and V^{IV}, respectively. This is in good agreement with the calculated vanadium stoichiometry from the XP spectrum on page 83. which suggested the as-received gasifier ash contained 85.3 % V^{V} and 14.7 % V^{IV}.

3.3.5 Fudge factor calibration line

There were three ways to calculate the vanadium(V) extraction yield:

(i) Based on the concentration in the post-reaction solution only. This was the quickest and simplest approach to calculate the extraction yield by calculating the ratio of the total mass of V^{V} in the solution to the total mass of V^{V} in the gasifier ash.

(ii) Based on the concentration in the residue only. This was a more time-consuming approach as the solids had to be digested in a microwave and the number of samples was limited to the available space in the microwave. Only four triplicate samples could be prepared per day. The extraction yield

was calculated from the ratio of the total mass of V^V in the residue to the total mass of V^V in the gasifier ash.

(iii) Based on the concentration in both the solids and the liquids. This was the most accurate but most time-consuming approach, as the V^V concentration of both the residue and the solution had to be measured. This approach eliminates the assumption of uniform V^V concentration in the gasifier ash, as the extraction yield could be calculated from the ratio of the total V^V in the solution to the total V^V in the residue and the solution combined.

Figure A9-1 in the appendices shows the extraction yield for different methodologies. It was noticed that there was a systematic error in the V^V extraction yield in approach (i) compared to approaches (ii) and (iii). Further investigation into the § revealed that the volume of the post-extraction solution was dependent on the V^V concentration which could be corrected if the density of the post-reaction solution was known as a function of concentrations of the dissolved species. The density variations could be sufficient to affect the results, leading to a systematic error. Hence, a calibration line was established so that the extraction yields could be corrected with a correction factor as a function of V^V concentration in the solvent.

A stock solution of tetramethylammonium polyvanadate was made by dissolving 32.16 g 99.6 % V_2O_5 in 200 cm^3 2.78 mol dm^{-3} TMA^+OH^-. The stock solution of V^V was diluted subsequently with fresh 2.78 mol dm^{-3} TMA^+OH^- to the desired concentrations and the densities were measured using a Mettler-Toledo DM40 density meter at 20 °C. The density measurements are shown in Figure 3-59(a); the fresh 2.78 mol dm^{-3} TMA^+OH^- solution had a density of approximately 1 020 kg m^{-3} which was close to the manufacturer's datasheet. As the vanadium(V) concentration increased, the solution density also increased linearly by 0 to 90 kg m^{-3}.

As the extraction yields were calculated based on the concentration of vanadium(V) in the solution, it was of great importance to correct the extraction yields based on the correction factor explained below:

As per the definition, the density of a liquid was calculated from the following equation:

$$\rho_{\mathrm{TMAH+V^V}} = \frac{\text{Total mass}}{\text{Total volume}} \qquad \text{(Equation 3-8)}$$

Which can be written specifically for the leach solution:

$$\rho_{TMAH+V^V} = \frac{m_{V_2O_5} + m_{TMAH}}{V_{TMAH+V^V}} \quad \text{(Equation 3-9)}$$

The mass of vanadium pentoxide can be written as a function of the V^V concentration:

$$m_{V_2O_5} = \left[\frac{\nu_{V_2O_5} M_{V_2O_5}}{\nu_{V^V} M_{V^V}}\right] C_{V^V} V_{TMAH+V^V} \quad \text{(Equation 3-10)}$$

Where $\nu_{V_2O_5}$ and ν_{V^V} represent the stoichiometric ratios in Reaction 3-4.

Substituting Equation 3-10 into Equation 3-9, and rearranging for V_{TMAH+V^V}:

$$V_{TMAH+V^V} = \frac{\rho_{TMAH} V_{TMAH}}{\left(\rho_{TMAH+V^V} - \left[\frac{\nu_{V_2O_5} M_{V_2O_5}}{\nu_{V^V} M_{V^V}}\right] C_{V^V}\right)} \quad \text{(Equation 3-11)}$$

Where $m_{V_2O_5}$ represents the mass (kg) of vanadium pentoxide, m_{TMAH} the mass (kg) of the 2.78 mol dm^{-3} TMA^+OH^- solvent, V_{TMAH+V^V} the volume (m^3) of the solvent and dissolved V^v, ρ_{TMAH+V^V} the density (kg m^{-3}) of the solution with dissolved V^V, C_{V^V} the elemental vanadium(V) concentration (kg m^{-3}), ρ_{TMAH} the density (kg m^{-3}) of the vanadium-free 2.78 mol dm^{-3} TMA^+OH^- solvent and V_{TMAH} the volume (m^3) of the vanadium-free 2.78 mol dm^{-3} TMA^+OH^- solvent.

The correction factor, ε, was defined by the ratio of the leach solution volume to the original volume:

$$\varepsilon = \frac{V_{TMAH+V^V}}{V_{TMAH}} \quad \text{(Equation 3-12)}$$

Substituting Equation 3-11 into the above equation:

$$\varepsilon = \frac{\rho_{TMAH}}{\left(\rho_{TMAH+V^V} - \left[\frac{\nu_{V_2O_5} M_{V_2O_5}}{\nu_{V^V} M_{V^V}}\right] C_{V^V}\right)} \quad \text{(Equation 3-13)}$$

Equation 3-13 relates the correction factor to the vanadium(V) concentration (C_{V^V}) in the post-extraction solution. The following equation shows the modified version of Equation 3-1 by which the extraction yields were calculated.

$$\gamma = \frac{\varepsilon V_{TMAH} C_{V^V}}{m_{ash} x_{V,ash}} \quad \text{(Equation 3-14)}$$

In order to simplify the calculations, a calibration line was generated as shown in Figure 3-59(b) from which the correction factors were calculated quickly and applied for the corresponding V^V concentrations measured by ICP-MS.

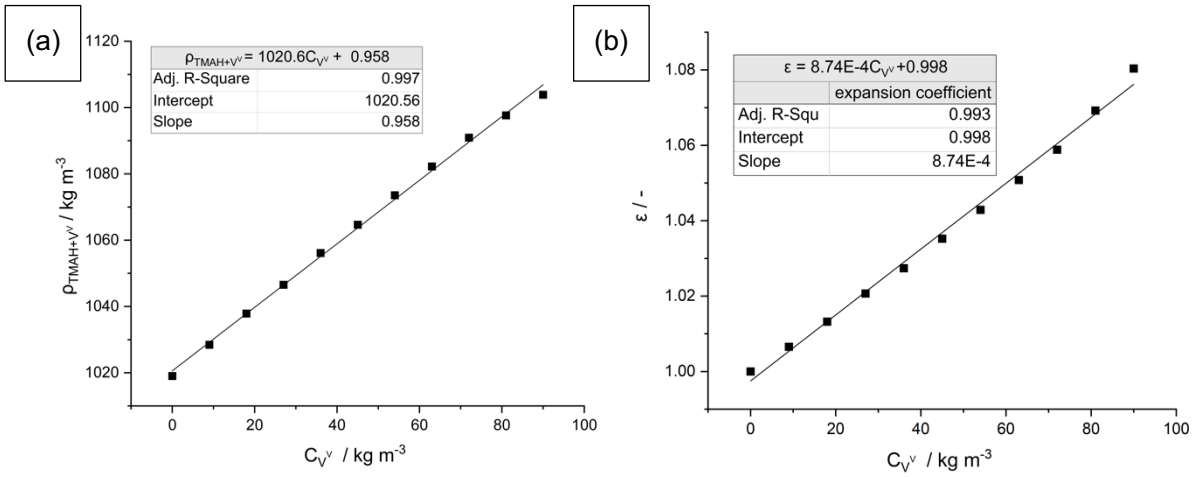


Figure 3-59. (a), left, Effects of V^V concentration on A: Density of TMA^+OH^- + V^V mixture, and (b), right, correction factor calibration line for TMA^+OH^- + V^V mixtures.

3.3.6 Kinetics study

3.3.6.1 Kinetic models

The leaching process data can be fitted to kinetic models, which are often utilised to elucidate the reaction kinetics for different limiting phenomena. The general equation used to describe the extraction kinetics of vanadium(V) is given by Equation 3-15 below.[152]

$$\frac{1}{3k_m}\gamma + \frac{R_0}{6D_e}\left[1 - 3(1-\gamma)^{\frac{2}{3}} + 2(1-\gamma)\right] + \frac{1}{k_r} \times \left[1 - (1-\gamma)^{\frac{1}{3}}\right] = kt = \frac{MC_0}{\sigma\rho R_0} \quad \text{(Equation 3-15)}$$

Where k_m represents the (solution phase) mass transfer coefficient, γ the vanadium(V) extraction yield, R_0 the (mean) radius of the vanadium bearing ash particles, D_e the mass transfer coefficient on the interface between the reactant and the product layer, k_r the reaction rate coefficient, M the vanadium molar mass, C_0 the initial concentration of the reactant at $t = 0$, σ the stoichiometric factor for TMA^+OH^-, ρ the density of the vanadium bearing ash particles and t the reaction time.

Equation 3-15 can be simplified under various rate-controlling conditions:

Model (A): The liquid boundary layer diffusion is the rate-controlling step:

$$\gamma = k_{bl}t \quad \text{(Equation 3-16)}$$

Model (B): The shrinking core model (SCM) is often used to explain the rate-controlling step when the leaching rate is limited to either the diffusion of reactant through a solid product layer, through the solution boundary, or the chemical reaction at the surface. Assuming that the particles are perfectly spherical, the chemical reaction is the rate-controlling step, the general kinetics equation may be simplified to Equation 3-17.

$$1 - (1 - \gamma)^{\frac{1}{3}} = k_r t \qquad \text{(Equation 3-17)}$$

Model (C): If the rate-controlling step is governed by the step of diffusion through the solid product layer covered the unreacted shrinking core, then Equation 3-18 is applied:

$$1 + 2(1 - \gamma) - 3(1 - \gamma)^{\frac{2}{3}} = k_d t \qquad \text{(Equation 3-18)}$$

When the chemical reaction is the rate-controlling step, a plot of Equation 3-17 against time is a straight line with gradient K_r. When diffusion through the product layer becomes rate-controlling, a plot of Equation 3-18 against time is a straight line with gradient K_d. The two aforementioned processes are used to describe leaching processes when only either chemical reaction or diffusion through the product layer is the rate-controlling step.

If interfacial transfer (phase transport from bulk solution to particle surface) and diffusion across the product layer both play a key role, another model is needed to account for both limitations. A fourth model which is the modified version of the shrinking core model was investigated in this work. This model was first proposed by Dickinson and Heal in around 2000.[153]

Model (D): The model assumed that the particles have a spherical shape with the initial and time-dependent radii of r_0 and r, respectively. The difference between the two radii is considered a:

$$r = r_0 - a \qquad \text{(Equation 3-19)}$$

An equation can be written to relate extraction yield to the particles' radii:

$$(1 - \gamma) = \frac{(4/3)\pi(r_0 - a)^3}{(4/3)\pi(r_0)^3} = \frac{(r_0 - a)^3}{(r_0)^3} \qquad \text{(Equation 3-20)}$$

Rearranging the above equation for a:

$$a = r_0\left(1 - (1 - \gamma)^{1/3}\right) \qquad \text{(Equation 3-21)}$$

And taking the first derivative of Equation 3-21 to account for an infinitely small change in a versus γ:

$$da = \frac{1}{3} r_0 (1-\gamma)^{-2/3} d\gamma \qquad \text{(Equation 3-22)}$$

For the leaching processes in which both interfacial transfer and diffusion across the product layer affect the reaction rate:

$$da/dt = DV_m 4\pi r^2 / L = kr^2/L \qquad \text{(Equation 3-23)}$$

Simplifying the above equation:

$$ada/r^2 = kdt \qquad \text{(Equation 3-24)}$$

Substituting Equation 3-19, Equation 3-21 and Equation 3-22 in Equation 3-24:

$$\frac{(1/3) r_0^2 (1-\gamma)^{-2/3} \left(1-(1-\gamma)^{1/3}\right) d\gamma}{r_0^2 (1-\gamma)^{2/3}} = kdt$$

$$\frac{1}{3}\left(1-(1-\gamma)^{\frac{1}{3}}\right)(1-\gamma)^{-4/3} d\gamma = kdt$$

$$\frac{1}{3}\left((1-\gamma)^{-4/3} - (1-\gamma)^{-1}\right) d\gamma = kdt$$

Integrating the above equation:

$$\frac{1}{3}\left[3(1-\gamma)^{-1/3} + \ln(1-\gamma) + \text{constant}\right] = kt$$

At time $t = 0$, $\gamma = 0$ so $\text{constant} = -3$, and:

$$\frac{1}{3}\ln(1-\gamma) + \left[(1-\gamma)^{-\frac{1}{3}} - 1\right] = kt \qquad \text{(Equation 3-25)}$$

The reaction rate coefficient, k, in the above equation can be expanded to account for any variables affecting the kinetics of extraction. The variables in this project included temperature, tetramethylammonium hydroxide concentration, sodium chlorite (oxidant) concentration and liquid-to-solid ratio. Equation 3-26 shows an expanded rate coefficient to account for the effect of these variables A similar approach has been used previously to account for the parameters affecting the reaction kinetics.[90,154-156]

$$k = k_0 [TMAH]^a [NaClO_2]^b \left[\frac{L}{S}\right]^c e^{\frac{-E_a}{RT}} \qquad \text{(Equation 3-26)}$$

Where k_0 represents the reaction rate coefficient; a, b, c the reaction order with respect to the solvent concentration, oxidant concentration and liquid to solid ratio, respectively. E_a represents the activation energy (J mol^{-1} K^{-1}), R the universal gas constant (J mol^{-1} k^{-1}) and T the reaction temperature (K).

Taking the logarithm of Equation 3-26:

$$\ln(k) = a\ln([TMAH]) + b\ln([NaClO_2]) + c\ln\left(\frac{L}{S}\right) + \frac{-E_a}{RT} + \text{constant} \qquad \text{(Equation 3-27)}$$

For a single variable system described by Equation 3-27, a log plot of the variables versus the corresponding reaction rate coefficients for any three points (within the studied range) should give a straight line with a gradient equal to the reaction order. Equation 3-27 together with the experimental data were used to determine empirically the unknown parameters in Equation 3-26.

3.3.6.2 Effect of temperature

Figure 3-60 shows the effect of the leaching temperature on the vanadium(V) extraction yield versus time for (a) without and (b) with the oxidising agent $NaClO_2$ added to the solution. The reaction conditions were: 550 rpm agitation speed, 10 cm^3 g^{-1} liquid-to-solid ratio, and the initial TMA^+OH^- concentration of 2.78 mol dm^{-3}. The maximum acceptable experimental error was set to be 3 %; any individual experiments having errors greater than this set value were repeated until the errors were within the acceptable range. In all cases, the filtered leach liquor was colourless, which is characteristic of the vanadium(V) oxyanion, VO_4^{3-}. The specific gravity of the gasifier ash was determined to be 2.38 (with respect to water), so no floated particles were noticed on the leaching solution surface. It was observed that the vanadium(V) extraction yields for both cases were related strongly to the leaching temperature. As expected, the leaching experiments without the oxidizing agent never reached the limiting extraction yield of vanadium(V), whereas once $NaClO_2$ was introduced to the system, the limiting yield was achieved in ca. 300 min reaction time at 90 °C. The extraction yields for the reaction temperatures of 70 °C and 80 °C reached close to the limiting extraction yield in approximately one day of leaching time (1440 min).

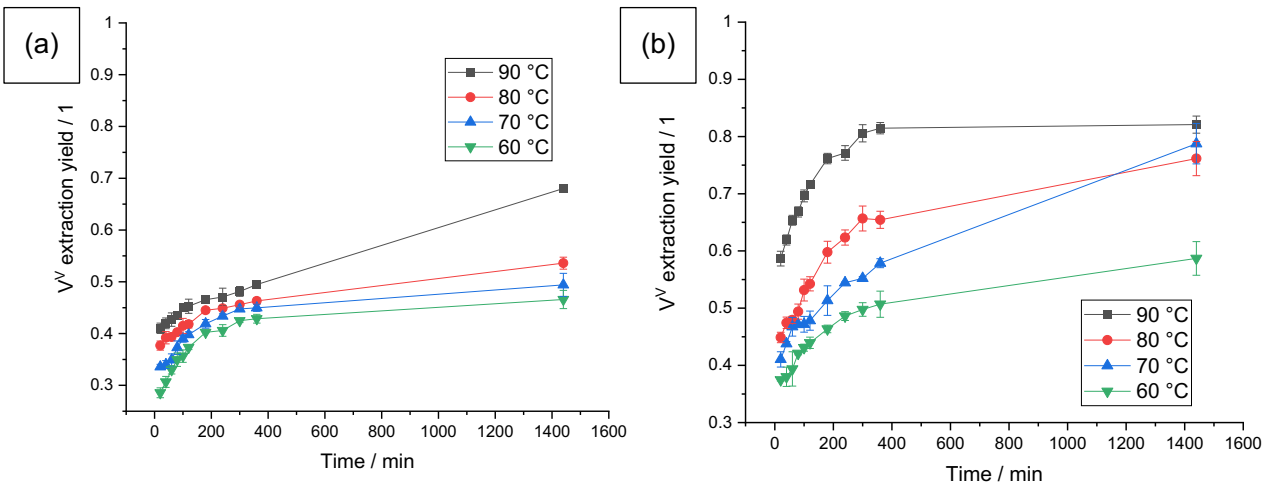


Figure 3-60. Effect of leaching temperature on time dependences of vanadium(V) extraction yields (a), left, as-received. (b), right in 0.221 mol dm^{-3} $NaClO_2$; 550 rpm, 10 cm^3 g^{-1}, 90 °C reaction temperature and 2.78 mol dm^{-3} TMA^+OH^- concentration.

Figure 3-61(a) and (b) show the fitted kinetics data from Figure 3-60(a) and (b), respectively. It is evident that Model (A), which was the simple boundary layer diffusion model, had the worst average fit to the experimental data, both with and without $NaClO_2$. For Models (B) and (C), even though the shrinking core model for diffusion through a product layer demonstrated greater conformity to the experimental data compared to the diffusion of reactant through the solution boundary layer model. However, the R^2 for both models were below 0.97, regardless of whether the leaching experiments were conducted under the oxidative leaching environment or not. The fitted kinetics data in Equation 3-25 (Model D) showed the best fit with $R^2 > 0.98$ for the case of oxidative leaching, whereas the fitted kinetics data from the non-oxidative leaching experiments had a relatively poor fit with $R^2 \approx 0.93$ in the same model.

Interestingly, although the extractable mixed vanadium oxides fraction of the gasifier ash contained 13.7 % V^{IV} and 69.3 % V^V, a V^V extraction yield close to the latter was achieved in ca. 1440 min under a non-oxidative leaching environment, whereas the limiting extraction yield (= total extractable mixed vanadium oxide) was achieved in 300 min by oxidative leaching at 90 °C. This implies that under the non-oxidative leaching environment, the vanadium(IV) network inhibited the access of the (TMA^+) OH^- ions to vanadium(V) sites.

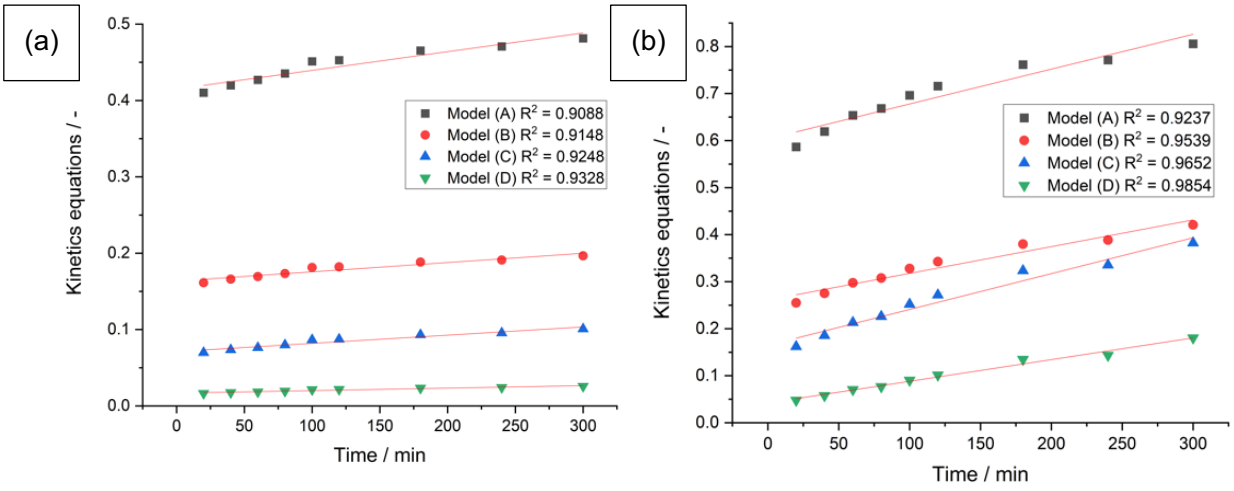


Figure 3-61. Time dependences of vanadium extraction yields fitted by the four kinetics equations in Model (A) to (D) for (a), left, as-received and (b), right, oxidatively, in 0.221 mol dm^{-3} $NaOCl_2$; 550 rpm, 10 cm^3 g^{-1}, 90 °C reaction temperature and 2.78 mol dm^{-3} TMA^+OH^- concentration.

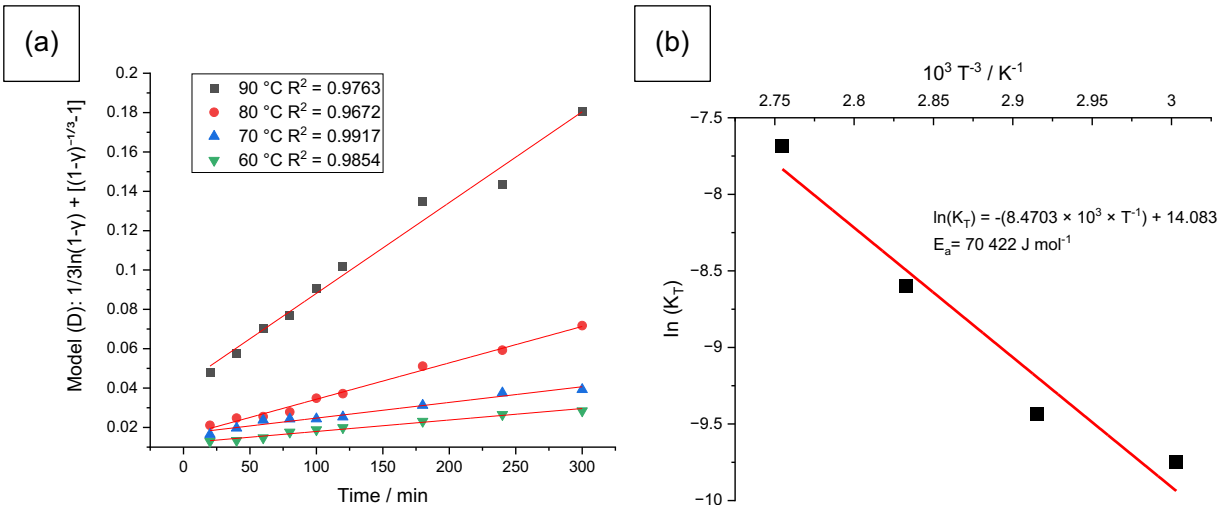


Figure 3-62. (a), left, Time dependences of vanadium(V) extraction yields fitted by Model (D), and (b), right Arrhenius plot for activation energy determination.

From the fitted data in Figure 3-61(a) and the explanation in the above paragraph, it can be concluded that the extraction mechanism for the non-oxidative leaching was likely to be a combination of different processes. For example, a fast dissolution of V_2O_5 via Model (B), followed by the diffusion of the TMA^+OH^- through $M_xV_2O_5$ aggregates to extract V^V, which could be explained by Model (C) and ultimately rather slow oxidation of the low valence vanadium by presumably the only available oxidant

source, dissolved oxygen over a very extensive period. Therefore, the non-oxidative leaching kinetics of vanadium(V) from the gasifier ash was not studied further in this chapter.

Table 3-6. Square of correlation coefficients of four kinetic models at four leaching temperatures in 0.221 mol dm^{-3} $NaOCl_2$; 550 rpm, 10 cm^3 g^{-1}, and 2.78 mol dm^{-3} TMA^+OH^- concentration.

	Kinetic equation			
Leaching Temperature / °C	**Model (A)** **Equation** 3-16	**Model (B)** **Equation** 3-17	**Model (C)** **Equation** 3-18	**Model (D)** **Equation** 3-25
90	0.9237	0.9539	0.9652	0.9854
80	0.9757	0.9843	0.9897	0.9917
70	0.9346	0.9452	0.9584	0.9673
60	0.9449	0.9534	0.9672	0.9763
Average	0.9447	0.9592	0.9701	0.9802

Table 3-6 lists the square of correlation coefficients (R^2) obtained from fitting Figure 3-60B data in the four models vs. temperature. It can be seen from the R^2 values that Equation 3-25 fitted the kinetic data better than the rest of the three models across all the temperatures studied, especially at higher temperatures. Hence, Equation 3-25/Model (D) was selected to describe the reaction mechanism of vanadium(V) dissolution from the gasifier ash, as well as to establish a model to predict extraction yields based on the reaction conditions.

Each set of data presented in Figure 3-62(a), has a gradient that is equal to the reaction rate constant k_T for the corresponding temperature. Figure 3-62(b) shows the Arrhenius correlation plot for the measured k_T values versus the studied temperatures. The Arrhenius correlation was indeed obeyed and the apparent activation energy, E_a, for the extraction of vanadium(V) from the gasifier ash was 70.4 kJ mol^{-1}. It should be noted that the calculated apparent activation energy (70.4 kJ mol^{-1}) is based on the

overall reaction and is not taking into account other various reaction mechanisms. For instance, it is evident from Figure 3-60 (b) that there is a significant dissolution of vanadium at early stage, i.e., first 30 minutes, followed by a slower dissolution at later stages. This is comparable with the results reported by Amer[157] who studied hydrometallurgical dissolution of vanadium from Egyptian black shale. It was proposed that the vanadium dissolution was initially controlled by the surface chemical reaction at the early stages followed by the diffusion of the materials through a product layer in the later to final stages of leaching. Teimouri et al.,[158] studied oxidative dissolution kinetics of pyrite in nitric acid solution. They reported that the mixed-controlled kinetics model describing both interfacial transfer and diffusion through product layer governed the dissolution kinetics. The activation energy was reported to be 44.3 kJ mol^{-1}. Liu et al.,[92] used $NaNO_3$ in highly alkaline solutions to treat vanadium-bearing slags. Their methodology was very similar to the approach used in this work because low valence vanadium compounds were oxidatively leached in highly alkaline solutions. They reported that 93.7 % of vanadium was extracted and the apparent activation energy was 105.5 kJ mol^{-1}, with the reaction being controlled by mass transfer in the product layer. It is quoted frequently in the literature that activation energy is an indicator for determination of the limiting step. For a diffusion-controlled solid-liquid process $\mathrm{E_a} < 20$ kJ mol^{-1}, whilst that of processes limited by other means i.e. falls between $40 < \mathrm{E_a} < 100$ kJ mol^{-1}.[159] The experimentally obtained apparent activation energy falls well in the middle of the latter case, confirming the reaction was unlikely to be solely a diffusion-controlled process. If the reaction was homogenous, the anodic and cathodic reactions were occurred almost instantly due to the fast electron transfer nature of such processes in aqueous medium. However, the heterogenous oxidative dissolution of vanadium(IV) from the gasifier ash involved the formation of an intermediate followed by the dissolution reaction at a reaction layer as shown in Figure 3-64. Hence, the rate determining step in the dissolution kinetics is the charge transfer across the solid-liquid interface.

Both the fit of the experimental data in Model (D) and the relatively high activation energy shows that the reaction was governed by the mixed-controlled kinetics model accounting for both the interfacial transfer and the diffusion of materials across the product layer. With the apparent activation energy known, Equation 3-26 can be written as:

$$k = k_0[TMAH]^a\,[NaClO_2]^b\left[\frac{L}{S}\right]^c e^{\frac{-70\,422}{RT}} \qquad \text{(Equation 3-28)}$$

3.3.6.3 Oxidative dissolution mechanism

The oxidative dissolution of vanadium(IV) is an electrochemical reaction that consists of cathodic and anodic reactions. The anodic dissolution of vanadium(IV) and the cathodic reduction of the oxidant, in this case sodium chlorite, take place simultaneously on the gasifier ash particle surface. The driving force for the reaction to happen is the difference in potential across the vanadium-bearing particle-solution interface.

As explained in the previous section, dissolution of vanadium(V) using TMA^+OH^- involved a combination of different mechanisms. Initially, fast dissolution of vanadium(V) particles governed by the surface chemical reaction. Then, Model (D) which is schematically shown in Figure 3-64 became the dominant mechanism where vanadium, oxidatively and non-oxidatively was leached out. In reality, during oxidative dissolution of vanadium(IV), V_2O_5 intermediate might not be merely formed at particle scale and instead other vanadium(V) intermediates might have formed, depending on the local pH. Nevertheless, the steps involved in the dissolution of both low and high oxidation state vanadium oxides in the gasifier ash include the following sequential steps: (1) bulk liquid transfer of reactants to the liquid-solid boundary layer (2) interfacial transfer of ionic liquid and oxidant (3) diffusion of reactants through a shrinking core particle where oxidative dissolution of vanadium(IV) and non-oxidative dissolution of vanadium(V) will take place at a reaction layer(4) the products and the unreacted fluid diffuse through the ash layer (5) transport of the products to the liquid-phase diffusion layer (6) fast transport of the products to the bulk liquid.

Figure 3-63 shows the SEM image of the residue at different magnifications. The wider picture reveals that the residue contained porous particles when compared to the pristine gasifier ash shown in Figure 3-65. The time-dependent concentration of the elements was also investigated and is shown from Figure 3-66 to Figure 3-68. It can be observed that the density of nickel and iron increased as the reaction time increased. The distribution of vanadium became more uniform across the sample as we transitioned from the pristine state Figure 3-65) to the equilibrium extraction yield (Figure 3-68), confirming the existence of unextractable nickel-vanadium compounds. The uniform distribution of iron, along with nickel and vanadium, may imply the

presence of iron-nickel-vanadium compounds in the residue; however, such a phase was not detected in the XRD diagram shown in Figure 3-57(b). The optical images confirmed the presence of a remaining product layer when the reaction reached the equilibrium extraction yield.

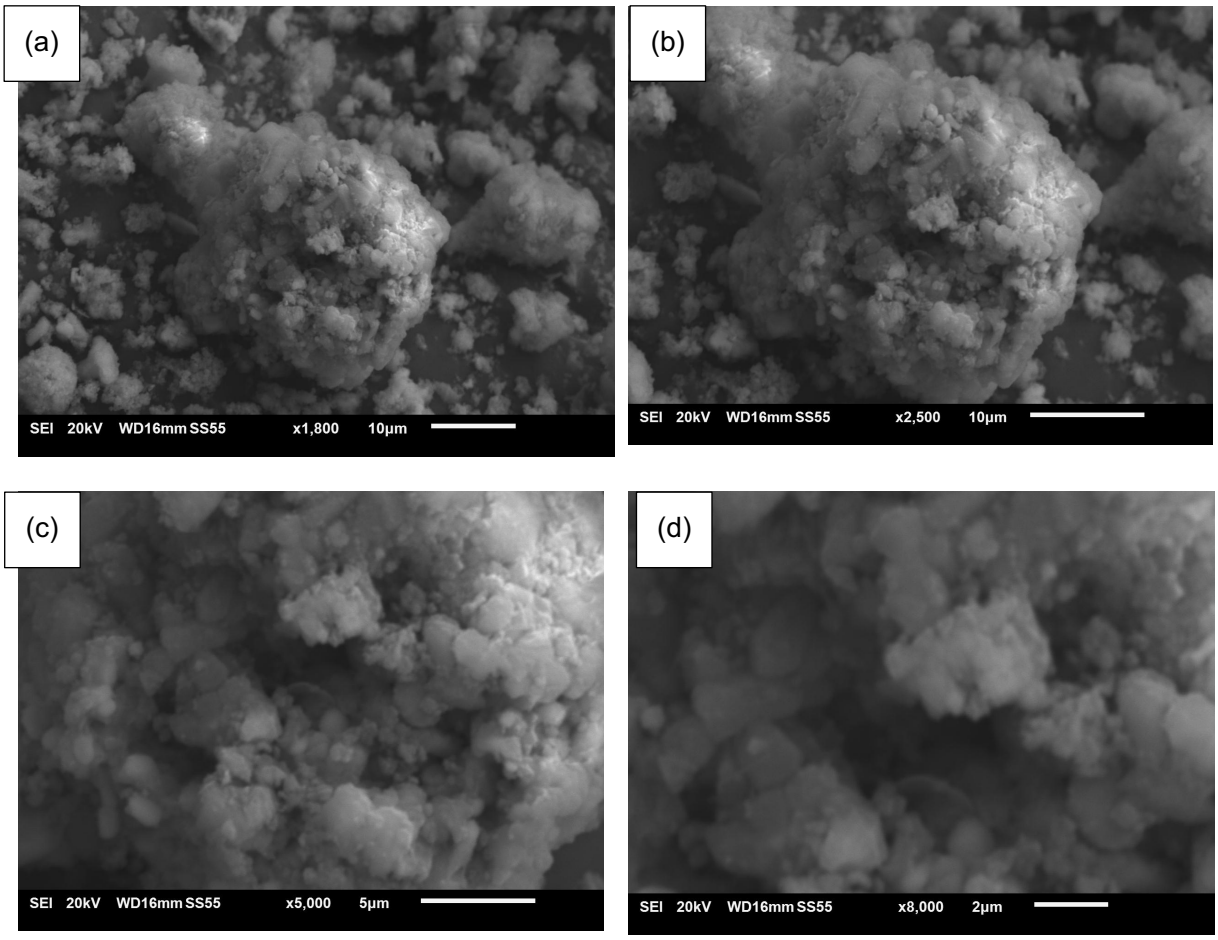


Figure 3-63. SEM images of the residue at the following reaction condition: in 0.221 mol dm^{-3} $NaOCl_2$; 550 rpm, 10 cm^3 g^{-1}, 90 °C reaction temperature and 2.78 mol dm^{-3} TMA^+OH^- concentration and 300 min reaction time. (a)1800x (b) 2500 x, (c)5000 and (d) 8000x magnifications.

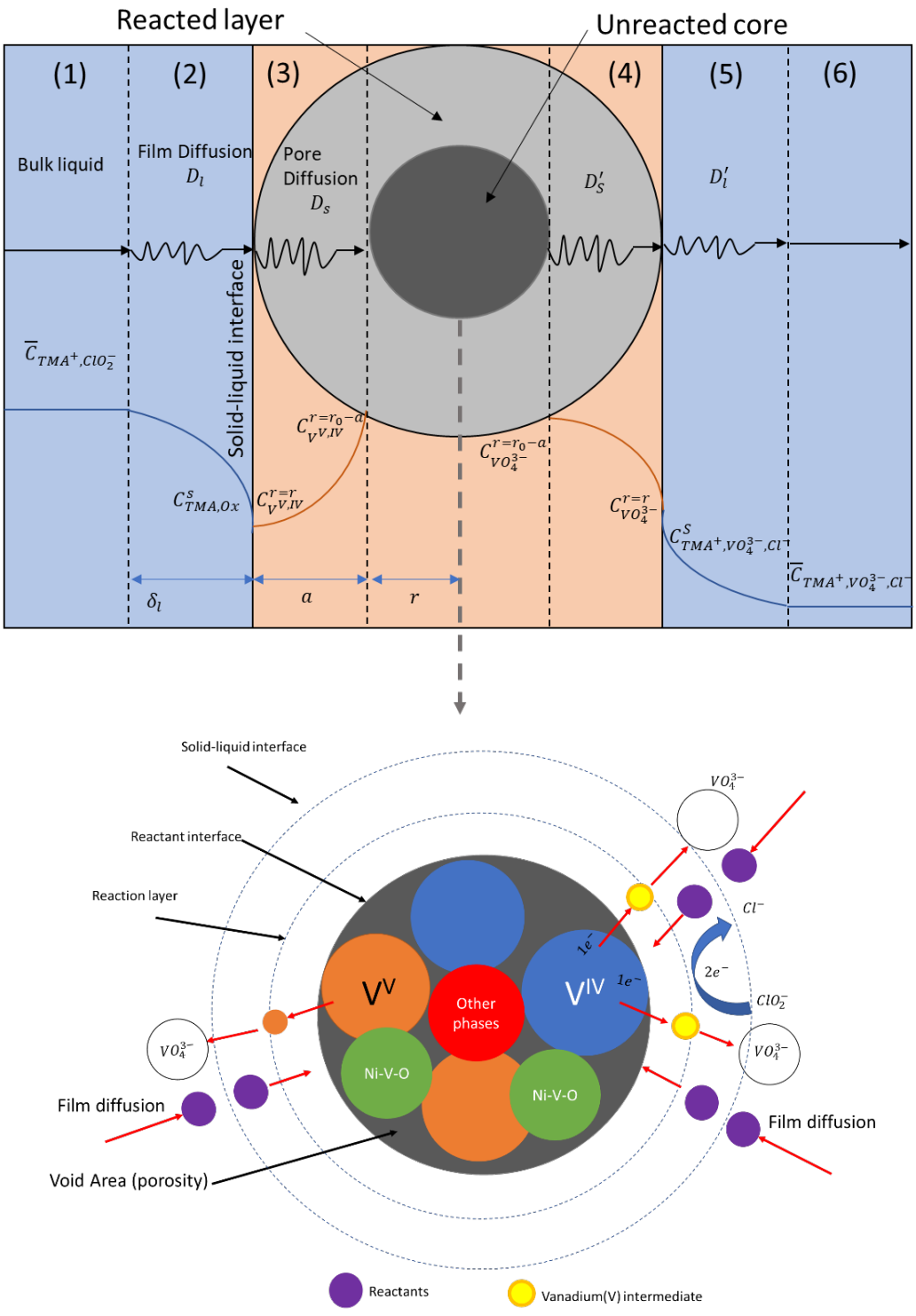


Figure 3-64. Schematic diagram of Model (D). The reaction is affected by both interface transfer and diffusion across product layer.

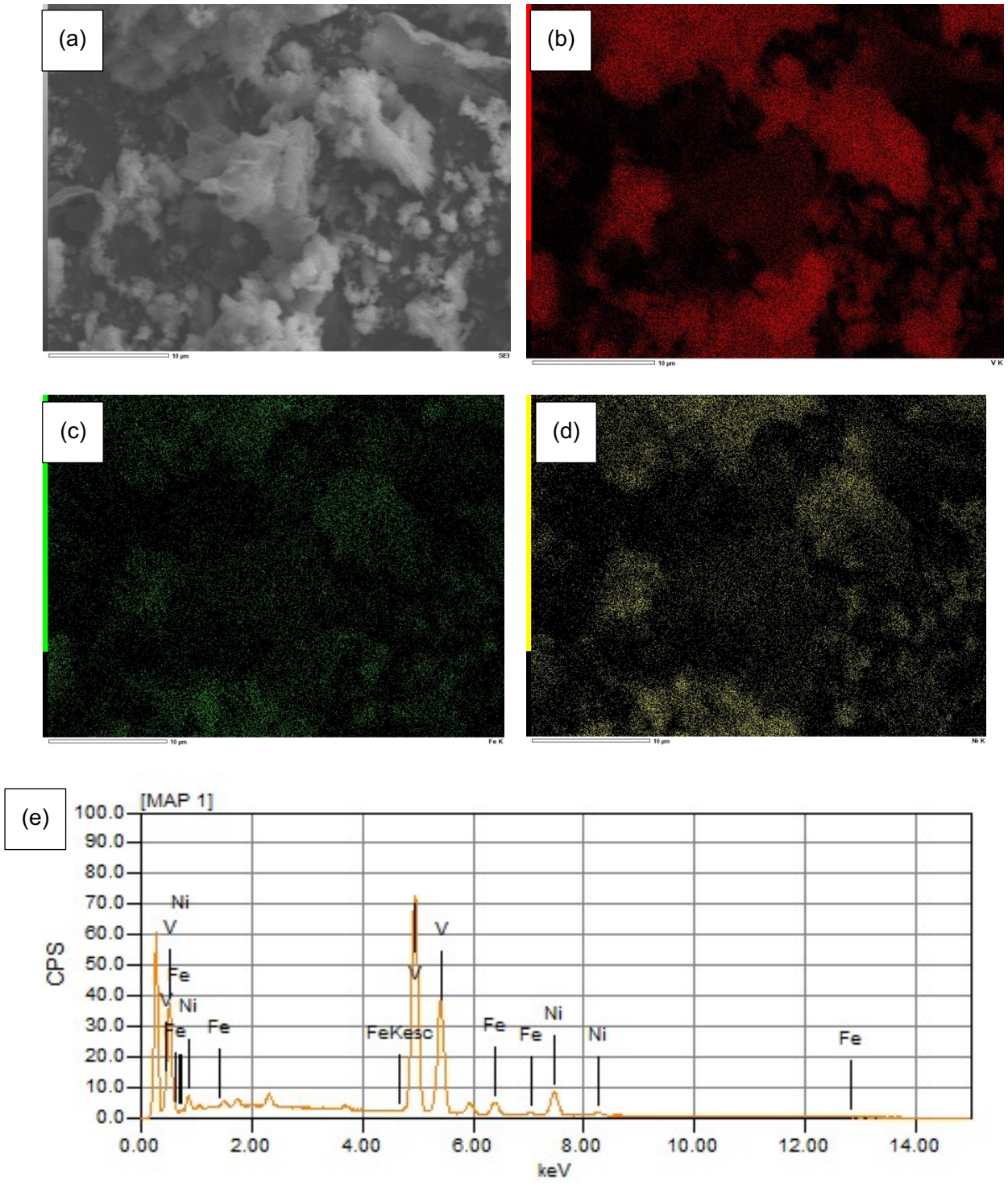


Figure 3-65. (a) SEM image of the pristine ash (b) vanadium distribution (c) Iron distribution (d) Nickel distribution and (e) the EDS spectra of CPS.

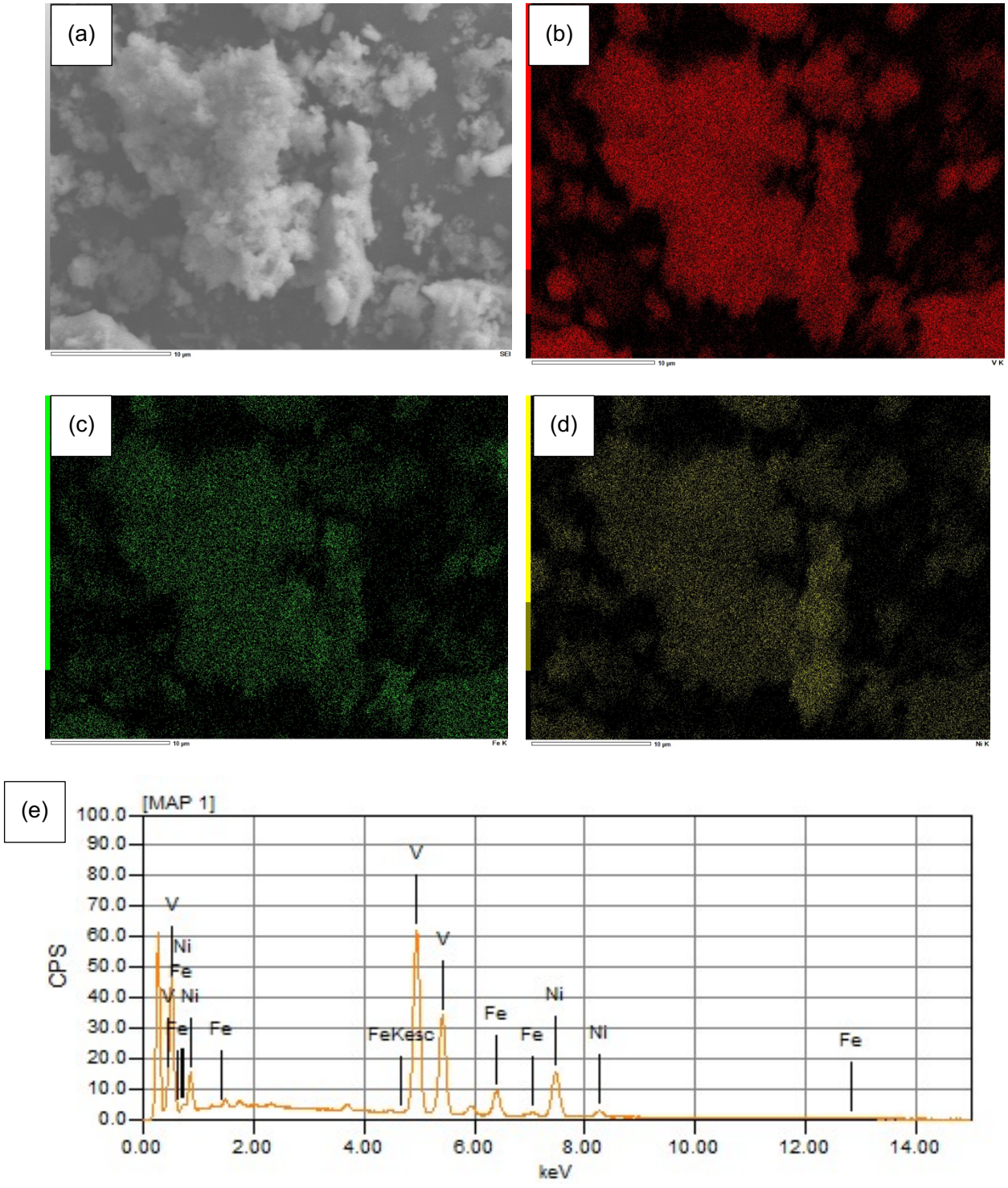


Figure 3-66. (a) SEM image of the gasifier ash after 15 min oxidative leaching (b) vanadium distribution (c) Iron distribution (d) Nickel distribution and (e) the EDS spectra of CPS.

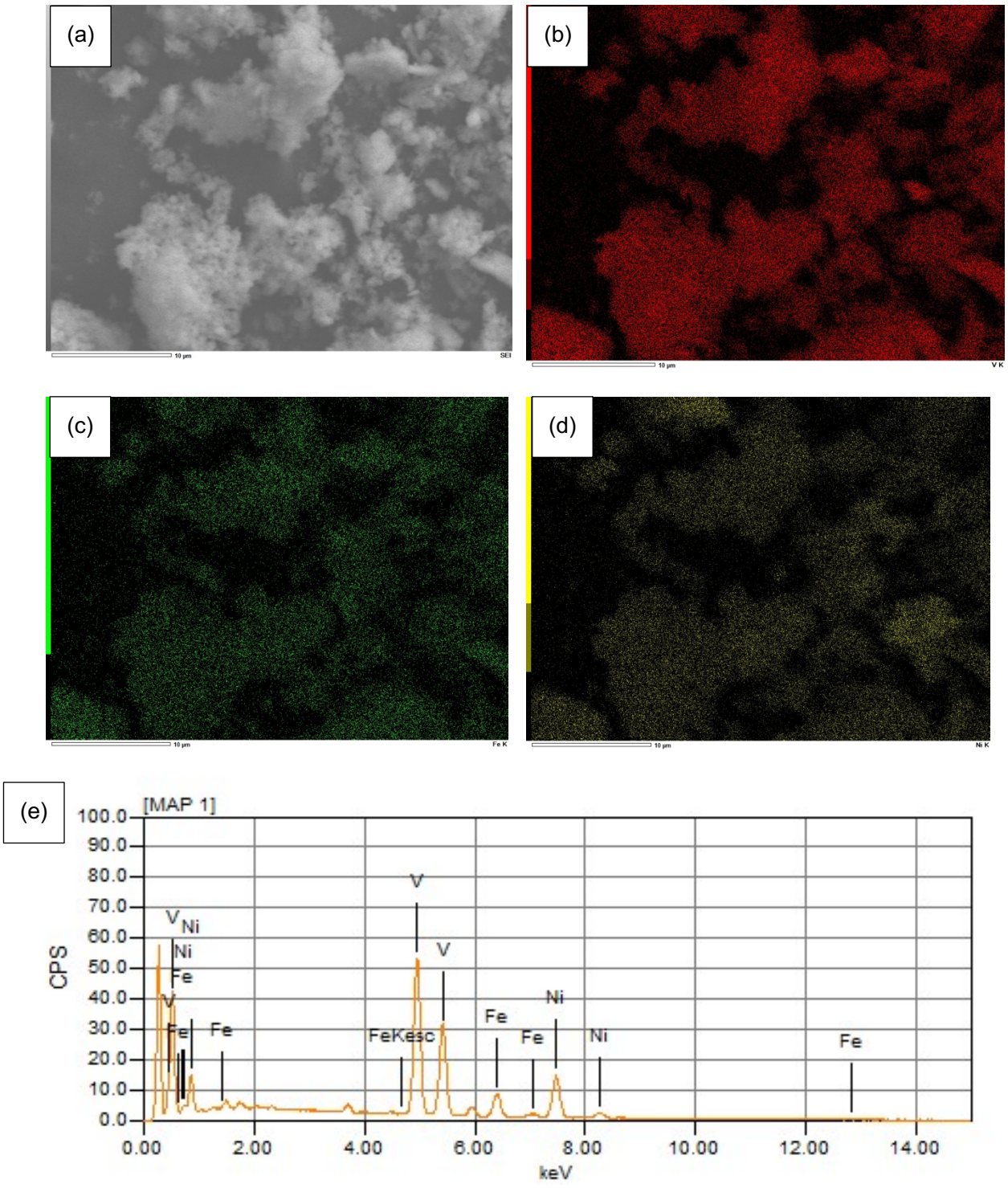


Figure 3-67. (a) SEM image of the gasifier ash after 30 min oxidative leaching (b) vanadium distribution (c) Iron distribution (d) Nickel distribution and (e) the EDS spectra of CPS.

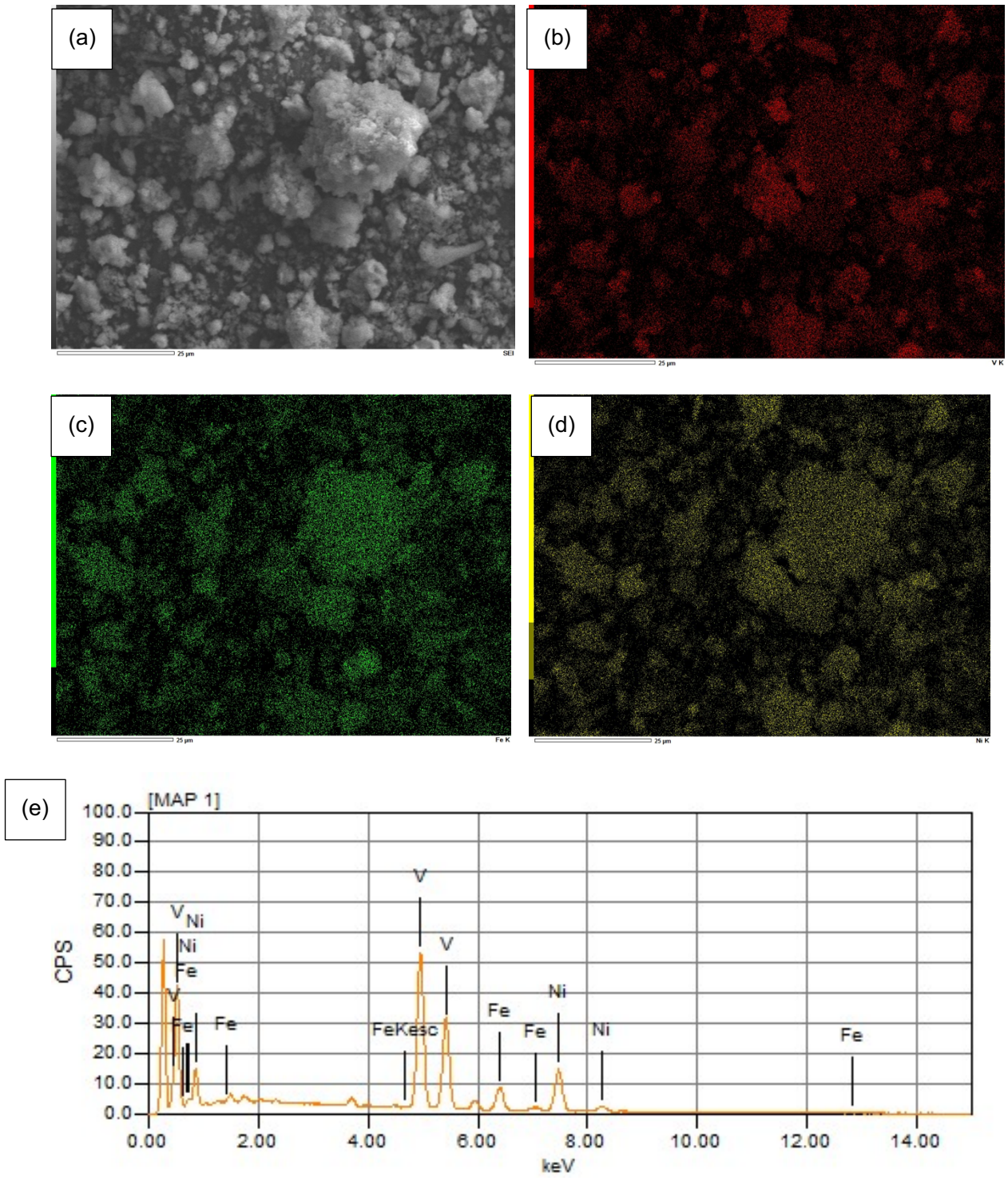


Figure 3-68. (a) SEM image of the gasifier ash after 300 min oxidative leaching (b) vanadium distribution (c) Iron distribution (d) Nickel distribution and (e) the EDS spectra of CPS.

3.3.6.4 Effect of TMA^+OH^- concentration

Figure 3-69(a) shows the effect of tetramethylammonium hydroxide concentration on the vanadium(V) extraction yield from the gasifier ash at 90 °C in the presence of 0.221 mol dm^{-3} $NaClO_2$. There was a strong relationship between the extraction yield and the solvent concentration; as the TMA^+OH^- concentration increased, the vanadium extraction yield increased, reaching the limiting extraction yield of vanadium(V) at ca. 300 min. Decreasing the concentration of the solvent decreased the number of available TMA^+ cations, and hence the frequency of collisions to the solid V^V in the ash. Moreover, the lesser the solvent concentration, the lesser the diffusion coefficient across the interface which ultimately resulted in a lower extraction yield.

The 1440 min vanadium(V) extraction was performed to identify the limiting extraction yield for oxidative leaching. It evident from Figure 3-69(a) that for any TMA^+OH^- concentrations less than 2.78 mol dm^{-3}, the limiting extraction yield was not achieved. From a process industrialisation point of view, a techno-economic assessment should be performed using an extensive set of data to optimise the solvent concentration versus extraction yield, extraction time and solvent recovery operating costs.

Figure 3-69(b) shows the fitted kinetics data in Model (D) for the different TMA^+OH^- concentrations. The gradient of each line corresponds to the solvent concentration rate coefficient (k_C). The gradient of each line was utilised to construct Figure 3-69(c), from which the value of a was calculated empirically to be 1.819. The relatively large positive reaction order indicates a strong dependence of the reaction kinetics on TMA^+OH^- concentrations. With the solvent concentration reaction order known, Equation 3-28 was revised as:

$$k = k_0[TMAH]^{1.819}\,[NaClO_2]^b \left[\frac{L}{S}\right]^c e^{\frac{-70\,422}{RT}} \qquad \text{(Equation 3-29)}$$

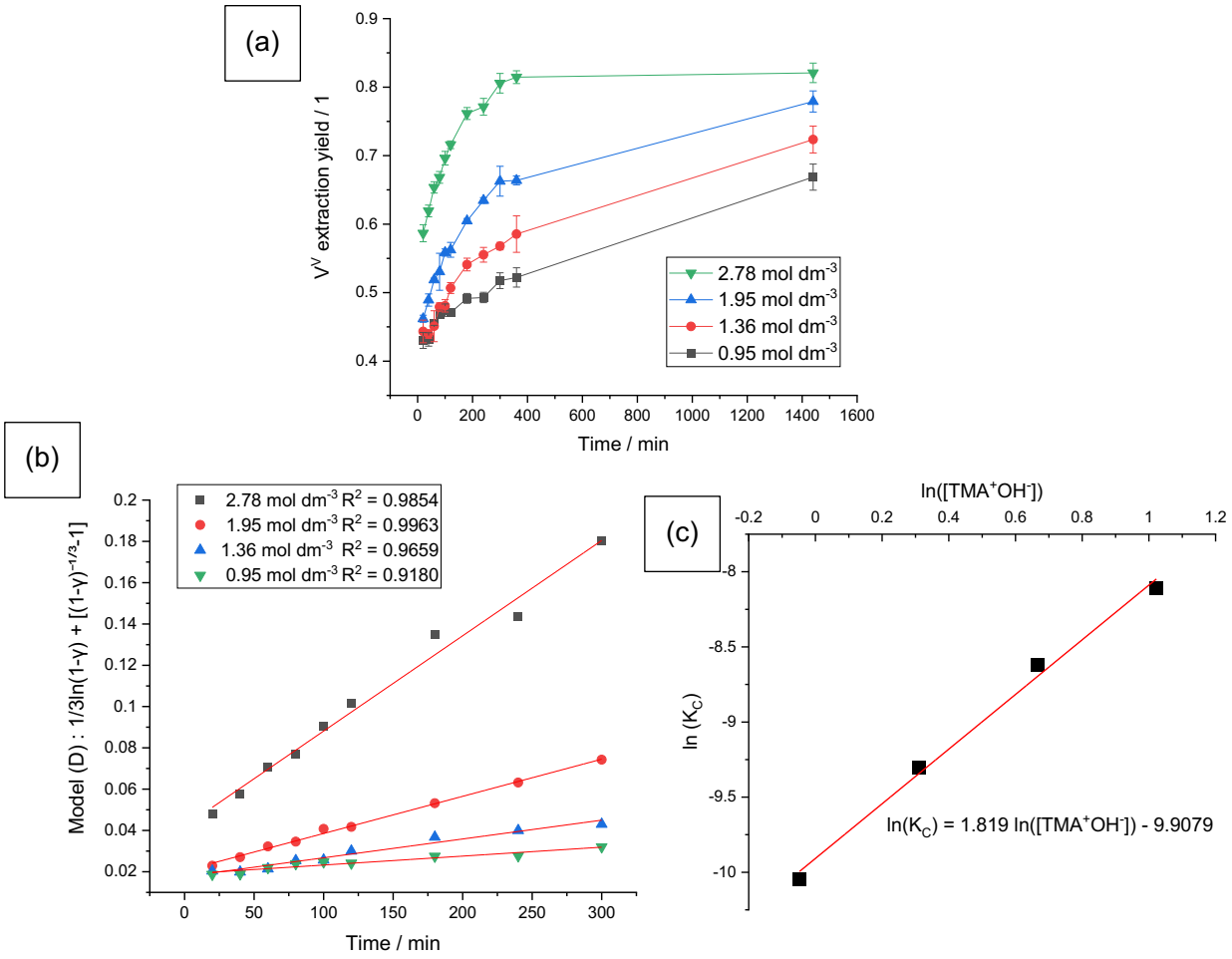


Figure 3-69. (a) top, Time dependence of vanadium(V) extraction yield for four different TMA^+OH^- concentrations. (b) bottom left, Data fitted for Model (D). (c) bottom right, Plot of K_C versus TMA^+OH^- concentration; 550 rpm, 10 $cm^3\ g^{-1}$, 0.221 mol dm^{-3} $NaClO_2$ and 90 °C reaction temperature.

3.3.6.5 Effect of oxidant ($NaClO_2$) concentration

Figure 3-70(a) shows the effect of increasing sodium chlorite concentration on increasing the extraction kinetics of vanadium(V). All oxidant concentrations studied eventually resulted in the limiting vanadium(V) yields, at least before 1440 min (1 day) of leaching time. Figure 3-70(b) shows the kinetic data fit to Model (D). The gradient of each line corresponds to the oxidising agent rate coefficient (k_0). These parameters were used to construct Figure 3-70(c) which enables determination of the reaction order with respect to the oxidising agent concentration, which was found to be 0.340, indicating a weak dependence of the reaction kinetics on $NaClO_2$ concentration. As

mentioned earlier, the reaction kinetics were limited by the interfacial transfer and diffusion of materials across the product layer, so limiting the effect of oxidant concentration.

With the reaction order with respect to oxidant concentration known, Equation 3-29 can be further extended:

$$k = k_0[TMAH]^{1.819}\,[NaClO_2]^{0.340}\left[\frac{L}{S}\right]^{c} e^{\frac{-70\,422}{RT}} \qquad \text{(Equation 3-30)}$$

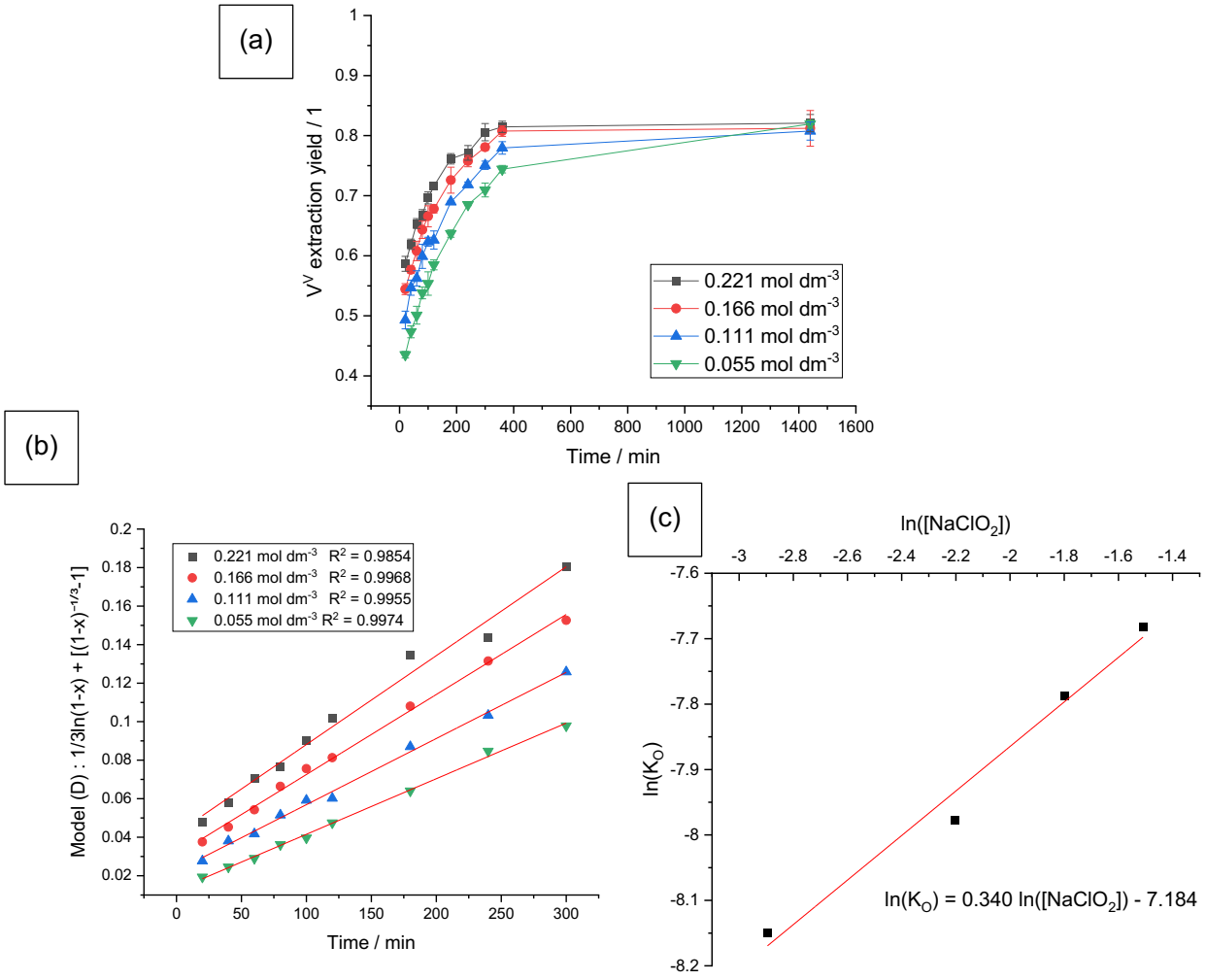


Figure 3-70 A: Time dependence of vanadium(V) extraction yield for four different $NaClO_2$ concentrations; B: Data fitted by Model (D.); C: log plot of effect of oxidant concentration on rate coefficient ; 550 rpm, 10 cm^3 g^{-1}, and 2.78 mol dm^{-3} TMA^+OH^- concentration.

3.3.6.6 Effect of liquid-to-solid ratio

Figure 3-71(a) shows the liquid-to-solid ratio/suspension density effect on the kinetics of vanadium(V) extraction, which increased with the liquid-to-solid ratio. Decreasing the solid-to-liquid ratio to values such as 7.5 cm^3 g^{-1} and 5 cm^3 g^{-1} resulted in slower reaction kinetics, but nonetheless the limiting extraction yield of vanadium(V) was achieved within ca. 1440 min (1 day) of leaching.

Figure 3-71(b) shows the kinetic data fit to Model (D). The gradient of each line corresponds to the L/S rate coefficient ($k_{L/S}$), values of which were used to construct

Figure 3-71(c) from which the reaction order with respect to the slurry density was determined to be 0.833, indicating a mild dependence. It was observed that the extraction kinetics behaviour for the liquid-to-solid ratio of 12.5 cm^3 g^{-1} was almost identical to that of 10 cm^3 g^{-1} as shown in Figure A9-2 in the appendix. This indicated that the reaction was limited by intraparticle diffusion over external diffusion through the particle interface; thus, the dataset was eliminated from the kinetics study.

With the slurry density reaction order known, Equation 3-30 was further extended to the following equation:

$$k = k_0[TMAH]^{1.819}\,[NaClO_2]^{0.340}\left[\frac{L}{S}\right]^{0.833} e^{\frac{-70\,422}{RT}} \qquad \text{(Equation 3-31)}$$

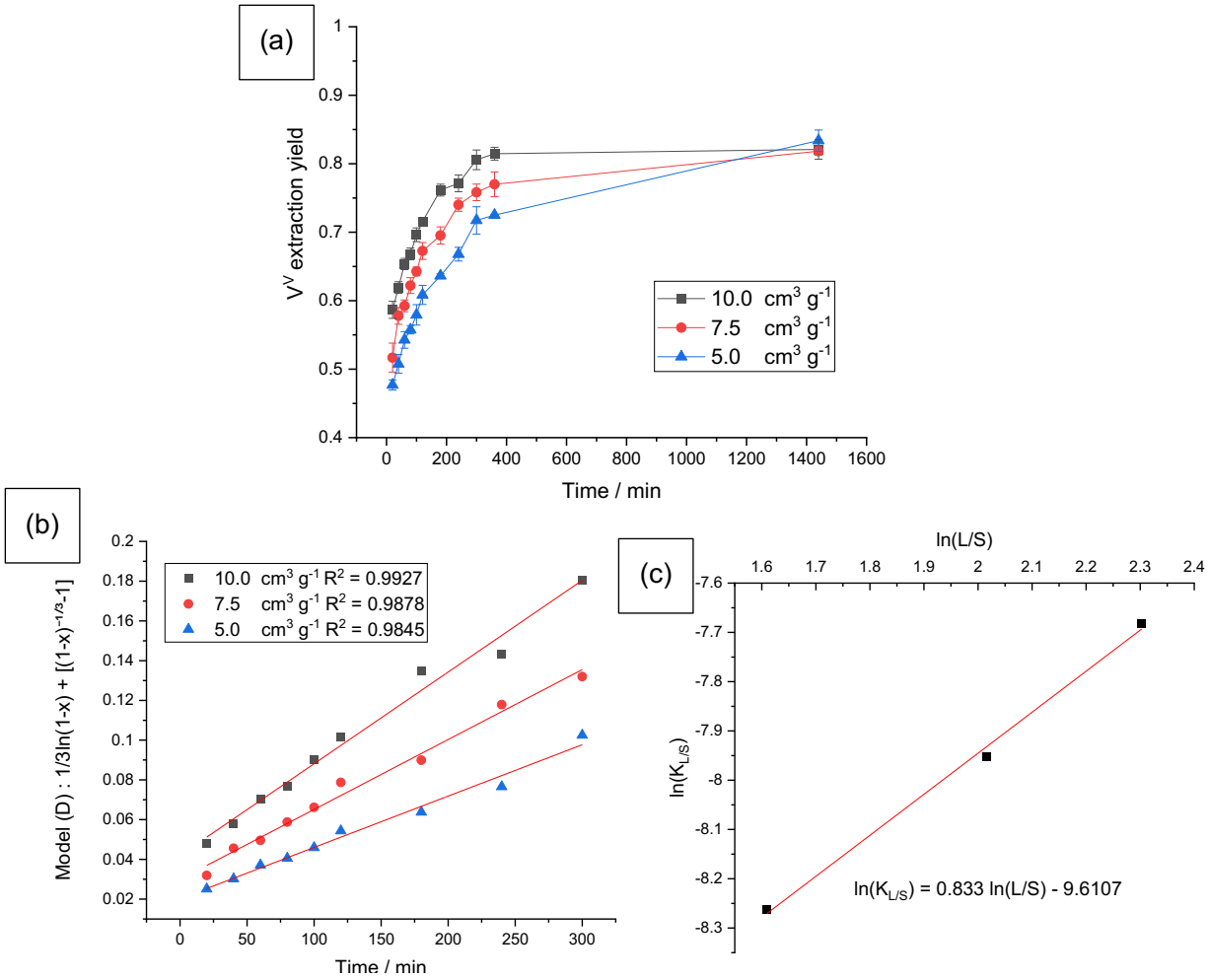


Figure 3-71. (a) top, Time dependences of vanadium(V) extraction yields for three different liquid-to-solid ratios. (b), bottom left, Kinetic data fitted to Model (D), and (c) bottom right, log plot of the rate coefficient and the liquid-to-solid ratio; 550 rpm, 0.221 mol dm^{-3} $NaClO_2$ and 2.78 mol dm^{-3} TMA^+OH^- concentration.

3.3.6.7 Complete model

The constant (k_0) in Equation 3-31 was evaluated from the intercepts of the log plots and found to be equal to 2.9 × 10^5 mol$^{-2.159}$ dm$^{5.992}$ g$^{-0.833}$ s^{-1} The complete model, Equation 3-32, shows a semi-empirical mathematical model by which the extraction yield can be predicted from the gasifier ash in TMA^+OH^- solution. The model had acceptable accuracy for prediction of the extraction kinetics of vanadium(V) at the upper range limit of the variables i.e., higher temperatures and/or time (see Table A1 in the appendices). The accuracy of the model decreased for shorter reaction periods, presumably because there was a sharp extraction yield due to the simple dissolution

of vanadium pentoxide at the very beginning of the reaction which could be explained by the shrinking particle model.

$$\frac{1}{3}\ln(1-\gamma) + [(1-\gamma)^{-\frac{1}{3}} - 1] =$$

$$2.9 \times 10^5\ [\mathrm{TMAH}]^{1.819}\ [\mathrm{NaClO_2}]^{0.340} \left[\frac{\mathrm{L}}{\mathrm{S}}\right]^{0.833} e^{\frac{-70\,422}{\mathrm{RT}}} t \quad \text{(Equation 3-32)}$$

3.4 Conclusions

In this chapter, oxidative and non-oxidative leaching of vanadium oxides was investigated from real gasifier ash using tetramethylammonium hydroxide solutions, with and without an oxidant. For the study to be applicable to other vanadium-bearing feedstocks, a series of control experiments were conducted to establish the effects of common concomitant cations on the precipitation behaviours of vanadium salts in the presence of the TMA^+ cations. The control experiments enabled identification of the non-extractable vanadium phases, as well as insoluble materials. Aluminium(III) and silicon(IV) which are the most abundant elements on Earth, did not show chemical interaction with TMA^+ cations, unlike Na^+ at high pH, potentially solving one of the biggest challenges for the hydrometallurgical extraction of vanadium(V) from vanadium-bearing materials.

A systematic error was discovered in the calculation of vanadium(V) recovery yield. It was revealed that the volume of the post-reaction solution was a function of the dissolved species and therefore, the final extraction yield was corrected using a fudge factor.

The combination of various techniques revealed that 17 % and 83 % of the vanadium oxides in the gasifier ash were an unextractable Ni-V-O phase and extractable mixed vanadium oxides, respectively. The mixed vanadium oxide phases(s) in the latter consisted of 69.3 % V^V and 13.7 % V^{IV} in the form of V_2O_5 + $M_xV_2O_5$ with M being a concomitant cation. The limiting equilibrium extraction yield of vanadium(V) was determined to be equal to the mass ratio of the extractable mixed vanadium oxides in the gasifier ash.

The existence of the low oxidation state vanadium phases in the gasifier ash required the use of an oxidant, for which sodium chlorite was chosen to create an oxidative leaching environment to extract vanadium(V) in the form of vanadium(V) oxyanions.

The extraction kinetics data showed that reaction rates were controlled by both the transfer of materials across the interface and the diffusion through a product layer, meaning the V^{IV} oxidation reaction was unlikely to be the limiting step.

The activation energy, calculated as 70.4 kJ mol^{-1} implied that the reaction kinetics were unlikely to be limited solely by the diffusion through the product layer. The heterogenous oxidative dissolution of vanadium(IV) from the gasifier ash involved the formation of an intermediate followed by the dissolution reaction at a reaction layer as shown in Figure 3-64. This confirms that Model (D) was the most suitable model to fit the experimental data, to account for both the interfacial transfer and the diffusion of materials across the product layer.

The dissolution behaviour of vanadium(V) can be predicted using a semi-empirical mathematical model as shown Equation 3-32, which was found to have acceptable accuracy for the prediction of the extraction kinetics of vanadium(V) at the upper range limit of the variables, i.e., higher temperatures and/or time (see Table A1 in the appendix section). The accuracy of the model decreased for shorter reaction periods, presumably because there was a sharp initial extraction yield due to the simple dissolution of vanadium pentoxide at the very beginning of the reaction that could be explained by the simple shrinking core model that was governed by the chemical reaction between the reactants.

$$\frac{1}{3}\ln(1-\mathrm{x}) + [(1-\mathrm{x})^{-\frac{1}{3}} - 1] =$$

$$2.9 \times 10^{5}\,[\mathrm{TMAH}]^{1.819}\,[\mathrm{NaClO_2}]^{0.340}\left[\frac{\mathrm{L}}{\mathrm{S}}\right]^{0.833} e^{\frac{-70\,422}{\mathrm{RT}}}\mathrm{t} \quad \text{(Equation 3-32)}$$

The following conditions were found to result in the limiting extraction yield of vanadium(V) in the shortest time: [TMA^+OH^-] 2.78 mol dm^{-3}, [$NaClO_2$] 0.221 mol dm^{-3}, slurry density 10 $cm^3\,g^{-1}$ and 90 °C reaction temperature.

4. Electrochemical recovery of vanadium(V) and the ionic liquid from the leach liquor

4.1 Introduction

This chapter was designed to establish a method to separate vanadium and the ionic liquid using lab-grade materials. The next chapter will utilise the findings for the recovery of vanadium(V) from the real gasifier ash sample.

Tetramethylammonium hydroxide (TMA^+OH^-) synthesis was first reported by Hofmann in 1851, and the synthesis route improved until 1905.

$$NMe_4X + MOH \rightarrow NMe_4OH + MX \qquad \text{(Reaction 4-1)}$$

The practical difficulty for the preparation of TMA^+OH^- from its salt was the solubility of MX in the reaction medium. If M, X and the solvent are chosen in a way that all the substances except MX are soluble, or at least much less soluble, then it is possible to purify TMA^+OH^- from the solution. M and X can be a pair of Ba^{2+}, SO_4^{2-} or Ag^+, I^-, in both of which cases the resulting salt, MX, is practically insoluble in the reaction medium, i.e., water. More elegantly, tetramethylammonium hydroxide is synthesised via the reaction between potassium hydroxide and tetramethylammonium chloride (preferably cold and concentrated) in methyl or ethyl alcohol, precipitating potassium chloride.[160] This was the only main synthesis route until 1993, when Yagi and Shimzu proposed a breakthrough synthetic route which was the 'synthesis of pure tetramethylammonium hydroxide solution free from chloride ions by electrolysis of its hydrogen carbonate salt'.[161] The reaction of dimethyl carbonate and trimethylamine in a stainless steel autoclave produces tetramethylammonium hydrogen carbonate. Electrolysis of the resulting solution results in the formation of tetramethylammonium hydroxide and the by-products shown in Reaction 4-8.

Anode:

$$2H_2O \rightarrow O_2 + 4H^+ + 4e^- \qquad \text{(Reaction 4-2)}$$

Anolyte:

$$TMA^+OCOOH^- + H^+ \rightarrow TMA^+ + H_2O + CO_2 \qquad \text{(Reaction 4-3)}$$

Membrane:

$$4\Phi^e_{TMA^+}[TMA^+(\text{anolyte}) \rightarrow TMA^+(\text{catholyte})] \qquad \text{(Reaction 4-4)}$$

$$4\left(1 - \Phi^e_{TMA^+}\right)[H^+(\text{anolyte}) \rightarrow H^+(\text{catholyte})] \qquad \text{(Reaction 4-5)}$$

$$4x\left(1 - \Phi^e_{TMA^+}\right)[H_2O(\text{anolyte}) \rightarrow H_2O(\text{catholyte})] \qquad \text{(Reaction 4-6)}$$

Cathode:

$$4H_2O + 4e^- \rightarrow 2H_2 + 4OH^- \qquad \text{(Reaction 4-7)}$$

Overall process reaction

$$TMA^+OCOOH^- + 6H_2O \rightarrow 4TMA^+OH^- + 2H_2 + O_2 + CO_2 \qquad \text{(Reaction 4-8)}$$

One year later in 1994, Yagi and Osamu published a study on 'Anion effect on the current efficiency during the preparation of tetramethylammonium hydroxide solution by electrolysis.'[162] They studied the relationship (charge yield) between the charge passed and the migrated TMA^+ ions for various anions such as hydrogen carbonate, formate, chloride, and sulfate.

Based on the above examples from the literature, tetramethylammonium hydroxide can be synthesised from a wide range of salts. The nature of the by-product in the anolyte is dependent solely on the nature of the TMA salt. For example, electrolysis of tetramethylammonium chloride results in the co-generation of chlorine gas, probably with oxygen, whereas the electrolysis of tetramethylammonium hydrogen sulfate results in the formation of sulfuric acid in the anolyte and tetramethylammonium hydroxide in the cathode chamber.

Evidently, TMA^+OH^- can be synthesised electrochemically from various TMA^+ salts including tetramethylammonium vanadate (TMA_3VO_4) or TMAV for short. TMA^+OH^- is driven by electro-migration through a cation exchange membrane (CEM) under an applied current. Cation exchange membranes can exclude uncharged molecules larger than the effective pore size, and other solid particles, and thus they act as a purification step for the recovered TMA^+OH^- from the TMAV solution. Membrane electrolysis not only separates charged species but performs water electrolysis directly in the leach solution. The core products of water electrolysis are the hydrogen gas and hydroxide ions at the cathode, and the oxygen gas and protons at the anode, so decreasing the pH of the anolyte and increasing the pH of the catholyte. The migration of the TMA^+ cations to the catholyte was predicted to leave negatively charged vanadium species in the anolyte, whereas electroneutrality in the catholyte is maintained by the charge on hydroxide ions generated at the cathode being balanced by the migrated TMA^+ cations.

The objectives of this part of the project were to:

- demonstrate the ion-permeable membrane separation of TMA^+ from a tetramethylammonium vanadate solution.
- describe the reaction mechanism by which vanadium(V) is recovered from the anolyte.
- From a techno-economic point of view, parameters such as vanadium deposition rate and the nature of the deposits were also the focus of this study.

4.2 Methodology

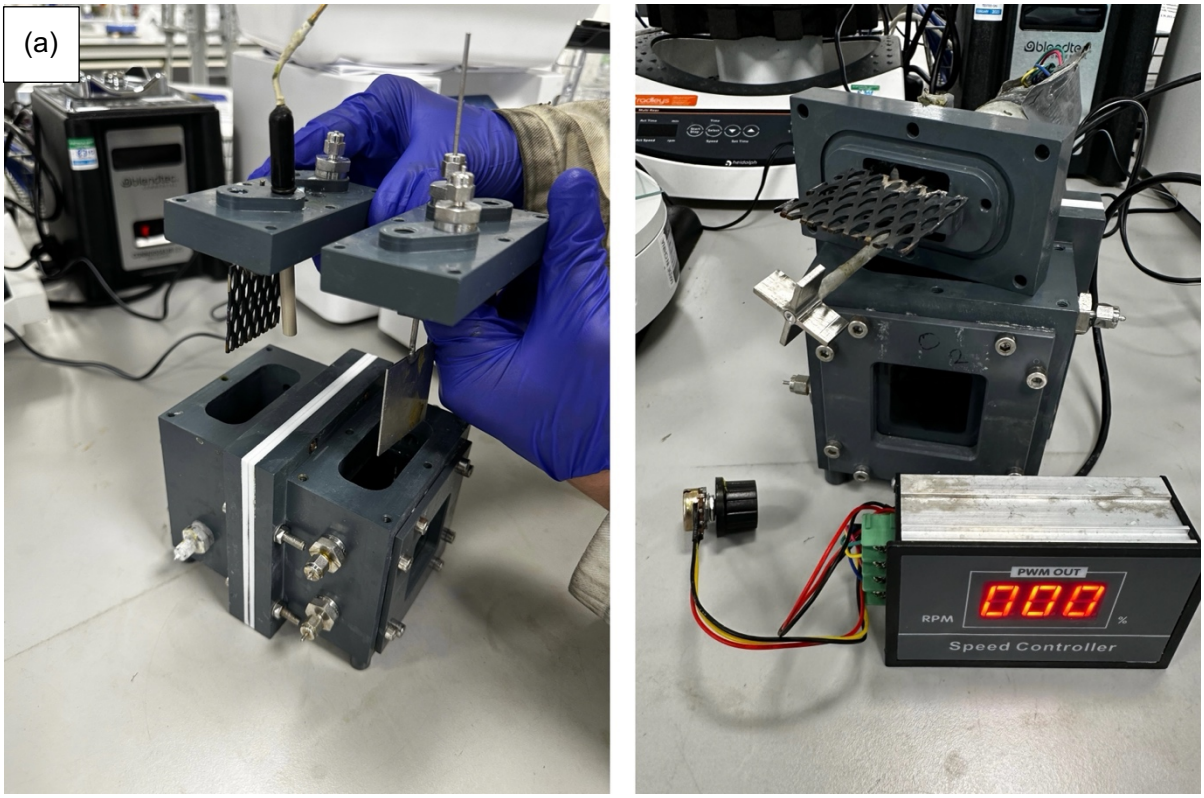
4.2.1 Membrane choice and preparation

The membrane-divided electrochemical reactor (ECR) was made of two 170 cm^{-3} polytetrafluoroethylene (PTFE) chambers, because of PTFE's exceptional chemical stability. The two chambers were separated via a 40 mm × 40 mm (DuPont) Nafion N424 perfluorosulfonic acid cation exchange membrane[163] (Sigma Aldrich Ltd.), carefully ensuring sides of membranes were correctly oriented in anolytes and catholytes. According to the manufacture's website, the shiny side of the membrane had to be facing towards the catholyte in order to avoid damaging the membrane.[164]

Ion exchange membranes tend to expand when in contact with aqueous solutions, so they were soaked in hot water for 2-3 hours to fully hydrate them to (i) maximise their ionic conductivity and (ii) in-situ expansion, before being placed in the reactor for the first time. From this point onwards, the membrane was always kept hydrated by storing the electrochemical reactor with the compartments filled with 0.02 mol dm^{-3} sulfuric acid solution and always having lids on top.

4.2.2 Electrochemical reactor equipment

Figure 4-1 shows a schematic diagram of the electrolysis experiment. In the membrane electrolysis experiments, the catholyte pHs increased due to the formation of stable TMA^+OH^-, while anolyte pHs decreased due to the formation of protonated vanadium compounds. Therefore, the catholyte and anolyte pHs were time-dependent. In the anolyte, V^V aggregates started to deposit onto the anode surface until a certain pH after which precipitated vanadium aggregates started to form in the solution. In order to keep the solids suspended, a titanium 4-flat-blade turbine was designed and built to order at the Imperial College Chemical Engineering Mechanical Workshop. The turbine



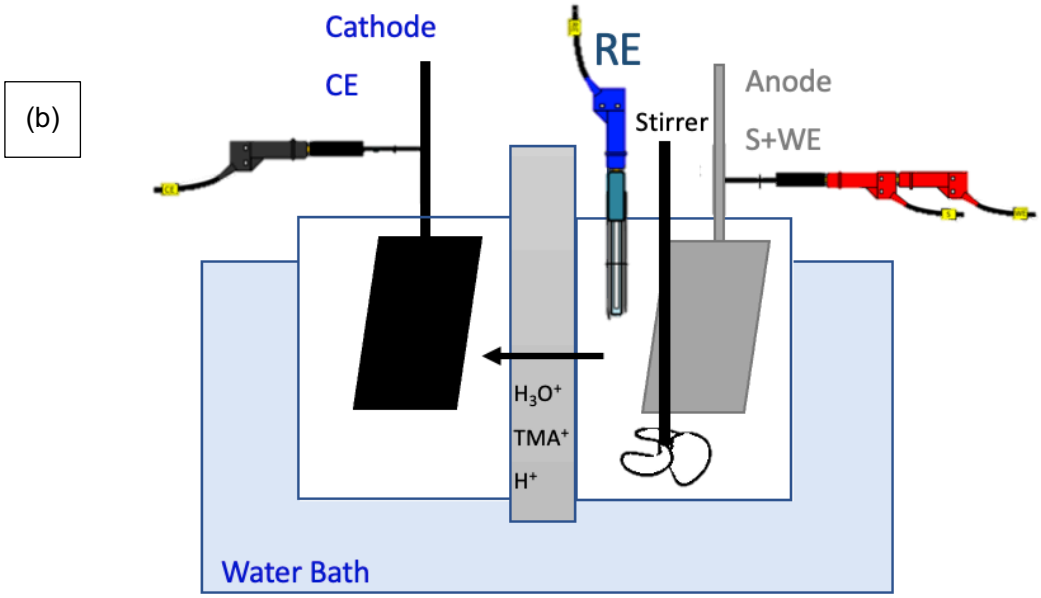


Figure 4-1. (a) Real pictures and (b) schematic of electrolyser. The anode compartment contained an agitator with a speed controller, an IrO2 coated titanium electrode connecd to the S+WE connectors and a reference electrode (RE). The counter electrode (CE) (cathode) was stainless steel 316.

was connected to a low voltage motor, altogether making the stirring system assembly, which was then screwed on the PTFE reactor lid and fixed in place with 10 mm clearance of the impeller from the bottom of the electrochemical reactor. The stirring speed was monitored and adjusted using a DC6-60V PWM motor speed controller with a digital display (Amazon UK). The agitation system not only ensured the solution was well-mixed, but also decreased the boundary layer thickness on the membrane, so increasing transport-controlled current densities.

The electrochemical reactor temperature was kept constant at 30 °C throughout the membrane electrolysis experiments using a water bath equipped with a heat exchanger coil and the stirring speed was always kept at 400 rpm.

A 40 mm × 40 mm 316 stainless steel (SS) plate was used as the cathode electrode and a 40 mm × 40 mm IrO_2 coated titanium mesh was used as the anode. Parameters such as the distance between the electrodes, surface area for each electrode and electrode material all remained constant throughout all the electrolysis experiments. A third electrode served as a reference electrode which was a leak-free Ag/AgCl in 3 mol dm^{-3} KCl reference electrode (model LF-5-100, ALVATEK, Southampton, UK). This specific electrode eliminated past issues such as clogging of the junction with sticky vanadium aggregates, if formed.

4.2.2.1 Three-electrode electrochemical cell

Figure 4-1 shows the three-electrode electrochemical cell used current flowing between the counter electrode (CE) and the working electrode (WE). Most experiments for which results are reported in this chapter used constant current (galvanostatic) mode, rather than potentiostatic mode, in which the electrode potential of the working electrode is controlled relative to the reference electrode (RE), which is kept in close proximity to the WE. However, in galvanostatic mode, the electrode potential of the 40 mm × 40 mm Ti/Ta_2O_5-IrO_2 anode mesh relative to the AgCl/Ag reference electrode could be monitored, to ensure the operating potential was at least sufficient to produce oxygen gas as predicted by Figure 4-6. The purpose of the working sense lead was to correct for the IR-drop down the current carrying cable of the working electrode, enabling monitoring of the working electrode potential. The counter electrode lead was connected to the 40 mm × 40 mm × 1.5 mm thick planar SS 316 counter electrode, the

S+WE lead was connected to the IrO_2 coated titanium electrode, and the reference electrode lead was connected to AgCl/Ag electrode.

4.2.3 Membrane-electrolysis and data analysis procedure

A 2 mol dm^{-3} stock solution of tetramethylammonium vanadate (i.e. V^V solution) was synthesised as follows: 400 cm^3 of 25 wt% (2.78 mol dm^{-3}) tetramethylammonium hydroxide solution from Sigma Aldrich was poured into a 500 cm^3 round bottom flask inside a fume hood. The flask was then placed on a hotplate and the solution was heated to 80 °C while being stirred using a magnetic stirrer bar. Exactly 73.04 g 99.6 % vanadium pentoxide (V_2O_5) was added slowly to the solution and left mixing overnight. The following day, a slightly tinted solution was achieved which was believed to be due to the physically observable black particles in the starting vanadium pentoxide powder. To obtain a clear solution, an arbitrary amount of activated charcoal was introduced to the flask and left to mix for two more hours to purify the solution. The black slurry was then vacuum filtered through a filter paper and a clear solution was collected in a Büchner filter flask. This clear solution was used as a stock vanadium(V) solution in the electrolysis experiments.

In a typical membrane-electrolysis experiment, the stock vanadium(V) solution was diluted with 2.78 mol dm^{-3} TMA^+OH^- solution. In this way, the vanadium(V) concentration was diluted while the TMA^+ concentration was kept constant, mimicking the kinetics experiments in which the same 2.78 mol dm^{-3} TMA^+OH^- solution at different reaction conditions resulted in different vanadium(V) extraction yields and concentrations. Although the results in **3.3.6 Kinetics study** showed that the TMA^+OH^- concentration had the greatest effect on the extraction yield, ultra-pure deionised water was also used to dilute both the TMA^+ concentration and the V^V concentration. This was done specifically to establish the effect of initial anolyte TMA^+ concentration on the charge yield for its membrane-electrolysis. Exactly 150 cm^3 of the diluted vanadium(V) solution, with a typical pH > 14, was measured in a measuring cylinder and transferred to the reactor's anolyte chamber, to which 2 cm^3 11 mol dm^{-3} sulfuric acid solution, was added. This was to maintain the ionic conductivity of the solution while transferring the TMA^+ ions to the cathode but did not cause a change in speciation of vanadium(V) as the pH was measured to be > 14. For the catholyte solution, 90 cm^3 ultra-pure deionised water was added to the chamber, to which 1 cm^3

2.78 mol dm^{-3} commercial TMA^+OH^- was added to increase the initial ionic conductivity of the solution at the beginning of the membrane electrolysis.

The electrodes were cleaned with 0.02 mol dm^{-3} sulfuric acid solution in a sonication bath for 15 minutes before each experiment. Subsequently, they were placed in the electrochemical reactor and connected to the corresponding connectors, as explained in **4.2.2.1. Three-electrode electrochemical cell** The data were recorded by Autolab PGSTAT302N by Metrohm AGb and the experiments were carried on potentiostatically unless otherwise stated.

4.2.4 UV-Vis calibration curve

According to Beer's law, the absorbance of a solution is directly proportional to the concentration of absorbing analytes in solution:

$$\text{Absorbance, } A_\lambda = -\log\left(P_\lambda / P_\lambda^0\right) = \log\left(P_\lambda^0 / P_\lambda\right) = \varepsilon \cdot c \cdot l \quad \text{(Equation 4-1)}$$

Where $P_\lambda{}^0$ and P_λ respectively represent the incident and transmitted spectral radiant powers at wavelength λ, ε_λ the molar absorption coefficient (m^2 mol^{-1}) at wavelength λ, c the concentration (mol m^{-3}) and l the optical path length (m).

This and Lambert's law hold only if spectral radiant powers are small, scattering is negligible, and multiphoton processes, excited state populations, and photochemical reaction rates are negligible

Several dilute TMA^+OH^- solutions were made with known concentrations, and their absorbances at the wavelength of strongest absorption were measured with a Shimadzu UV-2700 Spectrophotometer. A plot of the absorbance against the corresponding concentrations resulted in a straight line, which was utilised to derive the recovered TMA^+OH^- concentration in the catholyte.

4.2.4.1 TMA^+ concentration measurement

During the membrane-electrolysis experiments, a small amount (ca. 0.2 cm^{-3}) of the catholyte was sampled every 1.5 h. The sampled volume from the catholyte was reflected in the calculations. Then the samples were further diluted to a known volume, so that the resulting absorbances were in between the maximum and the minimum absorbances used to construct the calibration curve. The dilution coefficient is defined by:

$$\alpha_d = \frac{V_i}{V_f} \quad \text{(Equation 4-2)}$$

Where α_d represents the dilution coefficient, V_i is the initial volume to be diluted, V_f is the final volume of the diluted sample.

The concentration of the recovered TMA^+OH^- at sampling time ($C_{c,t}$) was calculated by correcting the measured concentration in the UV-vis with the dilution coefficient (α_d) explained above.

4.2.5 Charge yield (membrane transference coefficient)

The time dependant charge yield or transference coefficient was calculated from the ratio of the theoretical charge (Q_P) required to obtain TMA^+ ions the catholyte to the total actual charge (Q_t) passed through the electrochemical cell.

$$\Phi^e_{TMA^+{}_t} = \frac{Q_p}{Q_t} \quad \text{(Equation 4-3)}$$

The stoichiometric ratio of the number of electrons to the product (TMA^+OH^-) is unity, as can be seen from Reaction 4-2 to Reaction 4-8. Hence, the theoretical amount of charge required to form the product was calculated from the equation:

$$Q_p = F.C_{c,t_f}.V_{c,t_f} \quad \text{(Equation 4-4)}$$

The total charge passed through the electrochemical cell was calculated via the following equation:

$$Q_t = \int_{t=t_f}^{t=t_i} I(t)\,dt \quad \text{(Equation 4-5)}$$

The transference coefficient for the <u>end of the experiment</u> can be calculated by inserting Equation 4-4 and Equation 4-5 into Equation 4-3:

$$\Phi^e_{TMA^+} = \frac{F.C_{tf}.V_{c,t_f}}{It_f} \quad \text{(Equation 4-6)}$$

Where Q_p is the theoretical charge required for the amount of product obtained, in (C), Q_t is the total charge passed in (C), $\Phi^e_{TMA^+}$ is the charge yield, F is the Faraday constant which is 96485.33 (A s mol^{-1}), C_{c,t_f} is the measured concentration of TMA^+OH^- in the catholyte at the end of the electrolysis experiment in (mol dm^{-3}), V_{c,t_f} is the measured volume of the catholyte at the end of the electrolysis experiment in (dm^3), I is the applied current in (A) and t (s) is time.

4.2.6 TMA^+ recovery over time

The ratio of the total number of moles of recovered TMA^+ from the anode is described by Equation 4-7 as a function of time.

$$X_{TMA^+,t} = \frac{C_{c,t} \cdot V_{c,t}}{C_{a,t_i} V_{a,t_i}} \quad \text{(Equation 4-7)}$$

Where $X_{TMA^+,t}$ is the ratio of the TMA^+ recovered at time t with respect to the initial amount of TMA^+ present in the anolyte, $C_{c,t}$ is the catholyte concentration of TMA^+ at time t in (mol dm^{-3}), $V_{c,t}$ is the volume of catholyte at time t in (dm^3), C_{a,t_i} (mol dm^{-3}) is the initial concentration of TMA^+ in the anolyte, V_{a,t_i} is the initial volume of the anolyte in (dm^3).

The only challenging parameter to estimate is the volume of the catholyte for a given electrolysis time, as it changed due to: (i) superficial evaporation of water, leading to a reduction in the volume, (ii) water being converted to $2H_2O + 2e^- \rightarrow H_2 + 2OH^-$, leading to a reduction in the volume, (iii) formation of TMA^+OH^-, leading to an increase in the volume, (iv) and the migration of H_3O^+ from the anode to the cathode, leading to an increase in the volume, so the catholyte volume is a complex function of four different phenomena. A semi-empirical expression was made to account for the volume change as a function of time: after the electrolysis was finished, the change in the volume of the catholyte was measured and then divided by the elapsed electrolysis time. Assuming the volume change is linearly proportional with time, then the catholyte volume ($V_{c,t}$) was estimated for any given time.

4.2.7 Specific electrical energy consumption

The electrochemical reactor running costs, dominated by electrical energy costs, to which pumping costs need to be added, were calculated with respect to the V_2O_5-equivalent deposited materials as shown in Equation 4-8. Note that the only empirical parameters in this equation are (i) the reactor operating potential difference (U) which was measured by the potentiostat, and (ii) the charge yield which was calculated by Equation 4-6.

$$w^e_{V_2O_5} = \frac{(\nu_e) F \cdot |U|}{3.6 \Phi^e_{TMA^+} M_{V_2O_5}} \quad \text{(Equation 4-8)}$$

Where $w^{e}_{V_2O_5}$ represents the specific electrical energy consumption per unit mass of V_2O_5 produced in (kW h t_{V2O5}^{-1}), ν_e the reaction electron stoichiometry, U the reactor potential difference in (V), F the Faraday constant, $\Phi^{e}_{TMA^+}$ the (fractional) charge yield, and $M_{V_2O_5}$ the molar mass of V_2O_5 in (g mol^{-1}).

The cell potential difference, U, is predicted by the following equation:

$$|U| = E_{O_{2/H_2O}} - E_{O_{H_2O/H_2}} + |\eta_{H_2}| + \eta_{O_2} + \sum_i I.d_i/(A_i.\sigma_i) \quad \text{(Equation 4-9)}$$

Where E represents equilibrium potential(s) in (V), η overpotential(s) in (V) and the last term represents the sum of the ohmic potential losses due to current in (A) with path length d_i (m) passing through phase i of conductivity σ_i (A V^{-1} m^{-1}) and area A_i (m^2)

4.2.8 Deposition rate of vanadium(V) oxide aggregates

A specific ratio of the as-prepared tetramethylammonium vanadate(V) solution (synthesis procedure explained in **section 4.2.3**) was mixed with 2.78 mol dm^{-3} tetramethylammonium hydroxide solution (Sigma Aldrich Ltd.). Three solutions were made with 0.589, 0.883 and 1.178 mol dm^{-3} vanadium(V) concentrations, but all consisting of 2.78 mol TMA^+ dm^{-3}. Membrane electrolysis was started and continued until the anolyte reached pH 6. Simultaneously the anode was under observation to detect the first crystals being formed, when electrolysis was stopped, and the anode was removed from the electrochemical cell. Subsequently, both sides of the anode were placed on an absorbent paper towel to remove excess electrolyte solution with minimum loss of the deposit. Then the weight of the anode was recorded, and it was placed back into the electrolyser and the electrolysis was continued for 1 200 seconds. At each cycle, a new layer of vanadium(V) aggregates was formed on the anode. This cycle was repeated five times until the total elapsed electrolysis time reached 7 200 seconds. The final mass of anode was recorded and ultimately, the deposits were removed mechanically. The anodes were cleaned with 0.02 mol dm^{-3} sulfuric acid solution (see Reaction 4-9) in a sonication bath for 15 minutes before the next experiment.

$$V_2O_5 + H_2SO_4 \rightarrow (VO_2)_2SO_4(aq) + H_2O \quad \text{(Reaction 4-9)}$$

4.2.9 LC-MS for trace TMA^+OH^- analysis

For the stock solution, 12.612 g HPLC grade ammonium formate (Sigma Aldrich) was dissolved in 1 dm^3 of water. To this was added 98-100 % HPLC grade formic acid (Sigma Aldrich) until a pH of 3 was reached. Nine parts of HPLC grade water (Sigma Aldrich) were mixed with one part of the stock solution to make the aqueous mobile phase A. The organic mobile phase B was prepared by mixing nine parts of HPLC grade acetonitrile (Sigma Aldrich) with 1 part of the stock solution. The final concentration of the ammonium formate for both phases was 0.020 mol dm^{-3}.

To generate the calibration curve for estimation of the concentration of TMA^+ in the effluent, a stock solution of TMA^+OH^- was required which was purchased from Sigma Aldrich. The TMA^+OH^- stock solution was a 25 wt% TMA^+OH^- in water. This was diluted to 1 000, 500, 250, 125 and 25 ppm TMA^+ using ultra-pure de-ionised (DI) water. The same diluent DI water was used as the blank i.e. 0 ppm TMA^+.

4.2.10 TMA Vanadate Recovery from Residue

The dry weight of the post-reaction residue could be up to 60 % less than its wet weight, implying that there is a considerable recoverable fraction of the TMA_3VO_4 and TMA^+OH^- in wet residue. One of the extraordinary properties of TMA vanadate, a metal salt, is its great solubility in alcohols such as methanol, ethanol etc.

In a typical experiment, the residue was resuspended in methanol at an S/L ratio of 0.5 g dm^{-3} in a falcon tube. Subsequently, the suspension was mixed on a vortex shaker for half an hour, followed by centrifugation for half an hour at 3500 rpm. The top liquid phase was removed for trace TMA^+ analysis, the bottom phase was re-suspended in fresh methanol and the cycle was repeated three more times.

4.3 Results and discussion

4.3.1 Membrane electrolysis mechanism

The gasifier ash studied herein was from the Pernis refinery and contained over 20 metal oxides, of which vanadium(V) was dissolved successfully in TMA^+OH^- to produce solutions of high purity. Solutions containing the same TMA^+ and V^V concentrations as that obtained in the leach solution in the kinetics study were prepared for the membrane electrolysis experiments.

The anode chamber was filled with the as-prepared tetramethylammonium vanadate (TMAV) solution and the cathode chamber was filled with mostly ultrapure deionised water, together with 1 cm^3 of 2.78 mol dm^{-3} TMA^+OH^-. Oxygen and hydrogen gas were generated in the anode chamber and the cathode chamber as a result of the oxygen evolution reaction and the hydrogen evolution reaction, respectively.

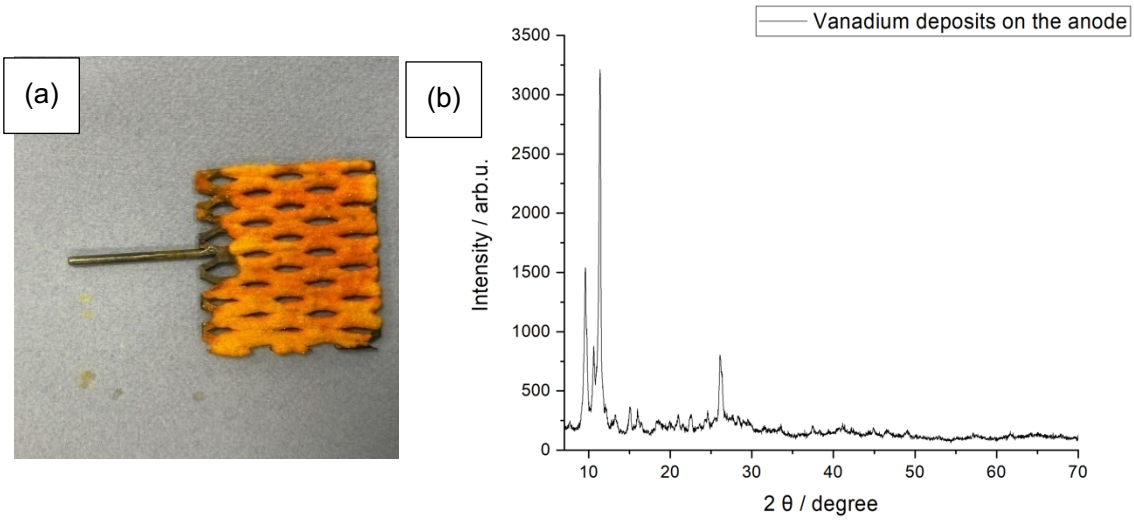


Figure 4-2. Control compound - (a), left, Dried anode deposits (b), right, X-ray diffraction pattern of the electrode deposits

The membrane allowed the migration of TMA^+, H^+ and H_3O^+ in the anolyte to the catholyte, in which they reacted with the generated OH^- ions to form TMA^+OH^- and H_2O. Proton migration rates were to be minimised, as implied by Reaction 4-2 to

Reaction 4-5 as they decrease charge yields for V^{V} migration as specifically shown by Reaction 4-4, so increasing the specific electrical energy consumption for V_2O_5 recovery, as evident from Equation 4-8. In the anolyte, the generated protons reacted with OH^- ions and vanadate ions (VO_4^{3-}), causing a decrease in the pH which changed the vanadium speciation as predicted by the activity pH diagram (Figure 4-7). On the other hand, the catholyte pH increased due to the formation of free hydroxide ions i.e., regeneration of TMA^+OH^- over time in the batch electrolysis experiments.

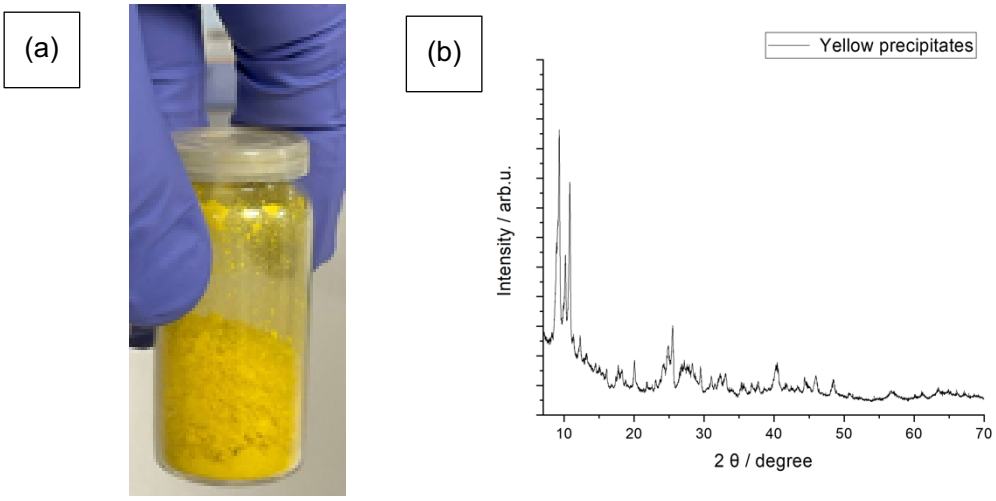


Figure 4-3. Control compound - (a), left, Dried precipitates of the anolyte pH < 3, Soxhlet treated and dried. (b), right, X-ray diffraction pattern of the precipitates.

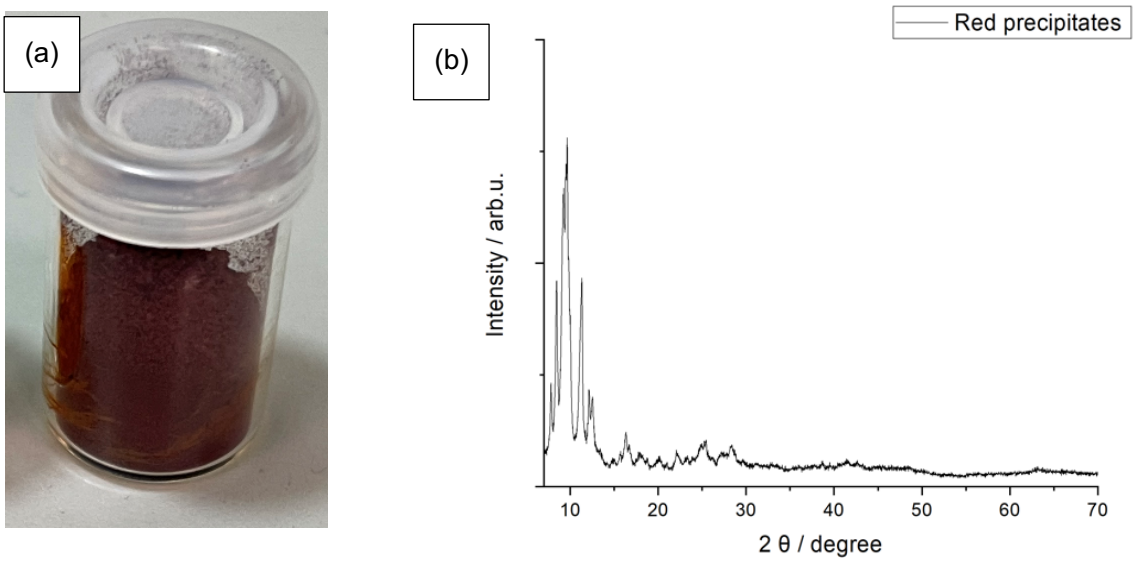


Figure 4-4. Control compound - (a) Control compound - Dried precipitates from prolonged membrane electrolysis of anolyte, pH = 2 (b) X-ray diffraction pattern the dried precipitates.

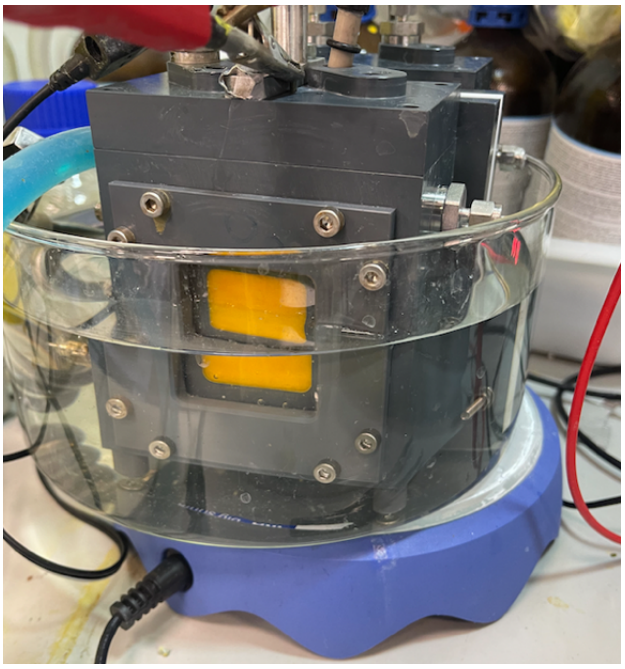


Figure 4-5. Typical electrolysis equipment. The anolyte pH < 3 caused rapid formation of hydrated $H_3TMA_3V_{10}O_{28}$ in the form of a yellow dispersion.

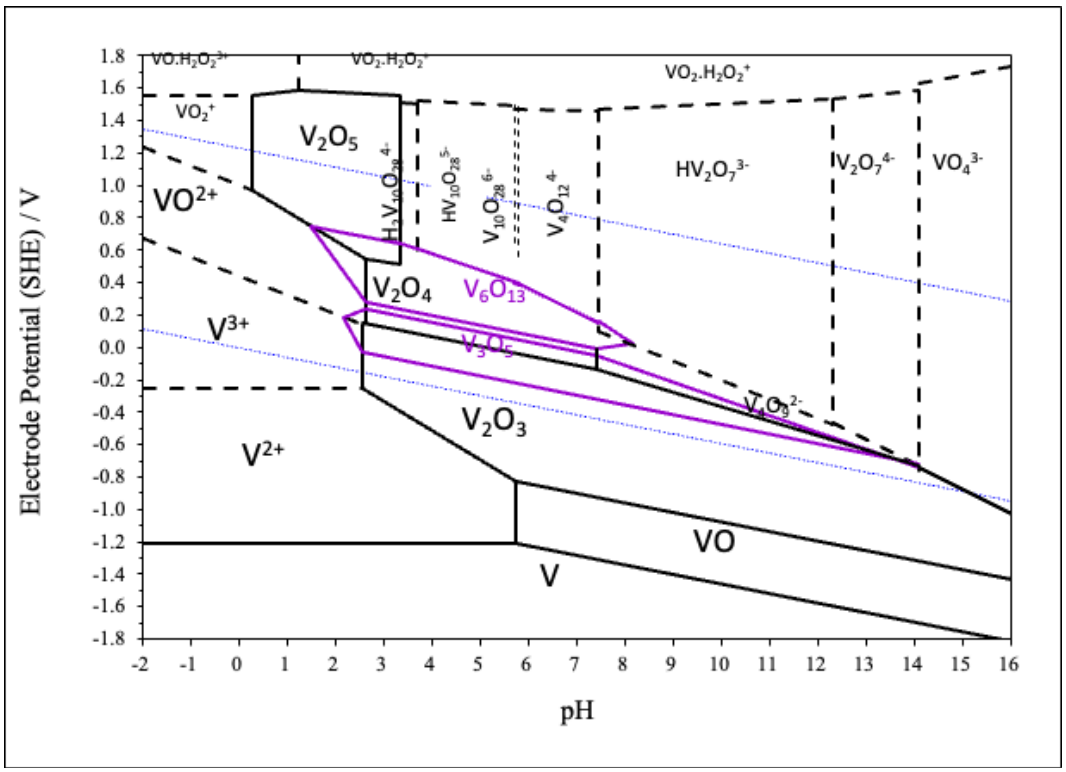


Figure 4-6. Potential-pH diagram for vanadium-H_2O system at 298 K, 0.1 MPa and activity of dissolved vanadium species = 10^{-1}

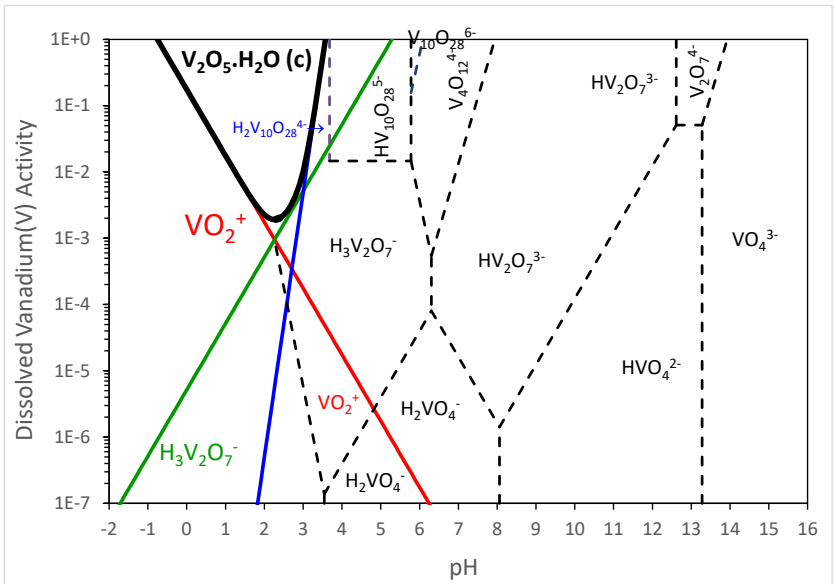


Figure 4-7. (reprinted Figure 2-3) V^V activity-pH diagram for species in equilibrium with $V_2O_5.H_2O$ at 298 K, 0.1 MPa. These calculations omitted consideration of the presence of TMA^+ ions, which, as reported below, were found to lead to formation of solid phases in addition to $V_2O_5.H_2O$.

The change in the vanadium(V) speciation can be predicted by the activity-pH diagram (Figure 4-7). The predominant dissolved species are vanadate ions (VO_4^{3-}) for solution pH > 14, $V_2O_7^{4-}$ and $HV_2O_7^{3-}$ ions for 7 < pH < 14, $V_4O_{12}^{4-}$ ions for 6 < pH < 7, $V_{10}O_{28}^{6-}$ ions at pH = 6, $HV_{10}O_{28}^{5-}$ ions for 4 < pH < 6, and $H_2V_{10}O_{28}^{4-}$ ions for 3 < pH < 4. However, these calculations omitted consideration of the presence of TMA^+ ions which were found to lead to formation of solid materials both at the surface of the anode and in the solution depending on the bulk pH. The explanation of the characterisation of the precipitated/deposited materials is described in section 4.3.7.

Reaction 4-11 to Reaction 4-14 list possible reactions during membrane electrolysis, causing the anolyte pH to decrease with time, migration of TMA^+ ions from anolyte to catholyte, and neutralisation of the OH^- ions by the generated protons, which were also partially, undesirably co-migrated with TMA^+ ions from anolyte to catholyte. Once the anolyte pH decreased to < 6, deposits started to form hydrated tetra-hydro-di-tetramethylammonium-decavanadate ($H_4TMA_2V_{10}O_{28}$), for which Figure 4-2(b) shows its diffractogram, at the surface of the Ti/IrO_2 anode, where the local pH was lower than bulk anolyte values. Continuing electrolysis caused formation of thicker deposits, as shown in Figure 4-2(a), until the anolyte pHs were < 3, when precipitates formed hydrated tri-hydro-tri-tetramethylammonium-decavanadate ($H_3TMA_3V_{10}O_{28}$), for which Figure 4-3(b) shows its diffractogram, turning the anolyte from clear deep orange to cloudy yellowish, as shown in Figure 4-5. Electrolysis was terminated when the anolyte pH was 2; deposits were scraped from the anode surface and dried for further analysis. The suspension was vacuum filtered, and the solids were purified in a Soxhlet extractor to remove any TMA^+ compounds that were soluble in methanol; Figure 4-3(a) shows the physical appearance of the recovered solids.

After prolonged electrolysis (i.e., 3x the theoretical charge), most of the TMA^+ ions had migrated from anolyte to catholyte, leaving deep red/brownish sticky precipitates containing high H^+/TMA^+ in the decavanadate anion $V_{10}O_{28}^{6-}$; Figure 4-4(b) shows its diffractogram. As for the precipitated vanadium(V) aggregates, these solids were further purified; Figure 4-4(a) shows the physical appearance of the product after a prolonged electrolysis period and further treatments in Soxhelt.

V_2O_5 Leaching (pH > 14):

$$30\ \mathrm{TMA^+} + 30\ \mathrm{OH^-} + 5\ \mathrm{V_2O_5(s, ash)} \rightarrow$$

$$30\ TMA^{+} + 10\ VO_4^{3-} + 15\ H_2O \qquad \text{(Reaction 4-10)}$$

V_2O_5 Recovery

Anode:

$$14\ H_2O \rightarrow 7\ O_2 + 28\ H^{+} + 28\ e^{-} \qquad \text{(Reaction 4-11)}$$

Solution 3 < pH < 6:

$$30\ TMA^{+} + 10\ VO_4^{3-}(aq) + 28\ H^{+}(aq) \rightarrow$$

$$H_4TMA_2V_{10}O_{28}\ (s) + 12\ H_2O + 28\ TMA^{+} \qquad \text{(Reaction 4-12)}$$

Cathode:

$$28\ H_2O + 28\ e^{-} \rightarrow 14\ H_2 + 28\ OH^{-} \qquad \text{(Reaction 4-13)}$$

Overall Electrolytic Process:

$$30\ TMA^{+} + 10\ VO_4^{3-} + 30\ H_2O \rightarrow H_4TMA_2V_{10}O_{28}\ (s)$$

$$+14\ H_2(g) + 7\ O_2\ (g) + [28\ TMA^{+} + 28\ OH^{-}] \qquad \text{(Reaction 4-14)}$$

$$H_4TMA_2V_{10}O_{28}(aq) \rightarrow 5\ V_2O_5(c, pure)$$

$$+ 2\ TMA^{+}OH^{-} + H_2O \qquad \text{(Reaction 4-15)}$$

(Details of Reaction 4-15 are explained in Page 201)

Overall Process:

$$5\ V_2O_5(s, ash) + 14\ H_2O \rightarrow 14\ H_2(g)$$

$$+7\ O_2\ (g) + 5\ V_2O_5(c,pure) \qquad \text{(Reaction 4-16)}$$

4.3.2 UV-Vis Calibration Curve for TMA^+

In order to calculate the recovered mass of the ionic liquid over time, the concentration of the ionic liquid was tracked in the catholyte. The most convenient approach was found to be the simple linear relationship between the peak absorbance intensity of the ionic liquid and concentration. A calibration line was required to convert the absorbance intensity of the samples to concentrations. Absorption spectra such as in Figure 4-8 (a) for TMA^+OH^- solutions appear not to have been reported in the literature hitherto. The calibration solutions were all colourless and the absorbance spectra of TMA^+OH^- samples prepared using 2.78 mol dm^{-3} TMA^+OH^- solution showed only one peak at ca. 208 nm. As shown in Figure 4-8 (a), the absorbance values at λ_{max} from different samples plotted against TMA^+OH^- concentration exhibited a linear relationship with a R^2 value of 0.9912. The calibration equation was used to determine concentrations of recovered TMA^+OH^- in the catholyte, based on the absorption peak of the collected samples from the catholyte at a given electrolysis time. Note that the calibration curve does not pass through the origin (0,0). This is because λ_{max} occurred in the near ultra-violet where the machine response for the absorbance at zero analyte concentration was very noisy.

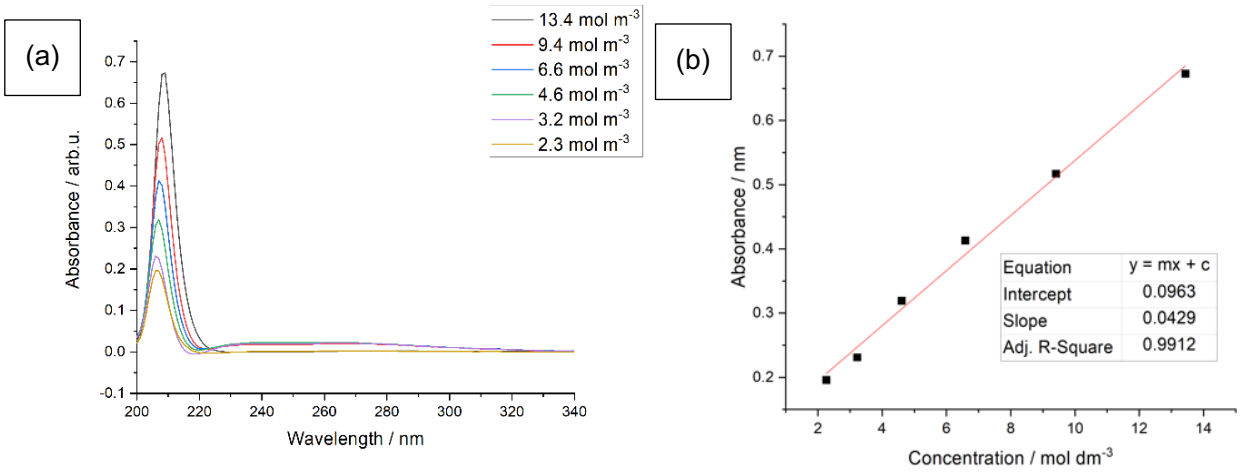


Figure 4-8 (a, left, Absorption spectra of TMA+OH- solutions of different concentrations in water (b), right, Effect of TMA+OH- concentration on peak absorbances of TMA+OH- solutions at λmax = 208 nm. Path length =10 mm

4.3.2.1 Effect of current density on vanadium(V) recovery by electrolysis

Electrolyses were carried out until the anolyte pH = 2, at which point aggregates of vanadium(V) particulates started to appear in the anolyte, thus constituting an end point. Figure 4-9 (a) shows the time dependence of fractional recovery of TMA^+ ions in the catholyte against time for the three nominal current densities of 700, 1 000 and 1 300 A m^{-2}. As expected, the rate of the total recovered TMA^+ increased with increasing current density, providing mass transport limited current densities were not exceeded.

Anolyte boundary layer thickness $\delta_a \approx 10^{-4}$ m | Membrane thickness $d_m \approx 10^{-4}$ m | Catholyte boundary layer thickness $\delta_c \approx 10^{-4}$ m

$$TMA^+{}_{x_a=\delta_a} \rightarrow TMA^+{}_{x_a=0} \rightarrow TMA^+{}_{x_m=0} \rightarrow TMA^+{}_{x_m=d_m} \rightarrow TMA^+{}_{x_c=0} \rightarrow TMA^+{}_{x_c=\delta_c}$$

Neglecting solution phase migrational transport in the electric field and very fast coupled homogeneous H^+-OH^- reactions in the membrane and catholyte, flux densities of TMA^+ ions from bulk anolyte to membrane surface are given by:

$$N_{TMA^+,a}(\text{mol m}^{-2}\text{ s}^{-1}) =$$

$$\frac{D_{TMA^+,a}(\text{m}^2\text{ s}^{-1})}{\delta_a(\text{m})}\left\{[TMA^+]_{x_a=\delta_a} - [TMA^+]_{x_a=0}\right\} \qquad \text{(Equation 4-10)}$$

Faraday's law:

$$j = F\sum_i z_i N_i \qquad \text{(Equation 4-11)}$$

$$\lfloor j_T \rfloor = \lfloor j_{TMA^+} \rfloor + \lfloor j_{H^+} \rfloor \approx$$

$$\left\lfloor FD_{TMA^+}\frac{\partial[TMA^+]}{\partial x}\right\rfloor + \left\lfloor FD_{H^+}\frac{\partial[H^+]}{\partial x}\right\rfloor \qquad \text{(Equation 4-12)}$$

For the range of anolyte compositions used, $[TMA^+] \gg [H^+]$, other than at high TMA^+ conversions and pH $\rightarrow$ 2, so:

$$\lfloor j_T \rfloor \approx \lfloor j_{TMA^+} \rfloor \approx \left\lfloor FD_{TMA^+}\frac{\partial[TMA^+]}{\partial x}\right\rfloor \qquad \text{(Equation 4-13)}$$

Assuming a linear concentration gradient across the hydrodynamic boundary layer / Nernst diffusion layer of mean thickness δ_a:

$$\lfloor j_T \rfloor \approx \lfloor j_{TMA^+} \rfloor \approx$$

$$\left|F\frac{D_{TMA^+}}{\delta_a}\left\{[TMA^+]_{x=\delta_a}-[TMA^+]_{x=0}\right\}\right| \qquad \text{(Equation 4-14)}$$

When the concentration at the membrane surface $[TMA^+]_{x=0} \rightarrow 0$, current densities become limited by mass transport (j_{L,TMA^+}):

$$j_{L,TMA^+} \approx F\frac{D_{TMA^+}}{\delta_a}[TMA^+]_{x=\delta_a} \qquad \text{(Equation 4-15)}$$

Hence, for the values F = 96,485.34 C mol^{-1}, initial bulk anolyte concentrations $[TMA^+]_{x=\delta_a}$ of 1 360, 1 950 and 2 780 mol m^{-3} and using physically reasonable, but estimated values of $D_{TMA^+} = 10^{-9}$ m^2 s^{-1} and δ_a = 10^{-4} m (responsive to local hydrodynamic conditions, so dependent on stirring rate), Equation 4-15 predicts transport controlled current densities of 1 312, 1 881 and 2 682 A m^{-2}. Importantly, these values are somewhat greater than the applied current densities of 700, 1 000 and 1 300 A m^{-2} (Figure 4-9 (a)) for 2 780 mol TMA^+ m^{-3}. Hence, by substitution of equation Equation 4-15 into Equation 4-14, concentrations of TMA^+ ions at the membrane surface (x = 0) can be estimated from:

$$\frac{[TMA^+]_{x=0}}{[TMA^+]_{x=\delta_a}} = \frac{j_{L,TMA^+}-j_{TMA^+}}{j_{L,TMA^+}} \qquad \text{(Equation 4-16)}$$

For the greatest initial concentration of 2 780 mol TMA^+ m^{-3}, and applied current densities of 700, 1 000 and 1 300 A m^{-2}, the initial (t = 0) surface concentration as fractions of the bulk value were 0.74, 0.63 and 0.52, whereas for the smallest concentration of 1 360 mol TMA^+ m^{-3}, the corresponding values were 0.47, 0.24 and 0.01. However, inclusion of TMA^+ ion migrational transport rates from bulk anolyte to membrane surface would have increased those initial values, but in batch experiments, depletion of TMA^+ ions in the anolyte by transport through the membrane, would have decreased them progressively with increased conversion.

Under conditions when applied current densities (j) were greater than transport limited values (j_{L,TMA^+}), excess current densities ($j - j_{L,TMA^+}$) would probably have caused water breakdown and injection of protons into the membrane, with consequential loss of charge yield ($\Phi^e_{TMA^+}$) and pH changes in anolyte and catholyte.

For $(j \geq j_{L,TMA^+})$:

$$\Phi^e_{TMA^+} = \frac{j_{TMA^+}}{j} = \frac{j_{TMA^+}}{j_{H^+}+j_{TMA^+}} \qquad \text{(Equation 4-17)}$$

Higher current densities led to the formation of OH^- in greater quantities consequently, creating a large driving force for TMA^+ ions to migrate to the catholyte. It can be clearly seen that a 300 A m^{-2} step change in the current density going from 700 A m^{-2} to 1 000 A m^{-2} caused a considerable decrease in the electrolysis time whereas going from 1 000 A m^{-2} to 1 300 A m^{-2} decreased the electrolysis time only slightly. Hence, 1 000 A m^{-2} current density was considered to be the optimum current density for studying the effect of other factors.

According to the Nernst-Planck equation (Equation 4-18), the molar flux density (N_i) of charged (infinitely dilute) electro-active solute species i with diffusion coefficient D_i to an electrode surface, is due to the vectorial sum of:

- (First term) their migration in an electric field ($\nabla\phi = j/\sigma$);
- (Second term) diffusion in a concentration (c) / activity gradient;
- (Third term) convection due to the local fluid velocity (v):

$$N_i \cong -(z_i F/RT) D_i c_i \nabla \emptyset - D_i \nabla c_i + c_i v \qquad \text{(Equation 4-18)}$$

Faraday's law relates the (sum of) molar flux densities to the electron flux (current) density, j, the sum of its partial current densities:

$$j = F \sum_i z_i N_i = j_{TMA^+} + j_{H^+} \qquad \text{(Equation 4-19)}$$

However, for transport in an ion-permeable membrane, the convective term in Equation 4-18 was assumed to approximate to zero, though electro-osmotic water transport would have been operative.

Mass balance on anolyte of (time-dependent) volume $V_{a,t}$:

$$V_{a,t} \frac{d[TMA^+]t}{dt} = V_{a,t}[TMA^+]_{t=0} - \frac{A_m . j\Phi_{TMA^+,t}}{F} \qquad \text{(Equation 4-20)}$$

Mass balance on catholyte of (time-dependent) volume $V_{c,t}$:

$$V_{c,t} \frac{d[TMA^+]t}{dt} = V_{c,t}[TMA^+]_{t=0} - \frac{A_m . j\Phi_{TMA^+,t}}{F} \qquad \text{(Equation 4-21)}$$

Where A_m (m^2) represents the membrane area

Hence, according to Equation 4-21, the concentrations of TMA^+ ions would be expected to increase approximately linearly with time and current density, depending

on the evolution of TMA^+ charge yield ($\Phi^{e}_{TMA^+}$), as anolyte compositions changed with time.

Figure 4-10 shows the transport of tetramethylammonium cations from the anode to the cathode without an applied electric field. It was revealed that the simple migration of the cations to the cathode was somewhat negligible over a long period of time. Therefore, the transport of the cations can be assumed to be attributed solely to the applied electric field.

Figure 4-9 (b) shows the time dependence of anolyte pH during electrolyses, for current densities of 700, 1 000 and 1 300 A m^{-2}, causing TMA^+ cations to migrate through the membrane from anolyte to the catholyte, driven by the electric field strength, $\nabla\phi = j/\sigma$, where σ represents the membrane conductivity. The TMA^+ molar flux density in the membrane can be approximated by:

$$N_{TMA^+,m} \approx -\left(\frac{zF}{RT}\right) D_{TMA^+,m} \cdot [TMA^+]_{x_m=0} \cdot \nabla\phi \qquad \text{(Equation 4-22)}$$

Water oxidation by Reaction 4-2 generated protons, causing the anolyte pH to decrease with time, with: (i) neutralization of the excess hydroxide ions in the anolyte,

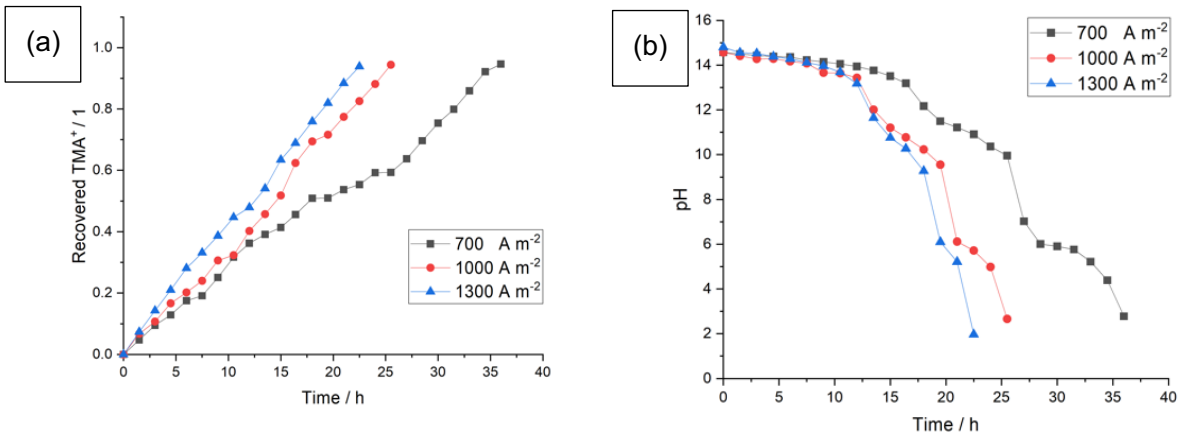


Figure 4-9. Time dependences of: (a), left, fractional TMA^+ recovery to catholyte, and (b), right, of anolyte pH; both for current densities of 700, 1 000 and 1 300 A m^{-2}. Initial TMA^+ concentration in anolyte = 2.78 mol dm^{-3}; initial vanadium(V) concentration in anolyte = 0.589 mol dm^{-3}.

and (ii) homogeneous chemical reactions changing vanadium(V) speciation, as predicted by Figure 4-7, and the condensation reaction, shown in Reaction 4-12. The decrease in anolyte pH resulted ultimately in the formation of vanadium(V) aggregates onto the anode surface for pH < 6, and at pH = 2-3, precipitate formation.

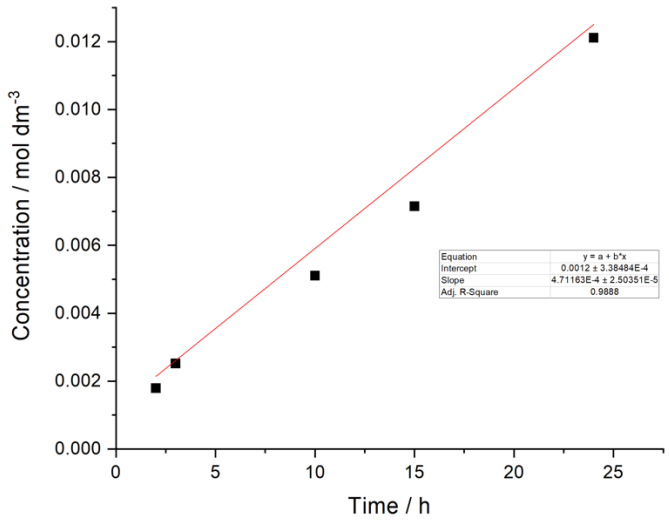


Figure 4-10. TMA^+ cations flux under zero electric fields.

4.3.2.2 Effect of initial vanadium(V) concentration on recovery by electrolysis

The vanadium(V) species at high TMA^+OH^- concentration (high pH) is predicted by the V^V activity-pH diagram (Figure 4-6) to be tetrahedral orthovanadate anions (VO_4^{3-}). For solutions containing constant TMA^+ concentrations, the greater the vanadium(V) concentration, the less the OH^- concentration to be neutralised by protons generated in the anolyte, so the shorter the electrolysis time. This is evidenced by Figure 4-11 (a) and (b), which show respectively the time dependences of the fractional conversion of TMA^+ ions in the catholyte, and the anolyte pH, together with the effects of initial vanadium(V) concentrations thereon. As the initial vanadium(V) concentration increased, the vanadium(V) precipitates formed at shorter electrolysis times, e.g. 25 hours for 0.589 mol V^V dm^{-3} vs. 20 hours for 1.178 mol V^V dm^{-3}. This was expected, as greater concentrations of TMA^+-bearing vanadium(V) aggregates then formed in the

anolyte, requiring smaller concentrations of TMA^+ cations to be transported to the catholyte.

Note that the selected initial vanadium(V) concentrations fall within the range of those reported in Chapter 3. In a real leaching process, a leach solution of high vanadium(V) concentration is strongly favourable when scaling up the process due to: (i) smaller volume of solvent (and equipment) required for processing the same weight of ash, resulting in decreased OPEX and CAPEX costs, (ii) the electrolysis time is decreased, leading to increased annual throughput. Having a higher initial vanadium(V) concentration in the leach liquor would require the ash to solvent ratio to be increased during the extraction process, possibly requiring a smaller unit for the recovery of vanadium(V) from the residue.

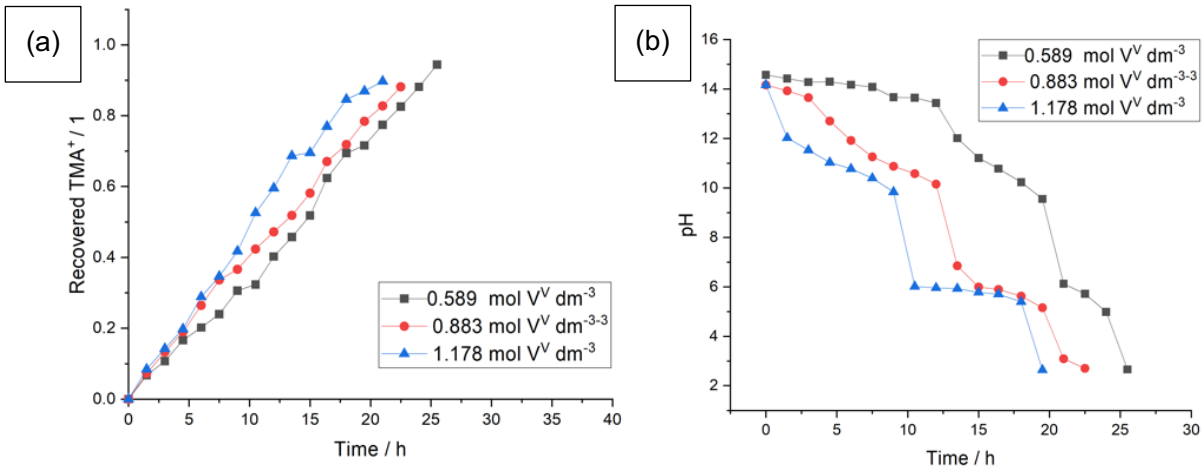


Figure 4-11. Time dependences of: (a), left, fractional recovery to the catholyte of TMA^+ ions, and (b), right, anolyte pH; both for 3 initial vanadium(V) concentrations. Initial TMA^+ concentration in anolyte = 2.78 mol dm^{-3}; current density = 1 000 A m^{-2}

4.3.2.3 Effect of Initial TMA^+ Concentration in the Anolyte on Vanadium(V) Recovery by Electrolysis

Figure 4-12 (a) shows the time dependences of fractional recovery of TMA^+ ions, transported from anolyte to catholyte, for initial TMA^+ concentrations of 1.36, 1.95 and 2.78 mol dm^{-3}, until vanadium(V) precipitates formed. Those precipitates formed at shorter times as the TMA^+ concentrations decreased, since for a constant vanadium(V) concentration, smaller amounts of TMA^+ ions were required to be transported to the catholyte, to reach pH = 2 in the anolyte, generating vanadium(V) aggregates. The decrease in the electrolysis time was such that halving the TMA^+ concentration decreased the electrolysis time from 25 h to 10 h. From industrial application point of view, decreasing TMA^+ concentrations has implications for both CAPEX and processing times. However, as explained in Chapter 3, the initial TMA^+OH^- concentration affects the equilibrium vanadium(V) extraction yield greatly. For example, it was shown that no initial concentration less than 2.78 mol dm^{-3} TMA^+OH^- was able to reach to the equilibrium extraction yield of ca. 83 %.

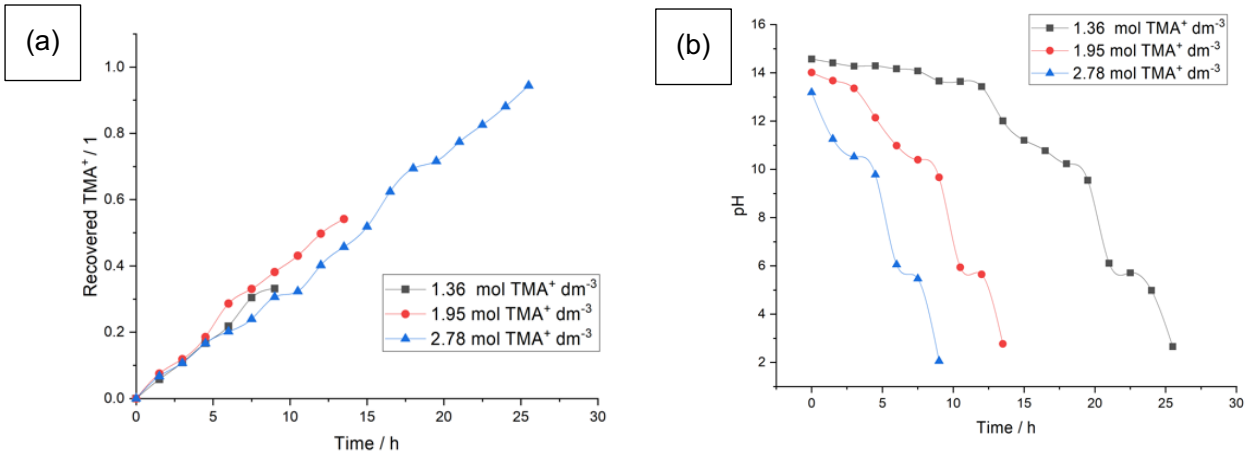


Figure 4-12. Time dependences of: (a), left, fractional TMA^+ recovery to the catholyte, and (b), right, anolyte pH; both for 3 initial TMA^+ concentrations. Initial vanadium(V) concentration in anolyte = 0.589 mol dm^{-3}; current density = 1 000 A m^{-2}

4.3.3 Specific Electrical Energy Consumption

A stoichiometric ratio of TMA^+ : V^V = 3 : 1 results in the formation of $[TMA^+]_3[VO_4^{3-}]$ at pH 14; i.e., for a solution containing 2.78 mol dm^{-3} TMA^+, the vanadium(V) concentration should be ca. 0.9 mol dm^{-3}. Figure 4-11 (b) shows that for a solution containing 0.883 mol dm^{-3} vanadium(V), the anolyte pH started to decrease immediately from pH 14, whereas for the anolyte containing 0.589 mol dm^{-3} vanadium(V), the pH decrease was delayed by 7.5 hours. This implies that the recovery of vanadium(V) in the form of deposited or precipitated aggregates, started with the transport through the membrane of the 'excess' TMA^+ ions to the catholyte until its pH was ca. 14, at which the activity-pH diagram (Figure 4-6) predicts VO_4^{3-} ions are the predominant vanadium(V) species. Thereafter, Reaction 4-11 to Reaction 4-14 became the dominant reactions. Hence, the electron stoichiometry in Equation 4-8 would be split into: Electron stoichiometry for excess TMA^+OH^- recovery is variable which is a function of vanadium(V) / TMA^+ concentration, i.e. ν_{e1} = f(TMA^+:V^V), and electron stoichiometry for $H_4TMA_2V_{10}O_{28}$ generation which is fixed for that specific product, i.e. ν_{e2} = f($H_4TMA_2V_{10}O_{28}$) = 5.6 because according to Reaction 4-11 to Reaction 4-15, there are 28 electrons transferred for 5 moles of V_2O_5 produced. Essentially, if the electrolyte's initial TMA^+ : V^V = 3 : 1, the electron stoichiometry is equal to ν_{e2} = f($H_4TMA_2V_{10}O_{28}$) = 5.6.

The following equation is a modified version of Equation 4-8 considering the two described electron stoichiometries.

$$w^e_{V_2O_5} = \frac{\left(\nu_{e,TMA^+:V^V} + \nu_{e,H_4TMA_2V_{10}O_{28}}\right) F \cdot |U|}{3.6 \Phi^e_{TMA^+} M_{V_2O_5}} \qquad \text{(Equation 4-23)}$$

$$\nu_{e,TMA^+:V^V} = \frac{[TMA^+]_i - 3[V^V]}{\frac{[V^V]}{\nu_{V:V_2O_5}}} \qquad \text{(Equation 4-24)}$$

Where $w^e_{V_2O_5}$ represents the specific electrical energy consumption per unit mass production of V_2O_5 in kW h t_{V2O5}^{-1}, $\nu_{e,TMA^+:V^V}$ the electron stoichiometry for the transport of excess TMA^+ to the cathode until TMA^+: V^V = 3:1, $\nu_{e,H_4TMA_2V_{10}O_{28}}$ is the electron stoichiometry for the formation of $H_4TMA_2V_{10}O_{28}$ deposits from $[TMA^+]_3[VO_4^{3-}]$, U represents the cell potential difference at pH 6, F the Faraday constant, $\Phi^e_{TMA^+}$ the charge yield until pH 6, $M_{V_2O_5}$ is the molar mass of V_2O_5 in g mol^{-1} and $\nu_{V:V_2O_5}$ the stoichiometric ratio of elemental vanadium to V_2O_5. $[TMA^+]$ is the initial concentration

of the TMA cations in in the anolyte (mol dm^{-3}), $[V^{V}]$ is the concentration of vanadium(V) in the anolyte.

Charge yield and cell potential difference are time dependant. For a continuous process of refining vanadium(V), specific pH has to be chosen as the operating pH which corresponds to a specific cell potential difference. The following sections report the electrical energy required for the continuous deposition of one tonne of V_2O_5 equivalent vanadium(V) aggregates onto the anode. The effect of the experimental conditions such as charge yields, and the cell potential differences were from when the anolyte pH was ca. 6 in Equation 4-23. This is because the deposition of the vanadium(V) aggregates was found to begin at pH 6.

4.3.3.1 Effect of Current Density

Figure 4-13 shows the effect of current density on charge yield, specific electrical energy consumption and cell potential difference at pH ca. 6. The results revealed that as the current density increased, the cell potential difference decreased which was also predicted by Equation 4-9 where it was shown that the ohmic potential drop is a function of current density. As the current density increased, the magnitude of the ohmic potential drop in the electrolyte, membrane, busbars etc. also increased. Ultimately, a higher current density resulted in a higher cell potential difference, which directly increased specific electrical energy consumptions, as predicted by Equation 4-23.

It can also be seen from Figure 4-13 that the charge yield decrease on increasing current densities from 700 to 1 000 A m^{-2} was significantly less than the charge yield decrease from 1 000 to 1 300 A m^{-2}, indicating that the mass transport rate to the membrane was the limiting factor for the transport of the TMA^{+} to the catholyte at lower current densities. Thus, increasing the current density from 1 000 to 1 300 A m^{-2} increased only the transport of protons to the catholyte which then reacted with the OH^{-} ions, wasting energy. A decrease in charge yield implies that a smaller fraction of the total energy input was used to generate the products, resulting in increasing specific electrical energy consumption.

Overall, high current densities such as 1 300 A m^{-2} not only decreased charge yield but also increased the cell potential difference both of which resulted in a higher specific electrical energy consumption.

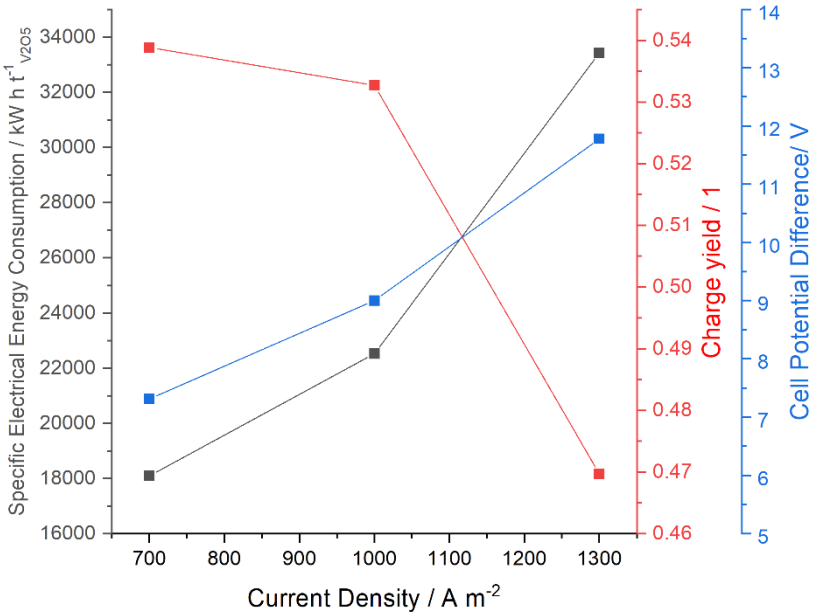


Figure 4-13. Effect of current density on both charge yield and specific electrical energy consumption. Initial TMA^+ concentration in anolyte = 2.78 mol dm^{-3}, initial vanadium(V) concentration in anolyte = 0.589 mol dm^{-3}

4.3.3.2 Effect of Initial Vanadium(V) Concentration

Figure 4-14 shows the effect of initial vanadium(V) concentration in the anolyte on charge yield, specific electrical energy consumption and cell potential difference. The results revealed that the cell potential decreased as the initial vanadium(V) concentration increased. According to Equation 4-9, the higher the conductivity of the electrolyte, the lower the ohmic potential drop. Hence, as the V^V concentration increased, the solution conductivity increased, resulting in lower cell potential differences. Figure 4-14 also shows that charge yields increased with increasing vanadium(V) concentration. This is because for greater vanadium(V) concentrations, protons generated at the anode would have a higher chance to react with the vanadium(V) species (see Reaction 4-12) rather than passing through the membrane to the catholyte and reacting with the generated OH^- which is considered as a waste of energy. Moreover, an increase in the vanadium concentration leads to a reduction of the TMA^+ electron stoichiometry ($\nu_{e,:TMA^+:V^V}$) as shown in Equation 4-23.

Overall, increasing vanadium(V) concentration decreased cell potential difference, increased charge yield and decreased electron stoichiometries, so decreasing specific electrical energy consumptions, as shown in Figure 4-14.

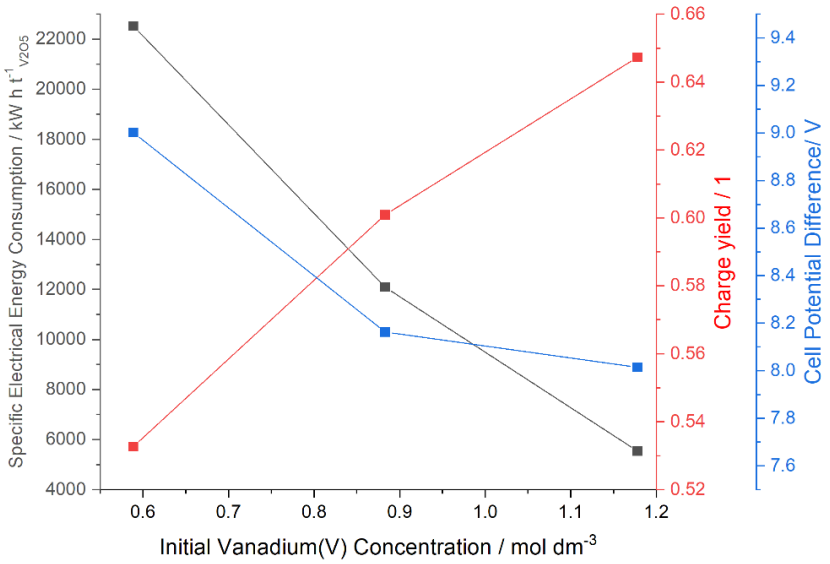


Figure 4-14. Effect of initial vanadium(V) concentration on charge yields and specific electrical energy consumptions. Initial TMA^+ concentration in anolyte = 2.78 mol dm^{-3}; current density = 1 000 A m^{-2}

4.3.3.3 Effect of initial TMA^+ Concentration in Anolyte

Figure 4-15 shows the effect of TMA^+ concentration in the anolyte on charge yield, specific electrical energy consumption and cell potential difference. The last term in Equation 4-9 implies that the cell potential difference is the sum of the ohmic potential losses due to current I (A) with path length d_i (m) passing through phase i of conductivity σ_i (A V^{-1} m^{-1}) and area A_i. In this set of experiments all the aforementioned parameters (I, d_i, σ_I, and A_i) stayed constant. It should be noted that although the initial TMA^+ concentrations were different, the y-axes in Figure 4-15 were calculated for when pH was 6, and so the TMA^+ concentrations theoretically were the same for all three scenarios. Hence, as Figure 4-15 also suggests, the cell potential differences were largely independent of initial TMA^+ concentrations as expected because all the parameters affecting the cell potential differences were constant for all three scenarios.

Nevertheless, charge yields decreased as the initial TMA^+ concentration increased. Decreased charge yields and increased electron stoichiometries together increased specific electrical energy consumptions as evident from Equation 4-23 and experimentally proven in Figure 4-15.

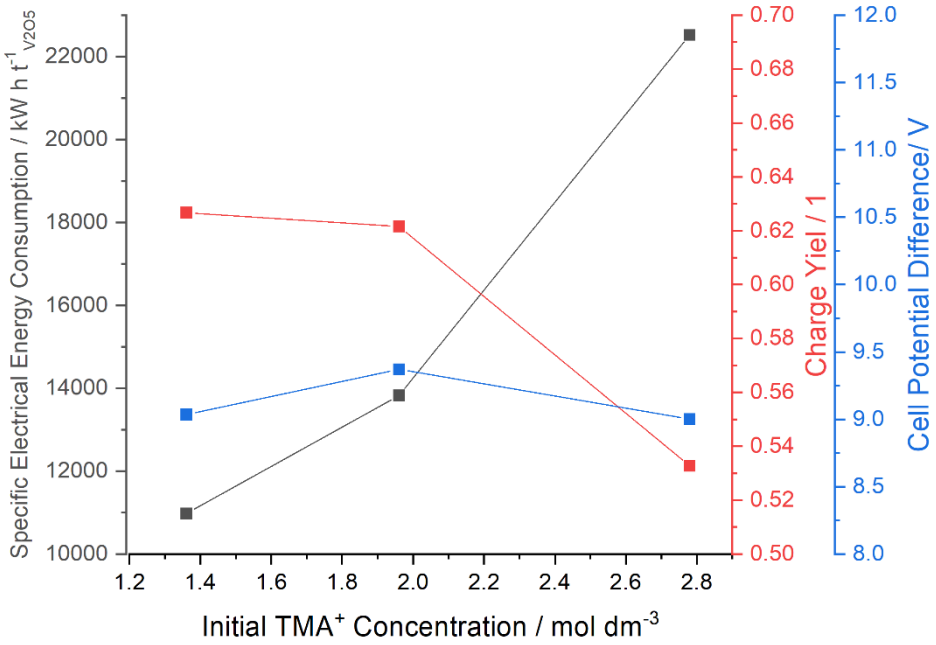


Figure 4-15. Effect of initial TMA^+ concentration on charge yield and specific electrical energy consumption. Initial vanadium(V) concentration in anolyte = 0.589 mol dm^{-3} , Current density = 1000 A m^{-2}

4.3.3.4 Specific Electrical Energy Consumption Summary

For an optimum single pass vanadium(V) leaching, the lowest electrical energy consumption was found to be ca. 11 000 kW h t^{-1}_{V2O5} for the case of 0.589 mol dm^{-3} V^V and 1.36 mol dm^{-3} TMA^+OH^-. Although it is crucial to minimise electrical consumption, factors such as leaching kinetics, vanadium extraction yield, vanadium deposition rate etc. are also important. Based on the results found from the Chapter 3, 0.883 mol dm^{-3} V^V and 2.78 mol dm^{-3} TMA^+OH^- could be a great operating point which corresponded to a specific electrical energy consumption of 12 100 kW h t^{-1}_{V2O5}. The vanadium(V) + TAM^+ electrolysis process is principally similar to the chloralkali process. With optimisation of the electrochemical cell design and the solution conductivity, the cell potential difference can be as low as the practical cell potential difference (3 V) used

in the chloralkali process[165], giving an optimised specific electrical consumption of 4 430 kW h t^{-1}_{V2O5}.

4.3.4 Deposition rate of vanadium(V) phases

The relationship between initial vanadium(V) concentration in the anolyte and the weight gain of the anode over time is shown in Figure 4-16 (a). The derivative of weight gain with respect to time, which is the slope of the trendline, provides an industrially crucial parameter that is deposition rate per unit area, Θ_{dr}. This parameter is utilised to estimate the electrode area required for a scaled-up process with a known throughput. Figure 4-16 (b) shows the deposition rate for the studied vanadium(V) concentrations. With an increase in vanadium(V) concentration, the deposition rate per unit area primarily increased and then decreased. When the initial vanadium(V) concentration was 0.883 mol dm^{-3}, the deposition rate reached its maximum value of 0.845 g m^{-2} s^{-1}. As the concentration of vanadium increased to 1.178 mol dm^{-3}, the deposition rate decreased from 0.845 to 0.665 g m^{-2} s^{-1}. This is because, in the process of deposition,

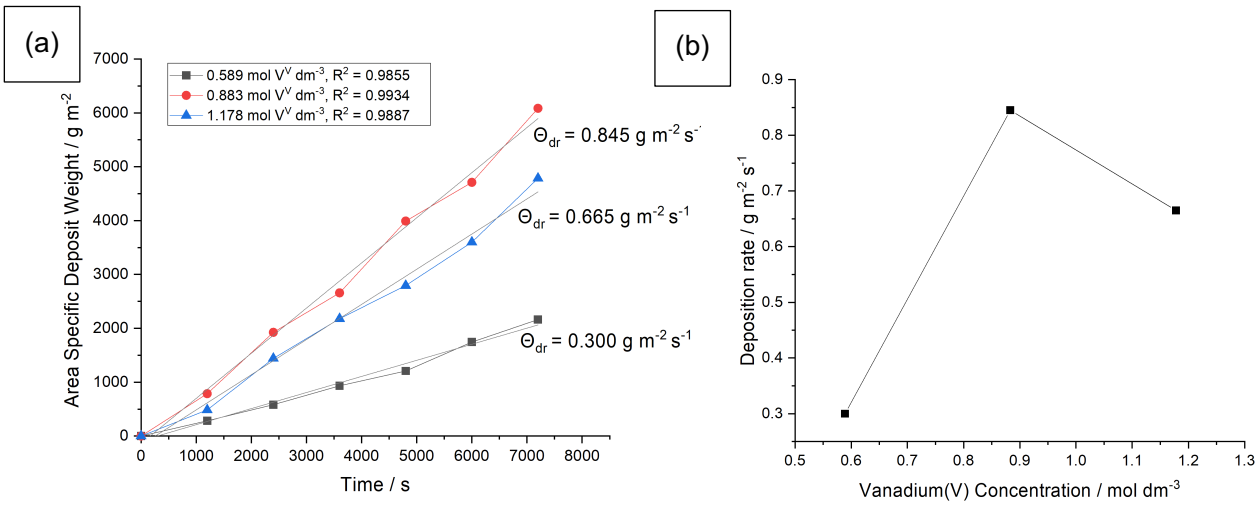


Figure 4-16. (a), left, Time dependence of measured weight of deposits per unit area of anode. (b), right, Effect of vanadium(V) concentration on deposition rate of deposits per unit area.

vanadium could not deposit independently of the anode solution, but it was possible to deposit with TMA^+ and H^+. When the concentration of vanadium increased, the concentration balance among every component was broken, which could influence the

deposition rate. This effect has been previously reported in the literature. In a study by Yu et al.,[166] a plateau shaped profile was reported for the deposition of NiFeW at different Na_2WO_4 concentrations.

4.3.5 TMA^+ Recovery from Residue

Quaternary ammonium ionic liquids are generally considered to be 'expensive' depending on the complexity of the cations, the type of anions, and the number of synthesis and purification steps. Hence, it is of great importance to accurately evaluate the recovery efficiency of each step involved in the ionic liquid/vanadium(V) recovery process. Liquid chromatography-mass spectroscopy is a powerful analytical technique with the capabilities of high-pressure liquid chromatography with lesser complexities integrated with a mass spectrometer for accurate quantification of ionic liquid in the left-over residue.

Tetramethylammonium cations have an integer mass to charge (m/z) ratio of 74. It can

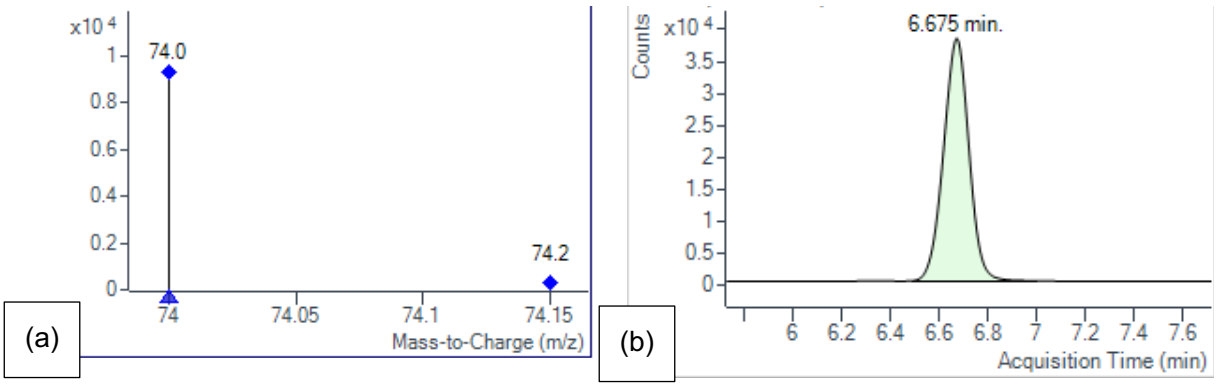


Figure 4-17 (a), left, Mass spectrum of TMA^+ and (b), right, Retention time of TMA^+ At 74 m/z.

be clearly seen from Figure 4-17(a) that the largest peak in the mass spectrum is at m/z = 74 along with a negligible peak at 74.2 which is an isotope. Figure 4-17(b) shows that the corresponding mass to charge ratio had a retention time of 6.675 minutes which was carefully monitored for the counts of the TMA^+ cations. Subsequently, a calibration line was constructed using 6 reference concentrations as shown in Figure 4-18 (a). Although the intercept was expected to be nil, this is not the case in this

calibration curve. The intercept value is negligible therefore it is reasonable to say the error is due to the system noise, especially in this case where $R^2 = 1$.

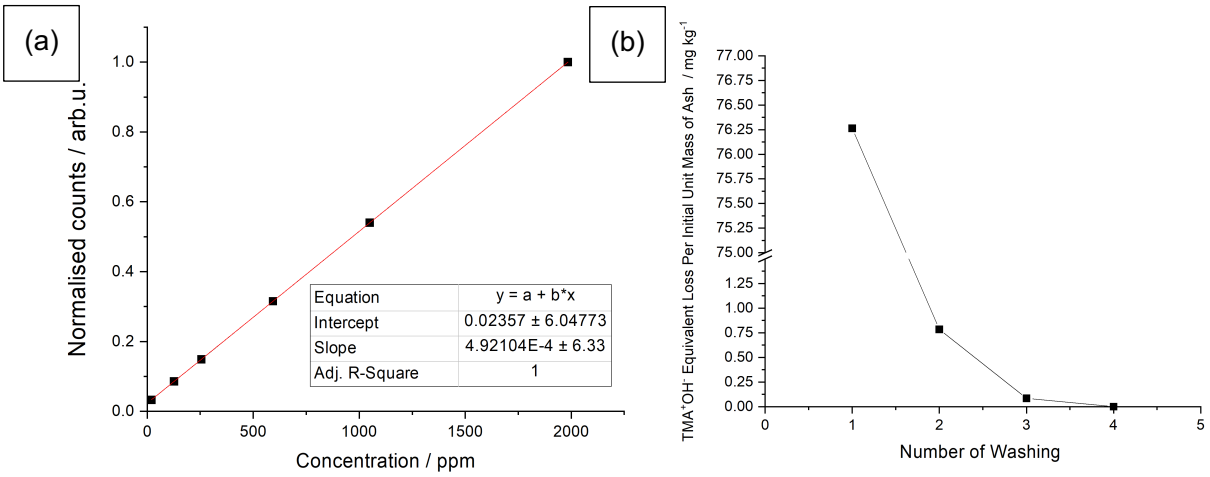


Figure 4-18 (a) Calibration curve for TMA+ concentration from LC-MS using 6 different reference solutions of TMA+OH-. (b) TMA+OH- equivalent loss per initial unit mass of ash for different number of washing steps.

Left-over residue contains TMAV which can be extracted using water or methanol. Methanol is superior to water for this application due to being extremely selective for the dissolution of TMAV whereas water may dissolve a wide range of metal oxides, depending on the solution pH. Consequently, the residue was re-suspended in methanol and then centrifuged to result in a clear top phase called the first washing. This cycle was repeated, and the top phase of each sample was analysed via LC-MS for TMA^+ concentration determination in the wash. Figure 4-18 (b) shows TMA^+OH^- equivalent loss per unit mass of raw ash used for the extraction of vanadium. The results suggest that each washing step reduced the TMA^+ concentration in the residue by approximately 90 % until the third washing after which the TMA^+ concentration went below the detection limit of the LC-MS detector. In other words, the residue became TMA^+ free after four washings, according to the best available technique.

4.3.6 Vanadium(V) Processing routes

As stated in section 4.3.1, aggregates of $H_4TMA_2V_{10}O_{28}$ started to deposit on the surface of the Ti/Ta_2O_5-IrO_2 electrode and once the solution pH < 3, precipitates of

$H_3TMA_3V_{10}O_{28}$ started to appear in the anolyte, which were highly undesirable. The solution heterogeneity led to the membrane blockage and eventually a sharp increase in the cell potential difference to maintain the set current for instance, the cell potential difference reading was momentarily as high as 14 V. Sometimes, the overhead mixer stopped working due to the formation of large sticky lumps of $H_3TMA_3V_{10}O_{28}$ between the anode and the impeller, especially for the solutions containing a high initial concentration of vanadium(V). Reaction 4-12 which is essentially acid/base neutralisation reaction (also called the condensation reaction), can be balanced for the formation of $H_3TMA_3V_{10}O_{28}$ as represented by Reaction 4-17 below:

For solution pH < 3:

$$30\ TMA^+ + 10\ VO_4^{3-}(aq) + 27\ H^+(aq) \rightarrow$$

$$H_3TMA_3V_{10}O_{28}\ (s)\ 12\ H_2O + 27\ TMA^+ \qquad \text{(Reaction 4-17)}$$

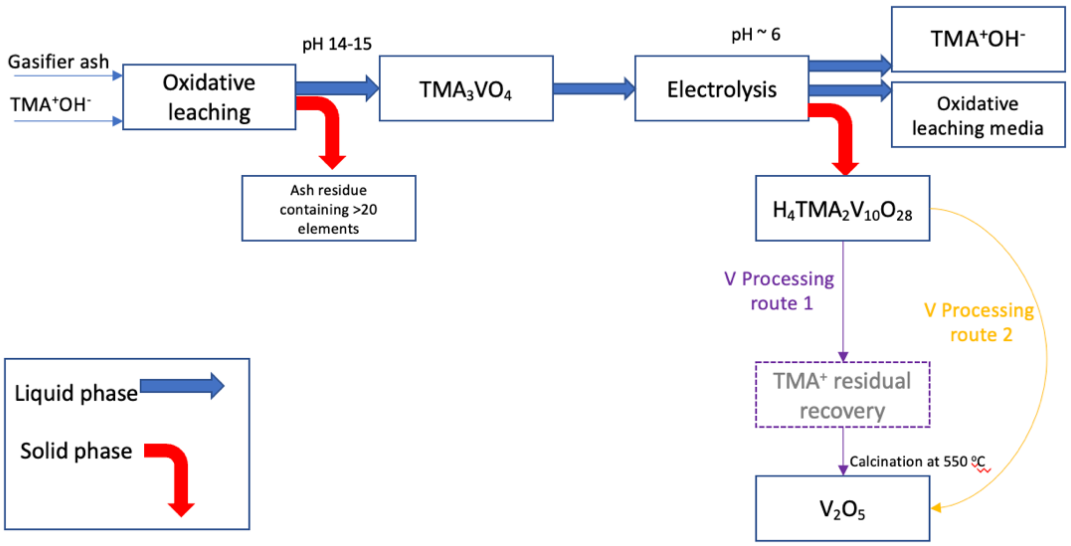


Figure 4-19 Simplified process flow diagram of the ionoLeach process to produce pure V_2O_5 by membrane electrolysis, depicted for the two vanadium processing routes.

To avoid the troublesome $H_3TMA_3V_{10}O_{28}$ precipitates, the operating pH was maintained at pH = 5 – 6, at which aggregates of vanadium(V) compounds were deposited onto the anode. A simplified process diagram of the ionoLeach process is shown in Figure 4-19, in which TMAV solutions are electrolysed until a solution pH of 6, and the resulting deposits are treated with the corresponding Vanadium(V) Processing Routes explained below:

4.3.6.1 Vanadium Processing route 1

Vanadium(V) Processing Route 1 describes an approach by which ultra-pure vanadium pentoxide is synthesised from gasifier ash with no ongoing chemical requirement. To achieve this, the loss of TMA^+ must be minimised in both the post-reaction residual ash, to be discarded/sold, and the TMA^+ ions that formed vanadium(V) aggregates during membrane electrolysis. The residual TMA^+ (and the vanadate) was recovered from the post-reaction ash through methanol scrubbing, as explained in **4.3.5**. To maximise TMA^+ recovery from the electrolysis process, a processing step was integrated with the ionoLeach process to recover the 'locked' TMA^+ from the deposits of $H_4TMA_2V_{10}O_{28}$.

Vanadium(V) Processing Route 1 Description:

A solution of TMAV was electrolysed in the membrane-divided electrochemical reactor under the following experimental conditions: current density of 1 000 A m^{-2}, TMA^+ concentration of 2.78 mol dm^{-3} and vanadium(V) concentration of 0.883 mol dm^{-3}. The starting pH was ca. 14. As the electrolysis process proceeded, the anolyte pH decreased and $H_4TMA_2V_{10}O_{28}$, its diffractogram shown in Figure 4-2(b), started to deposit onto the anode. The deposits were scraped from the anode, and it was replaced in the anode chamber. Subsequently, the solution pH was increased by addition of excess TMAV solution, and the electrolysis was continued. This cycle can be repeated, and the solids can be collected in a semi-batch mode. On larger scales, this process can be arguably performed continuous using rotary drum electrodes and knife blades, continuous feed of TMAV and removal of TMA^+OH^- from the cathode.

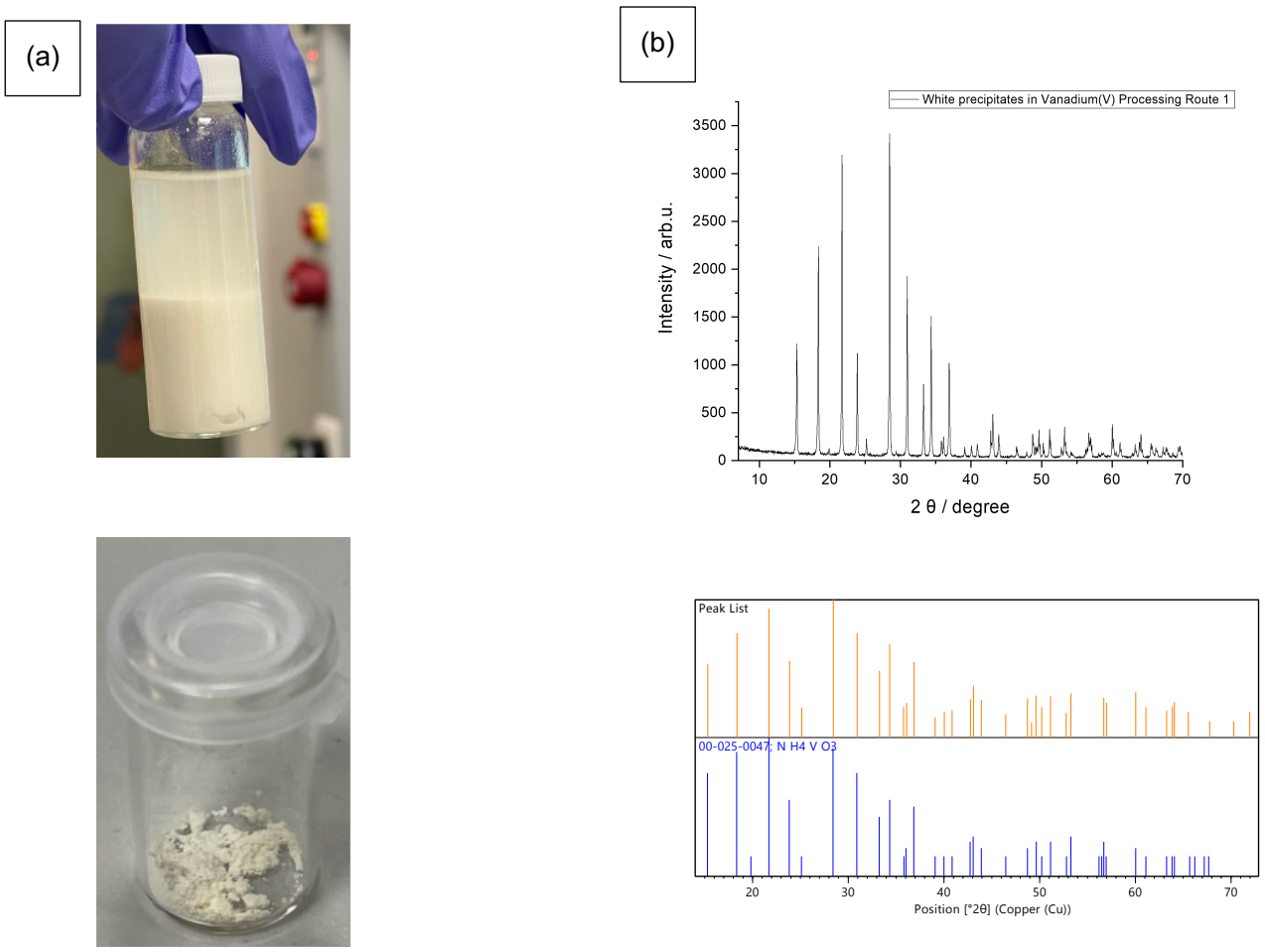


Figure 4-20 Control compound – (a) left, Post-reaction suspension and dried solids of the AMV reaction and (b), right, X-ray diffraction pattern of the white solids recovered from the precipitates from the ammonia exchange process (Reaction 4-8).

The collected $H_4TMA_2V_{10}O_{28}$ solids were mixed with water, methanol, and ammonium hydroxide, with methanol not participating in the ammonium metavanadate (AMV) precipitation reaction (see Reaction 4-8) but acting only as an antisolvent. After drying in a vacuum oven at 60 °C overnight, the product of this reaction was a white crystalline precipitate of ammonium metavanadate (NH_4VO_3), the diffractogram of which is shown in Figure 4-20(b).

Subsequently, the recovered NH_4VO_3 was calcined in a furnace. Calcination of ammonium metavanadate is very common in the vanadium processing industry to obtain pure vanadium pentoxide. Industrially, the ammonia generated from the calcination reaction would be recycled back to the process as indicated by Reaction

4-19 and Reaction 4-20. Hence, there would be no ongoing chemical use in this Vanadium(V) Processing route, in which only one mole of water is produced, as indicated by Reaction 4-20 which is the overall reaction.

AMV precipitation reaction

Table 4-1. Kinetics study of Reaction 4-8 with three variables: temperature, NH_4OH concentration, and $H_4TMA_2V_{10}O_{28}$ loading.

$$H_4TMA_2V_{10}O_{28}(aq) + 10\ NH_4OH\ (aq) \xrightarrow{\text{in methanol}}$$

$$10\ NH_4VO_3(s) + 2\ TMA^+ + 2\ OH^- + 6H_2O\ (l) \qquad \text{(Reaction 4-18)}$$

$$10\ NH_4VO_3 \rightarrow 5\ V_2O_5 + 10\ NH_3 + 5\ H_2O \qquad \text{(Reaction 4-19)}$$

$$10\ NH_3 + 10\ H_2O \rightarrow 10\ NH_4OH \qquad \text{(Reaction 4-20)}$$

Overall

$$H_4TMA_2V_{10}O_{28}(aq) \rightarrow$$

$$5\ V_2O_5\ (c, pure) + 2\ TMA^+OH^- + H_2O \qquad \text{(Reaction 4-21)}$$

The kinetics of the AMV precipitation reaction were recognized to be dependent on the: (i) reaction temperature (ii) NH_4OH concentration and (iii) mass loading of $H_4TMA_2V_{10}O_{28}$ in the ternary mixture of water-ammonia-methanol. Table 4-1 shows the reaction kinetics results for the conditions studied. Completion of the reaction was indicated when the solution colour changed from yellowish to white; then the corresponding time was recorded. According to the results, temperature and ammonium hydroxide concentration were directly proportional to the reaction kinetics.

Reaction completion time / min	Temperature / °C	28 wt% NH_4OH (in water) loading in methanol / (V/V)%	H4TMA2V10O28 loading / g dm-3
45	45	70	50
60	45	70	100
60	45	50	75
90	35	70	75
255	35	50	75
255	35	50	100
255	35	50	50
255	45	30	50
330	35	50	75
330	45	30	100
450	25	70	50
1day	25	70	100
1 day	35	30	75
1.5 days	25	50	75
-	25	30	100
-	25	30	50

The fastest reaction kinetics were achieved for the case of the highest studied temperature (45 °C), the greatest ammonia solution concentration (70 v/v%) and smallest $H_4TMA_2V_{10}O_{28}$ concentration (50 g dm^{-3}). Interestingly, the solution never turned white (i.e., AMV never formed) when both the temperature and the ammonia

loading were set to their lowest values. In summary, the ammonia exchange kinetics were favoured for higher temperatures, followed by higher ammonia loadings and finally lower slurry density.

The collected NH_4VO_3 was dried on a filter paper in a fume hood under ambient temperature. The calcination of the dried AMV was performed at 550 °C for a total duration of up to 3 hours. The calcination procedure was similar to that of frequently reported in the literature[167-169]: The XRD pattern of the resulting V_2O_5 is shown in Figure 4-21(b).

4.3.6.2 Vanadium(V) Processing route 2

The previous route (Vanadium Processing route 1) was designed for the maximum recovery of TMA^+ with no ongoing chemical use, at the cost of process complexity. From an industrial point of view, it has CAPEX implications with arguably lower operating costs implications than for Vanadium(V) Processing Route 2, in which the process complexity was decreased at the cost of higher operating costs.

Vanadium Processing Route 2 Description:

A solution of TMAV was electrolysed in the membrane-divided electrochemical reactor under the following experimental conditions: current density of 1 000 A m^{-2}, TMA^+ concentration of 2.78 mol dm^{-3} and vanadium(V) concentration of 0.883 mol dm^{-3} corresponding to an initial pH of ca. 14. As the electrolysis process proceeded, the anolyte pH decreased and $H_4TMA_2V_{10}O_{28}$ started to deposit onto the anode. The deposits were eliminated by mechanical means and the anode was replaced in the anode chamber. Subsequently, the solution pH was increased by addition of excess TMAV solution, and the electrolysis was continued. This cycle can be repeated, and the solids were collected in a semi-batch mode. In larger scales, this process can be performed continuously using rotary drum electrodes and knife blades, with continuous feed of TMAV into the anolyte and removal of TMA^+OH^- from the catholyte, if the practical challenges of building such electrochemical reactors could be overcome. The collected $H_4TMA_2V_{10}O_{28}$ was calcined in a programmable muffle oven at 550 °C for up to 3 hours, bypassing the residual TMA cation recovery. The resulting product was pure V_2O_5 with an X-ray diffraction pattern identical to that in Figure 4-21(b).

Thermal decomposition of $H_4TMA_2V_{10}O_{28}$ generated N_2, CO_2, H_2O and V_2O_5, so TMA^+ cations were lost. This is the simplest method by which most of the TMA^+ was

recovered in the catholyte and some was lost due to direct calcination of vanadium(V) aggregates i.e., 2 moles of TMA^+ per could be lost per 10 moles of V^V recovered. For every 1000 kg of V_2O_5 produced, 200 kg of TMA^+OH^- equivalent would be lost in this vanadium(V) processing route.

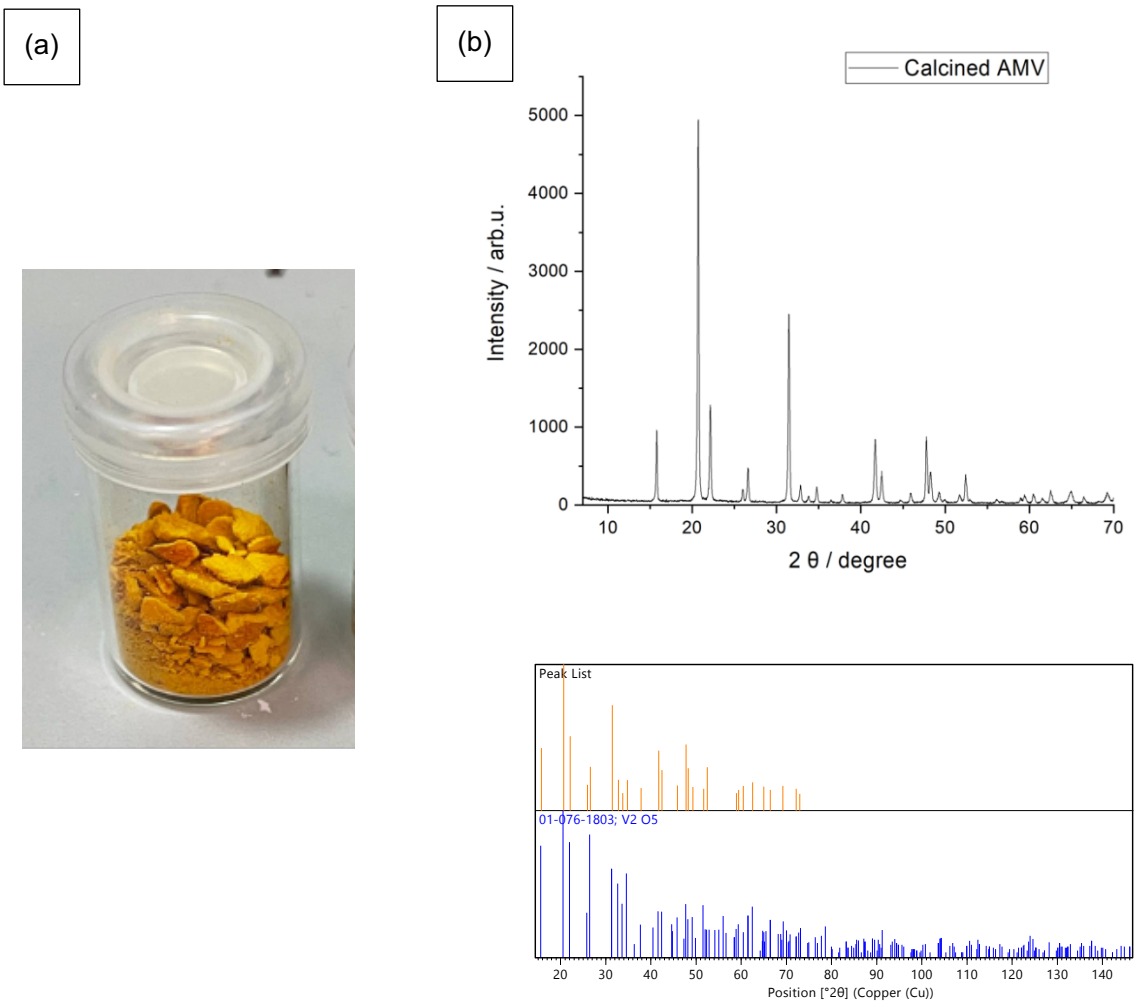


Figure 4-21. (a), Control compound - left, Lumps of V2O5 collected after calcination of NH_4VO_3 and (b), right, X-ray diffraction pattern of the calcination product which was identical to the V_2O_5 reference patterns.

4.3.7 Characterisation of the vanadium(V) aggregates

4.3.7.1 Core Structure Determination

A wide range of techniques was used to investigate the chemical structure of the deposited and precipitated vanadium(V) aggregates in the anode chamber. Figure 4-6 was employed as the roadmap for the determination of the thermodynamically stable vanadium species as a function of pH in the aqueous electrochemical system.

It was observed that the vanadium(V) aggregates started to deposit onto the surface of the anode when the anolyte solution pH reached ca. pH = 6, but the precipitates were not formed until pH < 3. Combining this with the potential-pH diagram (Figure 4-6), which did not consider TMA^+ ions, it can be deduced that the recovered solid materials have a general formula of $H_xTMA_yV_{10}O_{28}$ where x + y = 6.

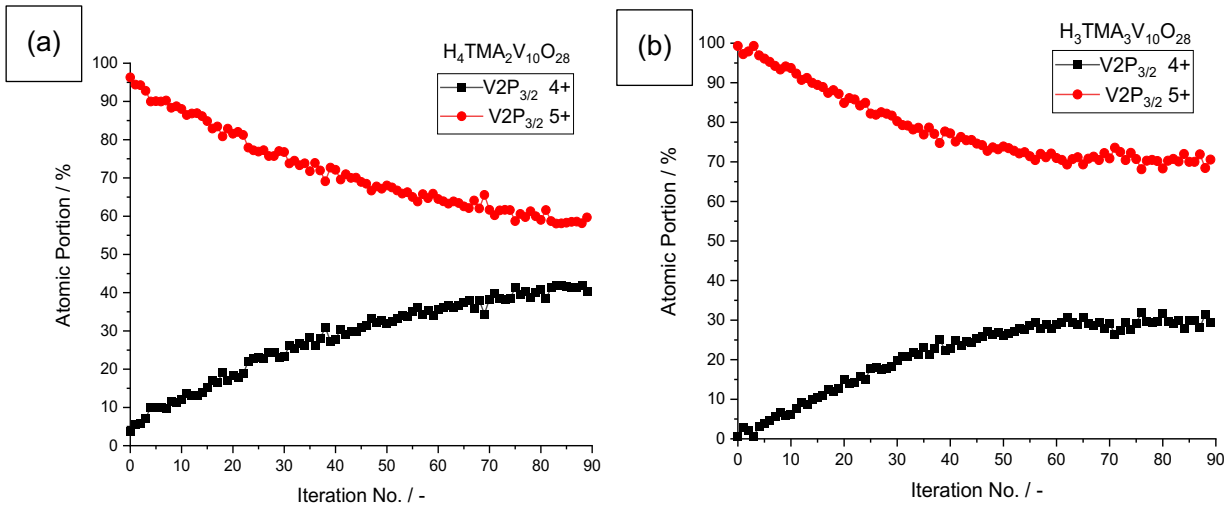


Figure 4-22. Data from X-ray photoelectron spectroscopy (XPS) of vanadium(V) aggregates and precipitates: atomic percent of V^{IV} and V^{V} in the $V2P_{3/2}$ environment as a function of iteration number. Each iteration is 3 scans for 0.15 s each at a power of 80 W on an area of 400 μm^2 (a), left, for the deposited vanadium aggregates onto the surface of the electrode for a solution pH of 3 < pH <6 and (b), right, for compounds precipitated from anolyte at pH < 3.

XPS iterations were performed on a specific point of the sample from which two distinct peaks were detected within the $V2P_{3/2}$ region. The atomic percent of each curve was analysed via the Avantage software, and the results are shown for the deposited and the precipitated vanadium aggregates in Figure 4-22 (a) and (b), respectively. The

iterations were performed under ultrahigh vacuum (UHV) conditions in which samples were subjected to pressures of $8x10^{-9}$ kPa in the analysis chamber. Each iteration consisted of 3 scans for 0.15 s each at a power of 80 W on an area of 400 μm^2. Lack of oxygen and applying high energy density to the sample commonly cause self-oxidation of organic compounds, resulting in the formation of CO_2 gas in the XPS chamber.[170] This phenomenon is analogous to what is shown in Figure 4-22 (a) and (b). The absence of oxygen and the introduction of such high energy density via X-rays (photons) incident on the sample caused the self-reduction of $H_xTMA_yV_{10}O_{28}$ via the donated electrons by the V^V species. Therefore, as the iteration number increased, the V^V atomic portion decreased, while the V^{IV} atomic portion increased in both plots. The data reached a steady state at which the atomic portion did not change with increasing iteration number, because all the protons in $H_xTMA_yV_{10}O_{28}$ aggregates were used to reduce the vanadium. When the iteration started, there were 10 moles of V^V in each mole of vanadium aggregate material ($H_xTMA_yV_{10}O_{28}$). In Figure 4-22 (a), the vanadium atomic portion is split into 6 moles of V^V and 4 moles of V^{IV} after 89 iterations. Hence, 4 moles of H^+ resulted in the reduction of 4 moles of V^V to V^{IV}, so x =4 in $H_xTMA_yV_{10}O_{28}$. Knowing x + y = 6, it can be concluded that the deposited materials had a chemical formula of $H_4TMA_2V_{10}O_{28}$.

Similarly, Figure 4-22(b) was utilised to establish the chemical formula of the precipitated vanadium aggregate material as undergo self-reduction under XPS conditions. According to these results, the precipitated vanadium(V) aggregates had a chemical formula of $H_3TMA_3V_{10}O_{28}$. The possible reaction mechanism for the self-reduction of the deposited and the precipitated materials are proposed by Reaction 4-23 and Reaction 4-26, respectively.

Oxidation

$$H_4TMA_2V_{10}O_{28} \rightarrow {H_4TMA_2V_{10}O_{28}}^{4+} + 4e^- \qquad \text{(Reaction 4-22)}$$

Reduction

$$4e^- + {H_4TMA_2V_{10}O_{28}}^{4+} \rightarrow 2H_2O + TMA_2(4\,V^{IV} + 6\,V^{V})O_{26} \qquad \text{(Reaction 4-23)}$$

Overall

$$H_4TMA_2V_{10}O_{28} \xrightarrow{\text{X-ray energy}}$$

$$2H_2O + TMA_2(4\,V^{IV} + 6\,V^{V})O_{26} \qquad \text{(Reaction 4-24)}$$

Similarly for the precipitated aggregates:

Oxidation

$$H_3TMA_3V_{10}O_{28} \rightarrow H_3TMA_3V_{10}O_{28}{}^{3+} + 3\,e^- \qquad \text{(Reaction 4-25)}$$

Reduction

$$3\,e^- + H_3TMA_3V_{10}O_{28}{}^{3+} \rightarrow$$

$$1.5\,H_2O + TMA_3\,(\,3\,V^{IV} + 7\,V^{V})O_{26.5} \qquad \text{(Reaction 4-26)}$$

Overall

$$H_3TMA_3V_{10}O_{28} \xrightarrow{\text{X-ray energy}}$$

$$1.5H_2O + TMA_2(\,3\,V^{IV} + 7\,V^{V})O_{26.5} \qquad \text{(Reaction 4-27)}$$

The inferred chemical species of $H_4V_{10}O_{28}^{2-}$ and $H_3V_{10}O_{28}^{3-}$ are different to that of those known to exist in aqueous solutions, which are commonly depicted in activity-pH diagrams of V-H_2O such as Figure 4-7. A possible explanation for the formation of these unprecedented compounds is that polyoxometalates (POMs) like the decavanadate anion can accept or donate electrons. The anions of $H_nV_{10}O_{28}^{(6-n)-}$ undergo multiple steps of protonation depending on the solution pH. As the pH is decreased the 'n' value is increased up to a certain protonation state where the cation constructs stable aggregates with the protonated decavanadate. The results revealed that tetramethylammonium cations facilitated the construction of solid-state clusters with the triprotonated decavanadate ($H_3V_{10}O_{28}^{3-}$) when the solution pH < 3 and aggregates of tetraprotonated decavanadate ($H_4V_{10}O_{28}^{2-}$) at the surface of the anode where anode surface pH << bulk pH. This is analogous to the findings by Dewan et al., [171] who reported the synthesis and characterisation of a triprotonated decavanadate ($H_3V_{10}O_{28}^{3-}$) with tetraalkylammonium salts. According to their study: 'Intermolecular O-H...O hydrogen bonds involving the surface protons leads to the formation of an unprecedented zigzag chain of the $H_3V_{10}O_{28}^{3-}$ anions.' Truebenbach et al. [172] detected $H_4V_{10}O_{28}^{2-}$ ions in the characterization of isopoly metal oxyanions using electrospray time-of-flight mass spectrometry. They attributed the formation of these unique species to the limitation of protonation and solvation of the protonated decavanadate at different pH.

4.3.7.2 Stoichiometric Determination of Hydrates

The aggregates exist in the form of hydrated ions. Upon heating the samples to high temperatures, the aggregates decomposed to solid V_2O_5 and volatile compounds. The stoichiometric ratio of the hydrates was determined by the thermogravimetric analysis (TGA) technique.

Complete dehydration of $H_4TMA_2V_{10}O_{28}.xH_2O$ (Figure 4-23 (a)) did not occur until approximately 350 °C with the net weight loss of 8.3 % in the 50-350 °C range which corresponds very well with the loss of all the water molecules present in $H_4TMA_2V_{10}O_{28}.5H_2O$, 8.4 %. On the other hand, the net weight loss due to the decomposition of dehydrated $H_4TMA_2V_{10}O_{28}.5H_2O$ (i.e., $H_4TMA_2V_{10}O_{28}$) to V_2O_5 from 350 °C onwards was calculated to be 15.7 %. Hence, the net weight loss due to the decomposition of the entire volatile components was calculated to be 24 %. What is interesting about the data in Figure 4-23 (a) is the clear evidence of reoxidation (weight

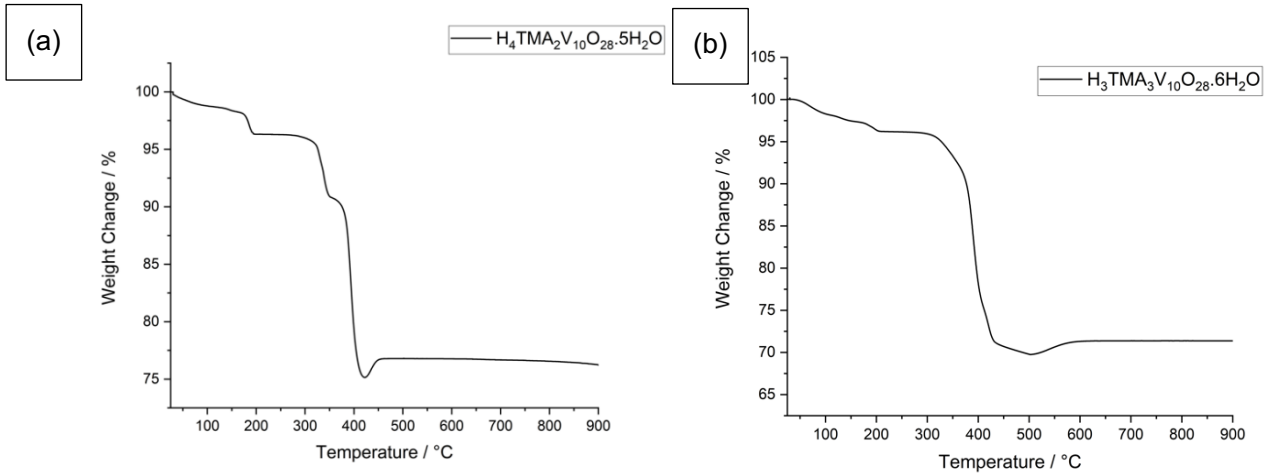


Figure 4-23. Thermogravimetric analysis (TAG) data for formation of V_2O_5 by decomposition of (a), left, $H_4TMA_2V_{10}O_{28}.5H_2O$, MW = 1199.75 g mol^{-1} and (b), right, $H_3TMA_3V_{10}O_{28}.6H_2O$, MW = 1290.89 g mol^{-1}.

gain) of V^{IV} starting at 410 °C, which is in agreement with the XPS results. Upon continued heating the net weight change reached a steady state value of 76.6 %, closing the mass balance together with the composition of the volatile compounds with less than 1 % error.

Assuming complete dehydration of $H_3TMA_3V_{10}O_{28}.xH_2O$ (Figure 4-23 (b)) occurred at around the same temperature as the deposited aggregates, the net weight loss of 7.2 % in the 50-350 °C range was attributed to the loss of the water molecules in $H_3TMA_3V_{10}O_{28}.6H_2O$, 7.5 %. On the other hand, the net weight loss due to the decomposition of dehydrated $H_3TMA_3V_{10}O_{28}.6H_2O$ (i.e. $H_3TMA_3V_{10}O_{28}$) to V_2O_5 was calculated to be 21.2 %. Hence, the net weight loss due to the decomposition of the entire volatile compounds was 28.7 %. Reoxidation of V^{IV} is evident from the TGA curve, which is in agreement with the XPS results. Upon continued heating, the net weight change reached a steady state of 70.4 %, closing the mass balance together with the composition of the volatile compounds with less than 1 % error.

4.4 Conclusions

Membrane electrolysis of $[TMA]_3[VO_4]$ resulted in the recovery of TMA^+OH^- to the catholyte, leading to an increase in the solution pH over time. In the anolyte, the pH decreased over time due to the continuous removal of TMA^+ ions by migration through the cation-permeable membrane and neutralisation of OH^- ions by the protons generated by water oxidation at the anode. As the anolyte pH decreased, TMA^+ polyoxovanadates underwent stepwise protonation, replacing the TMA^+ ions. When the solution pH = 6, aggregates of vanadium(V) compounds, with the chemical formula of $H_4TMA_2V_{10}O_{28}.5H_2O$, started to deposit onto the surface of the anode. As the electrolysis proceeded and the solution pH < 3, new vanadium(V) aggregates with the chemical formula of $H_3TMA_3V_{10}O_{28}.6H_2O$ appeared in the anolyte. This was highly undesirable because the aggregates led to membrane blockage and eventually a sharp increase in the cell potential difference at constant current density.

To avoid the troublesome $H_3TMA_3V_{10}O_{28}.6H_2O$ precipitates, the operating pH had to be maintained at pH = 5 – 6, at which aggregates of vanadium(V) compound(s) were deposited onto the anode. Two vanadium processing routes were proposed in this project:

1) The vanadium(V) aggregates deposit continuously onto the surface of the anode when the solution pH = 5-6. Using a ternary ammonia-methanol-water mixture, it is possible to synthesise NH_4VO_4 from $H_4TMA_2V_{10}O_{28}.5H_2O$ while recovering the ‘locked’ TMA^+ ions from the deposited materials. Calcination of NH_4VO_4 results in the formation of recyclable ammonia gas and crystalline

V_2O_5. This process was designed to produce ultra-pure vanadium pentoxide from the gasifier ash with no ongoing chemical requirement, at the cost of higher process complexity.

2) In this vanadium(V) processing route, the vanadium deposit ($H_4TMA_2V_{10}O_{28}.5H_2O$) is calcined directly to V_2O_5, leading to a loss equivalent to 200 kg worth of TMA^+OH^- per 1 000 kg V_2O_5 produced.

To maximise recovery of both TMA^+ ions and vanadium(V), LC-MS results showed that the residue become TMA^+ free after resuspending the residue in methanol four times at a solid to liquid ratio of 1 g residue: 2 cm^3 fresh methanol.

The optimum deposition rate onto the anode was found to be 0.845 g m^{-2} s^{-1} for the following conditions: initial [TMA^+] = 2.78 mol dm^{-3}, initial [V^V] = 0.883 mol dm^{-3} and j = 1 000 A m^{-2}, leading to a specific electrical energy consumption of 12 100 kW h t^{-1}_{V2O5} with a cell potential difference (U) of 8.2 V and an apparent charge yield of 0.6. With optimisation of the electrochemical cell design and the solution conductivity, the cell potential difference is expected to be decreased to 3 V, giving an optimised specific electrical consumption of 4 430 kW h t^{-1}_{V2O5}.

5. Indirect electrochemical oxidation of the gasifier ash: Practical procedure to maximise the extraction of vanadium from the gasifier ash

5.1 Introduction

This chapter combines the findings from the previous chapters with the electrooxidation technique to provide insights for maximizing the recovery of vanadium(V) while minimizing the effort required for post-reaction cleaning processes.

When it comes to designing a technique for hydrometallurgical extraction of vanadium oxides from sources other than the conventional vanadium bearing magnetite ores, it is of absolute necessity to have a good understanding on the nature of vanadium oxides as well as the rest of metal oxides. Vanadium-bearing slags contain high oxidation state vanadium oxide as well as low oxidation state vanadium. Therefore, the vast majority of the published research on the extraction of vanadium from vanadium-rich steel slags highlighted the use of roasting-assisted leaching processes that served two purposes: (i) oxidation of low oxidation state vanadium, (ii) production of a water-soluble vanadate phase at the cost of producing highly hazardous exhaust gasses.[63] Several publications describe the sub-molten salt (SMS) process, to overcome the salt-roasting environmental problems. The process utilises the leaching of vanadium-bearing feedstocks in oxidising highly alkaline solutions, such as NaOH/KOH with $NaNO_3$ at 200-400 °C, enabling vanadium(V) extraction yields of up to 95 %.[50,173,174] The metals separation/purification downstream are particularly dependant on the nature of the vanadium slag and have long been a challenge in the hydrometallurgy industry.[63]

A secondary source of vanadium can be gasifier ash obtained from the gasification of refinery feedstocks, involving high-temperature partial oxidation of coke to produce syngas. Due to the oxygen deficiency in the gasification process, partially oxidised vanadium materials were detected in the gasifier ash sample, as explained in Chapter 3. Subsequently, it was demonstrated that the vanadium extraction kinetics increased significantly when sodium chlorite was introduced to the TMA^+OH^- solution, without which the oxidation of low oxidation state vanadium occurred by the dissolved oxygen alone at atmospheric pressure. It was evident that during the oxidative leaching of vanadium oxide materials, sodium chlorite was consumed in the aqueous phase, which is economically unviable and environmentally unsustainable for scale-up purposes.

Electrobleaching is a process by which hypochlorite is produced by electrooxidation of chloride ions at the anode of an undivided electrochemical reactor. One of the main

advantages of electrobleaching over conventional chemical bleaching is that the reduced form of the oxidant in the electrolyte is regenerated in-situ. This technique has been reported for the whitening of yellowish matter in cellulosic materials such as cotton fabrics which regenerates the precursor chloride ions in the aqueous phase. The available literature has particularly focused on alkali metal hypochlorites, such as sodium and potassium.[175-177] Ionic liquids (ILs) are frequently known as 'designer solvents', because of the significant degree of fine-tuning of their physio-chemical properties offered by modification of their constituent anions and cations. These tuneable properties were used to advantage to maintain process circularity, i.e. no on-going chemical use for the extraction of vanadium(V) from gasifier ash.

The idea in this part of the project is to generate hypochlorite via an electrochemical procedure merely in the presence TMA^+ cations to avoid cross contaminations. The generated quaternary ammonium hypochlorite which is an oxidising agent can oxidise low valence vanadium compounds to some forms of vanadium(V) compounds in the gasifier ash which then be leached to the solution. Electrochemical generation of quaternary ammonium hypohalite salts was reported by Boal et al.,[178] in 2012.

The objectives of this part of the project were to:

- Demonstrate electrooxidation of low valence vanadium in the gasifier ash using in-situ generated hypochlorite with tetramethylammonium counter ions.
- Describe the purity of the leached vanadium(V) in the leach liquor and in the electrodeposited materials.
- Investigate the feasibility for the direct use of the deposited materials such as $H_4TMA_2V_{10}O_{28}$ to synthesise VRFB electrolyte.

5.2 Methodology

5.2.1 Electrooxidation experimental setup

Figure 5-1 shows a schematic diagram of the undivided electrolysis experiment.

A 40 mm × 40 mm 316 stainless steel plate was used as the cathode and a 40 mm ×40 mm dimensionally stable anode (DSA) RuO_2 coated titanium electrode – DSA-Ti/RuO_2 was used as the anode. Ruthenium dioxide was chosen because it is widely

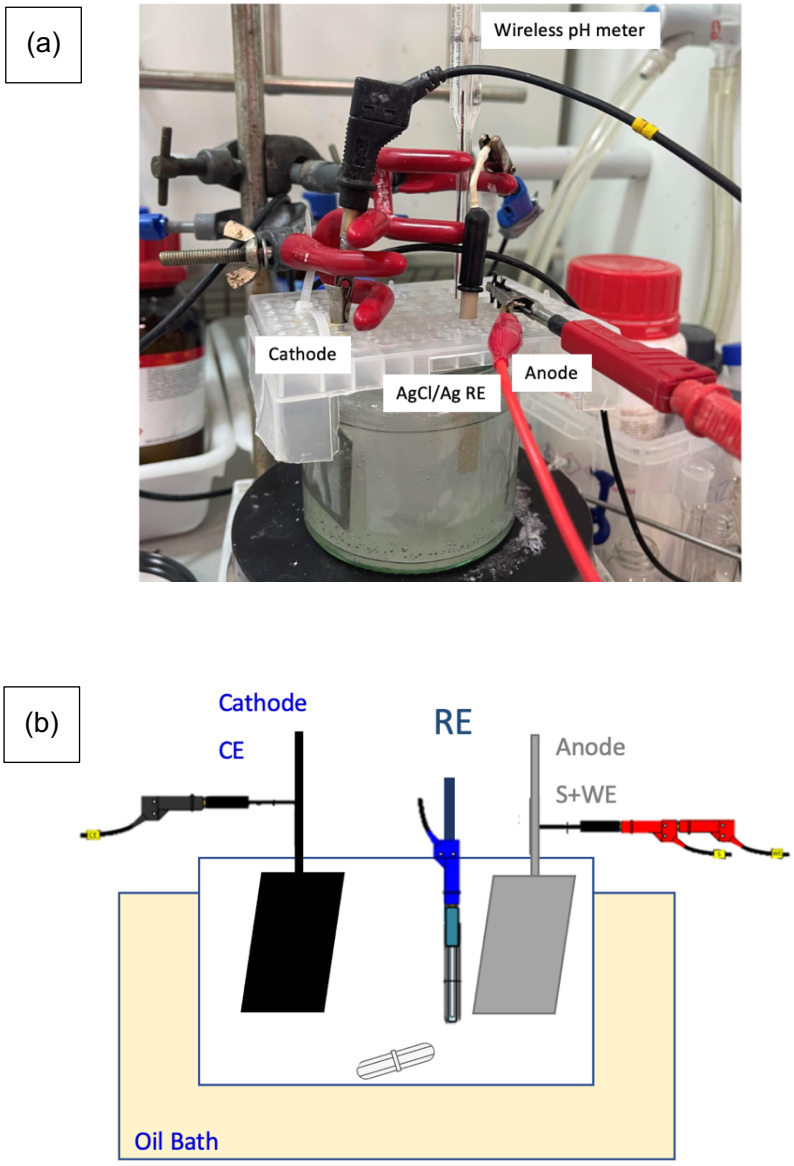


Figure 5-1. (a) Real picture and (b) schematic of undivided electrochemical reactor. The anode was a dimesonally stable RuO_2 coated titanium electrode (DSA-Ti/RuO_2) connected to the S+WE connectors, the counter electrode (CE) (cathode) was stainless steel 316 and the Ag/AgCl reference electrode. Solution was agitated using a magnetic stirrer bar.

known as a chlorine evolution catalyst and is commonly used as in the Chlor-alkali industry.[179] Parameters such as inter-electrode gap, area ratio of the electrodes and electrode materials all remained constant throughout the electrolysis experiments. A third electrode served as a reference electrode, which was a leak-free AgCl/Ag in 3

mol dm^{-3} KCl reference electrode (model LF-5-100, ALVATEK, Southampton, UK). The purpose of the reference electrode was to monitor the electrode potential against the reference electrode potential.

Similar to the membrane electrolysis experiments, the undivided electrolysis experiments were performed in three-electrode system mode with current flowing between the counter electrode (CE) and the working electrode (WE). The experiments were conducted in galvanostatic mode, i.e., constant current while monitoring the cell potential difference.

As the solution was heterogeneous, aggregates of solids were occasionally found between the electrodes and the reactor wall. Magnetic stirrer bars were used to ensure bulk anolyte was well-mixed and, on some occasions, glass stirring rods were used to disperse accumulated aggregates. The temperature of the electrochemical reactor was controlled using an oil bath equipped with a heat exchanger coil.

5.2.2 Electrooxidation procedure

A chlor-quaternary ammonium electrolytic system was assembled and used to generate tetramethylammonium hypochlorite for in-situ oxidation of low oxidation state vanadium solids in the gasifier ash to extractable V^{V} with $TMA^{+}OH^{-}$ solutions. The set-up used in implementing the experimentation of this section is shown in Figure 5-1.

The electrolyte solution was made by dissolving 27.96 g of 98 % tetramethylammonium chloride (Sigma Aldrich) into 250 cm^3 of ultra-pure deionised water to obtain 0.5 mol dm^{-3} $TMA^{+}Cl^{-}$ solution. The solution was then transferred to a round glass jar in which the anode and the cathode were placed subsequently with a 10 mm inter-electrode gap. The electrolyte was preheated for approximately 30 minutes to the desired temperature and then 10 g of the gasifier ash was added slowly to the jar and the electrolysis experiment was started immediately in galvanometric mode. The ratio of ash to electrolyte volume, solid to liquid ratio, was kept at 1:25 g cm^{-3} throughout the experiments and the solution pH was monitored continuously on-line using inoLab Multi 9620 IDS and WTW™ SensoLyt™ 900-P IDS wireless pH meter and adjusted to ca. 8 by the dropwise addition of diluted $TMA^{+}OH^{-}$ solution.

After the electrooxidation experiment was finished, the suspension was centrifuged in 50 cm^3 falcon tubes, and the solids were recovered by simply decanting the supernatant liquid phase. The recovered solids of oxidised materials were then utilised

as a feed to leach vanadium(V) in the following reaction conditions: 5 h reaction time, 90 °C, 2.78 mol dm^{-3} TMA^+OH^- solution and liquid-to-solid ratio of 10 cm^3 g^{-1}. Finally, the residue was separated from the leach liquor, resuspended in arbitrarily large amounts of methanol, and subsequently vacuum filtered to remove any remaining soluble tetramethylammonium vanadate. The residual materials were dried in a vacuum oven overnight and weighed upon cooling to obtain the total solids weight for mass balance analysis. The unextracted portion of vanadium oxides in the residue was analysed by microwave digestion followed by inductively-coupled plasma emission – mass spectrometry (ICP-MS). The difference between the total vanadium mass in the as-received gasifier ash and the total vanadium mass in the residue was considered as the total extracted vanadium(V) mass. The extraction yield was calculated from the ratio of the total extracted vanadium mass to the total vanadium mass in the as-received gasifier ash.

5.2.3 Cyclic Voltammetry of TMA^+ containing vanadium(IV) sulfate

The electrochemical measurements were carried out with a three-electrode system: a 1.5 cm^2 carbon felt working electrode, a leak-free AgCl/Ag in 3 mol dm^{-3} KCl reference electrode (model LF-5-100, ALVATEK, Southampton, UK), and a platinum coil counter electrode.

To make the reference electrolyte containing 1.6 mol dm^{-3} V^{IV} in 3 mol dm^{-3} free sulfuric acid, 13.04 g of vanadium(IV) oxide sulfate pentahydrate (Sigma Aldrich, 97 %) was added to a 50 cm^3 measuring flask and to it was added as-prepared 3 mol dm^{-3} sulfuric acid, then sonicated for 1 hour in a sonication bath. The $TMA^+HSO_4^-$ electrolyte additive was synthesised via the following procedure: exactly 25 cm^3 of the commercial 2.78 mol dm^{-3} TMA^+OH^- solution was added to a 100 cm^3 round bottom flask in an ice bath. To this was added slowly 25 cm^3 of the as-prepared 2.78 mol dm^{-3} sulfuric acid solution. The solution was put in a rotary evaporator to remove excess water until a viscous white material appeared on the bottom of the flask. The flask was then transferred to a vacuum oven and left at 60 °C overnight. White, hard, shiny solid $TMA^+HSO_4^-$ was scraped from the flask using a plastic spatula. The big chunks were crushed mechanically to powder and stored in a vial, ready to use as additive to the reference electrolyte to mimic the direct use of $H_4TMA_2V_{10}O_{28}$ in making a VRFB electrolyte.

5.2.4 V^V purity in the calcined solids

Scanning Electron Microscope

The morphology and surface chemistry of each powder sample was characterised by a JOEL 6010LA scanning electron microscope (SEM) equipped with secondary electron imaging (SEI). The third feature of the microscope which was energy-dispersive spectroscopy (EDS) which was used to study the chemical characterization/elemental analysis of materials.

5.2.5 Specific Electrical Energy Consumption

The electrooxidation reactor running costs, dominated by electrical energy costs to which heating costs need to be added, were calculated for the V_2O_5-equivalent extracted materials in the final product (see Equation 5-1). t_{equ} in the following equation is defined as the electrooxidation time required to achieve the equilibrium extraction yield in the leach reactor, even though the electrooxidation reactor and the leach reactor were operating separately.

$$w^{e}_{V_2O_{5,EB}} = \frac{|U|.I.t_{equ}}{0.06\ .x_{V_2O_5}\ .m_{ash}.\gamma_{equ}} \qquad \text{(Equation 5-1)}$$

Where $w^{e}_{V_2O_{5,EB}}$ represents the specific electrical energy consumption per unit mass of the V_2O_5-equivalent extracted materials in (kW h t_{V2O5}^{-1}), I is the current applied in (A), U is the reactor potential difference in (V), t_{equ} is the time at which the final extraction yield reached equilibrium in (min), $x_{V_2O_5}$ the V_2O_5-equivalent extracted vanadium(V) from the gasifier ash, m_{ash} is the mass of ash used in the batch electrooxidation experiment in (g), and γ_{equ} is the equilibrium extraction yield of vanadium(V).

The cell potential difference, U, is the sum of the equilibrium cell potential difference, anode and cathode overpotentials and the sum of the ohmic potential losses, as shown in Equation 5-2.

$$U = E_{Cl_2/Cl^-} - \left|E_{H^+/H_2}\right| + \eta_{Cl_2} + \left|\eta_{H_2}\right| + \sum_i I.R_t \qquad \text{(Equation 5-2)}$$

Where U represents the cell potential difference in (V), E the equilibrium potentials in (V), η overpotentials in (V), and the last term represents the sum of the ohmic potential losses due to current I (A) and R_t the ohmic potential losses in current collectors, separator, and electrolyte, allowing for additional resistance caused by gas bubbles.

5.3 Results and discussion

5.3.1 Reaction Mechanism

The electrooxidation experiments were conducted in such a way that the partially oxidised vanadium in the gasifier ash was oxidised to vanadium(V) through a heterogenous reaction at near-neutral pH then the solids were used as a feedstock in a separate chemical reactor for the leaching experiments. Although it would have been ideal if the electrooxidation of the solids could occur at high pH which could in theory result in one-pot oxidation and leaching vanadium(V), the initial tests showed that electrolysis of the suspension at high pH (i.e. pH> 14) had little to no effects on the leaching kinetics. This can be understood better by looking at the commercial production of sodium hypochlorite (bleach). Sodium hypochlorite is stable at high pH, however, in-situ electrochemical production of chlorine gas is not feasible in the presence of sodium hydroxide solution at high pH, presumably due to the dominant production of O_2 over Cl_2 at high pH. Hence, industrial sodium hypochlorite production[180] with high active chlorine contents involves direct reaction of separately produced chlorine gas with caustic soda solution as shown in the following reaction:

$$Cl_2 + 2NaOH \rightarrow NaClO + NaCl + H_2O \qquad \text{(Reaction 5-1)}$$

Electrochemical production of hypochlorite is merely used for in-situ disinfection purposes and the process is operated at near-neutral pH.[181] When electrical charge is applied to an aqueous solution containing chloride ions, anodic reactions result in the production of a number of chlorine-containing oxidants, which create active chlorine in the medium. Batch electrolysis of the TMA^+Cl^- solution in the presence of the gasifier ash, containing mixed vanadium oxides at near-neutral pH leads to the following sequence of reactions:

Anode Reactions

Chloride ions are oxidised to chlorine at the anode surface, leading to a two- electron transfer reaction.

$$\Phi^{e}_{Cl_2}(2Cl^- \rightarrow Cl_2 + 2e^-) \qquad \text{(Reaction 5-2)}$$

The rate of Reaction 5-2 may be transport or kinetically controlled, determined by (i) chloride ion concentration, (ii) current density, and (iii) prevailing hydrodynamic conditions. In this study, sufficient overpotential was maintained for a relatively high

chloride concentration to allow Reaction 5-2 turn into kinetic transport control for high conversion of chloride ions to hypochlorite.

Cathode Reactions

Water splitting occurs at the surface of the cathode, generating hydrogen gas which was the only gaseous product at this electrode.

$$2H_2O + 2e^- \rightarrow 2OH^- + H_2 \qquad \text{(Reaction 5-3)}$$

Solution Reactions

Chlorine is formed by Reaction 5-2 at the anode diffusion layer. This is because the pH close the anode diffusion layer, where the hydrolysis Reaction 5-4 and Reaction 5-10 produce protons, decreases to values at which chlorine is the stable product, as shown in Reaction 5-2. Moving away from the anode diffusion layer, chlorine is hydrolysed at the anode reaction layer to hypochlorous acid, chloride ions and protons (Reaction 5-4). The hydrolysis reaction occurs fast within the anode reaction layer if the bulk electrolyte pH is close to neutral or slightly alkaline.

$$Cl_2 + H_2O \rightarrow HClO + Cl^- + H^+ \qquad \text{(Reaction 5-4)}$$

For solutions having bulk pH near neutral or alkaline, hypochlorous acid dissociation takes place as shown in Reaction 5-5 for which $pK_a \cong 7.5$.

$$HClO \rightleftarrows H^+ + ClO^- \qquad \text{(Reaction 5-5)}$$

The reaction medium was heterogeneous, with the gasifier ash particles in contact with the oxidizing solution. XPS analysis (Chapter 3) revealed that that the vanadium oxide in the gasifier ash consisted of 13.7 % V^{IV} and 86.3 % V^{v}. According to the potential-pH diagram (Figure 4-6), V_2O_4 (c) is predicted to be the stable phase of V^{IV} and $V_4O_{12}^{4-}$ ions as the stable species of V^{V}, but at a limited concentration around near neutral pH. Therefore, mixing the ash which contained both V^{IV} and V^{V} oxides with the 0.5 mol dm^{-3} TMA^+Cl^- solution resulted in the partial dissolution of vanadium(V) oxide as shown by

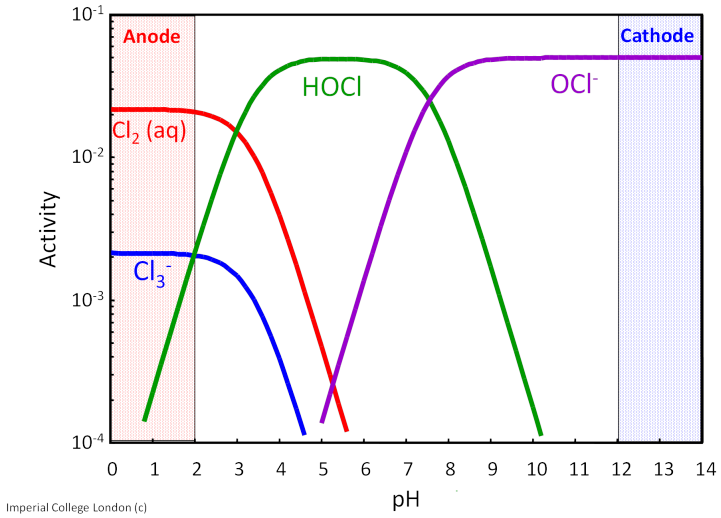


Figure 5-2. Activity-pH diagram for chlorine-water system at 298 K. Initial chloride activity = 0.5 mol dm^{-3}, conversion = 0.1 and P(Cl_2) = 101.325 kPa.

Reaction 5-6 with no changes in the aqueous speciation of V^{IV} oxides, other than by reduction of absorbed atmospheric oxygen.

$$2\,V_2O_5 + 2H_2O \rightarrow V_4O_{12}^{4-} + 4\,H^+ \qquad \text{(Reaction 5-6)}$$

Under the standard conditions, the saturation concentration of polyoxovanadates is expressed by Equation 5-3, which predicts the equilibrium concentration of $V_4O_{12}^{4-}$ ions to be 2×10^{-4} mol dm^{-3} (equivalent of 4×10^{-4} mol dm^{-3} V_2O_5) at pH 8.

$$\log([V_4O_{12}^{4-}]) = -35.7 \times 10^{-4} + 4\,pH \qquad \text{(Equation 5-3)}$$

However, the system in this study was influenced by the chloride ions concentration and temperature. For comparison purposes, Trypuc´ et al. investigated the solubility of NaCl + V_2O_5 + H_2O systems from 20 to 50 °C. They reported that the solubility of V_2O_5 was ca. 1.1×10^{-3} mol dm^{-3} at 50 °C for 0.806 mol dm^{-3} NaCl concentration, pH was not mentioned in the study.[182] It is reasonable to assume that during the preheating step

and before the electrolysis experiment was started: (i) vanadium(V) dissolution reached equilibrium when the ash was mixed with the 0.5 mol dm^{-3} TMA^+Cl^- solution and (ii) dissolved vanadium(V) activity had a negligible effect on the electrooxidation process.

Once the hypochlorite ions were formed as shown by Reaction 5-5, the ions make their way towards the low valence vanadium in the gasifier ash caused by the potential difference. As can be seen from Reaction 5-7, electrooxidation of V_2O_4 to crystalline V_2O_5 could occur due to two electrons being donated from V_2O_4 to the generated hypochlorite ions, causing their reduction to chloride ions (Reaction 5-8).

Equation 5-5 and Equation 5-6 describe the electrode potential equations for the oxidation and reduction reactions involved in the electrooxidation process, respectively. The activity-pH diagram for chlorine water system is shown in Figure 5-2 for 0.5 mol dm^{-3} chloride activity at 298 K from which the activity of other Cl-containing species can be estimated at different pH. With the ClO^- activity and pH known, E_{red} is predicted to be 1.21 V and E_{ox} is predicted to be -0.23 V, leaving E_{rxn} = + 0.98 V for Reaction 5-9 to shift forward.

$$E_{rxn} = E_{red} - E_{ox} \qquad \text{(Equation 5-4)}$$

Oxidation

$$V_2O_4(c) + H_2O \rightarrow V_2O_5(c) + 2\,e^- + 2\,H^+ \qquad \text{(Reaction 5-7)}$$

$$E_{ox} = E_{V_2O_5/V_2O_4}\,(SHE)/\,V = 0.7067 - 0.0592\,pH \qquad \text{(Equation 5-5)}$$

Reduction

$$ClO^- + 2H^+ + 2e^- \rightarrow Cl^- + H_2O \qquad \text{(Reaction 5-8)}$$

$$E_{red} = E_{ClO^-/Cl^-}(SHE)/V = 1.7176 - 0.0592pH$$

$$+ 0.296\log([ClO^-]) - 0.296\log([Cl^-]) \qquad \text{(Equation 5-6)}$$

Overall reaction:

$$V_2O_4(c) + ClO^- \rightarrow V_2O_5(c) + Cl^- \qquad \text{(Reaction 5-9)}$$

Reaction 5-9 suggests that during the electrooxidation experiments, the vanadium(IV) oxide phase reacted with the in situ generated hypochlorite ions water to generate

vanadium pentoxide and chloride ions. The by-product chloride ions meet the anode surface again as a reactant of Reaction 5-2.

Figure 5-3(a) shows the physical appearance of the electrooxidised gasifier ash after it was heat treated at 350 °C. Yellow/orangeish particles appeared on the bulk ash, whereas no such particles were observed from heat treated as-received gasifier ash, indicating that the electrooxidation process was the cause of oxidation of the V^{IV} phase.

One of the key advantages of the electrooxidation process is the in situ electrogeneration of hypochlorite compared to when a chemical oxidant used such as sodium chlorite. In the chemical process, the oxidant must be replenished when it is exhausted, leading to an increase in both the waste volume and processing costs. However, the electrogeneration process enables simultaneous production and consumption of the reagents necessary for the continuity of the low oxidation state vanadium electrooxidation process. Hence, electrooxidation of the gasifier ash using the aforementioned technique is a circular process with no on-going chemical needs.



Figure 5-3. Physical appearance of the electrooxidised ash. Yellow particles appeared after the electrooxidation step.

Loss Reactions

The following loss reactions could also occur in addition to the above reactions:

In parallel to the chlorine oxidation reaction, water is oxidised at the anode reaction layer to the oxygen gas and protons, according to Reaction 5-10. DSA-Ti/RuO_2 was chosen as the anode material because of its relatively low Cl_2 overpotential and higher O_2 overpotential which allows the evolution of Cl_2 in preference to O_2.

Anode Loss Reaction $\left(1 - \Phi^{e}_{Cl_2}\right) 2\,H_2O \rightarrow\ O_2 + 4\,H^+ +\ 4\,e^-$ (Reaction 5-10)

Hypochlorite ions may be transported to the cathode, where they are reduced to chloride ions. Unfortunately, there are limited ways to avoid the hypochlorite cathodic reduction Reaction 5-11, especially for batch reactors. Kuhn et al.[183] suggested using relatively large area ratio of anode to cathode or using cathodic $Mg(OH)_2$ and $(Ca)OH_2$ films formed in Mg^{II} and Ca^{II} containing solutions due to the high pH produced by Reaction 5-3. A thin dark layer of V^{III} oxide was formed onto the surface of the cathode and predicted by Figure 4-6. This thin layer could similarly act as a barrier between the SS cathode and the hypochlorite ions in the solution to retard the cathodic reduction of hypochlorite ions to chloride ions. Future studies will be required to elucidate the effect of the thin V^{III} layer on the performance of the electrooxidation process.

Cathode Loss Reaction

$$ClO^- +\ H_2O +\ 2\,e^- \rightarrow 2\,OH^- +\ Cl^- \qquad \text{(Reaction 5-11)}$$

Chlorates form either by the electrochemical path or by chemical path in the bulk solution. In the electrochemical path, part of the generated HClO at the anode diffuses out to the bulk electrolyte, and some diffuses back to the electrode, where it is further oxidised to ClO_3^- by Reaction 5-12. In the chemical path, Ronco and Mishkin reported that hypochlorite ions were decomposed to chlorate ions with a 7.5 % reduction in the active chlorine concentration from 6 °C to 50 °C for Ti/RuO_2 electrode.[181] They concluded that high temperatures favour the reduction of hypochlorite. This can be advantageous for the kinetics of oxidation of the low oxidation state vanadium in the gasifier ash. Moreover, as shown in **3.3.6 Kinetics study** and will be further confirmed in this chapter, the rate of oxidation of V_2O_4 particles to crystalline V_2O_5 was controlled by the formation of an intermediate in the heterogeneous system. Therefore, the overall reaction rate is controlled by transport of the oxidant whether hypochlorite ions or chlorate ions, followed by the formation of the intermediate i.e., vanadium(V) phases

at the reaction layer rather than being controlled by the kinetics of the redox reaction which is generally fast anyway.

Anodic formation of chlorates

$$6\,\mathrm{HClO} + 3\,\mathrm{H_2O} \rightarrow\ 2\,\mathrm{ClO_3^-} + 4\,\mathrm{Cl^-}$$

$$+1.5\,\mathrm{O_2} + 12\,\mathrm{H^+} + 6\,\mathrm{e^-} \qquad \text{(Reaction 5-12)}$$

Chemical formation of chlorates

$$2\mathrm{HClO} + \mathrm{ClO^-} \rightarrow\ \mathrm{ClO_3^-} + 2\,\mathrm{Cl^-} + 2\,\mathrm{H^+} \qquad \text{(Reaction 5-13)}$$

5.3.2 Effect of Current Density and Temperature in Electrooxidation on V^V Extraction Yield

It is evident from the water-chlorine activity-pH diagram (Figure 5-2) that the activity of hypochlorous acid decreases drastically with increasing pH while the basic leaching kinetics of V^V is favoured at very high pH, i.e. > 14. Moreover, electrolysis of a chloride solution at high pH favours oxygen evolution rather than active chlorine. Preliminary experiments showed that electrolysis of a heterogenous mixture of 2.78 mol dm^{-3} TMA^+OH^- solution and the gasifier ash had little to no effects on the extraction yield of V^V, confirming that oxygen evolution was favoured over chlorine generation. Hence, to leach vanadium(V), two distinct steps were required: (i) electrooxidation the gasifier ash at near-neutral pH, (ii) basic leaching of V^V at very high pH in a separate reactor. Hence, regardless of the electrooxidation reaction conditions, the post-electrooxidised solids were used as a reactant (feed) for vanadium(V) leaching in 2.78 mol dm^{-3} at 90 °C for 6 hours and the final vanadium(V) extraction yield was calculated based on the vanadium content in the post-extraction residue.

Due to the simultaneous production and consumption of active chlorine, it was nearly impossible to accurately measure the generation rate in the heterogeneous medium. Kuznetsov et al., investigated the type of dependence of active chlorine concentration with time. They reported that in a stirred electrolytic cell, the active chlorine concentration increased with current density at a given time and the relationship was nearly linear for solutions containing ca. 0.5 mol dm^{-3} chloride concentration and current densities below 1 000 A m^{-2}.[184] The chloride concentration and the maximum current density used in this work were almost identical to that of reported by Kuznetsov

et al. Herein, it was assumed that the active chlorine concentration is linearly proportional to the applied current density.

The objective of this section was to investigate the effect of temperature and current density on the electrooxidation of V^{IV} oxide in the gasifier ash, and ultimately on the final extraction yield of V^{V}.

Discussion

Figure 5-4(a) shows the effect of current density during the electrooxidation reaction on the final extraction yield of vanadium(V). Low extraction yields were achieved at 0 A m^{-2} current density or zero active chlorine concentration. Increasing current densities to the electrochemical reactor containing tetramethylammonium chloride electrolyte solution caused active chlorine production, increasing vanadium(V) extraction yields up to a limit of 0.815 ± 0.005 after 9 hours, for current densities up to 1 000 A m^{-2}. The limiting extraction yield of V^{V} is in agreement with the results discussed in the Chapter 3: Under the ionoLeach process reaction conditions, 17-19 % of the total vanadium in the gasifier ash was unextractable V^{V} in the form of Ni-V-O phases leaving the remaining vanadium as extractable mixed vanadium oxides of which 69.3 % was V^{V} and 13.7 % was V^{IV}.

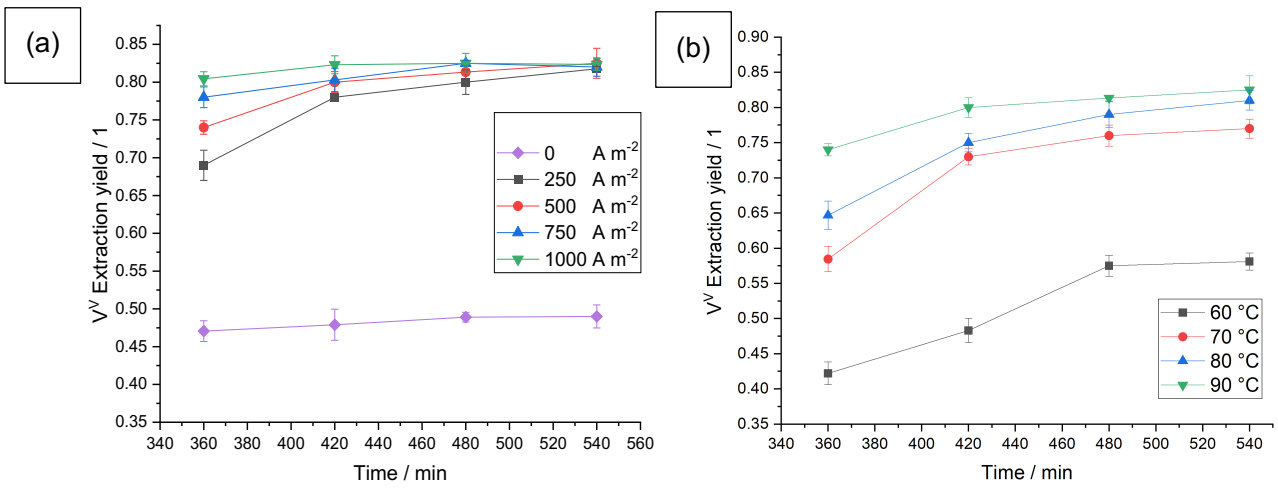


Figure 5-4. (a), left, Effect of current density on the final vanadium(V) extraction yield at 90 °C; (b), right, effect of temperature on the final vanadium(V) extraction yield at 500 A m^{-2}

Comparison of Figure 5-4(a) and Figure 5-4(b) shows clearly that temperature had a more significant effect on final V^V extraction yields than current density (active chlorine concentration). This is because there is a key distinction between fluid-solid kinetics and homogeneous kinetics: The reactive surface area rather than the concentration of the solid particles in the fluid phase directly affects the reaction rate of those particles dispersed in the fluid. This aspect makes the work extremely difficult because it is much more difficult to dynamically quantify surface area than concentration. The fact that the surface area typically does not decrease linearly with reactant conversion as concentrations do causes the kinetics to behave differently and makes it more difficult to interpret experimental results. Additionally, Salmi et al. reported that the reactive, accessible surface area is not always equal to the total surface area.[185] The interaction between active chlorine ions and the accessible reactive sites should be even more challenging during the electrooxidation process. Because vanadium(V) was formed as a solid product on the outer surface of the vanadium(IV) particles which was becoming a barrier between the active chlorine ions in the aqueous phase and the V(IV) oxide in the solid phase. Hence, the electrooxidation reaction was chemically controlled at the lowest reaction rate (bulk concentration = surface concentration), while the overall reaction was heavily dominated by the internal mass transfer when the rate constant increased due to increase in temperature, as evident from Figure 5-4(b).

5.3.3 Electrode Polarisation

Figure 5-5(a) shows the effect of current density on cell potential difference, recorded for the undivided electrolyser containing 0.5 mol dm^{-3} TMA^+Cl^- at 90 °C. Figure 5-5(b) shows the components of cell potential difference, expressed as Equation 5-2, in an ideal hypochlorite electrochemical reactor. In the levelized cell potential difference, the equilibrium potential terms are invariable for given redox couples and a set experimental condition. The overpotential terms greatly depend on the electrode material and for chlorine evolution on two-dimensional Ti/RuO_2 mesh anodes and the Tafel slope was reported to be ca. 30-40 mV $decade^{-1}$.[179,186] As Figure 5-5(a) suggests, the cell potential difference increased approximately linearly with increasing current density, confirming the contribution of ohmic losses in the form of IR. For hypochlorite production in an undivided electrochemical cell, Kelsall[179] reported that the main contribution to the ohmic losses is due to the formation of hydrogen bubbles at the reaction layer of the cathode.

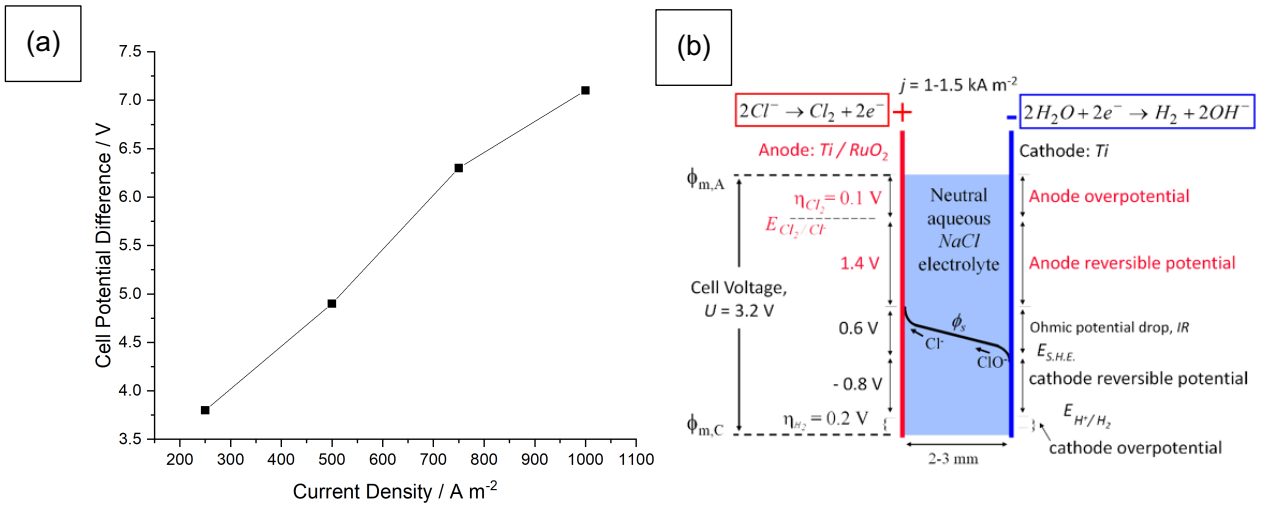


Figure 5-5(a), left, Polarization curve of electrode in 0.5 mol dm^{-3} TMA^+Cl^- solution, pH ca. 8 and 90 °C (b), right, Breakdown of cell potential difference for the production of hypochlorite in a 0.5 mol dm^{-3} NaCl at near-neutral pH.

Figure 5-5(b) predicts that the cell potential difference for electrochemical production of hypochlorite should be approximately 3.2 V at 1 000 A m^{-2}, whereas the cell potential difference for the electrooxidation of the gasifier ash was found to be approximately 7 V at the same current density. This is because the experimental temperature, the inter-electrode gap was different, and each contributed differently to the cell potential difference.

Possible explanations are as follows: In an ideal condition of continuous hypochlorite production, an interelectrode gap of 0.8 mm was required to obtain the minimum cell potential difference such as 3.2V for the following experimental conditions: 0.5 mol dm^{-3} NaCl, 288 K and electrolyte flowrate of 2 dm^{-3} min^{-1}.[187] Factors such as electrode height/length whether the solution is under force convection or any factors affecting the transport of the bubbles away from the electrode can also affect the minimum cell potential difference. For a batch reactor, a larger gap would be required to minimise cathodic reduction of the active chlorine species. Chinello et al, suggested 10 mm electrode gap[188],and Ronco and Mishking suggested 8 mm electrode gap for the optimal conversion of Cl^- to ClO^-. An inter-electrode gap of 10 mm was also used in this study which is 3 to 5 times higher than the value used in Figure 5-5(b). The relatively high inter-electrode gap along with the solution heterogeneity resulted in a

higher ohmic potential losses within the system, which caused a deviation between the predicted cell potential difference in Figure 5-5(b) and the measured cell potential difference.

5.3.4 Specific Electrical Energy Consumption

Figure 5-6 shows the specific electrical energy required in the electrooxidation step in order to achieve the equilibrium vanadium(V) extraction yield in the leach reactor. The specific electrical energy consumption (Equation 5-1) is directly proportional to both the applied current density and the electrooxidation time (t_{equ}) to reach limiting conversion. Although the optimal electrooxidation time decreased with increasing current density (see Figure 5-4(a)) which in turn was expected to decrease the specific electrical energy consumption, the specific electrical energy consumption increased almost linearly with increasing current density. The inverse relationship between the current density and the electrooxidation time confirms that the reaction was heavily dominated by the internal mass transfer at the interface of the solid materials because an increase in the active chlorine concentration (current density) in the liquid phase increased the rate of reaction only slightly, whereas, relatively speaking, it resulted in significant increase in the specific electrical energy consumption per unit mass of V_2O_5-equivalent extracted materials. The specific electrical energy consumption for the electrooxidation of the gasifier ash can be added to the calculated specific electrical energy required to recover V_2O_5-equivalent vanadium(V) from Chapter 4 to calculate the total specific electrical energy required for oxidative leaching V^V from the gasifier ash.

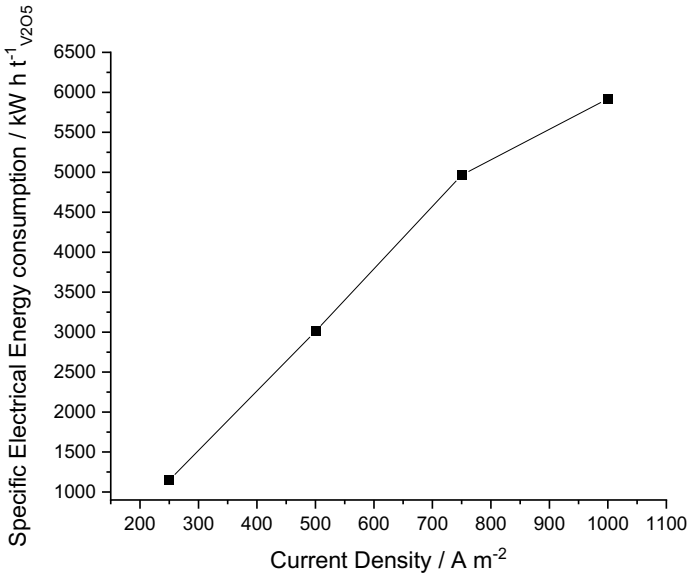


Figure 5-6. Effect of current density on specific energy required for the electrooxidation process to produce 1 tonne of V_2O_5. Experimental conditions: 0.5 mol dm^{-3} TMA^+Cl^- solution, pH ca. 8, 90 °C for time = equilibrium extraction yield time.

5.3.5 Product characteristics and purity

Leach solution composition

The vanadium from the electrooxidised gasifier ash was concentrated in the leach liquor to 0.883 mol dm^{-3} and then was electrolysed in a membrane-divided electrochemical reactor, according to the procedure explained in the Chapter 4.

As covered comprehensively in Chapter 3, alkylammonium cations, similar to ammonium cations, have unfavourable chemical interaction with aluminium(III) and silicon(IV). From the solubility viewpoint, alkylammonium vanadate salts, opposite to ammonium vanadate salts, are highly soluble at pH > 14. The selectivity feature of tetramethylammonium hydroxide, together with the extraordinary solubility of tetramethylammonium vanadate, provide an exceptional solvent for the selective extraction of vanadium(V) from industrial by-products (i.e. gasifier ash). Study of vanadium(V) purity in both leach solutions and final products are equally important to address impurities accumulation in a continuous vanadium refining hydrometallurgical process. The composition of the leach liquor is shown in Figure 5-8, which shows that

the leach liquor obtained from leaching the electrooxidised gasifier ash, contained vanadium with 99.8 % purity. This is very promising to produce highly pure vanadium(V) products (i.e. V_2O_5) in the next processing step. Conversely, sodium and/or chromium can be potential problematic impurities in the solution, due to their accumulation in continuous recycling systems, but can be removed by crystallisation as sodium sulfate for example. Future studies will be required to elucidate the effect of continuous solvent recycling on accumulation of impurities.

Surface Characteristics

The shrinking particle model (see e.g. Levenspiel, 1999)[189] assumes that all products, at their formation, crack away or dissolve from the surface of the particle. On the contrary, the product layer model[185] proposes that a porous product layer is formed around the reacting particle causing an increase in mass transfer resistance, since the reactant in the aqueous phase has to diffuse through this porous layer before reaching new reactant surface. It can be also seen from Figure 5-7 that the V^{V} particles formation on the surface of the V^{IV} particles which were the fundamental cause of the relatively slow electrooxidation process by retarding the diffusion rate of the oxidant through the newly formed solid product layer.

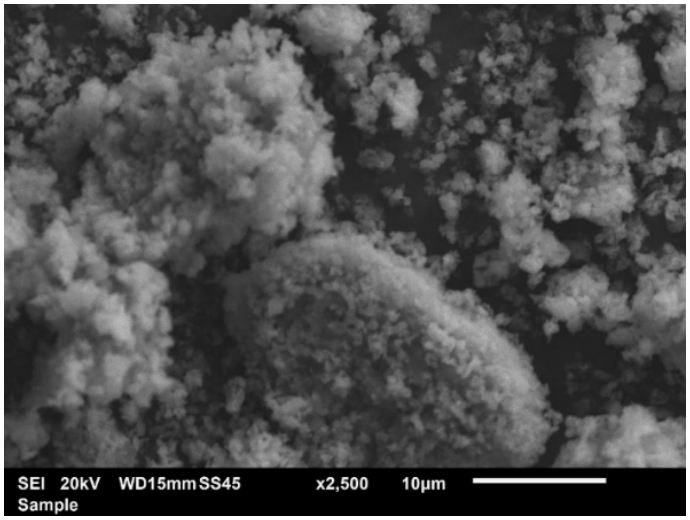


Figure 5-7. SEM image of oxidised V^{IV} to V^{V} flakes after some electrooxidation period in 0.5 mol dm^{-3} $TMA^{+}Cl^{-}$ solution.

Figure 5-10(a) shows the SEM micrographs of a typical sample of the $H_4TMA_2V_{10}O_{28}$ aggregates. The obtained phase was constituted of irregular 'deep-fried battering-like' polyoxovanadium nanometric 2D sheets that were stacked in a lamella structure. From EDX analysis (Figure 5-10(b)), the surface composition corresponded to $H_4TMA_2V_{10}O_{28}$ structures, suggesting that the only metal/non-volatile element in the deposited materials was vanadium. In fact, the electrochemical deposition step slowly

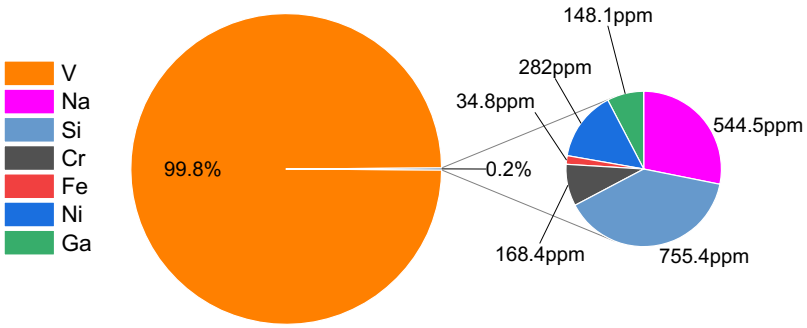


Figure 5-8. Chemical composition of leach liquor obtained from electrooxidised gasifier ash.

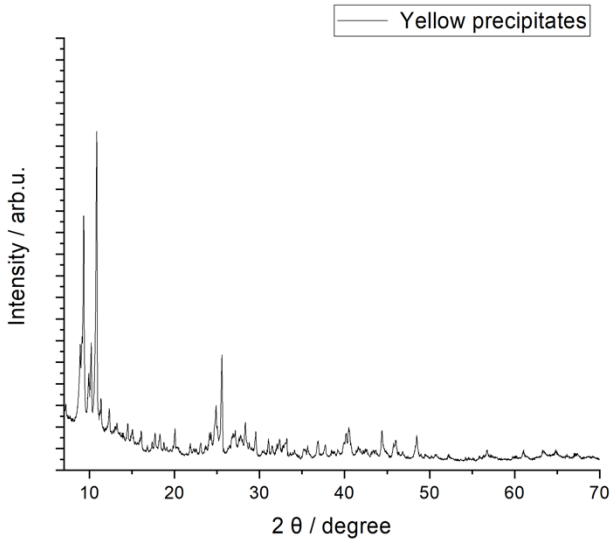


Figure 5-9. Real sample - XRD diagram of the yellow precipitates obtained from the electrolysis of the leach liquor.

stacked up the nanometric $H_4TMA_2V_{10}O_{28}$ sheets which even further purified the vanadium(V) from the leach liquor.

The $H_4TMA_2V_{10}O_{28}$ aggregates were calcined at 550 °C, resulting in the formation of short needle-like V_2O_5 crystals with lengths of 2 - 5 µm, as shown in Figure 5-12(a). Figure 5-12(b) shows the EDX spectrum of the needle-like V_2O_5 microstructures. The surface composition resulting from the EDX spectrum analysis suggested that the only metal/non-volatile element in the calcined materials was vanadium. In fact, ultrapure vanadium pentoxide was extracted successfully and separated from over 20 elements in the gasifier ash. There was also an insignificant C peak in the EDX spectrum that might have been due to the carbon tape to which the sample was loaded, or simply the adsorbed carbon materials from the environment.

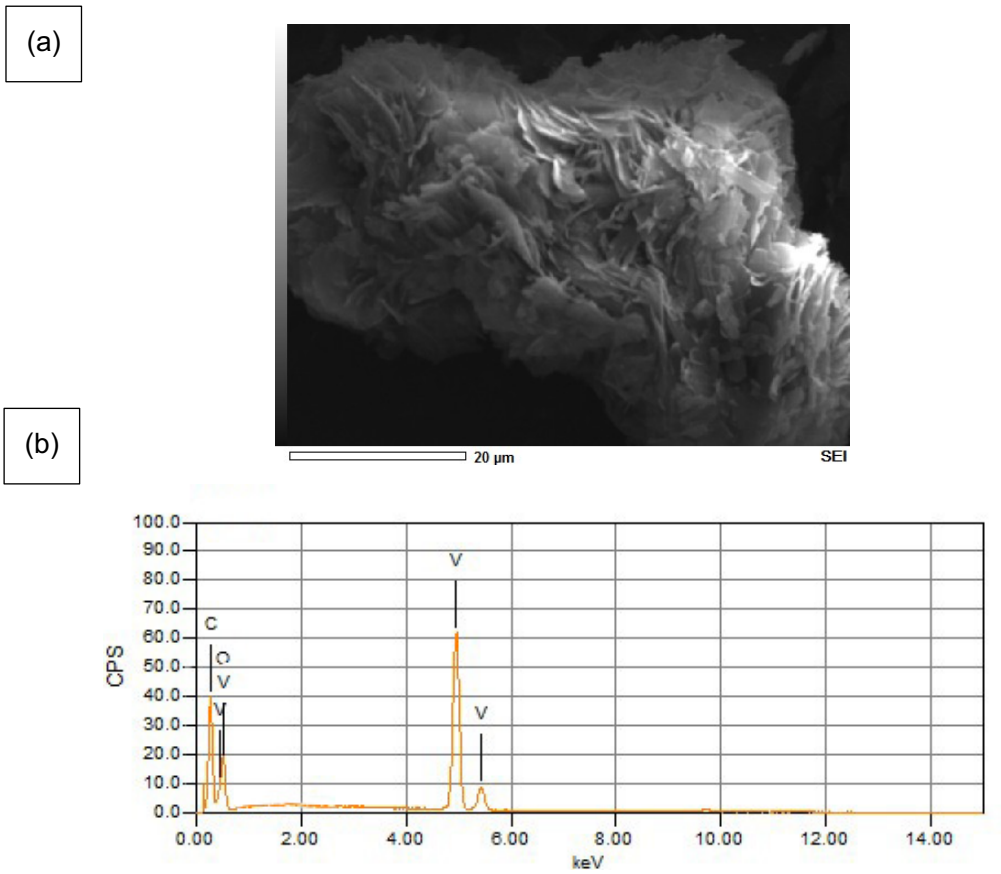


Figure 5-10. $H_4TMA_2V_{10}O_{28}$ morphology and composition: (a) top SEM image and (b), bottom, energy dispersive X-ray spectroscopy elemental data from the crystal structures.

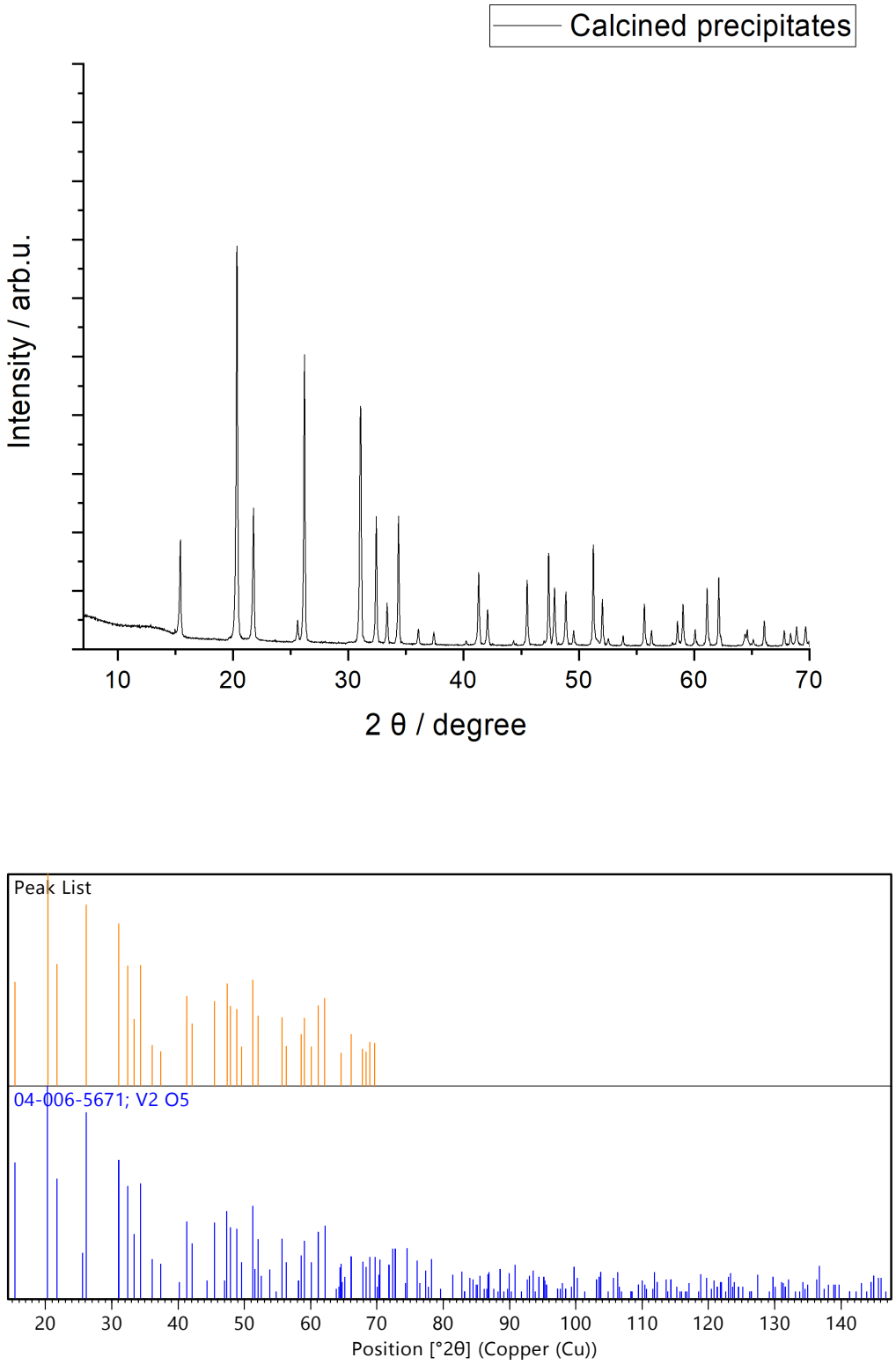


Figure 5-11. Real sample - XRD diagram of the calcined yellow precipitates.

It can be observed that the XRD patterns obtain in Figure 5-9 and Figure 5-11 from the real gasifier ash sample, correspond closely to those obtained from the lab-grade samples shown in Figure 4-3 and Figure 4-21 from the previous chapter, respectively. The purity of the extracted vanadium was measured using the energy dispersive X-ray spectroscopy technique (Figure 5.12(b)), which revealed that the vanadium pentoxide extracted from the gasifier ash was of ultra-pure quality.

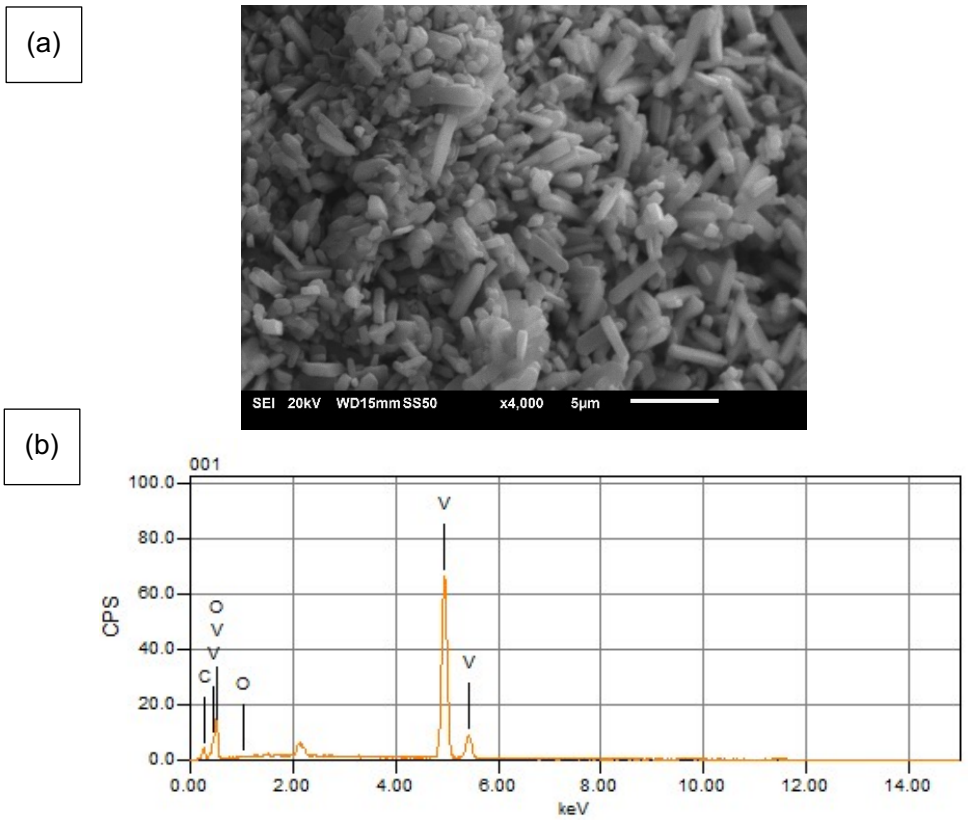


Figure 5-12. Needle-like V_2O_5 crystal morphology: (a), left, SEM image and (b), right, Energy dispersive X-ray spectroscopy elemental data from the crystal structures.

5.3.6 Cyclic Voltammetry

When the sun stops shining and wind is not blowing, energy storage systems (ESSs) such as flow batteries provide stored electricity to meet subsequent demand. Across all the flow battery technologies, the vanadium redox flow battery (VRFB) has gained significant attention by both researchers and industry for its long cycle life, full discharge ability, low running cost, fast response, environmentally benign nature and non-flammability.

Deprotonation: $2[VO_2(H_2O)_3]^+ \rightarrow 2VO(OH)_3 + 2H_2O + 2H^+$ (Reaction 5-14)

Condensation: $2VO(OH)_3 \rightarrow V_2O_5 + 3\,H_2O$ (Reaction 5-15)

There are limitations for the maximum stable concentration of vanadium(V) in the positive electrolyte of a VRFB. Reaction 5-14 and Reaction 5-15 indicate the mechanism by which vanadium(V) starts to precipitate above 40 °C. Essentially, it is the poor thermal stability of vanadium(V) that limits the concentration of vanadium ions to 20-25 W h dm^{-3}.[190] As a consequence, the two known major challenges with VRFB are the poor electrochemical activity of the active species and the poor thermal stability of the electrolyte. Li et al. used mixed acids of sulfuric acid and hydrochloric acid as the supporting electrolyte to overcome the stability problem within a temperature range of -5 to 50 °C.[191] However, chlorine evolution could be a significant challenge due to the introduction of chloride ions. The mixed acid system of sulfuric acid and organic acids were investigated by several researchers.[190,192,193] Despite them showing better stability and electrochemical properties than those conventional systems, higher prices of organic acid remain a challenge for commercialisation. Another approach to retard precipitation of vanadium species is to use additives, which is the most effective and economical strategy. Several organic and inorganic compounds such as alkali metal sulphates, borates and oxalates were reported as good stabilizers; however, the effects on enhancing the electrochemical kinetics was insignificant.[194] Additionally, the majority of the additives containing carboxyl and hydroxyl groups will be oxidised over time (i.e. long-term recycling) due to the oxidising property of vanadium(V).

The aggregates of $H_4TMA_2V_{10}O_{28}$ contain 2 moles of TMA^+ cations per 10 moles of V^V, with almost no detectable troublesome impurities. This section reports results of investigations of the possible usage of pristine $H_4TMA_2V_{10}O_{28}$ in vanadium redox flow batteries. Higher ratios of TMA^+ : V^V than 2 : 10 were used to investigate the effect of incomplete (partial) recovery of TMA^+ on the electrochemical activity.

Figure 5-13 shows voltammograms of a positive electrolyte containing 1.6 mol dm^{-3} V^{IV} sulfate with different amounts of $TMA^+HSO_4^-$; Only anodic peaks were evident over the potential range used, and assumed to be due to the oxidation of V^{IV} to V^V. Graphite felt electrodes are extensively used in VRFB technology due to being excellent materials for inhibition of gas evolution. However, in the CV experiments reduction (cathodic) peaks were not detected and the anodic peaks were only included in the diagram. Looking into the literature, Habekost[195] reported the same phenomena on a graphite electrode where it was reported that oxidation of V^{IV} to V^V was irreversible on graphite felt electrodes. It can be seen that with the addition of TMA^+HSO4^- to the electrolyte in

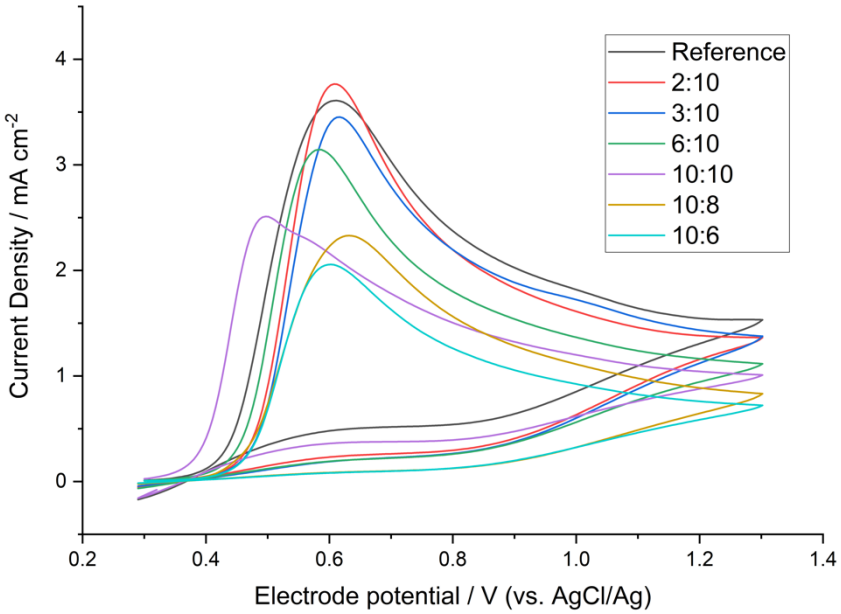


Figure 5-13. Cyclic voltammograms of the electrolyte with different additive amounts of $TMA^+HSO_4^-$ at room temperature at a scan rate of 20 mV s^{-1} on graphite felt electrode. Each curve had a different TMA^+ : V^{IV} ratio and the reference contained 1.6 mol dm^{-3} V^{IV} / 3M free H_2SO_4 with no TMA^+ cations.

the ratio of 2 : 10, TMA^+ : V^{IV}, the anodic peak current density increased by approximately 5 %. That molar ratio is identical to the ratio of TMA^+ : V in $H_4TMA_2V_{10}O_{28}$. Further increase in the TMA^+ concentration not only decreased the anodic peak, but also shifted the peak potential to less positive values. The preliminary voltammetric results demonstrated that it is possible to use pristine $H_4TMA_2V_{10}O_{28}$ in making VRFB electrolyte with no further purification. The advantage of using pristine $H_4TMA_2V_{10}O_{28}$ is the elimination of further processing steps, i.e., calcination to V_2O_5 to increase electrochemical activity. Wu et al. also reported that nitrogen-containing additives could result in higher mass transport and charge transfer rates of the V^{IV}/V^V couple, due to the favourable reactions between the nitrogen-containing additives and the carbon felt electrode surface.[192] Further study on the cathodic peaks and the electrolyte stability in the future could provide insights into utilisation of $H_4TMA_2V_{10}O_{28}$ or even $TMA^+HSO_4^-$ alone as additives in VRFB electrolytes.

5.4 Conclusions

The in situ electrogeneration of hypochlorite and its use in the oxidation of low oxidation state vanadium in the gasifier ash showed encouraging results. In-situ electrooxidation of the gasifier ash at near-neutral pH resulted in the oxidation of V^{IV} oxide to crystalline V^V oxide. In order to better understand the electrooxidation process of low oxidation state vanadium species, the effects of temperature and current density were investigated.

In the present methodology, temperatures of 60 – 90 C° and current densities of 250 – 1 000 A m^{-2} were applied with no on-going addition of hazardous reactants. Practically, an electrooxidation temperature of 90 °C resulted in the maximum limiting extraction yield of ca. 82 %. However, at an electrolyte solution temperature of 90 °C, all current densities within the range of 250 to 1000 A m^{-2} resulted in limiting extraction yields, achieved most slowly in 540 minutes at a current density of 250 A m^{-2}. The oxidation rate increased with increased temperature and was less dependent on the active chlorine concentration, which increased with applied current density. Vanadium(V) was formed as a solid product on the outer surface of the vanadium(IV) particles which became a barrier between the active chlorine ions in the aqueous phase and the V(IV) oxide in the solid phase. Hence, the electrooxidation reaction was chemically controlled at the lowest reaction rate (bulk concentration = surface

concentration), while the overall reaction was heavily dominated by the internal mass transfer when the rate constant increased due to an increase in temperature.

A cost benefit analysis will be required to define the optimum current density at which to operate the process, as increasing current densities decreased the time required to achieve the limiting extraction yield. The following parameters should be studied: heat loss to surroundings based on the extra time required for electrooxidation in the case of choosing lower current densities, plant throughput and capital cost due to the longer residence times of materials in the electrochemical reactor, and the electrical energy required to electrooxidised the gasifier ash. From an energy saving point of view only, and if heat loss to surrounding is negligible, electrooxidation of the gasifier ash at 250 A m^{-2} for 9 h at 90 °C appeared to be optimal, corresponding to a specific electrical energy consumption of 1 147 kW h t^{-1}_{V2O5}.

The vanadium(V) from the electrooxidised gasifier ash was concentrated in the leach liquor to a purity of around 99.8 %. The SEM and EDX analyses of the electrodeposited materials revealed that during membrane electrolysis, polyoxovanadium nanometric 2D sheets were stacking in a laminated structure, which also acted as a purification step to synthesise ultrapure vanadium aggregates of $H_4TMA_2V_{10}O_{28}$. Calcination of those aggregates resulted in the formation of short needle-like ultrapure (i.e. >99.99 %) V_2O_5 crystals. An attempt was made to investigate the feasibility of the use of pristine $H_4TMA_2V_{10}O_{28}$ as a VRFB electrolyte additive. Voltametric results revealed that the electrochemical performance of the electrolyte was increased by 5 % on addition of $TAM^+HSO_4^-$ at a TMA^+ : V^{IV} ratio of 2 : 10.

6. Techno-economic assessment of the ionoLeach chemical plant

6.1 Introduction

Techno-economic assessment is a useful tool for evaluation the commercial potential of a new technology. High-level cost estimates were made in this section of the project to establish a comparative tool for evaluating the economic potential of different pathways.

The techno-economic assessment of a commercial ionoLeach plant required the integration of the theoretical mass and energy (M&E) balance, cost data and the cash flow as depicted in Figure 6-1. The mass and energy balance data established the inputs and the outputs of the process. This information was important for both cost determination and data collection for the ionoLeach process plant in addition to inputs to the cash-flow model.

The minimum break-even price differential for V_2O_5 and (or its derivatives) was estimated to achieve a positive net present value (NPV) over a specified period and discount rate. Three pathways were designed, each following a key fundamental rule.

Pathway 1 was designed for minimal carbon footprint or ongoing chemical inputs with a highly pure V_2O_5 output. Pathway 2 produces one of the following products: V_2O_5 flakes or vanadium flow battery electrolyte, depending on the vanadium processing route. Because of the high purity of vanadium in the leach liquor, Pathway 3 takes the leach liquor and directly produces a Vanadium Redox Flow Battery (VRFB) electrolyte.

A sensitivity analysis was included to visualise the uncertainties for this first-of-a-kind (FOAK) plant which was proposed to be built next to the Pernis Refinery in the

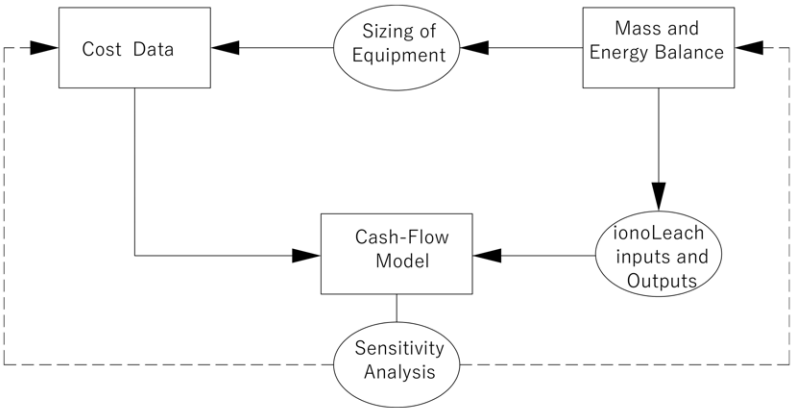


Figure 6-1. Schematic of the techno-economic assessment study for the ionoLeach process.

Netherlands. Finally, the best pathway was chosen from the economic advantage and ease processing point of views and the economic indicators were re-calculated using not-too-conservative input parameters.

The objectives of this part of the project were to:

- Create a tool to compare the economic viability of each pathway
- Perform sensitivity analysis to identify weak points in the assessment
- Make recommendations for future studies and optimisations

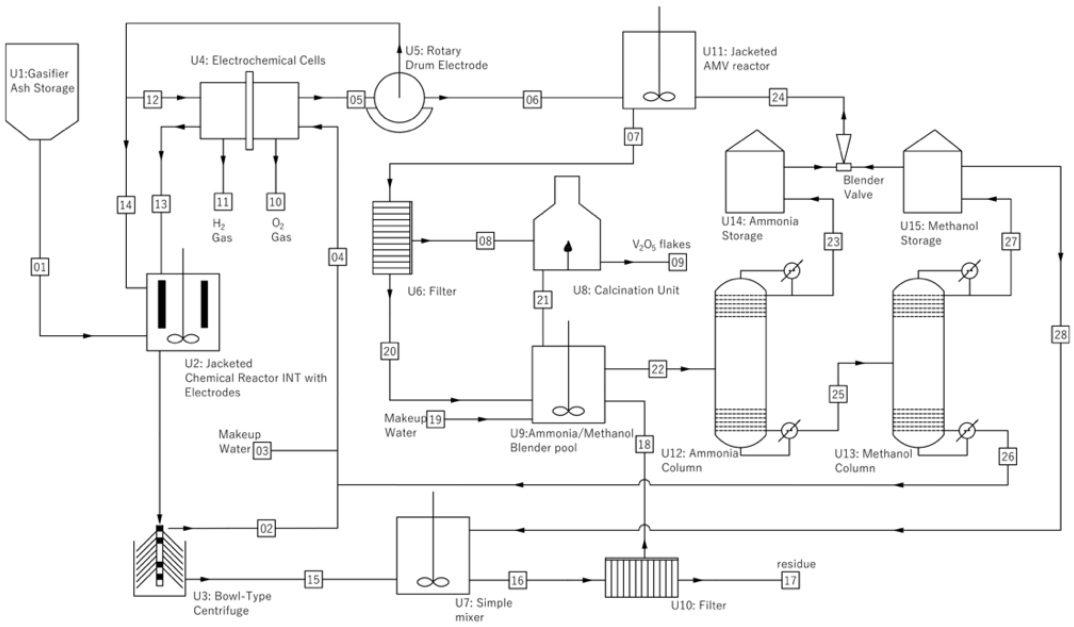


Figure 6-2. Process flow diagram for pathway 1 – base case pathway.

When conducting techno-economic calculations, there are several general considerations to keep in mind. First and foremost, accurate and reliable data is essential. This includes information on raw material costs, equipment prices, energy consumption, labor expenses, and other relevant factors. Market prices and demand projections must also be carefully analyzed to estimate product sales and revenue potential. Additionally, it is important to consider the time value of money and discount rates to properly evaluate the profitability of the project over its expected lifespan. Sensitivity analysis should be performed to assess the impact of potential variations in key parameters and assumptions. Furthermore, regulatory and compliance costs should be accounted for to ensure adherence to environmental and safety standards. Finally, the scalability and flexibility of the project should be considered, as future

expansions or modifications may be necessary to adapt to changing market conditions. By addressing these general considerations, techno-economic calculations can provide valuable insights into the feasibility and profitability of a proposed project. Herein, combinations of several techniques were used to conduct the techno-economic assessment with a set of assumptions which were clearly stated in this chapter.

6.2 The studied pathways and the scenarios

Figure 6-2 shows the process flow diagram for the base case pathway (Pathway 1) which was designed to produce ultra-pure vanadium pentoxide with zero carbon footprint and no ongoing chemical inputs. Pathway 2 and Pathway 3 operating units were modified according to Table 6-1. The removal of vanadium(V) aggregates may be achieved continuously using rotary drum electrodes and knife blades (Figure 6-3).

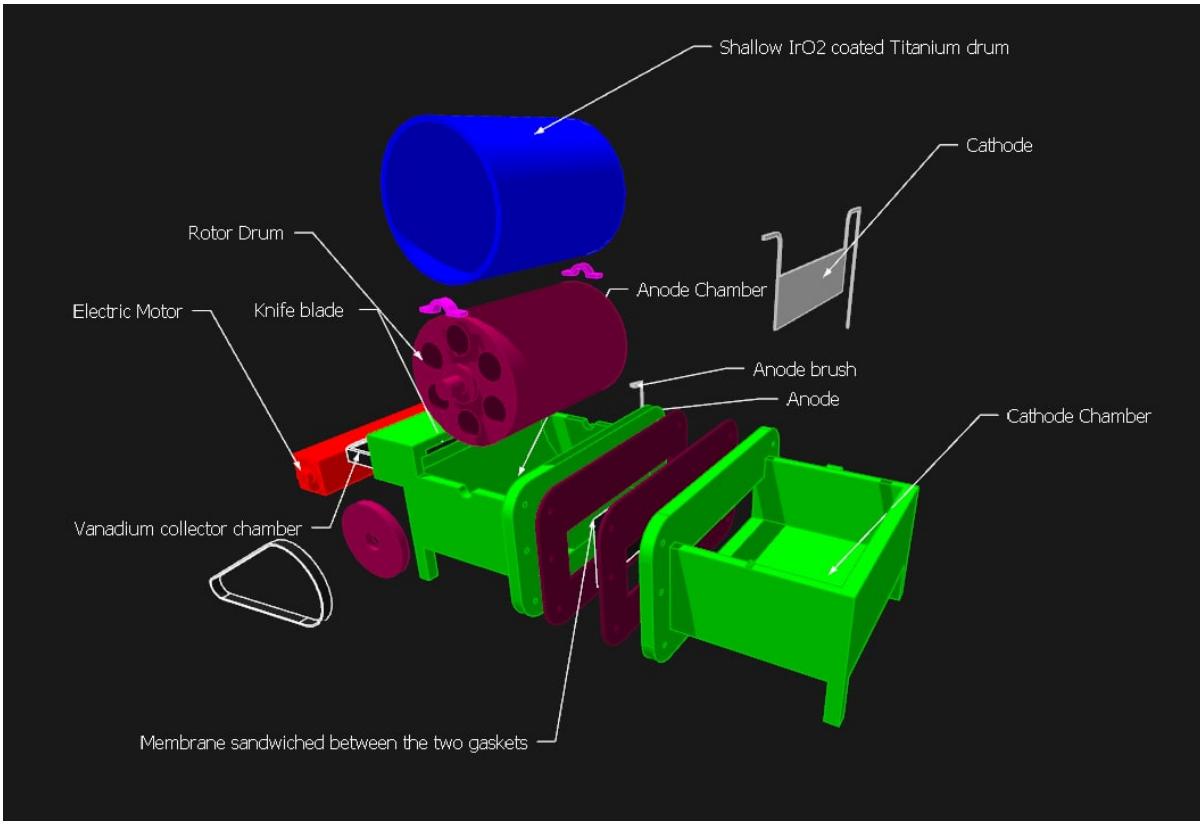


Figure 6-3. Schematic of the proposed electrochemical reactor whereby vanadium(V) aggregates can be continuously removed.

Pathway 2 and Pathway 3 were considered to decide on process alternatives (to Pathway 1) and to generate a list of recommendations for the commercialisation potential of the vanadium recovery process using the ionoLeach technology.

Pathway 2 includes the electrolyser unit and its auxiliary equipment but the deposited vanadium compound ($H_4TMA_2V_{10}O_{28}$) to the surface of the electrode is directly calcined to V_2O_5, therefore, no distillation columns were required to maximise the recovery of the ionic liquid. Pathway 3 has the minimum capital requirement for the final product which is a VRFB electrolyte. The electrolyser and the distillation units, combined with their auxiliary equipment have been eliminated. The leach solution is directly converted into a vanadium flow battery electrolyte with no solvent recovery.

Table 6-1. The selected pathway and their corresponding products

Pathway	Highlights	Product
Pathway 1	No ongoing chemical input No waste or tailings produced Zero apparent carbon footprint Sustainable Circular economy Ultra-high pure vanadium output	V_2O_5
Pathway 2	Distillation columns and associated storage eliminated Deposits of $H_4TMA_2V_{10}O_{28}$ are calcined directly in the furnace Fewer operating units than Pathway 1. No solid or liquid wastes are produced but the CO_2 gas and the N_2 gas are released into the atmosphere. Unit U9 is replaced with a flash drum to recover methanol from the TMA-Water-Vanadium solution.	V_2O_5
Pathway 3	Leach solution is directly converted to vanadium flow battery electrolyte No recovery units are designed for the solvent, the TMA^+ stays in the electrolyte. The residues are treated with methanol and a flash drum was designed to separate the TMA-Water-Vanadium solution from methanol.	Electrolyte solution (V^{IV}, TMA^+, H_2SO_4)

6.3 Estimation of Fixed Capital Investment

6.3.1 Introduction

A model for the fixed capital investment cost was constructed based upon the estimation of the purchased equipment cost which each is a function of the theoretical mass and energy balance. For more complex units such as distillation columns, ASPEN® 11 was used to estimate the size and the required capital investment.

6.3.2 Purchased equipment cost

The cost curve method given by (Equation 6-1 assumes the purchased cost of equipment has a power-law relationship with the equipment size plus a constant.

$$C_e = a + b\,S^n \qquad \text{(Equation 6-1)}$$

Where C_e is the purchased equipment cost on a U.S. Gulf Coast basis, Jan. 2010 (CEPCI = 532.9, NF refinery inflation index = 2281.6), a, b are cost constants, S is a size parameter with variable units depending on the equipment type and n is an exponent for that equipment type.

The only variable in the above equation is the size parameter, S, which was estimated from the M&E balance data for each operating unit. Towler and Sinnott tabulated[196] the values of a, b and n for a specific range of S.

6.3.2.1 Electrodes costs - Membrane electrolysis

The cost of the electrodes can be estimated if the total area of the electrodes is known. For the divided reactor, the endpoint of the solvent recovery unit is integrated with IrO_2 anode and stainless steel 316 cathode sheets. The following expression ((Equation 6-2) defines the required electrode area for a given vanadium pentoxide-equivalent flowrate to the electrochemical cells.

$$A_{IrO_2} = \frac{\dot{M}_{V_2O_5}}{\dot{d}_{H_4TMA_2V_{10}O_{28}}} \times \frac{M_{H_4TMA_2V_{10}O_{28}}}{M_{V_2O_5}} \times \frac{f_{hydrate}}{f_{contact}} \qquad \text{(Equation 6-2)}$$

Where A_{IrO_2} is the total required area of the IrO2 sheet in the scaled-up process that is in contact with the electrolyte in (m^2), $\dot{M}_{V_2O_5}$ is the V_2O_5 equivalent flowrate of vanadium to the electrochemical cell in (t $year^{-1}$), $\dot{d}_{H_4TMA_2V_{10}O_{28}}$ is the experimentally determined deposition rate of $H_4TMA_2V_{10}O_{28}$ on to the IrO_2 electrode in (t m^{-2} $year^{-1}$), $M_{H_4TMA_2V_{10}O_{28}}$ is the molecular weight of $H_4TMA_2V_{10}O_{28}$ = 1109.71 g mol^{-1}, $M_{V_2O_5}$ is the

molecular weight of V_2O_5 = 181.88 g mol^{-1}, $f_{hydrate}$ is an experimentally determined factor to take into account the hydrates in the vanadium(V) aggregates. $f_{contact}$ is the fraction of the electrode submerged in the electrolyte solution = 0.33.

6.3.2.2 Electrode costs - Oxidative chemical reactor

The leaching tank is integrated with a RuO_2 anode and SS316 cathode. It was assumed that the total electrode area required for the scaled-up process is directly proportional to experimental A_e (volumetric electrode area). The capacity was calculated according to the set mass flowrate and a residence time of 5 hours to be consistent with the kinetic studies. The following expression describes the total RuO_2 area required for the oxidative leaching reactor.

$$A_{RuO_2} = A_e \times \dot{V}_{Sol} \times t_r \qquad \text{(Equation 6-3)}$$

$A_{RuO_2}$is the total required area of the RuO_2 electrode in the scaled-up process in (m^2), A_e is the volumetric electrode area, experimentally determined electrode area per unit volume, in (m^2 m^{-3}). $\dot{V}_{Sol}$ is the volumetric flow rate of the solvent in (m^3 s^{-1}) and t_r is the residence time of the solvent in (s).

6.3.3 Total cost of the divided reactor

Tetramethylammonium hydroxide recovery in the ionoLeach process is in principle similar to the Chlor-alkali process except oxygen gas is the only by-product of the anolyte. Therefore, cost-to-capacity (CTC) method was applied to approximate the capital cost of the installed divided electrochemical reactor cost.

The capital cost of the Chlor-alkali process was reported to be around \$200 000 t^{-1} Cl_2 day^{-1} capacity[197], which is in agreement with the investment cost of the recent Dow-Mitsui chlor-alkali plant (411 \$MM) with a chlorine production capacity of 800 000 tons per year.[198-200] The capital costs which were based on the Cl_2 production capacity were converted to per ton of H_2 produced capacity in order to be used in the estimation of the electrolyser cost in the ionoLeach process. This information and the six-tenth rule were used in the following cost-to-capacity equation (Equation 6-4)[201] to estimate the investment costs associated with the installed electrolyser reactor for the desired chlorine-equivalent H_2 capacity.

$$C_2 = C_2 \left(\frac{S_2}{S_1}\right)^n \qquad \text{(Equation 6-4)}$$

Where C is the capital expenditure, S is the chlorine-equivalent H_2 capacity in tonne H_2 per day and n is the scale factor.

6.3.4 Distillation Column investment cost via ASPEN®

Distillation columns are considered complex units in chemical process plants. Sizing, and consequently cost estimation of such complex units require detailed knowledge of the vapour-liquid equilibrium (VLE) between the homogeneous liquid phase and the liquid phase.

The DSTWU columns in ASPEN® 11 were used to simulate the performance of the distillation columns during the fractionation of the mixture from the blender pool (U9) in Figure 6-2. In the case of a model based on the effective separation of components

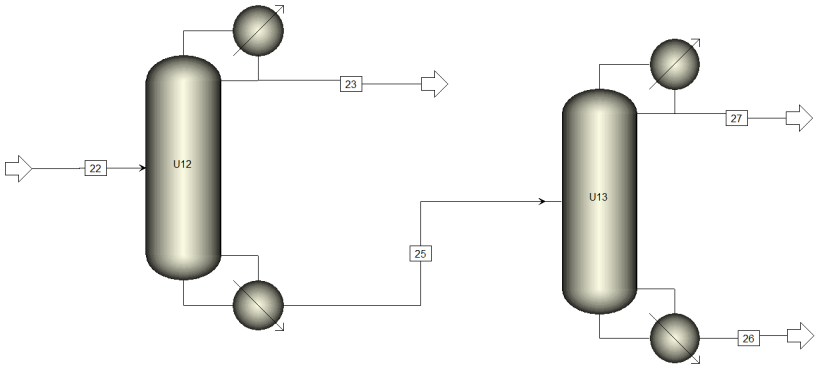


Figure 6-4. ASPEN® plus process scheme of the distillation columns for the ammonia and methanol recover in ionoLeach process.

with a minimum number of stages, the only needed specifications for the distillation columns are as follows: the minimum reflux ratio multiplier for the actual reflux ratio calculation (usually taken as 1.5)[202], desired top and bottom product concentrations, in addition to the condenser and the boiler pressures (124 kPa).[203]

Figure 6-4 shows the arrangements of the distillation columns in ASPEN®. The feed to the first distillation column was defined as a homogeneous mixture of NH_4OH (l), CH_3OH (l), and H_2O (l). It was assumed that tetramethylammonium salt presence, which has a low concentration, has a negligible effect on the VLE. Even though its presence lowers the vapour pressure of the water in the second distillation column

(U13), resulting in a reduction in the minimum reflux ratio that directly affects the capital cost and the operating costs.

For the property method, the built-in CHAO-SEA model was considered to be a suitable candidate. This method uses the Soave-Redlich-Kwong (SRK) equation of state and it was recommended by ASPEN®[204] for systems containing light gases and hydrocarbon.

6.3.5 Total Fixed Capital costs

The fixed capital cost estimate is based on the sum of the calculated C_e (purchased equipment cost) of the primary operating units required for the chemical processing plant. The following expression which accounts for the installation factors was used to estimate the cost of the installed purchased equipment.

$$C_{ISBL} = \sum_{i=1}^{i=M} C_{e,i,CS}\left[\left(1 + f_p\right) + \left(f_{er} + f_{el} + f_i + f_C + f_s + f_l\right)\right] \qquad \text{(Equation 6-5)}$$

Where for fluids-solids processes: $C_{e,i}$ is the purchased equipment cost of equipment i in carbon steel, M is the total number of pieces of equipment, f_p is the installation factor for piping = 0.6, f_{er} is the installation factor for equipment erection = 0.5, f_{el} is the installation factor for electrical work = 0.2, f_i is the installation factor for instrumentation and process control = 0.3, f_C is the installation factor for civil engineering work = 0.3, f_s is the installation factor for structures and buildings = 0.2 , f_l is the installation factor for lagging, insulation, or paint = 0.1.

(Equation 6-5 is also known as the Inside Battery Limits (ISBL) cost expression for chemical process plants. (Equation 6-6 was employed to account for the Outside Battery Limits (OSBL) and other indirect factors for the total fixed capital investment.

$$C_{FCI} = C_{ISBL}\,(1 + OS)(1 + D\&E + X) + C_{DC} + C_{ECell} \qquad \text{(Equation 6-6)}$$

$$C_{FCI} = \sum C_e \times 6.05 + C_{DC} + C_{ECell} \qquad \text{(Equation 6-7)}$$

Where for fluids-solids processes: OS is the offsites factor = 0.4, $D\&E$ is the Design and Engineering factor = 0.25, X is the contingency factor = 0.1, C_{DC} is the capital cost of the distillation columns and C_{ECell} is the capital cost of the electrochemical cells.

6.4 Estimation of Fixed Operating Costs

Manufacturing costs are described in units of money per unit of time i.e., USD per year whereas the capital costs are expressed in units of money i.e., USD and are one-time

purchase. Hence, the costs related to the manufacturing costs of the ionoLeach plant give the most important insight into the current and the future economic viability of the process. This can be then utilised by the investors for the investigation of long-term investment security in the shape of net present value (NPV), return of investment (ROI) and payback time. The method and the assumptions are explained in this subchapter to approximate the fixed operating cost

6.4.1 Cost of manufacturing

There are a large range of elements that affect the cost of manufacturing chemicals. The approach that was used to calculate the fixed operating costs in this section is similar to that reported in other chemical engineering design textbooks.[205-207] Turton et al.,[208] studied a wide range of chemical plants and came up with a methodology that can be used as a guid to estimate the direct manufacturing costs (DMC) described in Equation 6-9. In order to evaluate Equation 6-9, the key inputs to the process have to be known which are strongly dependant on the nature of the chemical plant. Key inputs for the cost of manufacturing in the ionoLeach process are listed in Table 6-2. Note that the cost of water treatment is not applicable to the base-case but is included for two other pathways.

The cost of manufacturing which is given in Equation 6-8, can be determined when the following factors are known:

1. Fixed capital investment (C_{FCI})
2. Cost of operating labor (C_{OL})
3. Cost of utilities (C_{UT})
4. Cost of waste treatment (C_{WT})
5. Cost of raw materials (C_{RM})

$$C_M = 0.28C_{FCI} + 2.73C_{OL} + 1.23(C_{RM} + C_{WT} + C_{UT}) \quad \text{(Equation 6-8)}$$

With the cost of manufacturing and the factors in Table 6-2 known, fixed operating cost, C_{FOC}, can be estimated using the following relationship. Turton et al. suggested that depreciation can be considered as 10 % of the fixed capital investment cost.[208]

$$C_{FOC} = C_{RM} + C_{WT} + C_{UT} + 2.215C_{OL} + 0.196\,C_M + 0.146\,C_{FCI} + \text{depreciation}$$

(Equation 6-9)

6.5 The minimum break-even price differential for V_2O_5

The model keeps track of all the revenues and the costs on yearly basis; uses indices to escalate costs and prices in future years; tracks the capital assets depreciation; estimates the working capital and applies taxes to the generated profits. Cash flow (CF) is a function of the saleable products Hence, the minimum break-even price differential for V_2O_5 was calculated using the Goal Seek function of Microsoft Excel by

Table 6-2. Key inputs for the analysis of cost of manufacturing.

Cost Item	Description of Factor	Symbol
Raw materials	Gasifier ash Water Tetramethylammonium hydroxide*	C_{RM}
Wastewater treatment	N/A	C_{WT}
Utilities	Major Oxidative Chemical Reactor (U2) Bowl-type centrifuge (U3) Electrochemical Cell (U4) Furnace (U8) Distillation columns (U12 and U13) Minor Pumps Conveyor belts General electricity use Simple mixers	C_{UT}
Operating labour	Cost of personnel required for plant operations	C_{OL}
Maintenance and repairs, Direct supervisory and clerical labour, operating supplies, laboratory charges	The charges that are functions of the fixed capital investment and the operating labour cost	$C_{overhead}$

setting the net present value (Equation 6-10) to zero in 20 years for the discount rate of 10.5 %. Any selling price above the "minimum" generates a positive NPV.

$$\mathrm{NPV} = \frac{\mathrm{CF}}{(1+\mathrm{i})^{\mathrm{t}}} = 0 \qquad \text{(Equation 6-10)}$$

Where NPV is the net present value with a cash flow, CF, and a discount rate of i in t time.

(Equation 6-11 describes the cash-flow after tax deduction. The profits from the saleable products, P, is the total revenue from selling (I) V_2O_5 or the derivatives as the major product and (b) Hydrogen gas and Residue as the minor products.

$$\mathrm{CF} = \mathrm{P} - (\mathrm{P} - \mathrm{D})\mathrm{t_r} \qquad \text{(Equation 6-11)}$$

Where P is the gross profit, D is the sum of tax allowances and $\mathrm{t_r}$ is the rate of taxation as a function of gross profit.

6.6 Plant Characteristics

The modelled commercial ionoLeach process performance in this chapter is based on the laboratory results. This section outlines the physical, operational and finance specifications of the proposed ionoLeach plant.

6.6.1 General Parameters

The values for the plant lifetime, construction and utilisation factor were taken from the industry standards[205-207,209] and checked against to some extant similar processes[198,210]. The ionoLeach plant was assumed to be similar to a typical process plant and it was reflected by the assumptions around the general characteristics of the plant. The "Bitumen Beyond Combustion – Phase 2" report[211] was used as a benchmark for the V_2O_5 production capacity of the ionoLeach plant. According to the report, a refinery with a bitumen refining capacity of 100 000 bpd has the potential to recover 360-1 100 tpa V_2O_5. Herein, the plant capacity was fixed for 1 000 tV_2O_5 per annum (0.119 tph). The specific electrical energy consumption of deposition of vanadium(V) aggregates onto the IrO_2 electrode was found to be 12 100 kWh tV2O5^{-1}. The minimum power required for the electrochemical cells can be calculated using Equation 6-12. Approximately 1.5 MW electrolyser will be required which is equivalent to ~1.9 MW design capacity for 80 % operating capacity or 10 units of 200 kW capacity.

Table 6-3. Summary of general plant parameters

Parameter	Value	Assumptions/Reference
Plant lifetime	20 years	Assumption
Plant capacity factor	80 %	Assumption
Plant capacity	1000 tV_2O_5/annum	Harding (2018)[211]
Electrochemical Cell Operating Power	1.4 MW	Determined by the plant capacity and the experimental results
Plant working days	350 days/annum	Towler and Sinnott (2013)[209]

Table 6-3 outlines the general parameters with respect to the assumptions or the references.

$$\mathrm{Po} = \mathrm{W}^{\mathrm{e}}_{\mathrm{V_2O_5}} \times \dot{\mathrm{M}}_{\mathrm{V_2O_5}} \qquad \text{(Equation 6-12)}$$

Where Po is the minimum power required for the electrochemical cell. $\dot{\mathrm{M}}_{\mathrm{V_2O_5}}$is the V_2O_5 equivalent flowrate of vanadium to the electrochemical cell in (t h^{-1}), $\mathrm{W}^{\mathrm{e}}_{\mathrm{V_2O_5}}$ is the specific electrical energy consumption in (kWh t^{-1} V_2O_5).

6.6.2 Process inputs

The inputs to the process were calculated using the material and energy balance data. The power requirements of the distillation columns were determined by ASPEN® to be 52.32 kW and the power required for the calcination unit (U8 in Figure 6-2) was determined from the ammonium metavanadate flowrate and its decomposition enthalpy (-1555 kJ mol^{-1})[212]. The thermophysical properties of aqueous solutions of sodium hydroxide were studied by Alexandrov (2004) [213]. This study was used to estimate the thermophysical properties of the 25 % tetramethylammonium hydroxide solution with the corresponding sodium hydroxide concentration. Table 6-4 lists the mass and energy inputs to the ionoLeach process.

6.6.3 Process Outputs

The ionoLeach process outputs were also estimated from the material and energy balance. The hydrogen gas and the oxygen gas production rates were calculated based on their stoichiometry ratio to V_2O_5 that were found experimentally. The residue

weight (dry basis) to the gasifier feed ratio was experimentally determined to be 0.425 which was used in the ionoLeach plant design. A summary of these outputs is included in Table 6-5.

Note that the total input of the gasifier ash to the process is 1710 tpa in Table 6-4 whereas the total output of the process is 1727.3 tpa (the sum of the V_2O_5 in the product stream and the residue). This is because the ash contained V^{IV} which must be oxidised to V^{V} in order to be leached out by the TMA^+ cations. Hence, the mass gain was from the oxidation of the partially oxidised vanadium.

Table 6-4. Summary of process inputs for a commercial ionoLeach plant

Parameter	**Quantity**
Annual input of gasifier ash	1710 tpa
Water	336.5 tpa (To cover the electrolysis/ water split to H_2 and O_2 gas)
Annual electricity consumption	9 673.3 MWh (Electrolyser) 637.5 MWh (Chemical reactor) 1319.4 MWh (Furnace) 439.5 MWh (Distillation columns)

Table 6-5. Summary of process outputs for the base-case

Material	**Quantity**
Vanadium production > 99.9 % purity	1000 tV_2O_5/annum
H_2 Gas	45.2 tpa
O_2 Gas	358.5 tpa
Residue	727.3 tpa

6.6.4 Financial Parameters and Indices

The financial parameters are of great importance to any techno-economic model and can potentially have a considerable impact on the overall economics of a plant. Since the location of the plant is known (Pernis, Netherlands), it is possible to accurately

determine the tax rate. The selected discount rate was the average between the suggested values of 9-12 % by NIST in “Economic Guide for Identifying and Evaluating Industry Research Investments” report.[214] The depreciation charge was introduced to the model to claim back the capital cost as a noncash charge over the plant life. Table 6-6 summarises the financial parameters used in this analysis.

Table 6-7 summarises the indices and the conversion factors used in modelling. This table was specifically generated because the costs reported in the chemical engineering textbooks are limited to time, location and the material of construction. Additionally, all good designs should cover a suitable degree of overdesign to allow uncertainties in the design data. Especially for new and unproven processes where it is likely to underestimate the equipment size.

Table 6-6 Summary of the financial parameters for the base-case

Parameter	Value	Assumptions/ Reference
Discount rate	10.5	The midrange suggested by NIST[214]
Corporate Tax Rate	15 % for €395 000 25.8 % on excess	belastingdienst.nl [215]
Depreciation Period	20 years	Assumption – based on length of plant operation
Depreciation rate	Flat 5 %	From the plant life estimation.
V_2O_5 Selling Price	$23 142 per ton	FastMarket[216]
TMA^+OH^- (dry basis) price	$12 000 per ton	Average of the quotes on Alibaba.com[217]
Electricity	$0.07 per kWh	ASPEN® Cost estimator tool[218]
Working Capital	10 % of FCI	Towler and Sinnott[209]

Table 6-7 Indices used in modelling

Index	Value
Location factor	1.19[209]
Chemical Engineering Plant Cost Index (CEPCI) index from 2010 to 2022	$CEPCI_{2010}$ = 532.9[209] $CEPCI_{2021}$ = 761.5[219]
Equipment Design Factor	15 %
EUR:USD index	1.1156[220]
GBP:USD index	1.3339[220]

6.7 Results and Discussion

This section gives insights into the economic performance of the plant for the three different pathways that produce one of the following vanadium oxide derivatives: vanadium pentoxide flakes, and vanadium redox flow battery electrolyte. The detailed

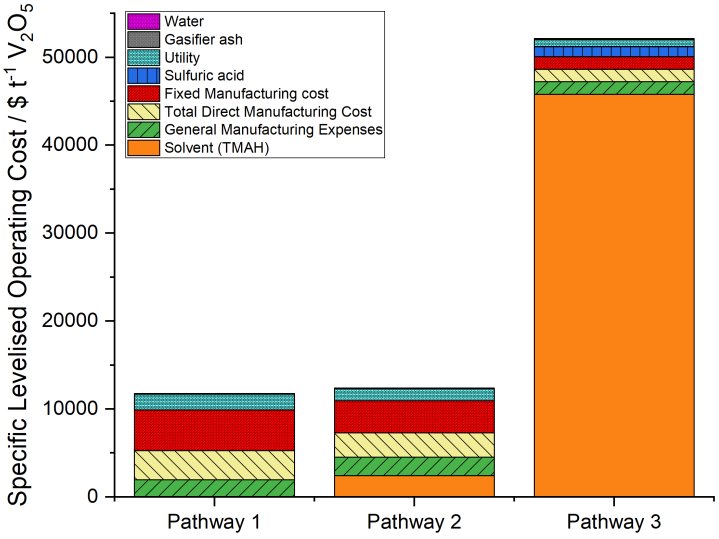


Figure 6-5. Comparison of the net levelised operating cost for the three pathways per ton of produced V_2O_5 (or equivalent).

breakdown of the total investment costs and the total operating costs were provided in the form of levelised costs for each pathway, allowing the identification of the largest contributing factors to the cost breakdown of each pathway. The economic performance of the ionoLeach plant was subsequently analysed across the three pathways including a sensitivity analysis on different parameters and the best-case optimisation.

6.7.1 Operating costs

The production cost covers all the annual costs associated with running the ionoLeach plant. Figure 6-5 shows the specific levelised operating cost for purified V_2O_5 (or equivalent) production. Across all three options, the contribution of water and gasifier ash was very low to the overall V_2O_5 production cost. This is because the net water input was low, and it was assumed that the as-received gasifier ash costs $50 less than the post-reaction residue which can be sold as a separate revenue stream.

This pathway was essentially a simplified process compared to Pathway 1 at the expense of the calcination of $H_4TMA_2V_{10}O_{28}$. It was shown in Chapter 4 that an electrolyte containing 2 mols of TMA per 10 moles of vanadium can result in 5 % enhancements in the electrochemical performance and thus, the calcination step might be bypassed. Nevertheless, the calcination of the vanadium(V) aggregates was chosen in Pathway 2 due to the lack of enough data to support the claim. Hence, 2 moles of TMA cations or equivalent to 2 moles of TMA^+OH^- should be 'consumed' or burnt to N_2 (g), CO_2 (g) and H_2O (g) per 10 moles of elemental V produced or equivalent to 5 moles of V_2O_5.

The number of functional units affects the Fixed, General and Direct manufacturing costs considerably. Hence, Pathway 3 was found to have the lowest overall manufacturing costs. Although the overall manufacturing costs had the following order Pathway 1 > Pathway 2 > Pathway 3, Pathway 3 showed overall the highest operating cost, almost five times that of Pathway 1 because no solvent recovery process was proposed for Pathway 3 and the ionic liquid with the vanadium together were assumed to be converted to VRFB electrolyte directly. Almost 90 % of the total operating cost in Pathway 3 was made up of the ionic liquid cost.

Table 6-8. The total operating cost of each pathway for ionoLeach V_2O_5

Pathway	**V_2O_5 specific operating cost**
Pathway 1	\$11 740 t^{-1}
Pathway 2	\$12 379 t^{-1}
Pathway 3	\$52 124 t^{-1}

Table 6-8 lists the specific operating costs for the proposed pathways. The base price for V_2O_5 was taken as \$23 142 per ton. It is evident that Pathway 1 and Pathway 2 were able to potentially generate a profit due to their specific operating costs being reasonably lower than the selling price of V_2O_5 alone, regardless of other small revenue streams such as H_2 gas, whereas the overall specific operating cost for Pathway 3 was already considerably higher than the selling price of V_2O_5, indicating that the feasibility of this pathway was subjected to (i) the performance of the electrolyte and (ii) the sensitivity analysis that will be explained in 6.7.3.

6.7.2 Total Investment Cost

The breakdown of the equipment costs and the total investment cost of each pathway are shown in Table 6-9. As it was expected, the total investment cost follows the degree of process complexity: Pathway 1 > Pathway 2 > Pathway 3. In comparison to the base-case, the removal of the distillation columns and their auxiliary equipment from Pathway 2 reduced the total investment cost by ca. $8.5 million or equivalent to 22 % of the total investment of the base-case (Pathway 1). Further reduction in the degree of the process complexity showed that Pathway 3 only required 23 % of the total investment of Pathway 1.

Table 6-9. Total investment costs and the contributing elements.

Installed Equipment	Pathway 1	Pathway 2	Pathway 3
Conveyors	$2 768 000	$1 845 000	$923 000
Pumps	$1 543 000	$1 080 000	$617 000
Tanks, Storage, and Jacketed Reactors	$3 714 000	$3 222 000	$3 222 000
Separators and Filters	$6 796 000	$4 563 000	$2 330 000
Hydrogen Processing Units	$355 000	$355 000	-
Furnace	$1 424 000	$1 424 000	-
Electrolyser	$10 559 000	$10 559 000	-
Distillation Columns	$2 373 000	-	-
Factors			
Location Factor multiplier	1.19	1.19	1.19
Working capital multiplier	1.10	1.1	1.05
Total Investment	$38 657 000	$30 170 000	$8 861 000

6.7.3 Economic Performance of an ionoLeach Commercial Plant

Key Findings

The ionoLeach plant was designed to have the annual input capacity of 1 710 ton gasifier ash and the annual output capacity of 1 000 ton V_2O_5 (or equivalent, depending on the pathway). Table 6-10 gives an overview of the key economic parameters of each pathway using the base-case input values tabulated in Table 6-6. The findings suggest that Pathway 3 was not economically viable, and Pathway 2 was the most economically viable pathway with the minimum V_2O_5 break-even price of $16 500 per ton and an IRR of 30 %. The payback time for this pathway was approximately 3.5 years which is equivalent to an ROI of 29 %. It should be noted that Pathway 2 was designed to reduce the CAPEX of pathway 1 at the cost of partially "consuming" the solvent. Hence, its economic viability is vulnerable to the price of TMA^+OH^-. The degree of the vulnerability is investigated in the next section.

Table 6-10. Summary of the key economic parameters

	NPV_{20}	**IRR**	**V_2O_5 break-even price**
Pathway 1	$37 000 000	25 %	$17 100 t^{-1}
Pathway 2	$41 000 000	30 %	$16 500 t^{-1}
Pathway 3	$(240 00 000)	-	$53 400 t^{-1}

Sensitivity Analysis

Figure 6-6 shows the sensitivity of NPV_{20} in spider diagrams for (a) Pathway 1 (b) Pathway 2 and (c) Pathway 3 using six key economic inputs: (1) the V_2O_5 selling price; (2) Electricity price; (3) Solvent (TMA^+OH^-) price; (4) CAPEX; (5) Discount rate; and (6) Cost-to-capacity scale factor of the electrolysis unit. The steeper the gradient of the line the greater the net change in NPV_{20} per unit percentage. The sensitivity analysis revealed that the V_2O_5 selling price had the greatest impact on both Pathway 1 and Pathway 2 with a positive slope whereas for Pathway 3, the steepest gradient was for the TMA^+OH^- price, confirming that the economic feasibility is primarily subjected to the solvent price followed by the V_2O_5 selling price.

The base value for the V_2O_5 selling price was determined by Fastmarket[216] to be $23 142 per ton of V_2O_5 for the typical commodity-grade of 98.5 %.The selling price of this commodity for a green future has seen large fluctuations in recent years, mainly due to its over 95 % dependency on the steel industry in addition to being geographically concentrated in certain places such as China and Russia. The most recent forecasted V_2O_5 price is $30 856 by 2025 which is mainly attributed to the increase in the market demand by VRFBs as well as the construction industry. Only a 1 % increase in the V_2O_5 selling price will increase the ionoLeach process NPV by nearly 3.78 % and 3.44 % for Pathway 1 and Pathway 2, respectively.

Tolwer and Sinnott suggested that an installation of factor of 6.05 can be used to determine the total fixed capital cost when the process contains both solid and liquid processing.[209] The sensitivity analysis was performed for the CAPEX to understand the effect of the assumed installation factors as well as to cover any miscellaneous equipment. The effect of CAPEX on NPV was found to be the second largest for both Pathway 1 and Pathway 2 but the magnitude of the gradients was found to be considerably lower than that of the V_2O_5 selling price. For Pathway 3, NPV dependency on CAPEX was very small which is due to its minimum functional unit requirements.

The electrolysis equipment is the heart of Pathway 1 and Pathway 2. Due to the large impact of the cost-to-capacity (CTC) scale factor on the capital cost of the electrolysis equipment, its effect was investigated separately from 0.5 to 0.7 with the base-case (0.6) being in the middle. An increase in the CTC scale factor indicates that large scale technologies can be downgraded more linearly so it has an inverse effect on the NPV as it is evident from Figure 6-6 (a) and (b). The CTC factor was found to be the third most impactful factor on the sensitivity of NPV with a magnitude identical to that of the CAPEX effect.

Although the effect was modest, electricity price gradient was found to follow the degree of the process complexity: Pathway 1 > Pathway 2 > Pathway 3 meaning the higher the number of functional units, the higher the electricity bill and so, the lesser the NPV.

The National Institute of Standards and Technology (NIST)[214] suggested a discount rate of 9-12 % which was used as the minimum and maximum values in the sensitivity analysis with the base-case (10.5 %) being in the middle. Unsurprisingly, the discount

rate was found to have an inverse relationship with NPV for Pathway 1 and Pathway 2. On the contrary, the NPV for the base-case of Pathway 3 was considerably negative so an increase in discount rate results in a net positive increase in NPV which economically means the net present value of the money that was lost during the lifetime of the plant had a smaller time value due to the higher discount rate.

Due to environmental concerns, Pathway 1 was designed in a way to maximise the recovery of the solvent. Hence, the gradient of the TMA^+OH^- price curve in the sensitivity analysis is zero whereas Pathway 2 and Pathway 3 consume TMA^+OH^- solvent partially and totally, respectively. Therefore, both have a negative gradient on

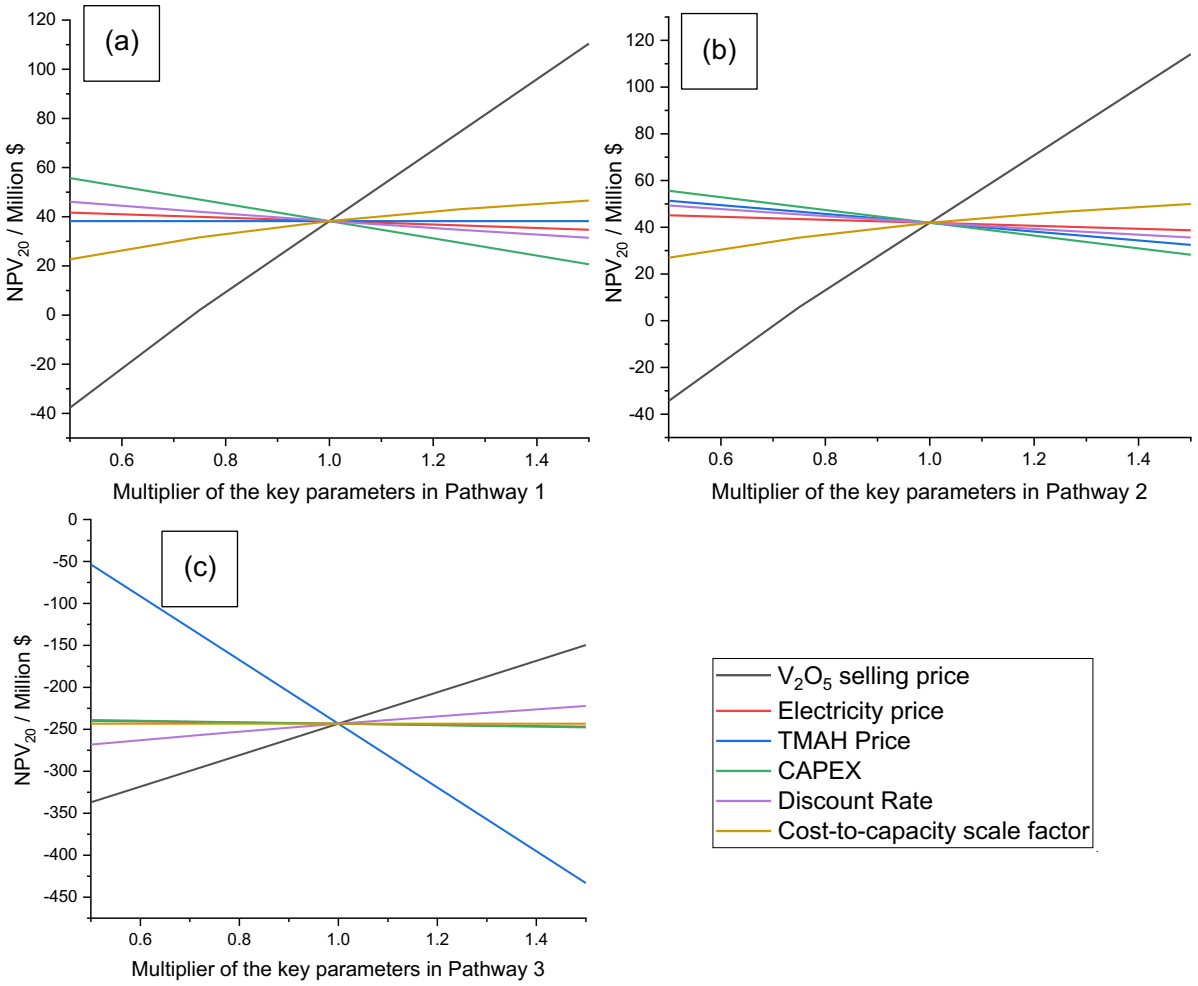


Figure 6-6. Major factors impacting the project's NPV_{20} for (a) top left, Pathway 1; (b) top right, Pathway 2 and (c) bottom, Pathway 3. Note that the multiplier points of 0.5 and the 1.5 for Discount rate correspond to 9 % and 12 %; and for cost-to-capacity scale factor to 0.5 and 0.7, respectively.

the chart. The TMA^+OH^- price effect in Pathway 3 has the steepest gradient confirming that even slight reductions in the purchase price of the solvent can greatly affect the project's NPV.

Now that the magnitude effect of each key economic input has been understood, the following statements are considered in determining accept-or-reject of the project:

- Pathway 1

The economic viability of this pathway is primarily dependent on the selling price of V_2O_5. The economic parameters of this model were used as a basis for the two other pathways

- Pathway 2

The sensitivity analysis revealed that the economic viability of this pathway was mostly dependant on the V_2O_5 selling price and TMA^+OH^- price, therefore, it is crucial to understand the combined effect of the two. Figure 6-7 (a) shows NPV as a function of TMA^+OH^- price and V_2O_5 selling price for pathway 2. It is evident that the economic viability of this Pathway can tolerate harsh fluctuations in the studied variables as it was (almost) only the minimum V_2O_5 selling price (\$11 571 t^{-1}) that generated a negative NPV while the rest of the scenarios generated a positive NPV over 20 years. It is interesting to note that for the base-case V_2O_5 selling price which is \$23 141 t^{-1}, even the highest studied TMA^+OH^- purchase price could generate \$30 million NPV, 26 % IRR and 25 % ROI.

Comparatively speaking, and taking NPV as the indicator for determining accept-or-reject of the project, the pathways can be compared by setting their NPV equal, then calculating the maximum economically competitive (MEC) TMA^+OH^- price. The Goal Seek function of Microsoft Excel was used to identify the MEC price for the ionic liquid. For Pathway 2 to become the viable pathway over Pathway 1, the maximum economically competitive TMA^+OH^- price was found to be \$14 360 per ton which is already 16.5 % higher than the base-case \$12 000 per ton.

A possible TMA^+OH^- synthesis route starts with the preparation of the tetramethylammonium ion via the reaction of trimethylamine and a methyl halide followed by an electrolysis reaction where the TMA^+OH^- is collected at the cathode. The minimum ongoing manufacturing (MOM) cost for the aforementioned synthesis

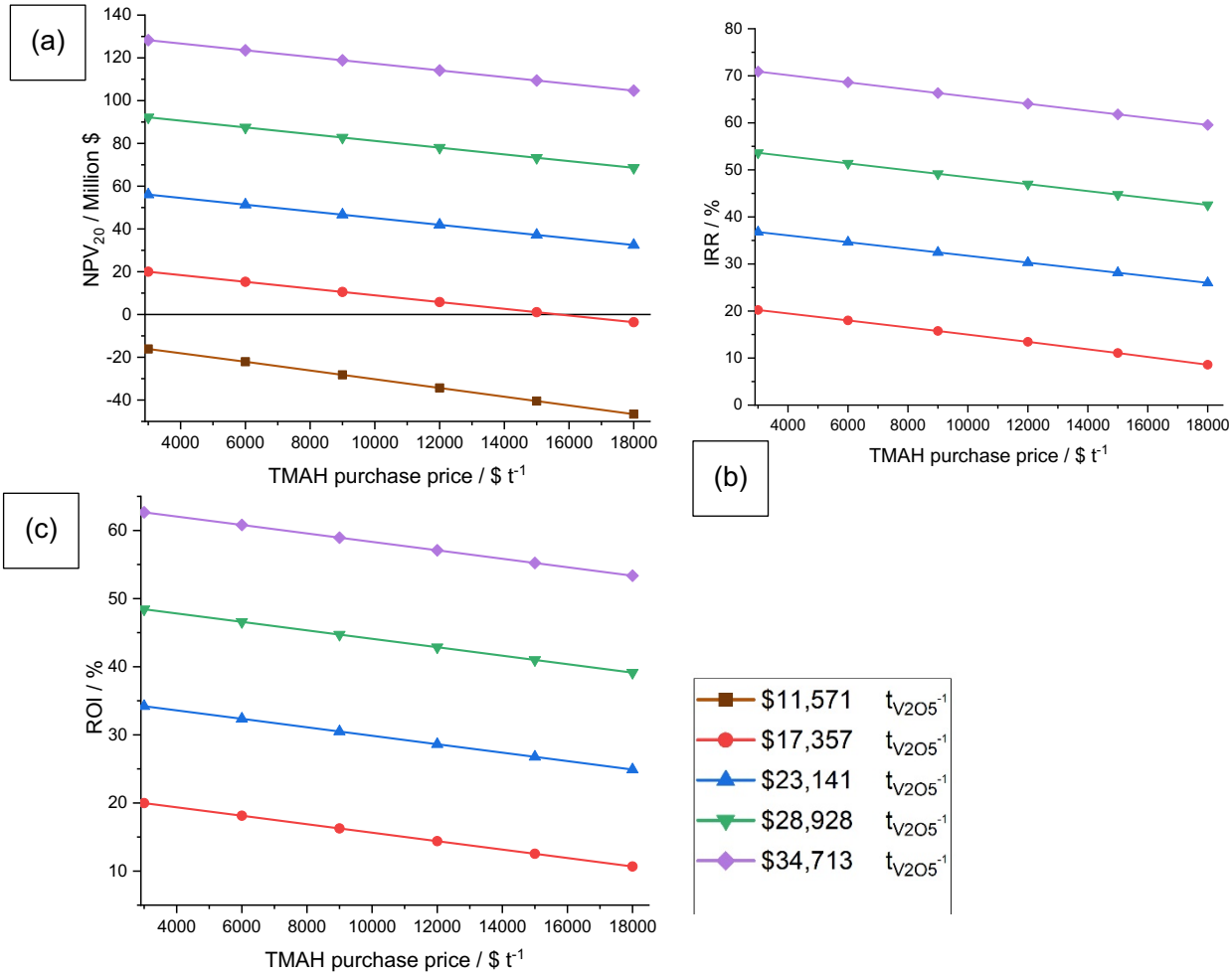


Figure 6-7. Impact of TMA^+OH^- price and V_2O_5 selling price on the (a), top left, NPV; (b) top right, (IRR) and (c) bottom, (ROI) of the ionoLeach plant for pathway 2. Base price for vanadium pentoxide = \$23 142 ton^{-1}.

route includes the chemicals and the electricity used during the electrolysis to produce TMA^+OH^-. A simple calculation revealed that the MOM cost can be as low as \$2 445 t^{-1} TMA^+OH^- on the dry basis. As MEC TMA^+OH^- price >> MOM cost, it can be safely concluded that Pathway 2 is more economically attractive as the ionic liquid price has a relatively large margin on top of the minimum ongoing manufacturing cost.

- Pathway 3

The same analogy as Pathway 2 was applied to Pathway 3 for a comparative study. The MEC TMA^+OH^- price was found to be \$2 079 per ton for this pathway to become the favoured pathway for investors over Pathway 1. The MEC price is lower than the

estimated MOM cost ($2 445 t^{-1}), indicating that Pathway 3 is the least attractive pathway.

Chen et al.[221] can be used as another basis for the bulk production price for two protic ionic liquids and they reported that triethylammonium hydrogen sulfate and 1-methylimidazolium hydrogen sulfate can be manufactured at the costs of $1 240 and $2 960–5 880 per ton, respectively. The cost of $2 079 per ton of TMA^+OH^- seems unrealistic as the process at a minimum requires more premium equipment.

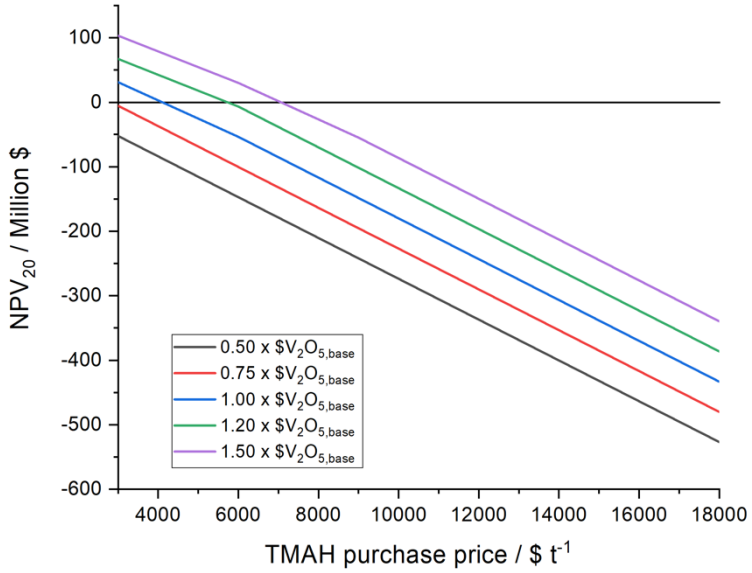


Figure 6-8. NPV sensitivity to TMA^+OH^- price for different V_2O_5 selling price. $\$V_2O_{5,base}$ = $23 142 t^{-1}

The sensitivity analysis revealed that Pathway 3 had the steepest slopes for both V_2O_5 selling price and TMA^+OH^- price. Hence, it is crucial to study the combined effect of the two on the economic indicators. Figure 6-8 represents the sensitivity of NPV to the variations in TMA^+OH^- price for different V_2O_5 selling prices for pathway 3. It is evident that even for the top range of V_2O_5 selling price such as 1.5x the base vanadium price, any TMA^+OH^- price over $8 000 per ton can drag the NPV to its break-even point.

With the base-case parameters, the break-even TMA^+OH^- price was found to be approximately $4 300. Overall, for Pathway 3 it was found not only economically infeasible to make electrolyte directly from the leach liquor but also the electrolyte was

Table 6-11. Less conservative input parameters

Parameter	Value	Reasoning
V_2O_5 selling price	\$27 770 t^{-1}	20 % premium was considered on top of the base-case price to account for the ultra-high purity of the product. The predicted selling price for V_2O_5 (98.5 % purity) is \$30 856 per ton by 2025.[216]
TMA^+OH^- (dry basis) purchase price	\$7 200 t^{-1}	The base-case price is five times the chemical inputs cost of making TMA^+OH^-. The new cost is 40 % lesser than the initial conservative assumption.
Discount rate	8.00 %	Discount rates of 5-6 % have been used in hydrometallurgical processes.[222,223] A discount rate of 8 % was considered to be a fairer value.
Equipment installation cost factor	5.00	A value between 4 to 6 is typically used.[209] The electrolyser cost alone was calculated separately, so a moderate value was considered for the lesser complex equipment.

Table 6-12 More realistic economic performance of Pathway 2

Economic indicator	Calculated values
NPV_{20}	\$105.2 Million
ROI	49.2 %
IRR	54.53 %
Total Investment	\$27.2 Million
Cash Flow	\$13.4 Million

shown to be inadequate for the VRFB applications due to having negative effects on the electrochemical performance of the vanadium(IV) species as described in 0.

6.1 Not-too-conservative ionoLeach techno-economics: Pathway 2

A combination of comparative and sensitivity analysis was conducted in 6.7.3. It was revealed that Pathway 2, with its moderate investment cost and high gross profit, is superior to the other pathways. The capital cost was reduced at the cost of partial decomposition of TMA^+OH^- which translates to a carbon emissions footprint of 387 tons of CO_2 per year. A carbon tax on excess CO_2 (or equivalent) emissions was considered to be ($80) per ton.[224] The yearly added emissions tax for the arbitrary emissions tax of $80 per ton will be $31 000 which is negligible compared to the yearly gross profit of $11.1 million.

Although the base-case was shown to be economically viable (Table 6-10), the input parameters were selected somewhat conservatively. Lesser conservative scenarios have been included which also considered the future changes. After all, Table 6-11 shows a more realistic and not-too-conservative input data and Table 6-12 shows the results using the corresponding input data. In summary, a commercial ionoLeach plant with the IRR of 54.53 % and the NPV of $105.2 million is attractive. However, from a technical point of view, a demonstration plant needs to be commissioned to serve as the iteration of equipment design and plant construction which ultimately give insight into the capital costs and the operating costs.

When scaling up a chemical processing plant, several considerations need to be taken into account. Firstly, the equipment and infrastructure must be appropriately sized to accommodate the larger production volumes. This involves selecting larger reactors, storage tanks, and other necessary equipment to handle increased throughput. Additionally, the process parameters and operating conditions must be carefully evaluated to ensure that the scaled-up plant can achieve the desired product quality and maintain process efficiency. Factors such as heat transfer, mass transfer, and reaction kinetics may change with scale, necessitating adjustments to maintain optimal performance. Moreover, safety considerations become even more critical during scale-up, as larger quantities of chemicals and energy are involved. Process hazards should be thoroughly assessed, and appropriate safety measures implemented to mitigate risks. Finally, economic feasibility and cost analysis play a crucial role in scaling up a

plant. The increased capital investment, operating costs, and potential economies of scale need to be evaluated to determine the financial viability of the expanded operation. By addressing these considerations thoughtfully, successful scaling up of a chemical processing plant can be achieved.

7. Conclusions, Further work, and recommendations

7.1 Conclusions

This research project has been conducted to develop a detailed understanding of vanadium(V) extraction behaviour from refinery waste feedstocks as an alternative using task specific ionic liquids followed by recovery of vanadium(V) in a sustainable approach thereby eliminating problems caused by the availability of the vanadium-containing ores and the hazardous emissions of processing such feedstocks. To cover those interests, this report has been tailored in four sections, each focussed on a critical part of the technology:

Chapter 3

The extractions were carried out by mixing gasifier ash with tetramethylammonium hydroxide solutions followed by ICP-MS analysis of the ionic liquid phase. Both as-received and post-extraction gasifier ash were characterised using the best available techniques such as XPS, XRD and ICP-MS to understand the extraction behaviour of vanadium(V). The combination of the aforementioned techniques revealed that the gasifier ash contained partially oxidised vanadium which could explain the poor extraction yield when no additives were used. The use of oxidising agents such as sodium chlorite had considerable effects in both extraction yields and extraction kinetics as expected. Vanadium(V) extraction yield as high as 81.5 ± 1.5 % were obtained with the following conditions in the shortest time: [TMA^+OH^-] 2.78 mol dm^{-3}, [$NaClO_2$] 0.221 mol dm^{-3}, slurry density 10 $cm^3\ g^{-1}$ and 90 °C reaction temperature.

The total vanadium in the gasifier ash was then split into unextractable (17 %) and extractable (83 %). All of the unextractable vanadium content was shown to be in the Ni-V-O phase and thus, the term “equilibrium extraction yield” was used when all the remaining vanadium in the residue was in the Ni-V-O phase. The extractable vanadium phase could not be accurately identified due to the complexity of the sample. However, it was revealed by XPS that the ash contained 69.3 % V^V and 13.7 % V^{IV}, possibly in the form of V_2O_5 + $M_xV_2O_5$ with M being a concomitant cation.

In order to make this work applicable to other feedstocks, control experiments were conducted using solutions containing TMA^+,V^V and a range of transition metals and non-transition metals such silicon and aluminium. Aluminium(III) and silicon(IV) which are the most abundant elements on Earth, did not show chemical interaction with TMA^+

cations, unlike Na^+ at high pH, solving one of the biggest challenges for the hydrometallurgical extraction of vanadium(V) from vanadium-bearing materials.

The extraction kinetics data showed that reaction rates were controlled by both the transfer of materials across the interface and the diffusion through a product layer, meaning the V^{IV} oxidation reaction was unlikely to be the limiting step. The high activation energy calculated as 70.4 kJ mol^{-1} implied that the reaction kinetics were unlikely to be limited overwhelmingly by the diffusion through the product layer. The heterogenous oxidative dissolution of vanadium(IV) from the gasifier ash involved the formation of an intermediate followed by the dissolution reaction at a reaction layer as shown in Figure 3-64. The dissolution kinetics of vanadium(V) followed a semi-empirical mathematical model as shown below:

$$\frac{1}{3}\ln(1-\mathrm{x}) + [(1-\mathrm{x})^{-\frac{1}{3}} - 1] = 2.9 \times 10^5\ [\mathrm{TMAH}]^{1.819}\ [\mathrm{NaClO_2}]^{0.340} \left[\frac{\mathrm{L}}{\mathrm{S}}\right]^{0.833} \mathrm{e}^{\frac{-70\,422}{\mathrm{RT}}}\mathrm{t}$$

Chapter 4

It was shown that vanadium and the ionic liquid can be separated via membrane electrolysis of tetramethylammonium vanadate solutions. Batch electrolysis pH was shown to be time-dependant causing an increase in the catholyte pH due to regeneration of TMA^+OH^- ionic liquid, and a decrease in the anolyte pH due to the protonation of vanadium(V) oxyanion species. As the anolyte pH decreased, TMA^+ polyoxovanadates undergo stepwise protonation and when pH = 6, aggregates of a novel vanadium compound with the chemical formula of $H_4TMA_2V_{10}O_{28}.5H_2O$, started to deposit onto the surface of the anode. Upon further electrolysis of the solution to pH < 3 another novel vanadium(V) compound which was undesirable appeared in the anolyte. The chemical formula of the compound was likely $H_3TMA_3V_{10}O_{28}.6H_2O$. Hence, it was suggested that anode to be fed with TMAV followed by continuously removing $H_4TMA_2V_{10}O_{28}.5H_2O$ at pH 6. Vanadium(V) was precipitated in an AMV precipitation process while recovering the 'locked' TMA^+ ions at the same time. NH_4VO_3 was calcined at 500 °C which resulted in an ultrapure V_2O_5 product. Alternatively, aggregates can be calcined directly thereby bypassing the AMV precipitation process at the cost of losing the equivalent of 200 kg worth of TMA^+OH^- per 1 000 kg V_2O_5 produced. The optimum deposition rate onto the anode was found to be 0.845 g m^{-2} s^{-1} for the following conditions: initial $[TMA^+]$ = 2.78 mol dm^{-3}, initial

$[V^{V}]$ = 0.883 mol dm^{-3} and j = 1 000 A m^{-2}, leading to a specific electrical energy consumption of 12 100 kW h t^{-1}_{V2O5}.

To maximise recovery of both TMA^{+} ions and vanadium(V), LC-MS results showed that the residue became TMA^{+} free after resuspending the residue in methanol four times at a solid to liquid ratio of 1 g residue: 2 cm^3 fresh methanol.

Chapter 5

As explained in Chapter 3, high vanadium(V) extraction yields can be achieved via oxidative leaching. However, addition of sodium chlorite has two main drawbacks (i) introduction of Na^{+} impurities to the solution which could potentially interfere the final purity of the product and (ii) any inputs would result in a production of at least an output in the form of by-products/tailings which is inherent. To overcome the aforementioned challenges, in situ electrogeneration of hypochlorite and its use in the oxidation of low oxidation state vanadium in the gasifier ash was investigated which showed encouraging results. In the present methodology, a 0.5 mol dm^{-3} $TMA^{+}Cl^{-}$ solution containing the gasifier ash was electrolysed at different temperatures and current densities. As a result of the electrooxidation process at pH 8, solid vanadium(V) was formed through a heterogenous oxidation reaction on the outer surface of the vanadium(IV) particles, becoming a barrier between the active chloride ions in the aqueous phase and the V(IV) oxide in the solid phase. Hence, the electrooxidation reaction was chemically controlled at the lowest reaction rate (bulk concentration = surface concentration), while the overall reaction was heavily dominated by the internal mass transfer when the rate constant increased due to increase in temperature. Practically, an electrooxidation temperature of 90 °C resulted in the maximum limiting extraction yield of ca. 82 % within the range of 250 – 1 000 A m^{-2}. From an energy saving point of view only, and if heat loss to surrounding is negligible, electrooxidation the gasifier ash at 250 A m^{-2} for 9 h at 90 °C appeared to be optimal, corresponding to a specific electrical energy consumption of 1 147 kW h t^{-1}_{V2O5}.

The vanadium(V) from the electrooxidised gasifier ash was concentrated in the leach liquor to a purity of around 99.8 %. The SEM and EDX analyses of the electrodeposited materials revealed that during membrane electrolysis, polyoxovanadium nanometric 2D sheets were stacking in a laminated structure, which also acted as a purification step to synthesise ultrapure vanadium aggregates of $H_4TMA_2V_{10}O_{28}$. Directly

calcination of the aggregates resulted the formation of short needle-like ultrapure (i.e. >99.99 %) V_2O_5 crystals.

Chapter 6

Three scenarios were considered in the techno-economic assessment of an ionoLeach chemical plant. The pathways and the corresponding economic performances were as follows:

- Pathway 1 was designed for no carbon footprint or ongoing chemical inputs with highly pure V_2O_5 output. The process complexity in this case was the highest as it required further treatments of the vanadium(V) aggregates. The capital investment required was found to be $39 million. This process is expected to generate $37 million NPV_{20} at a discount rate of 10.5%, 25% IRR with a V_2O_5 break-even price of $17 100 t^{-1}.
- Pathway 2 was designed to reduce process complexity at the cost of losing the solvent partially. In this pathway, vanadium(V) aggregates are calcined directly to N_2, CO_2, H_2O and V_2O_5 resulting in a loss of 200 kg of TMA^+OH^- equivalent for every 1000 kg V_2O_5 produced. The capital investment required was found to be $30 million. This process is expected to generate $41 million NPV_{20} at a discount rate of 10.5%, 30% IRR with a V_2O_5 break-even price of $16 500 t^{-1}.
- Pathway 3 takes the leach liquor containing vanadium with 99.8 % purity and produces Vanadium Redox Flow Battery (VRFB) electrolyte directly with no further treatments. The original solvent needs to be replenished thereby leading to a significant increase in the operating cost. The capital investment required was found to be $9 million. The returns on the investment was highly unfavourable with the V_2O_5 break-even price of $53 400 t^{-1}. Not only is this process economically unviable, but also the preliminary results in 0 demonstrated that too much excess TMA^+ impacted the electrochemical performance of the reference electrolyte negatively.

Overall, selective leaching of vanadium oxides from the gasifier ash was successfully demonstrated using tetramethylammonium hydroxide solutions. Leaching efficiency was improved via an electrooxidation process. The leached vanadium(V) and the ionic liquid were separated via membrane electrolysis with the only by-products being the hydrogen and the oxygen gas while consuming no chemical reagents.

7.2 Further work and recommendations

This work opened new insights to fundamental understanding for hydrometallurgical extraction of vanadium followed by recovery of solvent and vanadium via an electrochemical methodology.

This work particularly focused on leaching vanadium from a sample of petroleum ash with no further physical or chemical treatments on the sample itself. More studies are recommended to give insights on the effect of feedstock treatments on both the recovery yield and the reaction kinetics.

It was shown in Chapter 3 that Ni-V-O phase did not react in the presence of highly concentrated TMA^+OH^- solutions. It is frequently reported in the literature that vanadium in such spinel phases can be broken down to alkaline-leachable compounds. In the same chapter it was shown that Mn^{2+} precipitated at in the presence of TMA^+ at high pH while vanadium stayed dissolved. Presumably, addition of Mg, Mn or Ca oxides to the gasification units can inhibit the formation of such unextractable phases by the formation of Mg-V-O or Mn-V-O. Alternatively, the post-gasification ash can be roasted with the aforementioned metal oxides. Sodium roasting is not recommended as Na^+ ions are co-extracted during the leaching process. Whether inhibiting the formation of the spinel phases during the gasification process or roasting the post-gasification process ash both of which could potentially serve two purposes (i) maximising vanadium(V) extraction yield by sacrificing less valuable metal hydroxides such $Mg(OH)_2$ in the residue and (ii) simplifying the scaled-up process as the need for electrooxidation units might be eliminated.

It was proposed in 0 that continuous recovery of the vanadium(V) aggregates and the ionic liquid may be achieved continuous using rotary drum electrodes and knife blades, continuous feed of TMAV and removal of TMA^+OH^- from the cathode. However, deposition of vanadium(V) aggregates onto rotating drum electrodes can result in several problems caused by non-symmetrical geometries producing inhomogeneous spatial distributions of potential and current densities. Moreover, formation of the aggregates could lead to an increase in the magnitude of the cell potential difference. Mechanical removal of the aggregates could also damage the electrode/electrocatalyst. An alternative recovery process is recommended to be studied in the future in which TMA_3^+ VO_4^{3-} solution with the starting pH > 14 is

electrolysed to pH 8 where $TMA^+ VO_3^-$ is expected to form in the solution. In a separate chemical reactor, vanadium(V) is precipitated via the AMV precipitation process which results in the formation of NH_4VO_3 and $TMA_2^+SO_4^{2-}$ (Reaction 7-1) In a second divided electrochemical reactor, TMA sulfate can be electrolysed to sulfuric acid and TMA hydroxide as shown by Reaction 7-5. The resulting ammonia gas (Reaction 7-6) from the calcination of NH_4VO_3 can pass through the electrochemically generated sulfuric acid to regenerate ammonium sulfate (Reaction 7-7). The overall process uses no on-going chemicals (Reaction 7-8) and the in situ formation of the vanadium(V) aggregates can be overcome. Yet, some determining factors have to be addressed such as technoeconomic assessment, vanadium(V) purity, water balance and scalability.

$$2\,[\mathrm{TMA}]^+\,[\mathrm{VO_3^-}] + \,(\mathrm{NH_4})_2\mathrm{SO_4} \rightarrow$$

$$2\,\mathrm{NH_4VO_3}\downarrow \,+\, [\mathrm{TMA}]_2^+\,\mathrm{SO_4^{2-}} \qquad \text{(Reaction 7-1)}$$

Electrochemical reactor:

Anode:

$$\mathrm{H_2O} \rightarrow \tfrac{1}{2}\mathrm{O_2} + 2\mathrm{H^+} + \,+2\,\mathrm{e^-} \qquad \text{(Reaction 7-2)}$$

Membrane

$$2\,\mathrm{TMA^+(aq)} + \mathrm{SO_4^{2-}(aq)} + 2\,\mathrm{H^+(aq)} \rightarrow \mathrm{H_2SO_4(aq)} + 2\,\mathrm{TMA^+\,(aq)} \text{ (Reaction 7-3)}$$

Cathode:

$$2\,\mathrm{H_2O} + 2\,\mathrm{e^-} \rightarrow \,\mathrm{H_2} + 2\,\mathrm{OH^-} \qquad \text{(Reaction 7-4)}$$

(1) Overall Electrolytic Process:

$$2\,\mathrm{TMA^+(aq)} + \mathrm{SO_4^{2-}(aq)} + 2\,\mathrm{H_2O} \rightarrow [\,2\,\mathrm{TMA^+(aq)} + \,2\,\mathrm{OH^-}]$$

$$+\,\mathrm{H_2SO_4} + \mathrm{H_2} + \,1/2\,\mathrm{O_2} \qquad \text{(Reaction 7-5)}$$

(2) Calcination of AMV

$$2\,\mathrm{NH_4VO_3} \rightarrow \mathrm{V_2O_5} + 2\,\mathrm{NH_3} + \mathrm{H_2O} \qquad \text{(Reaction 7-6)}$$

(3) Ammonium sulfate regeneration

$$2\,\mathrm{NH_3} + \mathrm{H_2O} + \mathrm{H_2SO_4} \rightarrow \,(\mathrm{NH_4})_2\mathrm{SO_4} \qquad \text{(Reaction 7-7)}$$

Overall Process:

$$2\,[\mathrm{TMA}]^{+}\,[\mathrm{VO_3^{-}}] + 2\,\mathrm{H_2O} \rightarrow$$

$$[\,2\,\mathrm{TMA^{+}(aq)} + \,2\,\mathrm{OH^{-}}] + \,\mathrm{V_2O_5} + \,1/2\,\mathrm{O_2} \,+\, \mathrm{H_2} \qquad \text{(Reaction 7-8)}$$

Whilst exploiting the pathway to which this study has provided to extract. The following points need to be considered in order to make a final decision for full application:

- Accurate understanding of the solvent loss in both the residue and the products.
- Whether the ionoLeach process is applicable to certain feedstocks or can be applied to a wider spectrum of materials such as vanadium-bearing slags.
- Extraction and purification of other valuable metal oxides such as nickel oxide from the gasifier ash.
- Find a practical way to purify the ionic liquid solution from dissolved alkali metals such as sodium ions.

8. References

1. Limited TMA. Vanadium Consumptions and Applications 2022; https://www.tmtlimited.com.au/vanadium/. Accessed 08/11/2022, 2022.
2. Finance BNE. Global Storage Market to Double Six Times by 2030. 2017; https://about.bnef.com/blog/global-storage-market-double-six-times-2030/. Accessed 08/11/2022, 2022.
3. Kirsten Hund DLP, Thao P. Fabregas, Tim Laing, John Drexhage. *Minerals for Climate Action: The Mineral Intensity of the Clean Energy Transition.* Washington2020.
4. Systems IE. Vanadium Battery Recycling / Making a Sustainable Choice. https://invinity.com/cost-of-recycling-vanadium-batteries/. Accessed 06/07/2022, 2022.
5. Resilience for the Future: The UK's critical minerals strategy. 2022; https://www.gov.uk/government/publications/uk-critical-mineral-strategy/resilience-for-the-future-the-uks-critical-minerals-strategy. Accessed 22/11/2022, 2022.
6. P A J Lusty RAS, A G Gunn, N E Idoine. *UK criticality assessment of technology critical minerals and metals: Decarbonisation & Resource Management*2021. CR/21/120.
7. Emsley J. When the Earth moves so does the price of Vanadium. 2012; https://edu.rsc.org/elements/vanadium/2020031.article. Accessed 22/11/2022, 2022.
8. Vanadium Market fundamentals. 2022; https://www.bushveldminerals.com/about-vanadium/. Accessed 22/11/2022, 20222.
9. Vanadium Sources and Vanadium Production. 2022; https://vanitec.org/vanadium/making-vanadium. Accessed 22/11/2022, 2022.
10. Kumar D, Chalapathi Rao NV. Vanadium bearing titaniferous-magnetite mineralization from the Simdega area, Chhotanagpur Gneissic Complex, Eastern India. 01/13 2021.
11. Tulcan RXS, Ouyang W, Lin C, He M, Wang B. Vanadium pollution and health risks in marine ecosystems: Anthropogenic sources over natural contributions. *Water Res.* Dec 1 2021;207:117838.
12. López L, Lo Mónaco S. Vanadium, nickel and sulfur in crude oils and source rocks and their relationship with biomarkers: Implications for the origin of crude oils in Venezuelan basins. *Organic Geochemistry.* 2017/02/01/ 2017;104:53-68.
13. Elsayed I, Abdallah R, El-Naggar A, Mashaly M, Salem A. Characterization of Four Egyptian Crude Oils. *Nature and Science (ISSN: 1545-0740).* 01/01 2012;10.
14. Gomez-Bueno CO, Spink DR, Rempel GL. Extraction of vanadium from athabasca tar sands fly ash. *Metallurgical Transactions B.* 1981/06/01 1981;12(2):341-352.
15. Sönnichsen N. Oil production worldwide from 1998 to 2021. 2022; https://www.statista.com/statistics/265229/global-oil-production-in-million-metric-tons/. Accessed 22/11/2022, 2022.
16. Peng H. A literature review on leaching and recovery of vanadium. *Journal of Environmental Chemical Engineering.* 2019/10/01/ 2019;7(5):103313.
17. Zhang J, Zhang W, Li C. Purification of the Acidic Vanadium-Bearing Solution with a Novel Approach of Chemical Precipitation. *Metals.* 2021;11(4).
18. Rout A, Binnemans K. Influence of the ionic liquid cation on the solvent extraction of trivalent rare-earth ions by mixtures of Cyanex 923 and ionic liquids. *Dalton Transactions.* 2015;44(3):1379-1387.
19. Quijada-Maldonado E, Olea F, Sepúlveda R, et al. Possibilities and challenges for ionic liquids in hydrometallurgy. *Separation and Purification Technology.* 2020/11/15/ 2020;251:117289.
20. Alguacil FJ. Liquid-Liquid Extraction of Indium(III) from the HCl Medium by Ionic Liquid A327H+Cl− and Its Use in a Supported Liquid Membrane System. 2020;25(22):5238.
21. Alguacil FJ, Lopez FA. Insight into the Liquid–Liquid Extraction System AuCl4−/HCl/A327H+Cl− Ionic Liquid/Toluene. 2021;9(4):608.
22. Quijada-Maldonado E, Sánchez F, Pérez B, Tapia R, Romero J. Task-Specific Ionic Liquids as Extractants for the Solvent Extraction of Molybdenum(VI) from Aqueous Solution Using Different Commercial Ionic Liquids as Diluents. *Industrial & Engineering Chemistry Research.* 2018/02/07 2018;57(5):1621-1629.
23. Nayak S, Devi N. Studies on extraction of gallium (III) from chloride solution using Cyphos IL 104 and its removal from photodiodes and red mud. *Hydrometallurgy.* 2017/08/01/ 2017;171:191-197.
24. Dhiman S, Gupta B. Cyphos IL 104 assisted extraction of indium and recycling of indium, tin and zinc from discarded LCD screen. *Separation and Purification Technology.* 2020/04/15/ 2020;237:116407.
25. Mishra BB, Devi N. Solvent extraction and separation of europium (III) using a phosphonium ionic liquid and an organophosphorus extractant-A comparative study. *Journal of Molecular Liquids.* 2018/12/01/ 2018;271:389-396.
26. Vander Hoogerstraete T, Binnemans K. Highly efficient separation of rare earths from nickel and cobalt by solvent extraction with the ionic liquid trihexyl(tetradecyl)phosphonium nitrate: a process relevant to the recycling of rare earths from permanent magnets and nickel metal hydride batteries. *Green Chemistry.* 2014;16(3):1594-1606.

27. Zhao J, Yu Z, Liu H. Extraction of rare earths by undiluted [P666,14][NO3] and DEHEHP, and the recovery of rare earths from lamp phosphors. *Journal of Material Cycles and Waste Management.* 2019/11/01 2019;21(6):1518-1525.

28. Mahandra H, Faraji F, Ghahreman A. Novel Extraction Process for Gold Recovery from Thiosulfate Solution Using Phosphonium Ionic Liquids. *ACS Sustainable Chemistry & Engineering.* 2021/06/21 2021;9(24):8179-8185.

29. Ilyas S, Kim H, Srivastava RR. Separation of platinum group metals from model chloride solution using phosphonium-based ionic liquid. *Separation and Purification Technology.* 2021/12/01/ 2021;278:119577.

30. Rout A, Binnemans K. Liquid–liquid extraction of europium(iii) and other trivalent rare-earth ions using a non-fluorinated functionalized ionic liquid. *Dalton Transactions.* 2014;43(4):1862-1872.

31. Shi C, Jing Y, Xiao J, Wang X, Jia Y. Liquid-liquid extraction of lithium using novel phosphonium ionic liquid as an extractant. *Hydrometallurgy.* 2017/05/01/ 2017;169:314-320.

32. Wang L, Zhang G, Guan W, et al. Complete removal of trace vanadium from ammonium tungstate solutions by solvent extraction. *Hydrometallurgy.* 2018/08/01/ 2018;179:268-273.

33. Liu Z, Huang J, Zhang Y, et al. Separation and recovery of vanadium and aluminum from oxalic acid leachate of shale by solvent extraction with Aliquat 336. *Separation and Purification Technology.* 2020/10/15/ 2020;249:116867.

34. Imam DM, El-Nadi YA. Recovery of molybdenum from alkaline leach solution of spent hydrotreating catalyst by solvent extraction using methyl tricaprylammonium hydroxide. *Hydrometallurgy.* 2018/09/01/ 2018;180:172-179.

35. Corbett PJ, McIntosh AJS, Gee M, Hallett JP. Use of ionic liquids to remove harmful M2+ contaminants from hydrocarbon streams. *Molecular Systems Design & Engineering.* 2018;3(2):408-417.

36. de los Ríos AP, Hernández-Fernández FJ, Alguacil FJ, et al. On the use of imidazolium and ammonium-based ionic liquids as green solvents for the selective recovery of Zn(II), Cd(II), Cu(II) and Fe(III) from hydrochloride aqueous solutions. *Separation and Purification Technology.* 2012/09/03/ 2012;97:150-157.

37. Turgis R, Arrachart G, Michel S, et al. Ketone functionalized task specific ionic liquids for selective tantalum extraction. *Separation and Purification Technology.* 2018/05/08/ 2018;196:174-182.

38. Chauhan G, de Klerk A. Acidified Ionic Liquid Assisted Recovery of Vanadium and Nickel from Oilsands Bitumen. *Energy & Fuels.* 2021/04/01 2021;35(7):5963-5974.

39. Dai Z, Guan D, Liu Y, et al. Acid Leaching Process in Extracting Vanadium from Blast Furnace Slag in Panzhihua Vanadium Titanium Magnetite. Paper presented at: Advances in Energy and Environmental Materials; 2018//, 2018; Singapore.

40. Lekobotja M, Mojapelo M, Goso X, Lagendijk H. Recovery of vanadium from discard titaniferous magnetite slag using the soda ash roast-leach process. Paper presented at: 3rd Young Professionals Conference Innovation Hub, Pretoria, 9-10 March2017.

41. Wu K, Wang Y, Wang X, et al. Co-extraction of vanadium and chromium from high chromium containing vanadium slag by low-pressure liquid phase oxidation method. *Journal of Cleaner Production.* 2018/12/01/ 2018;203:873-884.

42. Gilligan R, Nikoloski AN. The extraction of vanadium from titanomagnetites and other sources. *Minerals Engineering.* 2020/01/15/ 2020;146:106106.

43. Branthaver JF. Influence of Metal Complexes in Fossil Fuels on Industrial Operations. *Metal Complexes in Fossil Fuels.* Vol 344: American Chemical Society; 1987:188-204.

44. Dechaine GP, Gray MR. Chemistry and Association of Vanadium Compounds in Heavy Oil and Bitumen, and Implications for Their Selective Removal. *Energy & Fuels.* 2010/05/20 2010;24(5):2795-2808.

45. Habashi F. *Handbook of extractive metallurgy*: Wiley-VCH; 1998.

46. Li X-s, Xie B. Extraction of vanadium from high calcium vanadium slag using direct roasting and soda leaching. *International Journal of Minerals, Metallurgy, and Materials.* 2012/07/01 2012;19(7):595-601.

47. Wang Z, Chen L, Aldahrib T, et al. Direct recovery of low valence vanadium from vanadium slag —— Effect of roasting on vanadium leaching. *Hydrometallurgy.* 2020/01/01/ 2020;191:105156.

48. Song W-C, Li K, Zheng Q, Li H. A Novel Process of Vanadium Extraction from Molten Vanadium Bearing Slag. *Waste and Biomass Valorization.* 2014/06/01 2014;5(3):327-332.

49. Xiao Q, Chen Y, Gao Y, Xu H, Zhang Y. Leaching of silica from vanadium-bearing steel slag in sodium hydroxide solution. *Hydrometallurgy.* 2010/09/01/ 2010;104(2):216-221.

50. Liu B, Du H, Wang SN, et al. A Novel Method to Extract Vanadium and Chromium from Vanadium Slag using Molten NaOH-NaNO3 Binary System. *AIChE Journal.* 02/01 2013;59.

51. Li X, Yu H, Xue X. Extraction of Iron from Vanadium Slag Using Pressure Acid Leaching. *Procedia Environmental Sciences.* 2016/01/01/ 2016;31:582-588.

52. Aarabi-Karasgani M, Rashchi F, Mostoufi N, Vahidi E. Leaching of vanadium from LD converter slag using sulfuric acid. *Hydrometallurgy.* 2010/04/01/ 2010;102(1):14-21.

53. Zhang J, Zhang W, Zhang L, Gu S. Mechanism of vanadium slag roasting with calcium oxide. *International Journal of Mineral Processing.* 2015/05/10/ 2015;138:20-29.

54. Yu L, Dong YC, Ye GZ, Sichen D. Concentrating of vanadium oxide in vanadium rich phase(s) by addition of SiO2 in converter slag. *Ironmaking & Steelmaking.* 2007/03/01 2007;34(2):131-137.

55. Dong M, Xue X, Yang H, Liu D, Wang C, Li Z. A novel comprehensive utilization of vanadium slag: As gamma ray shielding material. *Journal of Hazardous Materials.* 2016/11/15/ 2016;318:751-757.

56. Hobson AJ, Stewart DI, Mortimer RJG, Mayes WM, Rogerson M, Burke IT. Leaching behaviour of co-disposed steel making wastes: Effects of aeration on leachate chemistry and vanadium mobilisation. *Waste Management.* 2018/11/01/ 2018;81:1-10.

57. Zhang X, Liu F, Xue X, Jiang T. Effects of microwave and conventional blank roasting on oxidation behavior, microstructure and surface morphology of vanadium slag with high chromium content. *Journal of Alloys and Compounds.* 2016/11/25/ 2016;686:356-365.

58. Zhang X, Fang D, Song S, Cheng G, Xue X. Selective leaching of vanadium over iron from vanadium slag. *Journal of Hazardous Materials.* 2019/04/15/ 2019;368:300-307.

59. Li H-Y, Fang H-X, Wang K, et al. Asynchronous extraction of vanadium and chromium from vanadium slag by stepwise sodium roasting–water leaching. *Hydrometallurgy.* 2015/07/01/ 2015;156:124-135.

60. Yildirim IZ, Prezzi M. Chemical, Mineralogical, and Morphological Properties of Steel Slag. *Advances in Civil Engineering.* 2011/10/26 2011;2011:463638.

61. Li W, Zhang Y, Liu T, Huang J, Wang Y. Comparison of ion exchange and solvent extraction in recovering vanadium from sulfuric acid leach solutions of stone coal. *Hydrometallurgy.* 2013/01/01/ 2013;131-132:1-7.

62. Zhang X, Xie B, Diao J, Li XJ. Nucleation and growth kinetics of spinel crystals in vanadium slag. *Ironmaking & Steelmaking.* 2012/02/01 2012;39(2):147-154.

63. Lee J-c, Kurniawan, Kim E-y, Chung KW, Kim R, Jeon H-S. A review on the metallurgical recycling of vanadium from slags: towards a sustainable vanadium production. *Journal of Materials Research and Technology.* 2021;12:343-364.

64. Li J, Chen X, Wang B, et al. Effects of sodium and potassium on fusion characteristics of petroleum coke ash with high vanadium and nickel. *Fuel.* 2022/02/01/ 2022;309:122177.

65. Ibrahim AH, Lyu X, Atia BM, Gado MA, ElDeeb AB. Phase transformation mechanism of boiler ash roasted with sodium salt for vanadium extraction. *Journal of Material Cycles and Waste Management.* 2022/10/14 2022.

66. Jia L, Anthony EJ, Charland JP. Investigation of Vanadium Compounds in Ashes from a CFBC Firing 100 Petroleum Coke. *Energy & Fuels.* 2002/03/01 2002;16(2):397-403.

67. Rahimi G, Rastegar SO, Rahmani F, Gu T. Correction: Ultrasound-assisted leaching of vanadium from fly ash using lemon juice organic acids. *RSC Advances.* 2020;10(63):38378-38378.

68. Cai Z, Zhang Y. Phase transformations of vanadium recovery from refractory stone coal by novel NaOH molten roasting and water leaching technology. *RSC Advances.* 2017;7(59):36917-36922.

69. Zhang Y-M, Bao S-X, Liu T, Chen T-J, Huang J. The technology of extracting vanadium from stone coal in China: History, current status and future prospects. *Hydrometallurgy.* 2011/09/01/ 2011;109(1):116-124.

70. Wen J, Jiang T, Xu Y, Cao J, Xue X. Efficient extraction and separation of vanadium and chromium in high chromium vanadium slag by sodium salt roasting-(NH4) 2SO4 leaching. *Journal of industrial and engineering chemistry.* 2019;71:327-335.

71. Zhao Y, Wang W, Zhang Y, Song S, Bao S. In-situ investigation on mineral phase transition during roasting of vanadium-bearing stone coal. *Advanced Powder Technology.* 2017/03/01/ 2017;28(3):1103-1107.

72. Wang M, Huang S, Chen B, Wang X. A review of processing technologies for vanadium extraction from stone coal. *Mineral Processing and Extractive Metallurgy.* 2020/10/01 2020;129(3-4):290-298.

73. Li X, Wei C, Deng Z, et al. Recovery of Vanadium from H2SO4-HF Acidic Leaching Solution of Black Shale by Solvent Extraction and Precipitation. *Metals.* 2016;6(3).

74. Zhang Y, Zhang T-A, Dreisinger D, Lv C, Lv G, Zhang W. Recovery of vanadium from calcification roasted-acid leaching tailing by enhanced acid leaching. *Journal of Hazardous Materials.* 2019/05/05/ 2019;369:632-641.

75. Zhang J, Zhang W, Xue Z. Oxidation kinetics of vanadium slag roasting in the presence of calcium oxide. *Mineral Processing and Extractive Metallurgy Review.* 2017;38(5):265-273.

76. Peng H, Guo J, Zheng X, Liu Z, Tao C. Leaching kinetics of vanadium from calcification roasting converter vanadium slag in acidic medium. *Journal of Environmental Chemical Engineering.* 2018/08/01/ 2018;6(4):5119-5124.

77. Li M, Liu B, Zheng S, et al. A cleaner vanadium extraction method featuring non-salt roasting and ammonium bicarbonate leaching. *Journal of Cleaner Production.* 2017/04/15/ 2017;149:206-217.

78. Li H-Y, Wang K, Hua W-H, Yang Z, Zhou W, Xie B. Selective leaching of vanadium in calcification-roasted vanadium slag by ammonium carbonate. *Hydrometallurgy.* 2016/03/01/ 2016;160:18-25.

79. Zou X-Y, Peng Q-j, Ouyang Y-Z, Tian R-G. Research on the roasting process with calcium compounds for silica based vanadium ore. *Guocheng Gongcheng Xuebao(The Chinese Journal of Process Engineering)(China).* 2001;1(2):189-192.

80. Xiang J, Pei G, Huang Q, et al. A Multi-step Process for the Cleaner Utilization of Vanadium-Bearing Converter Slag. Paper presented at: Rare Metal Technology 2019; 2019//, 2019; Cham.

81. Gao H, Jiang T, Zhou M, et al. Effect of microwave irradiation and conventional calcification roasting with calcium hydroxide on the extraction of vanadium and chromium from high-chromium vanadium slag. *Minerals Engineering.* 2020;145:106056.

82. Li M, Zheng S, Liu B, et al. A Clean and Efficient Method for Recovery of Vanadium from Vanadium Slag: Nonsalt Roasting and Ammonium Carbonate Leaching Processes. *Mineral Processing and Extractive Metallurgy Review.* 2017/07/04 2017;38(4):228-237.

83. Ji Y, Shen S, Liu J, Xue Y. Cleaner and effective process for extracting vanadium from vanadium slag by using an innovative three-phase roasting reaction. *Journal of Cleaner Production.* 2017/04/15/ 2017;149:1068-1078.

84. Liu S, Wang L, Chou K. A Novel Process for Simultaneous Extraction of Iron, Vanadium, Manganese, Chromium, and Titanium from Vanadium Slag by Molten Salt Electrolysis. *Industrial & Engineering Chemistry Research.* 2016/12/21 2016;55(50):12962-12969.
85. Li X-s, Xie B, Wang G-e, Li X-j. Oxidation process of low-grade vanadium slag in presence of Na2CO3. *Transactions of Nonferrous Metals Society of China.* 2011/08/01/ 2011;21(8):1860-1867.
86. Yang K, Zhang X, Tian X, Yang Y, Chen Y. Leaching of vanadium from chromium residue. *Hydrometallurgy.* 2010/06/01/ 2010;103(1):7-11.
87. Zhi-Gan D, Cun-Xiong L, Chang W, Min-Ting L, Yan-Hui L, Hui-Ling WJMM. Research on New Process of Vanadium Extraction from Vanadium Containing Stone Coal by Acid Leaching under Oxygen Pressure. 2008;38(07):30.
88. Tian L, Xu Z, Chen L, Liu Y, Zhang T-a. Effect of microwave heating on the pressure leaching of vanadium from converter slag. *Hydrometallurgy.* 2019/03/01/ 2019;184:45-54.
89. Liu Z, Li Y, Chen M, et al. Enhanced leaching of vanadium slag in acidic solution by electro-oxidation. *Hydrometallurgy.* 2016/01/01/ 2016;159:1-5.
90. Li M, Wei C, Qiu S, Zhou X, Li C, Deng Z. Kinetics of vanadium dissolution from black shale in pressure acid leaching. *Hydrometallurgy.* 2010/09/01/ 2010;104(2):193-200.
91. Peng H, Liu Z, Tao C. Selective leaching of vanadium from chromium residue intensified by electric field. *Journal of Environmental Chemical Engineering.* 2015/06/01/ 2015;3(2):1252-1257.
92. Liu B, Du H, Wang S-N, et al. A novel method to extract vanadium and chromium from vanadium slag using molten NaOH-NaNO3 binary system. *AIChE Journal.* 2013;59(2):541-552.
93. Qiu S, Wei C, Li M, Zhou X, Li C, Deng Z. Dissolution kinetics of vanadium trioxide at high pressure in sodium hydroxide–oxygen systems. *Hydrometallurgy.* 2011/01/01/ 2011;105(3):350-354.
94. Peng H, Liu Z, Tao C. Leaching Kinetics of Vanadium with Electro-oxidation and H2O2 in Alkaline Medium. *Energy & Fuels.* 2016/09/15 2016;30(9):7802-7807.
95. Liu Z, Nueraihemaiti A, Chen M, Du J, Fan X, Tao C. Hydrometallurgical leaching process intensified by an electric field for converter vanadium slag. *Hydrometallurgy.* 2015/05/01/ 2015;155:56-60.
96. Hukkanen E, Walden H. The production of vanadium and steel from titanomagnetites. *International Journal of Mineral Processing.* 1985/08/01/ 1985;15(1):89-102.
97. Taylor PR, Shuey SA, Vidal EE, Gomez JC. Extractive metallurgy of vanadium-containing titaniferous magnetite ores: a review. *Mining, Metallurgy & Exploration.* 2006/05/01 2006;23(2):80-86.
98. Swinbourne DR, Richardson T, Cabalteja F. Understanding ferrovanadium smelting through computational thermodynamics modelling. *Mineral Processing and Extractive Metallurgy.* 2016/01/02 2016;125(1):45-55.
99. Zhang J-h, Zhang W, Zhang L, Gu S-q. A Critical Review of Technology for Selective Recovery of Vanadium from Leaching Solution in V2O5 Production. *Solvent Extraction and Ion Exchange.* 2014/04/16 2014;32(3):221-248.
100. Grzmil B, Wronkowski J. Removal of phosphates and fluorides from industrial wastewater. *Desalination.* 2006/03/01/ 2006;189(1):261-268.
101. Song Y, Qian F, Xiang LC. Research on phosphorus removal from swine wastewater by precipitation of calcium phosphate. *Huanjing Kexue/Environmental Science.* 06/01 2011;32:1679-1686.
102. Wen J, Jiang T, Zhou W, Gao H, Xue X. A cleaner and efficient process for extraction of vanadium from high chromium vanadium slag: Leaching in (NH4)2SO4-H2SO4 synergistic system and NH4+ recycle. *Separation and Purification Technology.* 2019/06/01/ 2019;216:126-135.
103. Xiong P, Zhang Y, Bao S, Huang J. Precipitation of vanadium using ammonium salt in alkaline and acidic media and the effect of sodium and phosphorus. *Hydrometallurgy.* 2018/09/01/ 2018;180:113-120.
104. Shi Y, Wang HJCMI. Separation of molybdenum and vanadium from spent catalysts. 2004;28(2):39-41.
105. Zhu H, Xiao X, Guo Z, et al. Adsorption of vanadium (V) on natural kaolinite and montmorillonite: Characteristics and mechanism. *Applied Clay Science.* 2018/09/01/ 2018;161:310-316.
106. He D, Feng Q, Zhang G, Ou L, Lu Y. An environmentally-friendly technology of vanadium extraction from stone coal. *Minerals Engineering.* 2007/10/01/ 2007;20(12):1184-1186.
107. Cai ZL, Feng YL, Zhou YZ, Li HR, Wang WD. Selective Separation and Extraction of Vanadium (V) Over Manganese (II) from Co-Leaching Solution of Roasted Stone Coal and Pyrolusite Using Solvent Extraction. *JOM.* 2013/11/01 2013;65(11):1492-1498.
108. Yang X, Zhang Y, Bao S, Shen C. Separation and recovery of vanadium from a sulfuric-acid leaching solution of stone coal by solvent extraction using trialkylamine. *Separation and Purification Technology.* 2016/05/30/ 2016;164:49-55.
109. Tavakoli MR, Dreisinger DB. Separation of vanadium from iron by solvent extraction using acidic and neutral organophosporus extractants. *Hydrometallurgy.* 2014/01/01/ 2014;141:17-23.
110. Shi Q, Zhang Y, Huang J, Liu T, Liu H, Wang L. Synergistic solvent extraction of vanadium from leaching solution of stone coal using D2EHPA and PC88A. *Separation and Purification Technology.* 2017/06/30/ 2017;181:1-7.
111. Li X, Guo Z, Li J, et al. Quenched electrochemiluminescence of Ag nanoparticles functionalized g-C3N4 by ferrocene for highly sensitive immunosensing. *Analytica Chimica Acta.* 2015/01/07/ 2015;854:40-46.
112. Hu G, Chen D, Wang L, et al. Extraction of vanadium from chloride solution with high concentration of iron by solvent extraction using D2EHPA. *Separation and Purification Technology.* 2014/04/07/ 2014;125:59-65.
113. Jayadas S, Reddy ML. Solvent extraction separation of vanadium(V) from multivalent metal chloride solutions using 2-ethylhexyl phosphonic acid mono-2-ethylhexyl ester. 2002;77(10):1149-1156.

114. Chen D, Zhao H, Hu G, et al. An extraction process to recover vanadium from low-grade vanadium-bearing titanomagnetite. *Journal of Hazardous Materials.* 2015/08/30/ 2015;294:35-40.
115. Li X-b, Wei C, Wu J, et al. Thermodynamics and mechanism of vanadium(IV) extraction from sulphate medium with D2EHPA, EHEHPA and CYANEX 272 in kerosene. *Transactions of Nonferrous Metals Society of China.* 2012/02/01/ 2012;22(2):461-466.
116. Zhao J, Hu Q, Li Y, Liu H. Efficient separation of vanadium from chromium by a novel ionic liquid-based synergistic extraction strategy. *Chemical Engineering Journal.* 2015/03/15/ 2015;264:487-496.
117. Bal Y, Bal KE, Cote G, Lallam A. Characterization of the solid third phases that precipitate from the organic solutions of Aliquat® 336 after extraction of molybdenum(VI) and vanadium(V). *Hydrometallurgy.* 2004/11/01/ 2004;75(1):123-134.
118. Ye G, Hu Y, Tong X, Lu L. Extraction of vanadium from direct acid leaching solution of clay vanadium ore using solvent extraction with N235. *Hydrometallurgy.* 2018/05/01/ 2018;177:27-33.
119. Wen J, Liu F, Cao H, Ning P, Zhang Y. Insights into the extraction of various vanadium species by primary amine. *Hydrometallurgy.* 2017/11/01/ 2017;173:57-62.
120. Nguyen TH, Lee MS. Solvent extraction of vanadium(V) from sulfate solutions using LIX 63 and PC 88A. *Journal of Industrial and Engineering Chemistry.* 2015/11/25/ 2015;31:118-123.
121. Kim H-I, Lee K-W, Mishra D, et al. Separation and recovery of vanadium from leached solution of spent residuehydrodesulfurization (RHDS) catalyst using solvent extraction. *Journal of Industrial and Engineering Chemistry.* 2014/11/25/ 2014;20(6):4457-4462.
122. Zeng L, Li Q, Xiao L. Extraction of vanadium from the leach solution of stone coal using ion exchange resin. *Hydrometallurgy.* 2009/07/01/ 2009;97(3):194-197.
123. Zhu X, Li W, Zhang Q, Zhang C, Chen L. Separation characteristics of vanadium from leach liquor of red mud by ion exchange with different resins. *Hydrometallurgy.* 2018/03/01/ 2018;176:42-48.
124. Hu Q, Zhao J, Wang F, Huo F, Liu H. Selective extraction of vanadium from chromium by pure [C8mim][PF6]: An anion exchange process. *Separation and Purification Technology.* 2014/06/27/ 2014;131:94-101.
125. Singh R, Mahandra H, Gupta B. Cyphos IL 102 assisted liquid-liquid extraction studies and recovery of vanadium from spent catalyst. *Minerals Engineering.* 2018/11/01/ 2018;128:324-333.
126. Pan B, Liu B, Wang S, et al. Ammonium vanadate/ammonia precipitation for vanadium production from a high vanadate to sodium ratio solution obtained via membrane electrolysis method. *Journal of Cleaner Production.* 2020/08/01/ 2020;263:121357.
127. Fang Q, Wei X, Yan H, Jiang C, Wang Y, Xu T. A Sustainable Electrochemical Method for the Production of Vanadium Pentoxide Using Bipolar Membrane Electrodialysis. *Industrial & Engineering Chemistry Research.* 2022/06/15 2022;61(23):8233-8241.
128. Petranikova M, Tkaczyk AH, Bartl A, Amato A, Lapkovskis V, Tunsu C. Vanadium sustainability in the context of innovative recycling and sourcing development. *Waste Management.* 2020/07/15/ 2020;113:521-544.
129. Navarro R, Guzman J, Saucedo I, Revilla J, Guibal E. Vanadium recovery from oil fly ash by leaching, precipitation and solvent extraction processes. *Waste Management.* 2007/01/01/ 2007;27(3):425-438.
130. Zhang YJTCJoPE. The green process engineering science. 2001;1(1):10-15.
131. Jung M, Mishra B. Vanadium Recovery from Oil Fly Ash by Carbon Removal and Roast-Leach Process. *Jom.* 2017;70(2):168-172.
132. Takahashi H, Fujiwara W, Sun H, Yoshida T, Matsushima Y. Extraction of Vanadium from Ammonia Slag under Near-Atmospheric Conditions. *Metals.* 2018;8(6).
133. Walker; J, Johnston J. J. Chem. Soc., Trans.,87, 955-961. 1905.
134. Revision of classification of tetramethylammonium hydroxide

(TMAH). In: Goods CoEotToD, Classification aotGHSo, Chemicals aLo, eds2021.
135. Zhou C, Li J, Wu L, et al. Friction-induced selective etching on silicon by TMAH solution. *RSC Adv.* Oct 22 2018;8(63):36043-36048.
136. Filby RH. Origin and nature of trace element species in crude oils, bitumens and kerogens: implications for correlation and other geochemical studies. *Geological Society, London, Special Publications.* 1994;78(1):203-219.
137. Carlin RT, Wikes JS. *J. of Mole. Catalysis.* 1990;63:125.
138. Yue H, Cheng G, Liu J, Xue X, Zhang W. A Novel Method of Recovery Vanadium from Vanadium Slag through CaO2-Briquetting Roasting Process. 2022;93(7):2100788.
139. Romanovskaia E, Romanovski V, Kwapinski W, Kurilo I. Selective recovery of vanadium pentoxide from spent catalysts of sulfuric acid production: Sustainable approach. *Hydrometallurgy.* 2021;200.
140. Rahimi G, Rastegar SO, Rahmani Chianeh F, Gu T. Ultrasound-assisted leaching of vanadium from fly ash using lemon juice organic acids. *RSC Adv.* Jan 7 2020;10(3):1685-1696.
141. Demeter M, Neumann M, Reichelt W. Mixed-valence vanadium oxides studied by XPS. *Surface Science.* 2000/05/20/ 2000;454-456:41-44.
142. Zimmermann R, Claessen R, Reinert F, Steiner P, Hüfner S. Strong hybridization in vanadium oxides: evidence from photoemission and absorption spectroscopy. *Journal of Physics: Condensed Matter.* 1998/06/29 1998;10(25):5697.
143. Mendialdua J, Casanova R, Barbaux Y. XPS studies of V2O5, V6O13, VO2 and V2O3. *Journal of Electron Spectroscopy and Related Phenomena.* 1995/04/26/ 1995;71(3):249-261.

144. Sawatzky GA, Post D. X-ray photoelectron and Auger spectroscopy study of some vanadium oxides. *Physical Review B.* 08/15/ 1979;20(4):1546-1555.

145. Burgess D. NIST Critically Selected Stability Constants of Metal Complexes: Version 8.0. In: Technology NIoSa, ed2019.

146. Smrčok Ľ, Bitschnau B, Filinchuk Y. Low temperature powder diffraction and DFT solid state computational study of hydrogen bonding in NH4VO3. *Crystal Research and Technology.* 09/01 2009;44:978-984.

147. Pérez-Benítez A, Bernès S. Redetermination of ammonium metavanadate. *IUCrData.* 2018/01/01/ 2018;3:x181080.

148. Liu S, Chen Y, Yu S, Zhang D, Xie G. Rapid Vanadium Extraction from Roasted Vanadium Steel Slag via a H2SO4–H2O2 System: Process and Mechanism. *ACS Omega.* 2022/07/26 2022;7(29):25580-25589.

149. Wang P-P, Xu C-Y, Ma F-X, Yang L, Zhen L. In situ soft-chemistry synthesis of β-Na0.33V2O5 nanorods as high-performance cathode for lithium-ion batteries. *RSC Advances.* 2016;6(107):105833-105839.

150. Cordoba R, Goclon J, Kuhn A, Garcia-Alvarado F. Theoretical Description, Synthesis, and Structural Characterization of beta-Na0.33V2O5 and Its Fluorinated Derivative beta-Na0.33V2O4.67F0.33: Influence of Oxygen Substitution by Fluorine on the Electrochemical Properties. *Inorg Chem.* Nov 16 2020;59(22):16361-16374.

151. Morgan B, Lahav O. The effect of pH on the kinetics of spontaneous Fe(II) oxidation by O2 in aqueous solution – basic principles and a simple heuristic description. *Chemosphere.* 2007/08/01/ 2007;68(11):2080-2084.

152. Ming-lei Gao X-xX, Lan-jie Li, He Yang, Rui-guo Bai, Hai-xue Wang. A novel method to extract vanadium from vanadium-bearing steel slag using sodium carbonate solution. *Physicochemical Problems of Mineral Processing.* 2018;54(3), 2018, 911-921.

153. Dickinson CF, Heal GR. Solid–liquid diffusion controlled rate equations. *Thermochimica Acta.* 1999;340-341:89-103.

154. Aydogan S, Aras A, Canbazoglu M. Dissolution kinetics of sphalerite in acidic ferric chloride leaching. *Chemical Engineering Journal.* 2005;114(1-3):67-72.

155. Dehghan R, Noaparast M, Kolahdoozan M. Leaching and kinetic modelling of low-grade calcareous sphalerite in acidic ferric chloride solution. *Hydrometallurgy.* 2009;96(4):275-282.

156. Li J, Yang Y, Wen Y, et al. Leaching Kinetics and Mechanism of Laterite with NH4Cl-HCl Solution. *Minerals.* 2020;10(9).

157. Amer AM. Hydrometallurgical processing of Egyptian black shale of the Quseir-Safaga region. *Hydrometallurgy.* 1994/07/01/ 1994;36(1):95-107.

158. Teimouri S, Potgieter JH, van Dyk L, Billing C. The Kinetics of Pyrite Dissolution in Nitric Acid Solution. *Materials (Basel).* Jun 13 2022;15(12).

159. Kohitlhetse I, Thubakgale K, Mendonidis P, Manono M. Investigating the Effect of Reaction Temperature on the Extraction of Calcium from Ironmaking Slag: A Kinetics Study. *Environmental Sciences Proceedings.* 2021;6(1).

160. James Walker JJ. C.—Tetramethylammonium hydroxide. *Journal of the Chemical Society, Transactions.* 1905;87:955-960.

161. Osamu Yagi SS. synthesis of pure tetramethylammonium hydroxide solution free from chloride ion by electrolysis of its hydrogen carbonate salt. *The Chemical Society of Japan.* 1993:2041-2044.

162. Osamu Yagi SS. Anion effect on the current efficiency during the preparation of tetramethylammonium hydroxide solution by electrolysis. *The Chemical Society of Japan.* 1994:2041-2044.

163. NafionTM Sulfonic Membranes. (n.d.). Nafion. Retrieved July 31, 2022, from https://www.nafion.com/en/products/sulfonic-membranes.

164. Merk. 2022; https://www.sigmaaldrich.com/GB/en/product/aldrich/563994, 2022.

165. Delfrate A. Chlorine–Alkaline Electrolysis – Technology and Use and Economy. *Hydrogen Science and Engineering : Materials, Processes, Systems and Technology*2016:41-56.

166. Yu JK, Sun H, Zhao LL, et al. Effects of electrolyte concentration and current density on the properties of electro-deposited NiFeW alloy coatings. *Bulletin of Materials Science.* 2017;40(3):577-582.

167. Ma Y, Wang X, Stopić S, et al. Preparation of Vanadium Oxides from a Vanadium (IV) Strip Liquor Extracted from Vanadium-Bearing Shale Using an Eco-Friendly Method. *Metals.* 11/27 2018;8:994.

168. El-Tawil SZ, Morsi IM, Ahmed Farag IS, Abdalla FHA. Pure vanadium pentoxide from boiler ash. *International Journal of Refractory Metals and Hard Materials.* 1992/01/01/ 1992;11(1):35-41.

169. Sun ZJGTFT. Analysis on new vanadium technologies and prospects of vanadium industry. 2012;33(1):1-7.

170. Kerherve G. ,2022, Self oxidation of organic materials in XPS chamber. Personal Communication - Royal School of Mines Imperial college.

171. Dewan A, Kakati D, Das B. Synthesis and crystal structure of a triprotonated decavanadate, [(C 6H5CH2)(CH3)3N] 3[H3V10O28].3H2O. *Indian Journal of Chemistry - Section A Inorganic, Physical, Theoretical and Analytical Chemistry.* 01/01 2010;49:39-44.

172. Truebenbach CS, Hercules DM, Houalla M. Characterization of isopoly tungstate using time-of-flight electrospray mass spectrometry. *Fresenius' Journal of Analytical Chemistry.* 2001/02/01 2001;369(3):335-341.

173. Wang Z-h, Zheng S-l, Wang S-n, et al. Research and prospect on extraction of vanadium from vanadium slag by liquid oxidation technologies. *Transactions of Nonferrous Metals Society of China.* 2014/05/01/ 2014;24(5):1273-1288.

174. Hui Bin Liu BL, Lan Jie Li, Shi Li Zheng, Hao Du, Shao Na Wang, Dong Hui Chen, Jian Qi, Yi Zhang. Novel Methods to Extract Vanadium from Vanadium Slag by Liquid Oxidation Technology. *Advanced Materials Research* 2011; 396-398:1786-1793.

175. Schreiber C, Zapp E, Aguiar CRLd, Brondani PB. Cotton fibers bleaching through in situ electrochemical generation of oxidant agents. *Research, Society and Development.* 2021;10(10).

176. Vitero F, Monllor P, Bonet-Aracil M, Morallon E, Quijada C. Electrobleaching of cotton fabrics in sodium chloride solution. *Vlakna a Textil.* 01/01 2017;24:32-36.

177. Barton LJ, Inventor. César QUIJADA TOMÁSFelipe Nicolás VITERO PÉREZPablo MONLLOR PÉREZMaría Angeles BONET ARACILEmilia MORALLÓN NÚÑEZ 2016.

178. Boal; AK, Rivera; S, Sanchez; J, Inventors; De Nora Miox Inc, assignee. Electrochemical Generation of Quaternary Ammonium Compounds.2012.

179. Ferrigno R, Comninellis C, Reid V, Modes C, Scannell R, Girault HH. Coplanar interdigitated band electrodes for electrosynthesis. Part 6. hypochlorite electrogeneration from sea water electrolysis. *Electrochimica Acta.* 1999/04/15/ 1999;44(17):2871-2878.

180. Zoller U, Sosis P. *Handbook of Detergents, Part F: Production*: CRC Press; 2008.

181. Ronco C, Mishkin GJ. *Disinfection by Sodium Hypochlorite: Dialysis Applications*: Karger; 2007.

182. Trypuć M, Kiełkowska U, Chałat M. Solubility Investigations in the NaCl + V2O5 + H2O System from 293 K to 323 K. *Journal of Chemical & Engineering Data.* 2002/07/01 2002;47(4):765-767.

183. Kuhn AT, Lartey RBJCIT. Electrolytic generation "in-situ" of sodium hypochlorite. 1975;47(4):129-135.

184. Kuznetsov NN, Bogoslovskii SY, Boldyrev VS. Specifics of studying electrochlorination in a student chemistry practical. *Journal of Physics: Conference Series.* 2019;1348(1).

185. Salmi T, Grénman H, Wärnå J, Murzin DY. New modelling approach to liquid–solid reaction kinetics: From ideal particles to real particles. *Chemical Engineering Research and Design.* 2013;91(10):1876-1889.

186. Cheng CY, Kelsall GH. Models of Hypochlorite production in electrochemical reactors with plate and porous anodes. *Journal of Applied Electrochemistry.* 2007/11/01 2007;37(11):1203-1217.

187. Kelsall GH. Hypochlorite electro-generation. I. A parametric study of a parallel plate electrode cell. *Journal of Applied Electrochemistry.* 1984/03/01 1984;14(2):177-186.

188. Chinello E, H. Hashemi SM, Psaltis D, Moser C. Editors' Choice—Solar-Electrochemical Platforms for Sodium Hypochlorite Generation in Developing Countries. *Journal of The Electrochemical Society.* 2019;166(12):E336-E346.

189. Levenspiel O. *Chemical Reaction Engineering*: Wiley; 1998.

190. Yang Y, Zhang Y, Liu T, Huang J. Improved properties of positive electrolyte for a vanadium redox flow battery by adding taurine. *Research on Chemical Intermediates.* 2017;44(2):769-786.

191. Li L, Kim S, Wang W, et al. A Stable Vanadium Redox-Flow Battery with High Energy Density for Large-Scale Energy Storage. *Advanced Energy Materials.* 2011;1(3):394-400.

192. Wu X, Liu J, Xiang X, Zhang J, Hu J, Wu Y. Electrolytes for vanadium redox flow batteries. *Pure and Applied Chemistry.* 01/19 2014;86.

193. Ding MA-O, Liu T, Zhang Y, Cai Z, Yang Y, Yuan Y. Effect of Fe(III) on the positive electrolyte for vanadium redox flow battery. (2054-5703 (Print)).

194. G. Wang JWC, X.Q. Wang, J. Tian, H. Kang, X.J. Zhu, Y. Zhang, X.J. Liu, R.L. Wang, J. *Electroanal. Chem.* 2013; 709:31–38.

195. Habekost AJWJoCE. Vanadium Redox Flow Batteries with Different Electrodes and Membranes. 2018;6(1):8-13.

196. Towler G, Sinnott R. *Chemical Engineering Design: Principles, Practice and Economics of Plant and Process Design*: Elsevier Science; 2012.

197. Ramdin M, Morrison ART, de Groen M, et al. High-Pressure Electrochemical Reduction of CO2 to Formic Acid/Formate: Effect of pH on the Downstream Separation Process and Economics. *Industrial & Engineering Chemistry Research.* 2019;58(51):22718-22740.

198. Flieger J, Grushka EB, Zelazko C. *J. Anal. Pharm. Chem.* 2014;1:1009.

199. Greaves TL, Drummond CJ. Protic Ionic Liquids: Properties and Applications. *Chem. Rev.* 2008;108:206.

200. Gryglewicz S, Rutkoswski M, Steininger M. *Fuel Proc. Technol.* 1991;27(3):279.

201. Holbrey JD, Seddon KR. *J. Chem. Soc., Dalton Trans.* 1999:2133.

202. CheGuide. McCabe Thiele Diagram. 2015; https://cheguide.com/mccabe_thiele.html. Accessed 21/04/2022, 2022.

203. Kuo PJ, Lee CL, Wang JH, Hsieh SY, Huang SC, Lam CF. Inhalation of volatile anesthetics via a laryngeal mask is associated with lower incidence of intraoperative awareness in non-critically ill patients. PLoS One. 2017;12(10):e0186337. https://doi. org/10.1371/journal.pone.0186337. *AORN Journal.* 2019/01/29 2019;109(2):256-261.

204. Howard KA, Mitchell HL, Waghore RH, Inventors. US patent 43595961982.

205. Ulrich GD. *A Guide to Chemical Engineering Process Design and Economics*: Wiley; 1984.

206. Peters MS, Timmerhaus KD, West RE. *Plant Design and Economics for Chemical Engineers*: McGraw-Hill Education; 2003.

207. Valle-Riestra JF. *Project Evaluation in the Chemical Process Industries*: McGraw-Hill; 1983.

208. Turton R, Bailie RC, Whiting WB, Shaeiwitz JA. *Analysis, Synthesis, and Design of Chemical Processes*: Prentice Hall; 2009.

209. Sinnott R, Towler, G. *Chemical Engineering Design Principles, Practice and Economics of Plant and Process Design*: Netherlands: Elsevier Science.; 2013.

210. Alfredsson NRVKA, Inventor. Method of recovering metals out of soot originating from the combustion of oil1976.

211. Harding K. *Bitumen Beyond Combustion - Phase 2 Report*: Alberta Innovates;2018.

212. Information NCfB. PubChem Compound Summary for CID 516859, Ammonium metavanadate. 2022; https://pubchem.ncbi.nlm.nih.gov/compound/Ammonium-metavanadate. Accessed 12/07/2022, 2022.
213. Alexandrov AA. The Equations for Thermophysical Properties of Aqueous Solutions of Sodium Hydroxide. *14th International Conference on the Properties of Water and Steam* Kyoto2004.
214. Thomas DS, Kandaswamy A. Economic Guide for Identifying and Evaluating Industry Research Investments. *NIST Advanced Manufacturing Series 200-8.* 2019.
215. belastingdienst. Naar de startpagina van de Belastingdienst. 2022; https://www.belastingdienst.nl/wps/wcm/connect/bldcontentnl/belastingdienst/zakelijk/winst/vennootschapsbelasting/tarieven_vennootschapsbelasting.
216. Fastmarkets. Vanadium pentoxide 98% V2O5 min, fob China, $/lb V2O5. 2022; https://www.fastmarkets.com/search?q=vanadium#nt=navsearch. Accessed 28/04/2022.
217. Alibaba. TMAH Tetramethyl Ammonium Hydroxide price. 2022; https://www.alibaba.com/product-detail/25-TMAH-Tetramethyl-Ammonium-Hydroxide-with_1600304701114.html?spm=a2700.7724857.normal_offer.d_title.538c2e94M7WIF6. Accessed 28/04/2022.
218. 11 A. ASPEN Capital Cost Estimator Tool. In: Hyprotech AT, ed2022.
219. CHEMICAL ENGINEERING PLANT COST INDEX. Jan 2022; https://digitallib.nipc.ir/ic/Portals/0/Introduce/cost%20index/cost%20index%202022-jan.pdf?ver=-Z9nX3zmQLJ3hza3AFfKFA%3D%3D, 23/04/2022.
220. US Dollar Spot Exchange Rates for 2022. 2022; https://www.exchangerates.org.uk/USD-GBP-spot-exchange-rates-history-2022.html#:~:text=Average%20exchange%20rate%20in%202022,GBP%20on%2013%20Jan%202022. Accessed 23/04/2022.
221. Chen L, Sharifzadeh M, Mac Dowell N, Welton T, Shah N, Hallett JP. Inexpensive ionic liquids: [HSO4]−-based solvent production at bulk scale. *Green Chem.* 2014;16(6):3098-3106.
222. Tran L-H, Tanong K, Jabir AD, Mercier G, Blais J-F. Hydrometallurgical Process and Economic Evaluation for Recovery of Zinc and Manganese from Spent Alkaline Batteries. *Metals.* 2020;10(9).
223. Todd S. Fayram CGA. NSC Hydrometallurgical Pressure Oxidation of Combined Copper and Molybdenum Concentrates. *Journal of Powder Metallurgy & Mining.* 2013;02(03).
224. GOV UK. Carbon emissions tax. 2022; https://www.gov.uk/government/publications/carbon-emmisions-tax/carbon-emmisions-tax#:~:text=All%20emissions%20that%20exceed%20the,of%20%C2%A316%20per%20tonne. Accessed 30/04/2022.

9. Appendix A

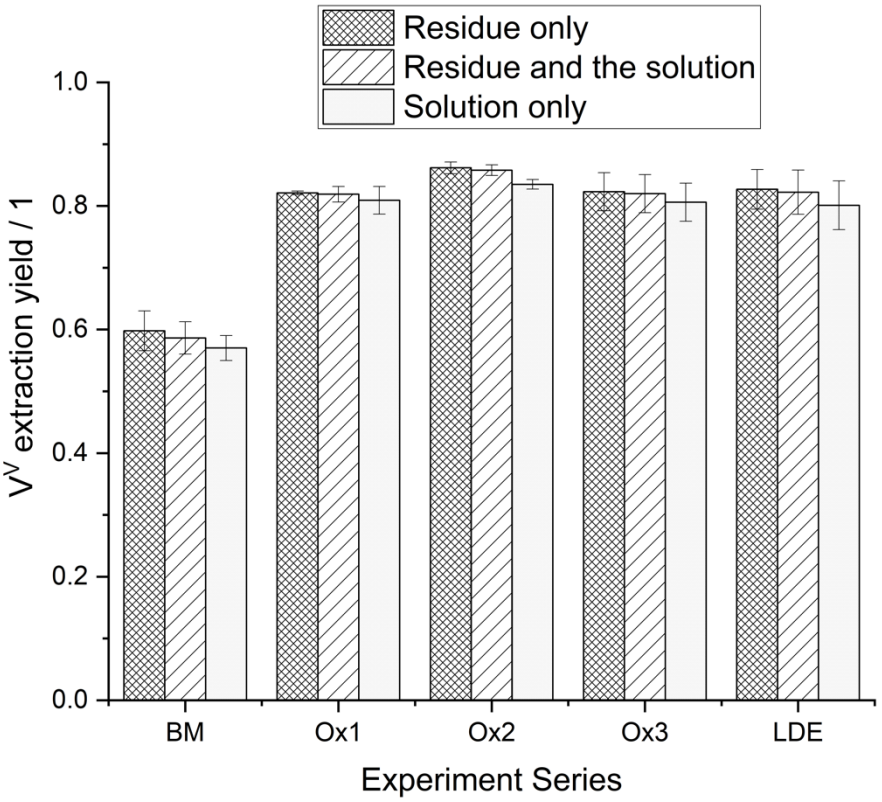


Figure A9-1. Vanadium(V) extraction yields based on three difference approaches for BM: Benchmark 960 min and no additives; Ox1: oxidative leaching experiment 1 with 0.2 mol dm^{-3} $NaClO_2$ and 300 min; Ox2: oxidative leaching experiment 2 with 0.4 mol dm^{-3} $NaClO_2$ and 300 min; Ox3: oxidative leaching experiment 3 with 0.2 mol dm^{-3} $NaClO_2$ and 300 min; LDE: long duration experiment , 7-day leaching with no additives.

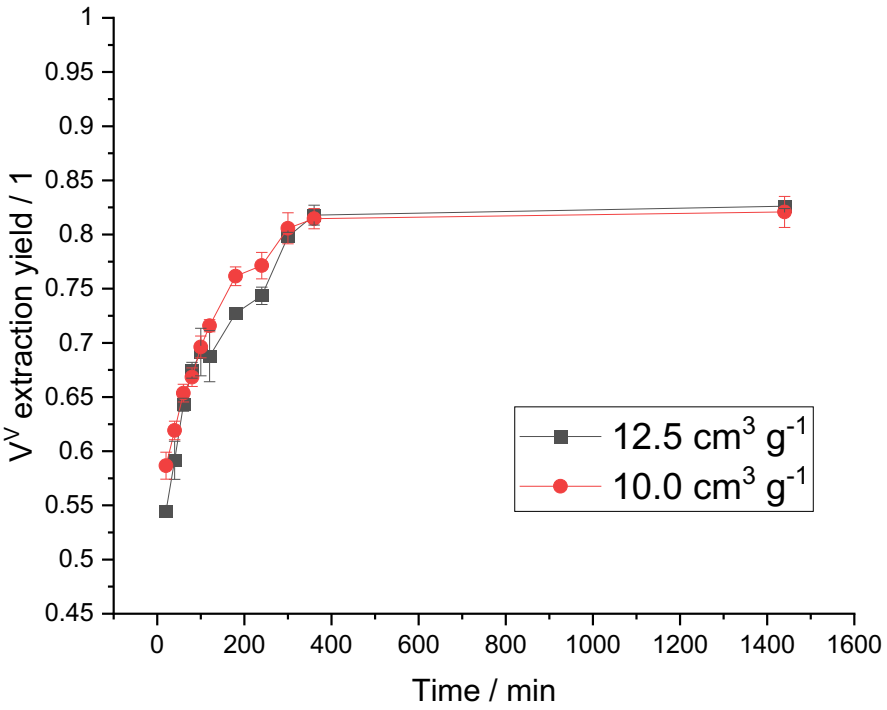


Figure A9-2. Time dependence of vanadium(V) extraction yields for liquid-to-solid ratios of 10 and 12 cm^{-3} g^{-1}.

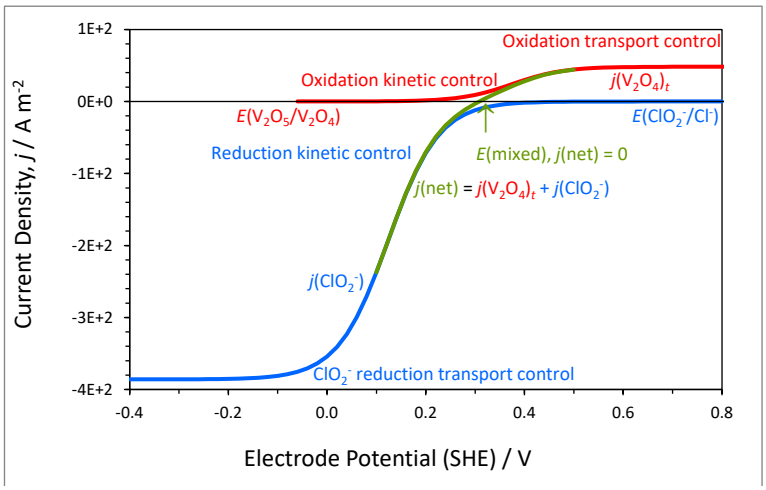


Figure A9-3. Schematic plot of mixed potential kinetics for (time / conversion dependent) oxidative dissolution of V2O4 by reduction of ClO2- ions. Spontaneous reaction occurs at Emixed at which jnet = 0

Table A1. Evaluated the left-hand side and the right-hand side of (Equation 3-32 for different reaction conditions

Manipulated Variable	Left Formula (measured)	Right Formula (predicted)	Error %
t = 240 min	0.1435	0.1350	6%
t = 300 min	0.1805	0.1687	7%
t = 360 min	0.1920	0.2025	5%
t = 240 min **[$NaClO_2$] = 0.221 mol dm^{-3}**	0.1315	0.1234	6%
t = 300 min **[$NaClO_2$] = 0.221 mol dm^{-3}**	0.1526	0.1543	1%
t = 360 min **[$NaClO_2$] = 0.221 mol dm^{-3}**	0.1827	0.1851	1%
t = 120 min **T = 35.15 K**	0.0371	0.0348	6%
t = 180 min **T = 353.15 K**	0.0511	0.0522	2%